وزارة التعليم العالي والبحث العلمي

BADJI MOKHTAR-ANNABA UNIVERSITY
UNIVERSITÉ BADJI MOKHTAR-ANNABA

جامعة باجي مختار- عنابة

FACULTY OF EARTH SCIENCES
DEPARTMENT OF GEOLOGY
LABORATORY : Laboratoire de Recherche de Géologie (LRG)

Year: 2025

T H E S I S

Presented to obtain the diploma of

Doctorate 3rd Cycle (LMD)

Discipline : Geology

Option : Mineral Resources, Geomaterials, and Environment

Title

The Troubia, Ain Diba and Ain Kissa Phosphorite Occurrences (Tebessa Region, NE Algeria): Sedimentology, Petrology and Geochemistry

Les indices de phosphates de Troubia, Ain Diba, Ain Kissa (Région de Tébessa, NE algérien) : Sédimentologie, gîtologie et géochimie

by

Diab Ibtissam

Defended publicly on: 11/02/2026

SUPERVISOR	LAOUAR Rabah	Professor	Badji Mokhtar University, Annaba
CO-SUPERVISOR	DEGAICHIA Amor	MCA	Larbi Tebessi University, Tébessa
PRESIDENT	TLILI Mohamed	MCA	Badji Mokhtar University, Annaba
EXAMINER	HALIMI Fahima	MCA	Badji Mokhtar University, Annaba
EXAMINER	DAAS-AMIOUR Mohamed	MCA	Frères Mentouri University, Constantine
EXAMINER	LEKOUI Abdelmalek	MCA	Mohamed Seddik Benyahia University, Jijel

Academic Year: 2025/2026

I did it الحمد لله

قال الله تعالى:

«وَيَرْزُقْهُ مِنْ حَيْثُ لَا يَحْتَسِبُ ۚ وَمَنْ يَتَوَكَّلْ عَلَى اللَّهِ فَهُوَ حَسْبُهُ ۚ إِنَّ اللَّهَ بَالِغُ أَمْرِهِ ۚ قَدْ جَعَلَ اللَّهُ لِكُلِّ شَيْءٍ قَدْرًا»

الآية 3 من سورة الطلاق. قران كريم

«And provides for him from where he does not expect. And whoever relies upon Allah - then He is sufficient for him. Indeed, Allah will accomplish His purpose. Allah has already set for everything a [decreed] extent».

Verse 3 of Surat At-Talaq. Holy Quran

"The mystery of human existence lies not just in surviving, but in finding something worth living for."

The Brothers Karamazov, 1880, Fyodor Dostoevsky.

"Success is 1% talent and 99% hard work."

Thomas Edison – American Inventor.

I dedicate...

The time has come to dedicate the fruit of many years of study! As a testament to your sacrifices, may every word of this thesis express my gratitude and deep appreciation:

I dedicate this work to myself, for the strength, determination, and resilience that carried me through this journey.

To myself, for believing, enduring, and never giving up.

To my mother, who instilled in me morals and respect, and inspired me with patience and ambition to achieve my dreams.

To my dear father, who taught me to work with sincerity, enjoy what I love, and be patient, strong, and honest in everything I do. My father is my role model.

To my dear brothers and sisters (Fanny, Chaouki, Radia, Besma, Seif, Mohcen, Tarak, and Maroua), who have always been a source of support and encouragement, shared my joy and sorrow, my success and my challenges, and taught me the meaning of love, sharing, and patience.

To my paternal aunts (Bouba and Nasira) and my maternal aunt (Halima), for their constant support.

To my friends (Mahbouba, Sakina, Thiziri, Iness, Samira, Ouafa, Imene, Rahima, Meriem, Ibtissem, Sabah, Sara, Fatima, Bilal, Khaled, Yahia, Abdelaziz, Hamed, and Houssem), whose friendship has brightened my days with love, support, and laughter, and made every challenge easier and more beautiful.

To everyone who taught me a letter, guided me with a step, or opened for me a door of light.

To all who love science and encourage knowledge, you are the ones who illuminate our paths with knowledge and wisdom.

Many thanks, and may God keep you safe.

∞ Ibtissam Diab. Phosphorites ∞

Acknowledgements

I would like to express my sincere gratitude to my thesis supervisor, **Prof. Rabah Laouar**. I cannot find the words to thank him, not only for supervising this thesis, but also for his research methodology and ethics. Thank you for your invaluable support in cultivating my academic and scientific character.

I wish to extend my heartfelt thanks to **Dr. Amor Degaichia** for his constant support and for always accompanying me in the field. The advancement of this research would not have been achievable without his invaluable help and support.

I would like to express my sincere thanks and gratitude to all those who have helped, supported and accompanied me, as well as to all those who have welcomed and supported me in my efforts to accomplish this work. Your support and encouragement have had a significant impact on this achievement and have directly contributed to my success and progress. To everyone who taught me a letter, guided me with a step, or opened for me a door of light:

Pr. Delphine Bosch from the University of Géosciences Montpellier France, for her assistance in conducting chemical analyses at the ICP-MS laboratory, Géosciences Montpellier France.

Dr. Olivier Bruguier from the University of Géosciences Montpellier France, for his assistance in conducting chemical analyses at the ICP-MS laboratory, Géosciences Montpellier France.

Pr. Ali Tlili from the University of Sfax (Tunisia) for his assistance in conducting chemical and mineralogical analyses in the mineralogical laboratory, Faculty of Sciences, Sfax University.

Pr. Salah Bouhlel from the University Tunis El Manar, Tunisia, for his assistance in conducting mineralogical analyses at the Laboratory of the Crystallography and Applied Thermodynamics, Faculty of Science, Tunis El Manar, Tunisia.

Pr. Rabah Kechiched from the University of Ouargla for his assistance in conducting Principal Component Analysis (PCA) analysis and for his invaluable support throughout all stages of this work.

Pr. Sihem Salmi Laouar for her insightful advice availability and the genuine interest she has shown in my work.

I would like to sincerely thank the honorable members of the jury: **Dr. TLILI Mohamed**, **Dr. Halimi Fahima**, **Dr. Daas-Amiour Mohamed**, and **Dr. LEKOUI Abdelmalek** for accepting to evaluate this work. I deeply appreciate your time, valuable comments, and constructive suggestions, which have greatly contributed to improving this thesis.

Pr. Mourad Zaabat from the University of Oum El Bouaghi, Algeria; for his assistance in conducting SEM-EDS analysis at the Institute of Applied Science and Technology, University Larbi Ben M'hidi Oum El Bouaghi, Algeria.

Dr. Thameur Mnif from the University of Sfax (Tunisia), for his assistance in conducting granolometry analyses at the Faculty of Sciences, Sfax University.

Dr. Sameh Dammak from the University of Sfax (Tunisia), for her assistance in conducting FTIR analyses in the physical laboratory at the Faculty of Sciences, Sfax University.

Mr. Djafar Alem for his efforts in sample preparation and thin section confections in addition of his encouragements.

Badji Mokhtar University- Annaba, for his for its funding of this training initiative.

of this training initiative. Special thanks go to the heads of the Geology department. Annaba, for their administrative support.

Dr. Faten Jaballi from the University of Sfax (Tunisia), for her welcomed and supported me in my efforts to accomplish this work.

PhD. Mahbouba Moussaoui from the University of Mohamed Seddik Ben Yahia Jijel, Algeria, for helping to prepare samples fro SEM analysis.

Mr. Mustapha Metiri and Mr. Hicham Brahmia for their assistance during supplementary SEM-EDS analyses at the School of Mines, Annaba.

Pr. Boufatouha Youcef from the University of Mohamed Seddik Ben Yahia Jijel, Algeria, who believed in my abilities and said words to me that remain etched in my mind to this day: «You deserve success ».

I would like to extend my sincere thanks to the Master's students that I had the honour of supervising alongside Professor Rabah Laouar: **Saley Hamadan RHISSA (**from Nigeria**), Abdoul Aziz Diallo (**from Mali**), Amani Antouri, and RAHEM Aimen Abd el mallek.**

I would like to extend my sincere thanks and appreciation to the **driver's bus**, the **residents** of Tebessa, the **director** of the accommodation, and the state **police** for their cooperation.

I would like to extend my sincere thanks to all the members of the **2000 Shaiba residence in Sidi Amar** (**Adel, Khemessi, Hichem, and Bouakaze**), for their cooperation and assistance in transporting and hiding the rocks.

I thank my entire family for their support throughout my journey. Each one, with their name, expresses my deepest gratitude.

Table of contents

Chapter I

An overview on phosphorites

Chapter II

Geological setting

Chapter III

Sedimentological study of the Troubia, Ain Dibba, and Ain Kissa phosphorites

Chapter IV

Petrography and mineralogy of the Troubia, Ain Dibba and Ain Kissa phosphorites

Chapter V

Geochemistry of the Troubia, Ain Dibba and Ain Kissa phosphorites

Chapter VI
Paleo-depositional environment and REE enrichment

List of Figures

List of Tables

Abstract

The phosphorite rocks in the northern basin of Tebessa region were deposited during the Upper Paleocene–Lower Eocene period around the Kasserine Paleo-Island, and coincide well with PETM events. These rocks are extensively studied across various scales, such as whole-rocks, particle separates, matrix, and grain-size fractions. Decimeter- to meter-thick phosphorite layers are interbedded within marls, dolostones, and silica-rich carbonate rocks. Although partly exploited in the early 20th century, the Troubia, Ain Dibba, and Ain Kissa deposits received limited exploration due to their lower P_2O_5 content and ore reserves. The present study aims to highlight the knowledge of their critical trace and REE contents, as well as the understanding of their paleo-depositional environment. Selected samples were analyzed using optical microscopy, XRD-FTIR, SEM-EDS, XRF, and ICM-MS methods. Petrographic data show that these phosphorites are mainly composed of pellets, coprolites, bioclasts and rare glauconite, gypsum, and detrital quartz grains. These constituents are cemented by calcareous, siliceous or rarely clayey matrix. Here, amorphous silica, represented by opal-CT; and crystalline silica represented by quartz grains. XRD, FTIR and SEM data reveal that phosphorites are composed of CFA, Opal-CT, quartz, dolomite, calcite, gypsum, and zeolites. This siliceous material may be originated from fragmented fossils of siliceous tests, and precipitated silica, or quartz detrital grains. The XRF and ICP-MS chemical analyses show that the studied phosphorites are not as rich neither in P_2O_5 nor in REE contents (average = 20.24 wt% and average = 252 ppm, respectively) as the southern basin Djebel Onk phosphorites. The highest Ce/Ce* and lowest Eu/Eu* anomalies are recorded in the relatively REE- and glauconite-rich lower layers, while the lowest Ce/Ce* and highest Eu/Eu* values, indicating more oxic conditions, characterize the glauconite-free, REE-poor upper layers. The redox-sensitive trace element (Cr, Ni, V, U) data display transition from relatively sub-oxic to oxic conditions (from the lower to the upper layers), indicating that slightly reducing conditions during early diagenesis enabled uptake both REE and trace element onto apatite and glauconite from pore waters through substitution and adsorption mechanisms. These features indicate that phosphorites from the northern basin were deposited, through upwelling currents, in a more open, shallower, oxygenated, fast sedimentation, and agitated environment during the Paleocene-Eocene phosphogenesis, with less PETM influence, in Tebessa region.

Keywords: Phosphorites, Northern basin, REE-enrichment, Upwelling currents, PETM, Paleo-depositional environment, Tebessa.

Résumé

Les roches phosphatées du bassin nord de la région de Tebessa se sont déposées au cours du Paléocène-l'Éocène autour de la paléo-Île de Kasserine, et coïncident bien avec les événements du PETM (Paleocene-Eocene Thermal Maximum). Ces roches ont fait l'objet d'études approfondies à différentes échelles, telles que roche totale, particules séparées, matrice et fractions granulométriques. Des couches de phosphate d'une épaisseur de quelques décimètres à plusieurs mètres sont intercalées dans des marnes, des calcaires dolomitiques et des calcaires riches en silice amorphe (silex). Bien qu'elles aient été partiellement exploitées au début du XXe siècle, les gisements de Troubia, Ain Dibba, et d'Ain Kissa ont fait l'objet d'une exploration limitée en raison de leur faible réserve. La présente étude vise à mettre en évidence les connaissances relatives à leur teneur en éléments traces et en terres rares, ainsi que la compréhension de leur paléo-environnement de dépôt. Les échantillons sélectionnés ont été analysés à l'aide des méthodes suivantes : microscopie optique, XRD-FTIR, SEM-EDS, XRF et ICM-MS. Les données pétrographiques montrent que ces phosphorites sont principalement composées de pellets, de coprolithes, de bioclastes et, plus rarement de glauconite, de gypse et de grains de quartz détritiques. Ces constituants sont cimentés par une matrice carbonaté, siliceuse ou, plus rarement argileuse. Ici, la silice amorphe (silex), représentée par l'opale-CT, et la silice cristalline, représentée par les grains de quartz. Les données XRD, FTIR et SEM révèlent que les phosphorites sont composées de CFA, d'opale-CT, de quartz, de dolomite, de calcite, de gypse et de rares zéolites. La silice peut provenir de fossiles fragmentés de tests siliceux, de silice précipitée ou de quartz détritique. Les analyses chimiques XRF et ICP-MS montrent que les phosphorites ne sont pas aussi riches en P_2O_5 ni en terres rares (moyenne = 20,24 % en poids et moyenne = 252 ppm, respectivement). Les anomalies Ce/Ce* les plus élevées et Eu/Eu* les plus faibles sont enregistrées dans les couches inférieures riches en REE et en glauconite, tandis que les valeurs Ce/Ce* les plus faibles et Eu/Eu* les plus élevées, indiquant des conditions plus oxydantes, caractérisent les couches supérieures pauvres en REE et exemptes de glauconite. Les données relatives aux éléments traces sensibles au l'oxydoréduction (Cr, Ni, V, U) montrent une transition de conditions relativement suboxiques à des conditions oxiques (des couches inférieures aux couches supérieures), indiquant que des conditions légèrement réductrices au début de la diagenèse ont permis l'absorption des ETR et des éléments traces par l'apatite et la glauconite à partir des eaux interstitielles par des mécanismes de substitution et d'adsorption. Ces caractéristiques indiquent que les phosphorites du bassin nord se sont déposées, par le biais de courants ascendants, dans un environnement

plus ouvert, moins profond, oxygéné, à sédimentation rapide et agité pendant la phosphogenèse du Paléocène-Éocène, avec une influence moindre du PETM, dans la région de Tebessa.

Mots-clés: Phosphorites, Bassin nord, Enrichissement en REE, Upwelling, PETM, Environnement paléo-sédimentaire, Tebessa.

ملخص

ترسبت صخور الفوسفات في الحوض الشمالي لمنطقة تبسة خلال فترة الباليوسين الأعلى والإيوسين الأدنى حول جزيرة القصرين القديمة، وتتزامن بشكل جيد مع أحداث PETM .دُرست هذه الصخور على نطاق واسع عبر مقاييس مختلفة، مثل الصخور الكاملة، وفواصل الجسيمات، والمصفوفة، وكسور حجم الحبيبات .تتراكب طبقات الفوسفات التي يتراوح سمكها بين ديسيمتر ومتر داخل صخور المارل والدولوستونات والكربونات الغنية بالسيليكا .على الرغم من استغلالها جزئيًا في أوائل القرن العشرين، إلا أن رواسب تروبيا وعين دبة وعين كيسة لم تخضع إلا لقدر محدود من الاستكشاف نظرًا لانخفاض محتواها من الفوسفور واحتياطياتها من الخام. تهدف هذه الدراسة إلى تسليط الضوء على معرفة محتواها من العناصر النادرة والأثرية، بالإضافة إلى فهم بيئتها الترسيبية القديمة .حُلّلت عينات مختارة باستخدام المجهر الضوئي، وتقنياتXRD-FTIR ، وSEM-EDS، وXRF، و.ICM-MS.تُظهر البيانات الصخرية أن الفوسفات تتكون بشكل أساسي من بيلات، وكوبروليت، وحطام عضوي، وحبيبات نادرة من الجلوكونيت والجبس والكوارتز الفتاتي. هذه المكونات مُثبتة بمصفوفة كلسية، أو سيليسية، أو نادرًا ما تكون طينية .هنا، السيليكا غير المتبلورة، ممثلةً بـopal-CT ؛ والسيليكا البلورية ممثلةً بحبيبات الكوارتز .تُظهر بيانات XRD و FTIRوSEM أن الفوسفات تتكون من CFA وOpal-CT والكوارتز والدولوميت والكالسيت والجبس والزيوليت .قد تكون هذه المواد السيليسية منشأها أحافير مجزأة من فحوصات سيليسية، وسيليكا مترسبة، أو حبيبات تفتيت الكوارتز. تُظهر التحليلات الكيميائية بتقنية XRF و ICP-MSأن الفوسفات ليست غنيةً بـ P_2O_5 أو بمحتوى العناصر الأرضية النادرة (متوسط = 20.24% وزناً ومتوسط = 252 جزء في المليون، على التوالي). سُجّلت أعلى شذوذات *Ce/Ce وأدنى شذوذ *Eu/Eu في الطبقات السفلية الغنية بالعناصر الأرضية النادرة والغلوكونيت، بينما تُميّز أدنى قيم *Ce/Ce وأعلى قيم*Eu/Eu ، والتي تُشير إلى ظروف أكثر أكسدة، الطبقات العليا الخالية من الغلوكونيت والفقيرة بالعناصر الأرضية النادرة. تُظهر بيانات العناصر النزرة الحساسة للأكسدة والاختزال (الكروم، النيكل، الفناديوم، اليورانيوم) انتقالًا من ظروف شبه مؤكسدة إلى ظروف مؤكسدة نسبيًا (من الطبقات السفلى إلى العليا)، مما يشير إلى أن ظروف الاختزال الطفيفة خلال مرحلة التكوّن المبكر أتاحت امتصاص كلٍّ من العناصر الأرضية النادرة والعناصر النزرة على الأباتيت والغلوكونيت من مياه المسام من خلال آليات الاستبدال والامتصاص. تشير هذه السمات إلى أن الفوسفات من الحوض الشمالي قد ترسبت، من خلال التيارات الصاعدة، في بيئة أكثر انفتاحًا وأقل ضحالة وأكسجينًا وترسيبًا سريعًا واضطرابًا أثناء فسفورية الباليوسين والإيوسين، مع تأثير أقل من احداث PETM، في منطقة تبسة.

الكلمات المفتاحية: الفوسفات، الحوض الشمالي، إثراء العناصر الأرضية النادرة، التيارت الصاعدة، PETM، البيئة الترسيبية القديمة، تبسة.

Introduction

Introduction

The phosphorite rocks in Algeria were deposited during the Upper Paleocene–Lower Eocene period in the western part of the Kasserine Paleo-Island, and coincide well with PETM events (Zachos et al., 2001; Zachos et al., 2007, 2008; Ounis et al., 2008; Buccione et al., 2021; Saouli et al., 2025). These phosphorites belong to the Tethyan phosphorite belt that extends easterly to the Middle East, where phosphogenesis occurred during the Upper Cretaceous–Eocene period (Sassi, 1974; Notholt, 1980; Sheldon, 1987; Notholt et al., 1989; Lucas and Prevot-Lucas, 1995; Lasheen et al., 2022). They are located mainly in the eastern part of the country, precisely in the Tebessa region, which belong to the Eastern Saharan Atlas domain. In this region, the giant Djebel Onk deposit, in the southern basin, now under exploitation, is one example of these deposits. However, in the northern basin minor deposits were identified, such as El Kouif, Dyr, and Tazbent deposits. These rocks have been extensively studied across various scales, such as whole-rocks, particle separates, matrix, and grain-size fractions in order to (a) evaluate their P_2O_5, trace, and rare earth element (REE) contents, (b) assess their economic potential, and (c) reconstruct the paleo-environmental conditions during their formation (e.g., Visse, 1952; Chabou-Mostefai, 1987; Bezzi et al., 2001, 2008; Dassamiour et al., 2013; Garnit et al., 2017; Kechiched et al., 2018; Kechiched et al., 2020; Dassamiour et al., 2021; Farhaoui et al., 2022; Boulemia and Adnet, 2023; Kechiched et al., 2024; Laouar et al., 2024; Aouachria et al., 2025). Besides, other studies were focused on the potentially hazardous elements (PHE) contents in phosphorite ores and their wastes across various sizes (Bezzi et al., 2012; Boumaza et al., 2021, 2023; Saouli et al., 2025), allowing for the evaluation of environmental impacts which pose environmental and health risks. From these studies, the petrographic data show that these phosphorites are mainly composed of pellets, coprolites, bioclasts, glauconites, gypsum, pyrite, and detrital quartz grains, which are cemented by

calcareous, siliceous or clayey matrix. Mineralogically, XRD and SEM data reveal that phosphorites are composed of CFA, Opal-CT, quartz, dolomite, calcite, gypsum, pyrite, clayey minerals and zeolites (heulandite-clinoptilolite). The amorphous silica is represented by opal-CT and crystalline silica is represented by detrital quartz. Geochemical studies show high REE concentrations in the southern basin, reaching ~2000 ppm in glauconite at Bled El Hadba (Laouar et al., 2024) and ~900 ppm in whole-rock and grain-size fractions of phosphorites at Kef Essenoun (Kechiched et al., 2018, 2020; Ferhaoui et al., 2022), compared to moderate contents in the northern basin (470 ppm at El Kouif and 290 ppm at Dyr; Kechiched et al., 2018, 2020). This indicates that phosphorites of the southern basin were more enriched in REE due to relatively reducing conditions that made favorable paleo-environmental conditions to REE uptake from both seawater and pore-water reservoirs during early diagenesis. These conditions are supported by the highest Ce/Ce* and lowest Eu/Eu* anomalies recorded in the lower layers, often are enriched in both REE and glauconite contents, as well as Y/Y* and La/Nd ratios, that highly contribute to glauconitization processes especially during early diagenesis, the relatively slow sedimentation rate and the simultaneous substitution and adsorption mechanisms for REE uptake. However, in the northern basin, the phosphorite show lowest Ce/Ce* and highest Eu/Eu* values which are characteristics of the glauconite-free and REE-poor upper layers, indicating more oxic conditions with limited PETM events, and faster sedimentation that contribute to poorer contents in glauconite (weak glauconitization processes). The redox-sensitive trace element (Cr, Ni, V, U) data display transition from relatively sub-oxic to oxic conditions (from the lower to the upper layers), indicating that relatively reducing conditions during early diagenesis enabled uptake trace element onto apatite and glauconite from pore waters through substitution and adsorption mechanisms.

Although partly exploited in the early 20th century, the Troubia, Ain Dibba and Ain Kissa deposits, which are located at about 10 km north of the Tebessa town, received limited

exploration due to their lower P_2O_5 content and ore reserves, and have never been subject to detailed petrological and geochemical investigations. The objectives of this study are to present, for the first time, the detailed petrographic and mineralogical features, as well as major, trace and REE geochemical investigations. To achieve these objectives, field observations and detailed descriptions of the lithological succession were made, and selected samples were analyzed using the following methods: optical microscopy, XRD, SEM-EDS, XRF and ICM-MS.

To facilitate the presentation of the results of this work, the following chapters organization is adopted:

- Chapter I includes an overview on phosphorites.
- Chapter II presents the geological setting of the studied areas.
- Chapter III addresses the sedimentological part of phosphate ores with implications on the mode of transport of phosphate particles.
- Chapter IV displays the petrographic and mineralogical features of the Troubia, Ain Dibba, and Ain Kissa phosphorites
- Chapter V provides a geochemical study of the Troubia, Ain Dibba, and Ain Kissa phosphorites.
- Chapter VI examines the paleo-depositional environement and REE enrichment.
- Conclusion.

Chapter I

An overview on phosphorites

Chapter I

An overview on phosphorites

Phosphorus (P) is a necessary element of all living cells and is involved in many metabolic processes (Albaum, 1952). It is crucial for starch synthesis, a fundamental building block of nucleic acids, possibly required for photosynthesis, a significant component of bones and teeth, and a process that many species use to make their shells. Phosphorus is one of the most important plant nutrients, yet it is rather scarce in most soils, and controlling plant growth greatly depends on its availability.

I. 1. Phosphate rocks

Marine phosphorites are biochemical rocks rich in phosphorus, with a P_2O_5 content of more than 18% (Boggs 2009). Phosphate minerals, which are utilized in many fields, are widely exploited as fertilizers (90%) and chemical (10%) industries (Lauriente, 1996).

I. 2. Phosphogenesis process

One of the most plausible hypotheses, proposed by Kazakov in 1930 and 1937, stems from oceanographic research findings. These studies revealed a notable trend: P_2O_5 concentrations in seawater increase with depth, being lowest in the photosynthesis-rich surface zone and highest at ~500 m. Upwelling currents create favorable conditions for phosphorite formation by rising cold, nutrient-rich deep waters, enriched in phosphorus (P) and silica (Si), to continental shelf margins (Cook and Shergold, 1984; Fig. I.1). After that, phosphorus is concentrated by bacteria at the sediment–water interface or in interstitial pore waters (Riggs, 1984). In warmer surface waters, pH levels rise while the partial pressure of CO_2 drops. This

shift prompts the precipitation of $CaCO_3$, followed by phosphates. Consequently, chemical phosphate sedimentation doesn't occur in deep areas, where CO_2 pressure is too high, nor in the photosynthesis zone where phosphorus is utilized. The range of around 50 to 500 meters emerges as the zone where phosphate precipitation predominantly occurs. This theory was later refined by Visse in 1952, who suggested a distinction between the genesis and accumulation environments (Kechiched, 2011).

The Cretaceous–Eocene period was marked by significant global climatic changes, geodynamic and tectonic evolution, Tethyan Circumglobal Current (TCC), and different paleogeographic settings (Scotese, 2008), which have favored the formation of these phosphorites (Föllmi, 1996; Abed et al., 2016). The latter are linked to the subduction/collision tectonics of the Tethys Sea between the African and Eurasian plates, which started in the late Cretaceous (e.g., Zargouni, 1984; Laville et al., 2004). These complex plate-tectonics created intra-plate paleo-highs and land uplift on the northern to northwestern Afro-Arabian platform, such as the Kasserine Island (Svoboda, 1989), the Ha'il, Rutba, and Sirhan highs, the Ga'ara Dome, and the Syrian Arc hinterland (Guiraud and Bosworth, 1997). Obstruction upwelling prevailed along these paleo highs, which are rich in silica (Si) and phosphorus (P). Moreover, the Tethyan Circum-global Current (TCC) is thought to have moved from east to west over the southern boundary of the Afro-Arabian continental shelf during the Late Cretaceous (Abed, 2013). In addition, global warming events, including the K/Pg and PETM, intensified weathering, nutrient flux and organic matter burial further, promoting widespread phosphorite deposition (Zachos et al., 2006, 2010; Zachos et al., 2008; Hessler et al., 2017; Keller et al., 2018; Buccione et al., 2021; Kechiched et al., 2024).

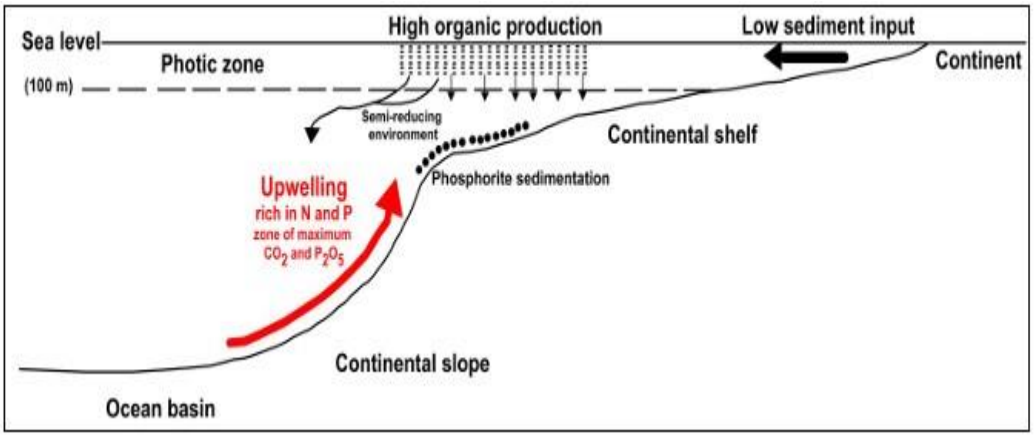

Fig. I. 1. Kazakov model of phosphogenesis (1930).

These deposits manifest in two primary types:

- **Continental shelf deposits:** characterized by light coloration, nodular or pseudo oolithic structures, frequent association with glauconite, and various quartzose detrital elements. These deposits seem to correlate with transgressions (Kechiched, 2011).
- **Borderline geosynclinal deposits:** These yield darker-colored ores with a pseudo-oolithic structure, generally accompanied by clayey exogangue and significant siliceous formations. This type of deposit is suggestive of a more regressive context (Kechiched, 2011).

I. 3. Classification of phosphate deposits

In general, calcium phosphate is found in magmatic rocks and in sedimentary rocks of various ages. We can conclude the origin of its deposits as follows:

I. 3. 1. Igneous phosphate deposits

This type of deposit is primarily associated with alkaline intrusive complexes. The most common rocks are nepheline syenites, carbonatites, and pyroxenites. These deposits, dominated by apatite-group minerals and ranging in age from Precambrian to Tertiary, supply about 10–20% of global phosphate production. Major producers are the Devonian Khibina Alkaline Complex of the Kola Peninsula of Russia (Fig. I. 2), Cretaceous alkaline carbonatite complexes Brazil, and South Africa's Phalaborwa Complex, with additional deposits in Canada,

Zimbabwe, Finland, Malawi, Uganda, and Sri Lanka (Habashi, 1985; Jasinski, 2016; Pufahl and Groat, 2016; Yerkebulan et al., 2023).

Fig. I. 2. The main quarry of Koashva magmatic phosphate deposit.

I. 3. 2. Sedimentary phosphorite deposits

The most remarkable platform deposits are associated with synclines. They form under an arid climate. The sedimentary facies are primarily of three types: granules or pseudo ooliths, nodules, and organic debris (coprolites and phosphatized fossils). The largest and most economically significant sedimentary deposits are found in North Africa, the Middle East, China, and the United States (Pufahl and Grimm, 2003; Jasinski, 2016). These deposits are extensive, stratiform ore layers formed through a combination of biological, oceanographic, sedimentological, and diagenetic processes (Pufahl and Groat, 2016). They are the predominant source of phosphate rock worldwide, found on all continents and accounting for about 95 % of global phosphate reserves (Howard, 1979). Most sedimentary phosphate deposits contain over 18 wt% P_2O_5, with a maximum of around 35 wt%. The Djebel Onk deposits (Fig. I. 3) are among this type, with resources that can reach 3 billion tons within the Djebel Onk basin (kechiched, 2011).

Fig. I. 3. Kef Essenoun quarry (Djebel Onk region–Algeria).

I. 3. 3. Guano phosphorite deposits

Guano-type phosphorite deposits originate from the accumulation of seabird or bat excreta rich in organic phosphorus, which undergoes diagenesis to form high-grade calcium phosphate (carbonate-fluorapatite). They typically occur on small oceanic islands, arid coastal regions, and limestone caves. Among these islands, the Ballestas Islands stand out, with the neighboring Chincha Islands about ten kilometers north, as the most renowned locations for guano in Peru (Fig. I. 4).

Fig. I. 4. Deposit of Guano-type in Chincha islands (Peru).

I. 2. 4. Metamorphic deposits

Metamorphic phosphorite deposits form through the transformation of pre-existing phosphorites under heat and pressure. They are rare, with P_2O_5 contents of 0.01–1.3%, and commonly host REE-bearing minerals such as monazite, apatite, and xenotime, exemple: The Jinping and Xinpu phosphorite deposits in the Sulu orogenic belt (Haizhou Group) in china (Elliott, 1973; Koritnig, 1978; Nash, 1984).

I. 3. 5. Phosphorite deposits resulting from weathering

Weathering-derived phosphorite deposits form when phosphorus is released from rocks in dissolved or particulate form. Bioavailable phosphorus is transported by rivers and windblown dust to oceans, where it supports biological productivity (Flicoteaux & Lucas, 1984; Benitez-Nelson, 2000; Filippelli, 2008).

I. 4. Distribution of sedimentary phosphorites around the world

I. 4. 1. On horizontal (geographic) scale

The largest phosphate deposits belong to the South Tethyan phosphogenic province, which extends from North Africa to the Middle East over approximately 5500 km (Notholt, 1985) (Fig. I. 5) and represents more than 85% of the known phosphate reserves in the world (Jasinski, 2016). The primary phosphate accumulations worldwide developed in low-latitude regions, approximately 10° to 20° (Cook and McElhinny, 1979). The most active phosphate deposits are concentrated along continental margins within subtropical areas of lower latitudes (Baturin, 1982). These areas with upwelling phenomena are chiefly found along the west coast of Africa, the east coast of the United States, and offshore regions of California, Peru, and Chile (El Bamiki, 2020). Plate tectonics significantly influenced the formation of substantial

phosphate reserves by shifting favorable margin zones for phosphogenesis toward lower latitudes, ensuring sustained phosphate productivity (Cook and McElhinny, 1979).

I. 4. 2. On vertical (time) scale

The phosphorites existence is known along the geological scale from the Precambrian to the Cenozoic eras (Cook, 1984) (Fig. I. 6). The oldest phosphate deposits occur in Late Neoproterozoic to Middle Cambrian deposits in China, Russia, Iran, Australia, and India, with smaller deposits are found elsewhere (Brasier and Callow, 2007; Papineau, 2010). Permian deposits formed the Phosphorus Formation, which occurs mainly in Idaho and Wyoming in the western United States (Sheldon, 1981, 1989; Hiatt and Budd, 2001; Piper and Link, 2002); Late Cretaceous–Eocene deposits are the Tethys phosphorus deposits, which are defined by deposits in the eastern Mediterranean, northern South America, north and northwestern Africa, and parts of the Caribbean Sea (Lucas, 1995; Follmi, 1996; Soudry et al., 2006; Marino et al., 2017); Miocene–Holocene deposits formed in the southeast USA and California, the Peru-Chile shelf, Mexico, Namibia-South Africa shelf, Atlantic Iberian coast and the eastern shelf of Australia (Burnett and Riggs, 1990; Riggs and Sheldon, 1990; Wigley and Compton, 2007; Gonzalez et al., 2016).

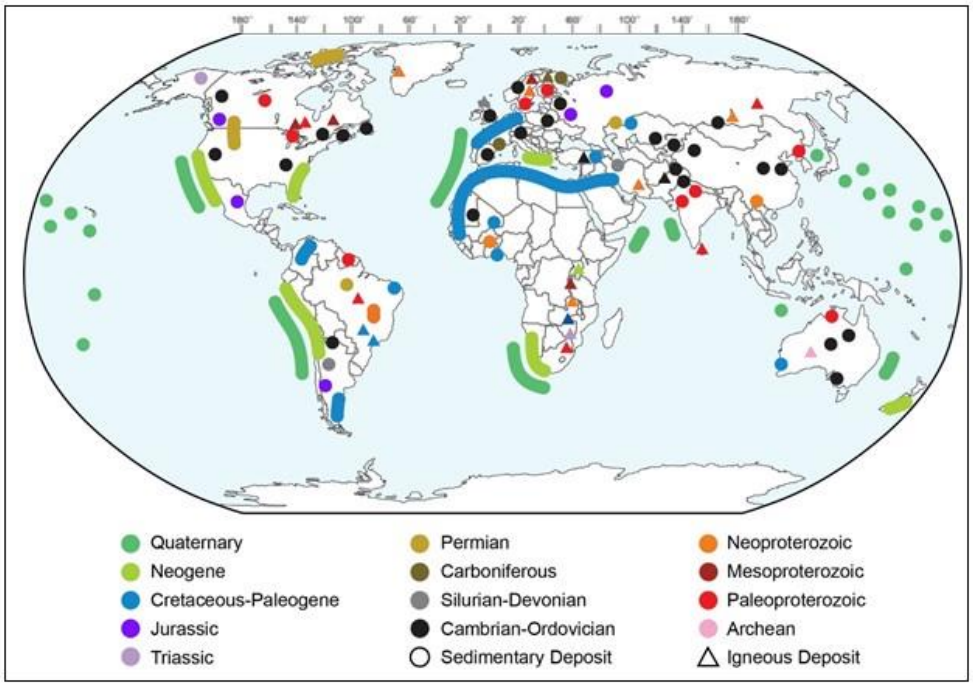

Fig. I. 5. Global distribution and ages of known sedimentary phosphorites (source: Pufahl and Groat, 2017; Godet and Follmi, 2021; Notholt et al., 1989; Glenn et al., 1994; Jasinski, 2016).

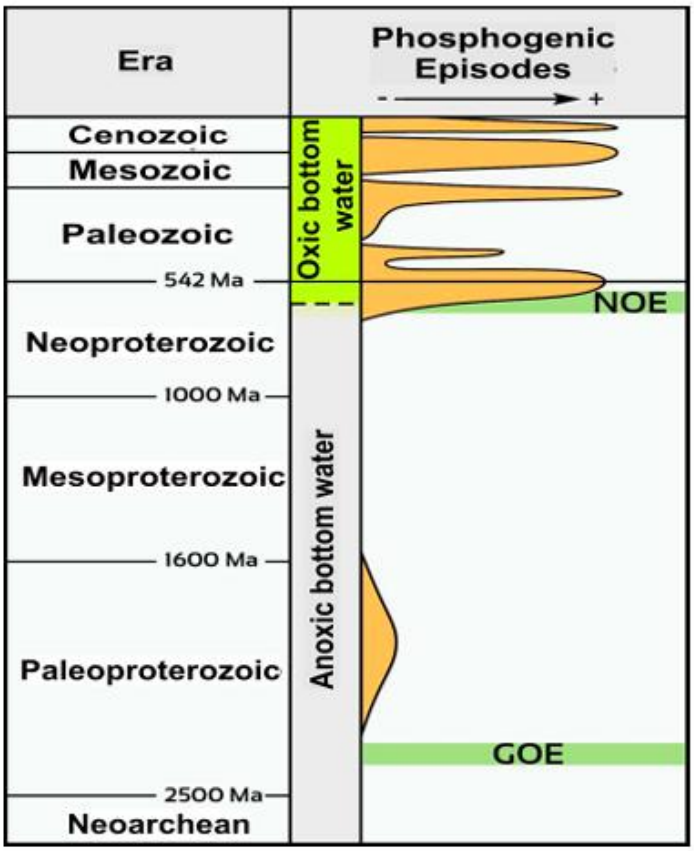

Fig. I. 6. Temporal distribution of the main phosphogenic events in earth's history (Pufahl and Groat, 2017). **GOE**=Great Oxidation Event, **NOE** =Neoproterozoic Oxygenation Event.

I. 5. Mineralogy

There are more than 200 minerals that contain ≥1% P_2O_5. However, apatite accounts for over 95% of all phosphorus in the crust of Earth (Palache et al., 1951; Altschuler et al., 1958; Deer et al., 1962; Ptáček, 2016). The phosphate mineral in a primary environment can exist in various forms and have high ability to absorb several elements as shown in tables I.1 and I. 2. The most common mineral found in sedimentary apatite is carbonate fluorapatite (CFA) or francolite, while the matrix is mainly composed of dolomite, calcite and opal-CT, with rare accessory minerals, such as gypsum, detrital quartz and zeolites (Galfati et al., 2010; Garnit et al., 2017; Kechiched et al., 2020; Diab et al., 2024; Fig. I. 7). Its structure allows for the substitution of various elements, such as monovalent (Na^+, K^+), divalent (Sr^{2+}, Pb^{2+}, Ba^{2+}, Mn^{2+}, Cd^{2+}), trivalent (REE^{3+}), tetravalent (Ce^{4+}, Th^{4+}, U^{4+}) elements, as well as hexavalent (U^{6+}) cation that can replace Ca; VO_4, As_2O_4, SO_2, SO_4 and CO_3 that can replace PO_4; Fluoride (F-) that can also partially or completely substitute for Cl- or OH (e.g., Provet and Lucas, 1980; Bonnot-Courtois and Flicoteaux, 1989; Rakovan and Hughes, 2000; Emsbo et al., 2015; Shaban, 2016; Zhu and Jiang, 2017; Hoshino, 2020). However, some trace elements may be adsorbed onto crystal surfaces or may be incorporated into other minerals, such as glauconite and other clay minerals, Fe-Mn oxyhydroxides, and organic matter (e.g., Abed et al., 2016; Laouar et al., 2024). In addition, the residual phosphogypsum (CaSO4) also contains significant concentrations of REE (Laurino et al., 2019).

Table I. 1. Some possible substitution in the apatite structure (modified after Nathan, 1984; Jarvis et al., 1994; Shaban, 2016).

Constituent ion	Substituting ion
Ca^{2+}	Na^{+}, K^{+}, Ag^{+}, Sr^{2+}, Mn^{2+}, Mg^{2+}, Zn^{2+}, Cd^{2+}, Ba^{2+}, Sc^{3+}, Y^{3+}, REE^{3+}, Bi^{3+}, U^{4+}, Ce^{4+}, Th^{4+}, U^{4+}, U^{6+}
PO_4^{3-}	CO_3^{2-}, SO_4^{2-}, CrO_4^{2-}, AsO_4^{2-}, VO_4^{3-}, CO_3, F^{3-}, CO_3, OH^{3-}, SiO_4^{4-}
F^{1-}	OH^{-}, Cl^{-}, Br^{-}, O^{2-}

Table I. 2. List of some important rare earth element (REE) phosphate minerals (modified after Rasmussen, 1996; Hoshino, 2020).

Name of the mineral	Chemical composition
Apatite	$Ca_5(PO_4)_3$ (OH, F, Cl),
Francolite	(Ca, Mg, Sr, Na)10(PO4, SO4, CO3)6F2-3
Florencite	$(REE)Al_3(PO_4)_2(OH)_6$
Crandallite	$(CaAl_3(PO_4)_2(OH)_6$
Gorceixite	$(BaAl_3(PO_4)_2(OH)_6)$
Fluorapatite	$Ca_5(PO4)_3F$
Hydroxyapatite	$Ca_5(PO_4)_3OH$
Carbonate-hydroxyapatite	$Ca_{10}(PO_4)_{6-x}(CO_3)x(OH)_{2-x-2y}(CO_3)y$
Monazite	(Ce, La, Nd, Th) PO_4,SiO_4
Xenotime	YPO_4
Phosphogypsum	$CaSO_4 \cdot 2H_2O$

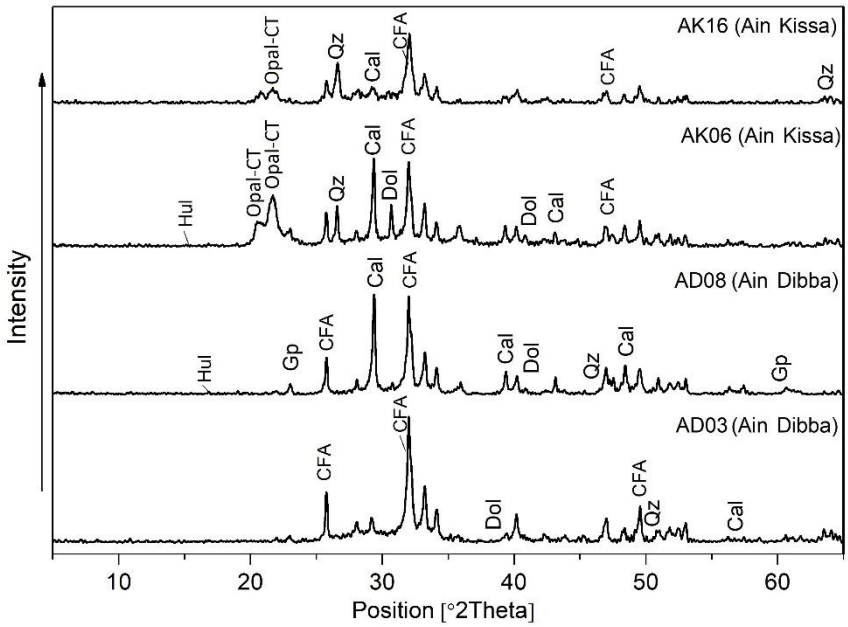

Fig. I. 7. X-ray diffraction pattern of the raw phosphorites from Algeria deposits (Diab et al., 2024).

I. 6. Geochemistry of phosphorites

I. 6. 1. Phosphate and REE concentrations

The sedimentary phosphate deposits that form in marine environments are of great importance due to their high content of P and rare earth elements:

- **P_2O_5 contents**

The average P_2O_5 content of the Upper Cretaceous and Paleocene phosphorite deposits on the Mediterranean belt ranges from 19 to 30 wt.% as follows: 25.67 wt.% in Egypt (Abou el-Anwar et al., 2017), 25.00 wt.% in Palestine (Soudry et al., 2013), 23.0 wt.% in Saudi Arabia (Meissner and Ankary, 1970), 23.0 wt.% in Iran (Salsani et al., 2020), 26.53 wt.% in Algeria (Bezzi et al., 2012), 19.50 wt.% in Jordan (Abed et al., 2016), 22.00 wt.% in Morocco (El Bamiki et al., 2021), 22.67 wt.% in Tunisia (Gallala et al., 2016), and 22.0 wt.% in Iraq (Benni, 2013).

- **REE contents**

The lanthanide series of elements (La, Ce, Pr, Nd, Pm, Sm, Eu, Gd, Tb, Dy, Ho, Er, Tm, Yb, and Lu) along with Y and Sc can be divided into light REY (LREY, La–Nd), middle REY (MREY, Sm–Dy), and heavy REY (HREY, Ho–Lu and Y) (Kynicky et al., 2012; Zhang et al., 2022; Zhang et al., 2024). The REE elements show high concentrations, in reaching ~2000 ppm in glauconite at Bled El Hadba (Laouar et al., 2024) and ~900 ppm in whole-rock and grain-size fractions of phosphorites at Kef Essenoun (Ferhaoui et al., 2022; Kechiched et al., 2018, 2020).

I. 6. 2. REE patterns and anomalies

The rare earth element (REE) data are often normalized to Post Archean Australian Shales (PAAS) using the data from (Taylor and McLennan, 1985; McLennan, 1989). Two groups of PAAS-normalized REEs patterns in phosphorite deposits have been distinguished: (1) seawater-like patterns marked by negative Ce anomalies and HREE enrichment (e.g., Jiang et al., 2007; Pi et al., 2013; Zhu et al., 2014; Xin et al., 2016) and (2) hat-shaped patterns characterized by MREEs enrichment and HREEs depletion (e.g., Bau and Dulski, 1996; Zhu et al., 2014). The calculation of $Ce/Ce^* = 3Ce_N/ (2La_N + Nd_N)$ and Cerium anomaly Ce_{an} = log Ce/Ce* are often taken from Wright et al. (1987), the calculation $Eu/Eu^* = Eu_N/(Sm_N + Gd_N)^{0.5}$ is usually taken from Taylor and McLennan (1985), $Pr/Pr^* = 2Pr_N/(Ce_N + Nd_N)$ is from Bau and Dulski (1996) and $Y/Y^* = 2Y_N/(Dy_N + Ho_N)$ from Fazio et al. (2007). N refers to PAAS normalized value in all the mentioned calculations. These anomalies are commonly used to track depositional environment conditions, paleo-redox conditions, and diagenetic processes that involved the marine phosphorites (Morad et al., 2001; Kechiched et al., 2020; Al-Bassam et al., 2021; Laouar et al., 2024). For example, weak negative Ce anomalies, positive Eu

anomalies, as well as Y/Y* and La/Nd ratios, and some sensitive trace elements, such as V, Cr, Ni and Co all show relatively reducing condition for the deposition and diagenesis of the southern basin of Tebessa phosphorites (Kechiched et al., 2020; Fig. I. 8). However, strong negative Ce and strong positive Eu anomalies indicate more oxic conditions (Kechiched et al., 2020).

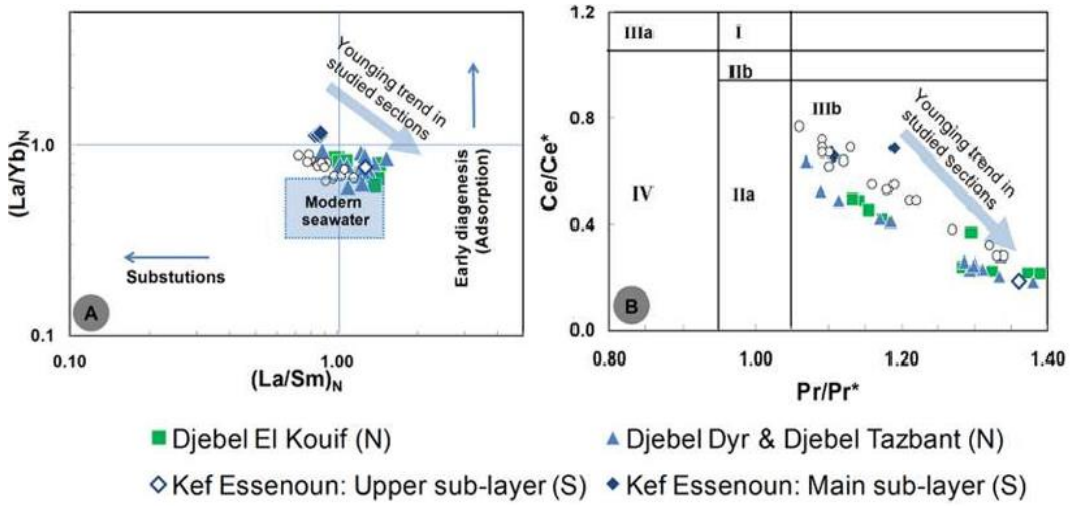

Fig. I. 8. (A) The $(La/Yb)_N$ vs. $(La/Sm)_N$ diagram (after Reynard et al., 1999) for the studied samples compared to Tunisian phosphorites (empty circles) (data after Kechiched et al., 2016; Garnit et al., 2017; this study). (B) Ce/Ce* vs. Pr/Pr* diagram after Bau and Dulski (1996) for the studied samples compared to Tunisian phosphorites (empty circles) (data after Kechiched et al., 2016; Garnit et al., 2017; this study). Field I: no anomaly; Field IIa: positive La anomaly causing apparent negative Ce anomaly; Field IIb: negative La anomaly causing apparent positive Ce anomaly; Field IIIa: real positive Ce anomaly; Field IIIb: real negative Ce anomaly; Field IV: positive La anomaly disguising positive Ce anomaly.

I.7. World's phosphorite production and reserves

Global production of phosphate rock in 2020, reached approximately 204.4 million metric tons. Key producers include China, Morocco, the United States, and Russia (Fig. I. 9a), collectively accounting for a large portion of global production (80%).

The primary reserve of phosphorite rock worldwide is concentrated in Morocco and Western Sahara, accounting for over 70% (50 billion tons), while China holds the second position with approximately 5% (3.2 billion tons) (Fig. I. 9b).

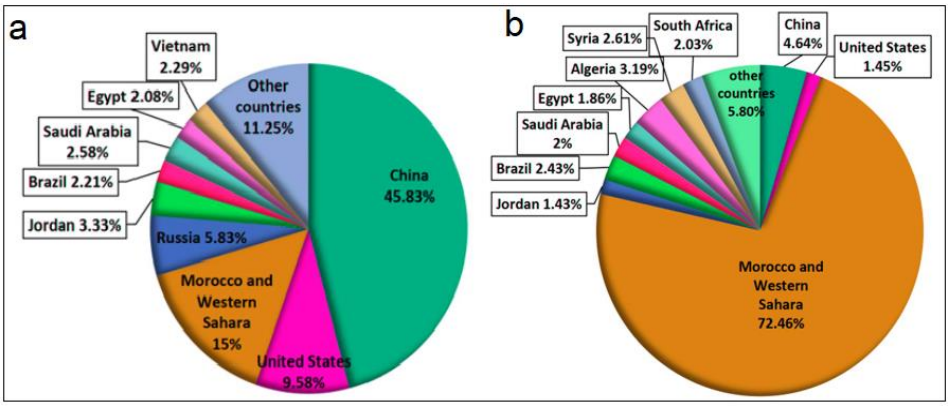

Fig. I. 9. (a) The worldwide production of phosphate rock in 2018, out of a total of 240 million tons, (b) global phosphate rock reserves for 2018. Data sourced from (USGS, 2020).

I. 8. Phosphate rocks use

- **Manufacture fertilizers**

The phosphorite rocks are mainly used to manufacture fertilizers (Fig. I. 10) because they contain substantial amounts of nutrient element phosphorus (over 18 wt% P_2O_5, with a maximum of around 35 wt%;), a vital nutrient for agriculture (Pufahl, 2010; Glenn et al., 1994; Pufahl and Groat, 2016).

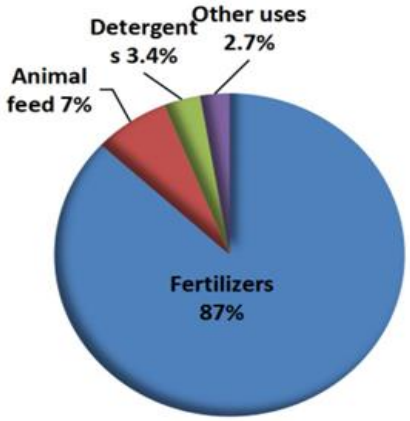

Fig. I. 10. Phosphorite use domains (Fertilizers International 460, 2014).

- **Industrial products and high-technology**

These rocks show high REEs concentrations and are considered as a promising unconventional resource for these elements (e.g., Emsbo et al., 2015; Garnit et al., 2017; Wu et al., 2018; Kechiched et al., 2020, Peiravi et al., 2021; Laouar et al., 2024). REEs are basic

components in several high-technology products (Fig. I. 11, and Fig. I. 12) such as lasers, guidance systems, electronic display systems, mobile phones, radar technology, and powerful electronic chips, metallurgy as alloys for various steel types (Golroudbary et al., 2022; Balaram, 2023a; Balaram et al., 2024; Santosh et al., 2024; Bai et al., 2024). Among these elements, the HREEs (Dy, Gd, Pr, and Sm) are particularly important for industrial products such as magnets, wind turbines, solar panels, computers, and several other defense applications (Uda et al., 2000; Akdogan and Ghosh, 2014; Jyothi et al., 2020).

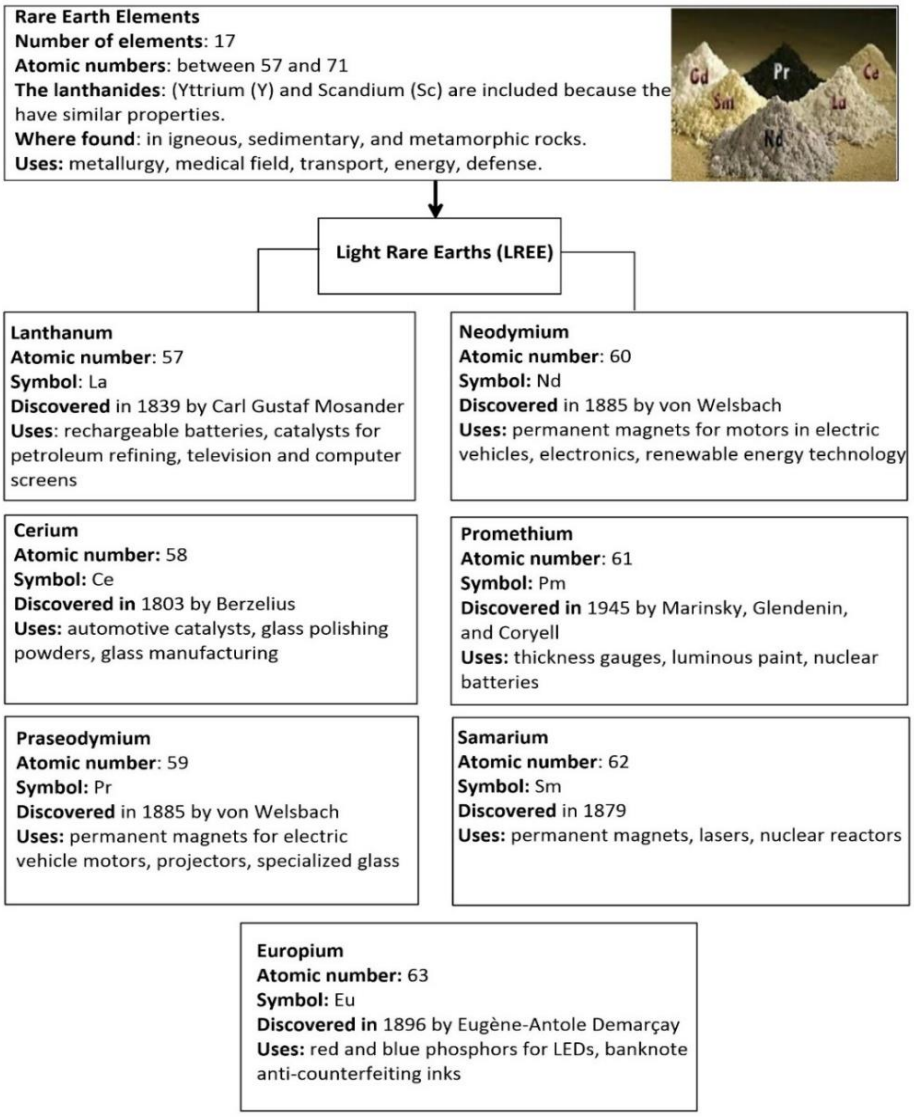

Fig. I. 11. Properties and applications of light rare earth elements (Uda et al., 2000; Akdogan and Ghosh, 2014; Jyothi et al., 2020).

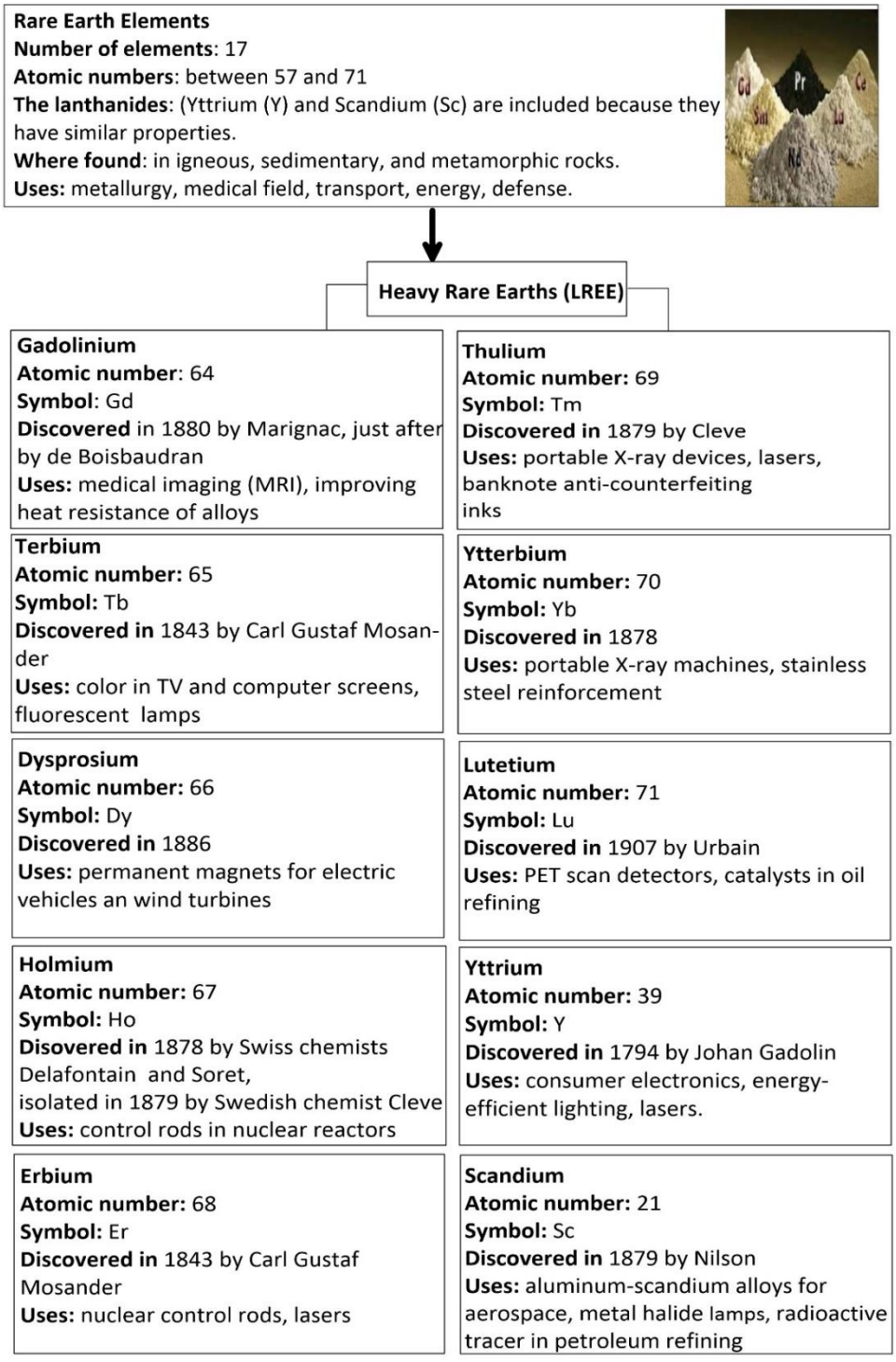

Fig. I. 12. Properties and applications of heavy rare earth elements (Uda et al., 2000; Akdogan and Ghosh, 2014; Jyothi et al., 2020).

I.7. Phosphorites and environmental impact

The phosphate ores are characterized by their high REE and PHE contents compared to other sedimentary rocks (e.g. Altschuler et al., 1967; Li, 2000; Laouar et al., 2024; Saouli et al.,

2025). Given that phosphorite is the primary raw material for fertilizer production, there are serious concerns about the potential transfer of these toxic elements into ecosystems and food chains (Suciu et al., 2022; Boumaza et al., 2024). Recently, the environmental impacts interested many researchers, especially for some potentially hazardous elements (PHE) in phosphorite ores and their wastes (e.g. Ferreira da Silva et al., 2010; Bezzi et al., 2012; Boumaza et al., 2021; Saouli et al., 2025), radioactivity of wastes (Djabou et al., 2023), which cause environmental and health risks (Khelifi et al., 2021; Khelif et al., 2020). Other studies are going on the development of eco-friendly REEs extraction technologies from phosphorite deposits, which have shown that trace metal speciation plays a crucial role in determining the environmental impact of these elements (Boumaza et al., 2023; Wu et al., 2024a, b; Saouli et al., 2025).

Chapter II

Geological setting

Chapter II
Geological setting

The sedimentary phosphorite rocks in Algeria that were deposited in two large basins (the Northern, and Southern Basins) in the Tebessa region, around the Kasserine Paleo-Island (currently at the Algerian-Tunisian border), have attracted the attention of many geologists because of their substantial economic P contents (e.g., Visse 1952; Durozoy, 1956; Ranchin 1963; Blès and Fleury., 1971; Kassatkine et al. 1980; Chabou-Mostefai 1987; Cielensky et al. 1988; Prian and Cortiel 1993; Kechiched et al., 2016, 2018, and 2020; Buccione et al., 2021; Boulemia et al., 2021; Laouar et al., 2024). The largest phosphorite accumulation in this region that was deposited during the upper Paleocene (Thanetian) – lower Eocene (Ypresian) period is mainly observed in the southern basin of the Kasserine Island, (e.g., the giant world class Kef Essenoun and Bled El Hadba deposits in Algeria), where the deposits are now under extensive exploration and exploitation, whereas the northern basin phosphorites, such as those of Dyr, Tazbent, El Kouif, show lower P contents and thinner layers, and therefore, are less prospective for exploration.

The studied Troubia, Ain Dibba, and Ain Kissa showings are other examples of the phosphrites located in the northern basin of Tebessa region (Fig. II. 1). These deposits are less enriched in both P_2O_5 contents and ore reserves than those of the southern basin (Djebel Onk complex). Therefore, they were paid little attention in terms of detailed studies and exploration programs, though they were partly exploited at the beginning of the 20^{th} century. The objectives of this chapter are to present the detailed petrological features of these phosphorites, along with the host carbonate layers. Based on field observations and existing geological maps, a number

cross-sections were carried out through the Troubia, Ain Dibba, and Ain Kissa phosphorite deposits, where about 80 samples were collected for petrographic study.

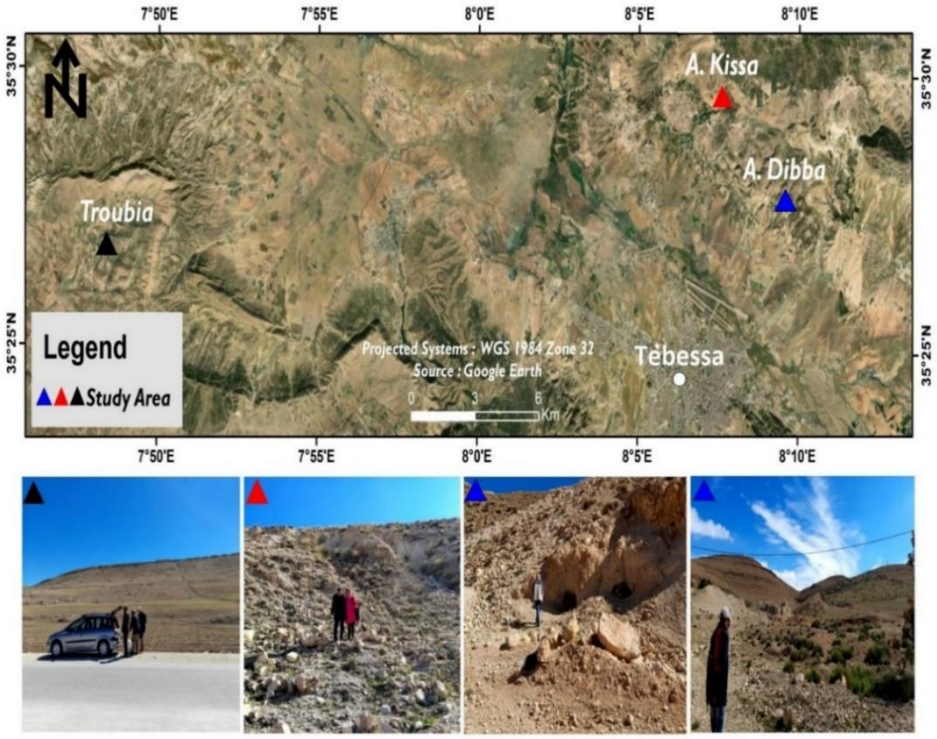

Fig. II. 1. Field photographs showing the Troubia, Ain Dibba, and Ain Kissa phosphorite outcrops.

II. 1. Geological setting

The Tebessa region is part of the Eastern Saharan Atlas of Algeria that extends northeasterly towards Tunisia. The geology and geodynamic contexts of this domain were investigated by many authors (e.g., Dubourdieu, 1956, 1959; Bouzenoune, 1993; Kowalski and Hammimed, 2000; Salmi-Laouar, 2004; Sami, 2011). Lithological facies of this area are characterized by Mesozoic to Cenozoic sedimentary rocks that are composed mainly of marls, limestones and sandstones, and can reach up to 9000 m in thickness (Cornet et al., 1952; Burollet et Stainfeld, 1956; Durozoy, 1956; Figs. II. 2 and II. 3). The oldest geological formations in this region belong to **the Triassic**, and consist of evaporitic sediments (Dubourdieu, 1956). **The Jurassic** sediments are absent, and **the lower Cretaceous** sediments, which starts with sandy clays of **the Barremian** become mainly calcareous during **the Aptian**,

then marly to calcareous during **the Albian** times. **The upper Cretaceous** sedimentation consists of alternating marls and limestones and continue until **the Paleocene-Eocene**. The latter period is marked by phosphatic sedimentation (up to 30 m thick) during **the Thanetian-Ypresian** times. The sedimentation becomes less calcareous, and more argillaceous and terrigenous during **the Oligocene-Miocene** period. **The Quaternary** deposits are composed of clays, sands and gravels of continental origin.

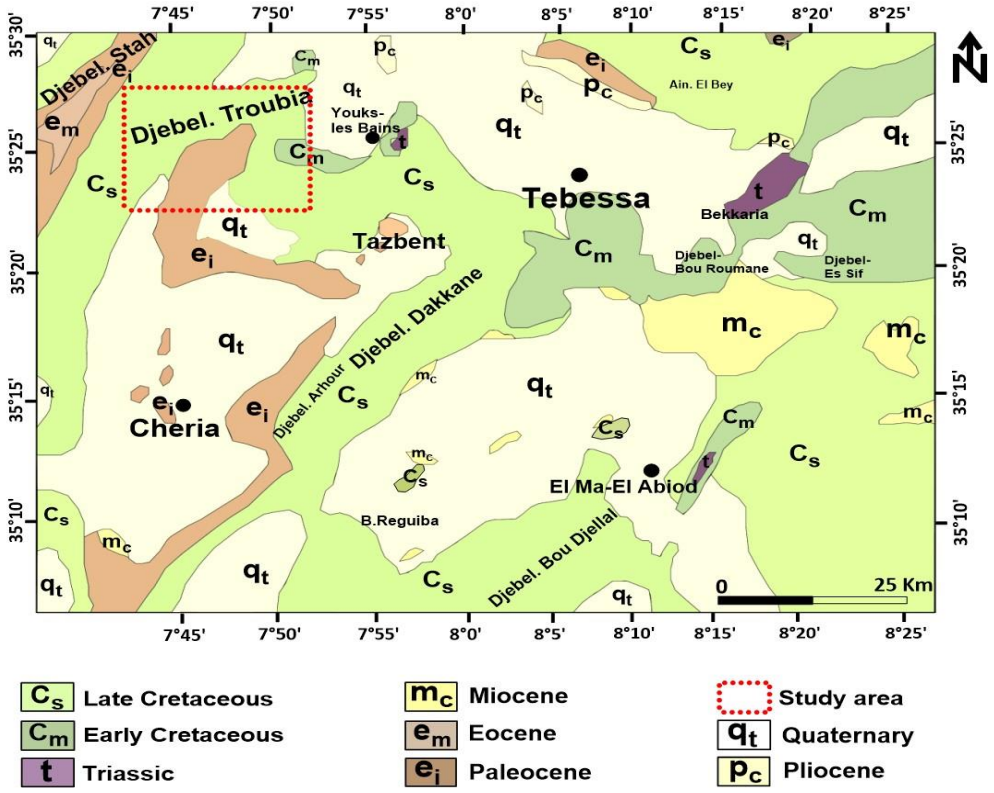

Fig. II. 2. Geological sketch map of the Tebessa region showing the location of Troubia deposit (extracted from the Geological Map Service of Algeria, 1951, modified after Cornet et al., 1952).

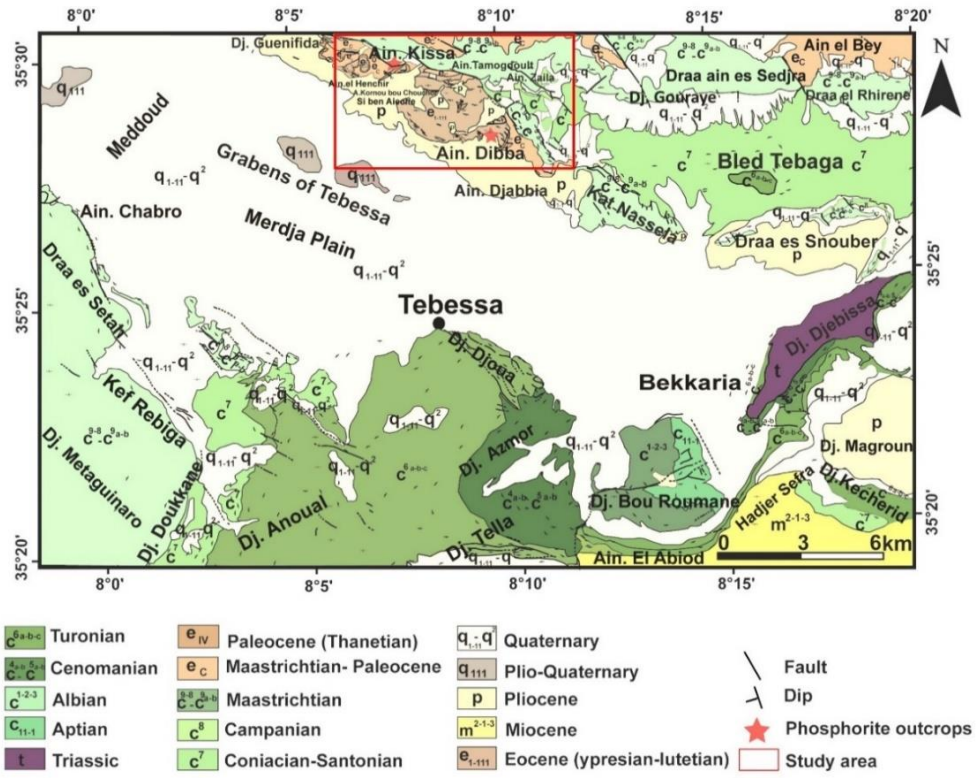

Fig. II. 3. Geological map of the Tebessa region, showing the location of the study area and the position of Ain Dibba and Ain Kissa deposits. (modified from Durozoy, 1956).

In this region, **the upper Paleocene-lower Eocene** period is characterized by large scale phosphorite deposition, which belongs to the large upper Cretaceous-Eocene phosphatic province that extends from north Africa to the Middle East. Phosphorite deposition is much more significant in the south of the Tebessa region (the southern basin), where the thickness of the phosphatic layers may reach 30 m (; Visse 1952; Cielensky et al., 1988), whereas in the north (the northern and western basins), the thickness of the phosphorite layers is much reduced (less than 10 m in Djebel Dyr, Troubia, Ain Dibba, Ain Kissa deposits, except at Djebel El Kouif where it may reach 15 m).

II. 1.1. Geological setting of the western basin (Troubia deposit)

In the western basin, the Troubia deposit is located about 27 km northwest of Tébessa town, belonging to the commune of Bir Mokadam, near the Tébessa Mountains in the eastern part of the Saharan Atlas (cf. Fig. II. 1). Troubia, following on from Djebel-Gaaga, continues

the belt of the Cheria high plateau to the north. It has an altitude of 1440 m, and is geographically limited by: Djebel Tazbant to the south-east, Hammamet to the north-east, and the localities of Bir M'kadem and Cheria plateau to the south.

Geologically, according to the geological map published by the Algerian geological mapping service at a scale of 1/50000 in 1952 (Cornet et al., 1952), the outcrop consists of Mesozoic-Cenozoic sedimentary successions that have witnessed, in a larger scale, intensive phosphogenesis from the Upper Cretaceous to the Early Eocene periods along the southern edges of the Tethys Ocean, as observed in the Tebessa region (Fig. II. 2). The detailed geological characterizations of the study area are taken from previous work carried out by various authors, such as Lambert (1947), Durozoy (1947), Gaud (1977), Ricard (1973). **The upper Cretaceous** (Turonian to Maastrichtian) sediments are characterized mainly by about 600 m thickness. **The Turonian** sediments are composed of beige, pinkish, and sometimes dark limestones marked by hematite, which outcrops in the north (Dj Es Senn, Dj Gaâga) and south (Outa Oum Khaled). **The Santonian** consists of blue-grey marls containing Globotruncana in Djebel Troubia, and is represented by grey marls and dark grey-black clays interbedded with dark grey pyritic shell-bearing limestones at the south of Oued Mellah, Dj. Manndra and Hassi El Karma, containing lamellibranches and bryozoans. **The Campanian** sediments are characterized by grey marls at depth, greenish on the surface, with gypsum crystals formed from pyrite decomposition. These marls are located around the Chéria plateau, with a thickness of 300-400 meters. **The Maastrichtian**, sediments show chalky white limestones, with upper layers rich in flint, and a thickness of about 250 m. **The basal Tertiary** is characterized by two divisions: the lower and middle Paleocene (Danian-Selandian) sediments consisting of 100 to 150 m thick black clay- marls in the Tazbent mountain, and, to the south, these sediments become thinner with a transition into chalky flint-bearing limestones. **The upper Paleocene (Thanetian)** sediments are composed of lumachellic limestone and marls, outcropping in the

south and on the edges of the Telidjene anticlines. **The lower and middle Eocene (Ypresian and lower Lutetian)** sediments consist of series of siliceous or marly layers appear in the north (Koudiat Kraa and Draa Belgacem), with marly brown-beige limestones containing phosphatic levels; followed by whitish gypsum-bearing limestones at Bir Touil. **The Mio-Pliocene** sediments are marked by alternating gypsiferous clays and yellow sands of about 60 meters thick. **The quaternary** sediments are composed of clays, sands and gravels of continental origin.

II. 1.2. Geological setting of the northern basin (Ain Kissa and Ain Dibba deposits)

In this area (Fig. II. 3), **the upper Cretaceous-lower Paleocene** (Maastrichtian-Danian-Selandian) sediments are characterized by about 300 m thick dark to yellowish, sometimes gypseous and pyritous marls and scarce centimeter-thick marly-limestone intercalations (Durozoy, 1956). **The upper Maastrichtian** sediments are part of El Haria formation (Burollet, 1956) which ranges in age from Early Maastrichtian to Early Eocene, and are characterized by metric deposits of marine dark to light gray laminated marls, with intercalations of centimetric benches of light gray clayey limestones, containing ammonites, and dark gray clayey limestones (Goolaerts et al., 2004; Djoulah et al., 2023). According to Sigal (1977), and Bellier (1985), the *Gansserina gansseri* Zone with the appearance of *Racemigumbellina f*ructicosa, corresponds to the middle part of the Maastrichtian, and the *Abathomphalus mayaroensis* Zone represents the late Maastrichtian. The absence of *A. mayaroensis* from upper most Cretaceous sediments of continental shells indicates that this species disappears prior to the K/T boundary (e.g. Robaszynski, 1986; Keller et al.,1988. Keller et al., 1995). The Maastrichtian ostracod associations recorded from the studied area are: *Acanthocythereis meslei, Aphrikanecythere phumatoides, Brachycythere oguni Reyment, Cristaeleberis thomasi, Cytherelloidea melleguensis, Kefiella maresi, Protobuntonia numidica Grekoff, Schizocythere sp. Donze et al.,*

Trachyleberidea tunisiensis and Xestoleberis tunisiensis Esker (Damotte and Fleury, 1987; Damotte, 1993).

The lower and middle-Paleocene (Danian-Selandian) sediments are marked by the transition from Cretaceous to Tertiary without significant disruption in the sedimentation. They consist of grey planktonic microfauna-rich marls that mark the passage from the Maestrichtian to Paleocene, and clayey, chalky limestone which are of Danian age (Dubourdieu, 1959). This corresponds to the period between the disappearance of the *Globotruncanidae* and the appearance of *Globorotalia pseudomenardii* BOLLI and Globotruncana pseudobulloides. (Damotte, 1995; Damotte and Fleury ,1987) and *Globorotalia pseudobulloides* PLUMMER (STAINFORTH et al., 1975).

The upper Paleocene (Thanetian) sediments are composed of 10 to 15 m thick marls and flint-bearing marly limestones, with decimeter to meter-thick phosphorite layers. This stage is marked by the first occurrence of *Globorotalia aequa* CUSH. and RENZ and *Gr. Pseudomenardii*, and ends with the last occurrence of *Gr. velascoensis* CUSH. (Damotte and Fleury, 1987).

The lower and middle Eocene (Ypresian and lower Lutetian) consists of whitish, flint-bearing marly limestones of ~5 m thick at the bottom, followed by massive, 50 to 60 m thick, flint-bearing limestones containing *Thersitea ponderosa, Nummulites atacicus*, *N. irregularis* var. *rollandi* and *N. pomelli* (Durozoy, 1956).

II. 2. Structural framework of northern basin

The sedimentary rocks of the eastern Saharan Atlas, where the northern basin belongs, were deformed during the Atlasic (Eocene) and Alpine (Miocene) tectonics, consequences of the subduction-collision events between Africa and Eurasia which started in the late Cretaceous (e.g., Zargouni, 1984; Laville and Fedan, 1989; Laville et al., 2004). These lithologies are now structured as NE-SW-directed synclines and anticlines (e.g., Dj. Dyr, Dj. El Kouif, Tazbent,

Ain Dibba, and Ain Kissa) that are crosscut by deep NW-SE and N-S-directed normal faults that contribute largely to the formation of graben structures, such as those of the Tebessa (Durozoy, 1956; Dubourdieu, 1956; Kadri et al., 2015; Fig. II. 4). These events contribute simultaneously to the uplift and exposure in places of the Triassic evaporitic formation, often within the hinge zones of the anticline structures (e.g., Dj Djebissa (Fig. II. 4); Dubourdieu, 1956; Durozoy, 1956). However, the Atlassic folds may have formed after the opening of some of the grabens (Chihi, 1984). Recently, Bencharef et al., (2022) showed that the Early Mesozoic extensional tectonic regime initiated some grabens in Tebessa region by creating the bounding normal faults, followed by Cenozoic strike-slip faults, when grabens opened as pull-apart basins. These structural configurations allow to forming isolated sub-basins and are characterized by sedimentary gaps. The NE-SW horizontal compressive regime resulted in NE-SW folds and NW-SE grabens, where some of these structures accumulated thick phosphate deposits along their edges (Kadri et al., 2015), such as those of Djebel Dyr and Djebel Onk Complex, and continental deposits in the emerged areas.

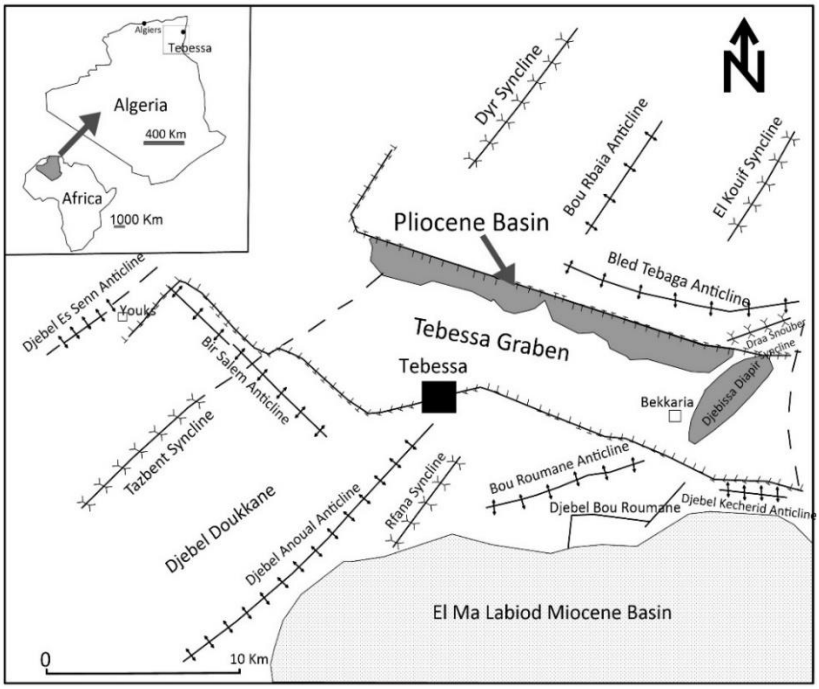

Fig. II. 4. Structural outline of the Tebessa Graben basin and its surroundings (after Durozoy, 1956).

II. 3. Paleogeography

The upper Paleocene-lower Eocene period in Tebessa region is characterized by large scale phosphorite deposition, which belongs to the large upper Cretaceous-Eocene phosphogenesis province that extends from north Africa to the Middle East along the southern edges of the Tethys Ocean (Sassi, 1974; Notholt, 1980; Sheldon, 1987; Notholt et al., 1989; Lucas and Prevot-Lucas, 1995; Lasheen et al., 2022). These phosphorite rocks were deposited around the Kasserine Paleo-Island in the Algerian-Tunisian borders (Lucas and Prevot-Lucas, 1996; Notholt and Jarvis, 1989; Garnit et al., 2017). This paleo-highs area in south and central Tunisia (Burollet, 1956; Vila, 1980; Zaier et al., 1998; Fig. II. 5) started uplift during the Turonian and continued until reaching its maximum expansion with sub-linear borders to the south and to the east, and irregular borders to the north during the Maastrichtian-Paleocene period. The Kasserine Island has significantly expanded, particularly to the Tunisian-Algerian border due to several tectonic events during the late Cretaceous-Eocene period, such as N-S, E-W and N120◦ directed compression that contribute largely to the expansion of this the uplift and emerged domain (Hlaiem, 1999; Kadri et al., 2015). During the Lower Eocene, the northern part of the Island experienced transgressive processes, whereas the southern and eastern boundaries kept the same shape as that of the previous stage. These paleo-highs structures played a crucial role in controlling sedimentary dynamics and depositional environments across the region. These tectonics along with upwelling of the Tethyan Circum-global Current (TCC) significantly influenced sediment dispersal patterns and uplift events created ideal depositional basins for phosphorites accumulations (Abed and Amireh, 1983; Abed, 2013). Obstruction upwelling prevailed along these paleo highs, which are Si- and P-rich, and contributed to the trapping of abundant organic-rich sediments in the Gafsa-Onk-Metlaoui basin, and other marginal basins such as Dyr, El Kouif and Ain Dibba (Belkacem et al., 2024).

In this area, **the upper Maastrichtian** is marked by a thick marl-shale series (El Haria Formation; Flandrin, 1948) which ranges in age from Early Maastrichtian to Early Eocene, and are characterized by rich and diverse planktonic microfauna at the base with a restricted number of species in the upper part (Burollet & Sainfeld 1956, Said 1978; Zaier 1984; Salaj 1990; Goolaerts et al., 2004; Djoulah et al., 2023). The marl thickness reaches a maximum of 700 m in the Tunisian trough in the Cretaceous/Tertiary boundary (K/T) such as those in El Kef, Ain Settara, and Sidi Nasseure (Dupuis et al., 2001; Robaszynski, 1986; Keller et al., 1988; Keller et al., 1995; Burollet, 1956), 300 m in Tébessa, at Asserdoune (Flandrin, 1948; Djoulah et al., 2023), and 70 m at Djebel Onk (Visse, 1951). **In the Upper Paleocene**, the marl thickness decreases, particularly in the Tébessa area, and is associated with the oyster-bearing lumachellian limestones and gypsum in the Gafsa area (Burollet, 1956). Several authors attributed the phosphorite deposits to the **Thanetian age** (Laffitte, 1939; Flandrin, 1948; Visse, 1951, 1952; Ranchin, 1963), while others dated the Chouabine and Oued Tselja sections, near Metlaoui, to the upper Paleocene–lower Ypresian (Ben Abdesselam, 1978). In both Algeria and Tunisia, **the Ypresian** consists of marls and marly limestones with flint, interbedded with phosphate horizons, where the first nummulites appear (Flandrin, 1948; Winnock, 1980). **The Lower Lutetian** marks a marine regression, represented by gypsum, marls, and limestones in the Tébessa area, and massive nummulitic limestones elsewhere in the region.

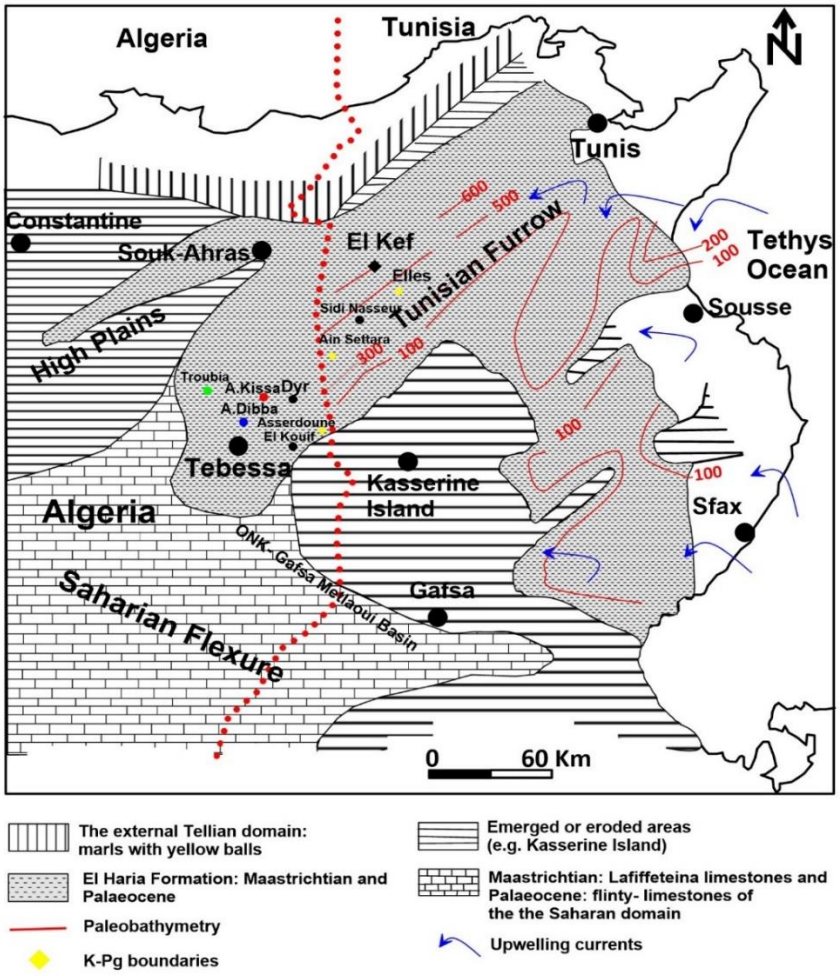

Fig. II. 5. Location of the study region within the palaeogeographic framework of the Eastern Algeria and Northern Tunisia during the Maastrichtian and Paleocene (after Burollet, 1956; Vila, 1980; Djoulah et al., 2023; Dupuis et al. 2001).

II. 4. Field observations and lithological description

II. 4. 1. The Troubia deposit

The study of the Thanetian phosphorite layers was carried out through an E-W-directed cross-section, across the Troubia deposit outcrop. The coordinates of this cross-section are: 35° 26' 58" N and 7°48'28" E (Fig. II. 6). The general dip of layers is about 30°. This deposit is of great interest to us because the phosphate layer outcrop, visible on the southern part of the Djebel-Troubia, extends from Koudiat-Chabor in the east to Ain-Kremoura in the west. These

superimposed layers have an average thickness of 60–80 cm and are covered by approximately 10 m of nummulitic limestone.

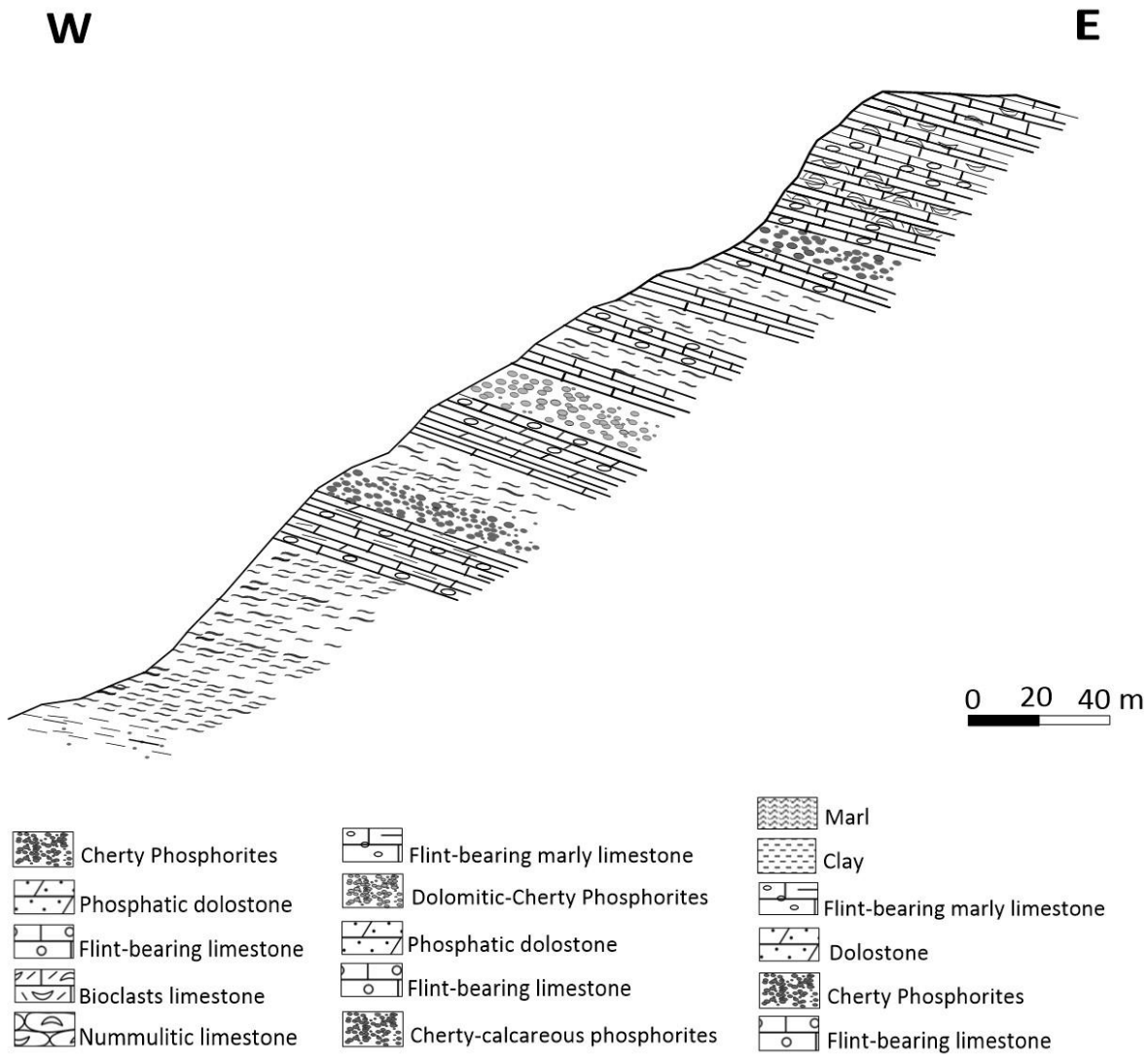

Fig. II. 6. Simplified geological cross-section through Troubia phosphorite deposit.

Based on field observations and the detailed description of the different facies encountered in the Troubia deposit (see Fig. II. 2, and II. 6), the lithological succession, from bottom to top, is described as follows:

At the bottom of the section, the sedimentary layers are mainly composed of the following units:

Marls: This unit is recorded in the lower part of the Troubia outcrop, where it appears relatively thick (Fig. II. 6, and Fig. II. 7). It is composed of grey to dark marl with clay intercalations and contains some bioclasts fragments.

Flint-bearing marly limestone (~ 2 m thick): This unit consists of beige to yellowish, semi-friable to hard, flint-bearing marly limestone with intercalations of beige, marly limestone levels (Fig. II. 7a). These facies are characterized by the presence of phosphatic particles, including beige to brown pellets, beige coprolites, brown bone fragments, and shark teeth.

Phosphatic dolostones (~ 2 m thick): This rock appears beige to grey, semi-friable to hard, and is interbedded with marly limestone (Fig. II. 7b). It contains an abundance of medium- to coarse-grained, poorly sorted phosphatic particles (pellets and bone fragments), and lithoclasts.

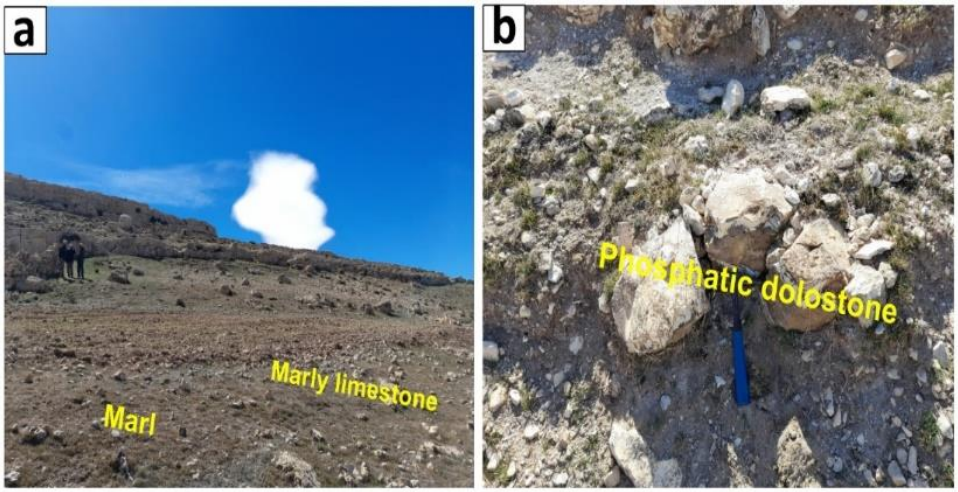

Fig. II. 7. Field photograph showing alternating clay, grey to much grey marl, beige to grey flint-bearing marly limestone, and beige to grey phosphatic dolostone of Troubia deposit.

The microscopic investigations show that the **dolostone rock** has a wackestone to packstone texture, and consists of sub-rounded, brown pellets within a micro-sparitic matrix with rhombohedral dolomite crystal growth (Fig. II. 8).

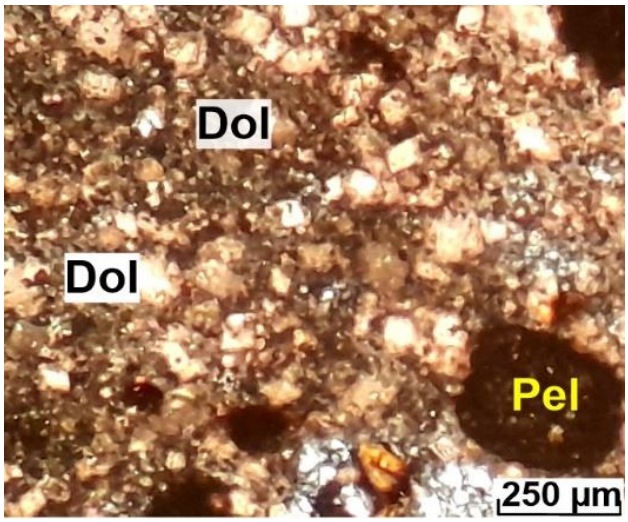

Fig. II. 8. Thin section photomicrograph showing a dolomitic rock containing sub-rounded, brown pellets (Pel), and rhombohedral dolomite crystal growth (Dol) within packstone textures.

Cherty phosphorites (~ 50 cm thick): This unit, of about 50 cm thick, is composed of hard and dark grey cherty phosphorites with centimeter-size kidney-like silica nodules. (Fig. II. 9). Here, the phosphorite consists of abundant, poorly sorted, medium to coarse-grained phosphatic particles and bioclasts, accounting for 65% by volume of the total rock within a siliceous cement. Their sizes range from 50 µm to 2 millimeters.

Fig. II. 9. Hand specimen showing hard, grey cherty phosphorite with abundant phosphatic particles from Troubia deposit.

Flint-bearing limestone (~ 2 cm thick): It is a hard, grey to beige limestone characterized by the presence of dark kidney-like silica nodules, with intercalations of clayey and black marl (Fig. II. 10a).

Flint-bearing marly limestone (~ 80 cm thick): It consists of light grey color, soft, layer, intercalations with marly levels (Fig. II. 10b).

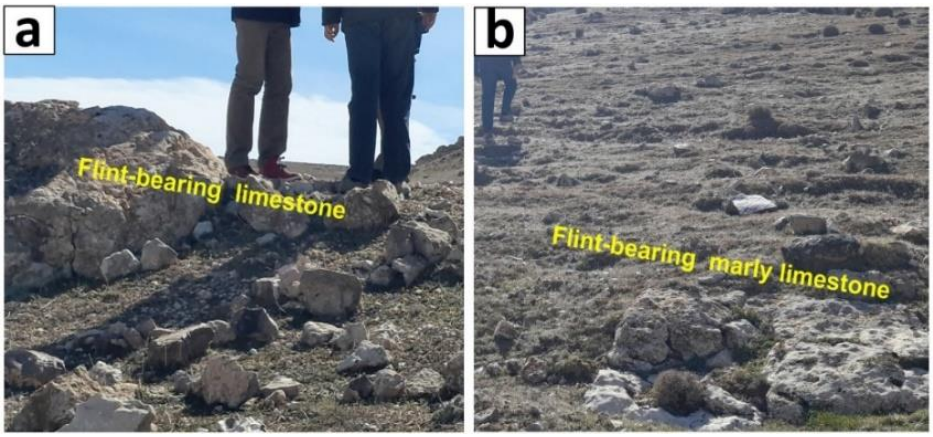

Fig. II. 10. Field photographs showing :(a) alternating beige to grey, flint-bearing marly limestone, and (b) beige, flint-bearing marly limestone from Troubia deposit.

Dolomitic-cherty phosphorites (~60 cm thick): This unit consists of grey, semi-friable to hard, medium to coarse-grained, dolomitic and slightly siliceous phosphorites with an average thickness of 60 cm (Fig. II. 11). It is composed of abundant phosphatic particles (pellets, coprolites, and fish teeth) within a calcareous-siliceous matrix.

Fig. II. 11. Hand specimen showing hard, grey dolomitic-cherty phosphorites with abundant medium to coarse-grained phosphatic particles from Troubia deposit.

Phosphatic dolostone (~ 80 cm thick): The dolostone rock consists of yellow to beige, semi-friable to hard layer (see Fig. 6, and Fig. II. 12). It contains an abundance of medium to coarse-grained phosphatic particles and is approximately 1.5 m thick.

Flint- bearing limestone (~ 80 cm thick): It is a hard, grey to beige, compact**,** characterized by the presence of dark kidney-like silica nodules, with intercalations of clayey and black marl (Fig. II. 12).

Fig. II. 12. Field photograph showing alternating beige to grey, flint-bearing marly limestone and beige, grey phosphatic dolostone from Troubia deposit.

Petrographically, the **dolostone rock** has a wackestone to packstone texture, and is composed of sub-rounded, brown pellets ranging in size from 250 to 400 µm, within a sparitic matrix and /or cement with rhombohedral dolomite crystal growth (Fig. II. 13).

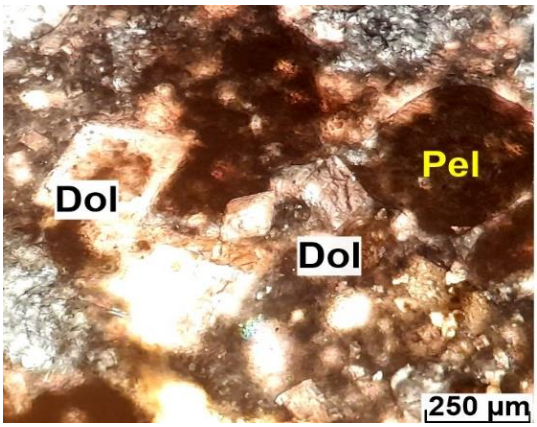

Fig. II. 13. Thin section photomicrograph showing a dolomitic rock containing sub-rounded, brown pellets (Pel), and rhombohedral dolomite crystal growth (Dol) within sparitic matriw and /or cement.

Cherty and cherty-calcareous phosphorites (~ 80 cm thick): This unit comprises 40 cm-thick grey, hard, medium-to-coarse-grained calcareous-cherty phosphorites containing abundant coprolite and fish tooth particles ranging in size from 50 µm to 2 mm (Fig. II. 14). These particles account for 65% of the total rock volume. The phosphorites become darker grey, harder and display siliceous cement towards the top, forming cherty phosphorite with centimeter-sized, kidney-shaped silica nodules containing poorly sorted, medium-to-coarse phosphatic particles.

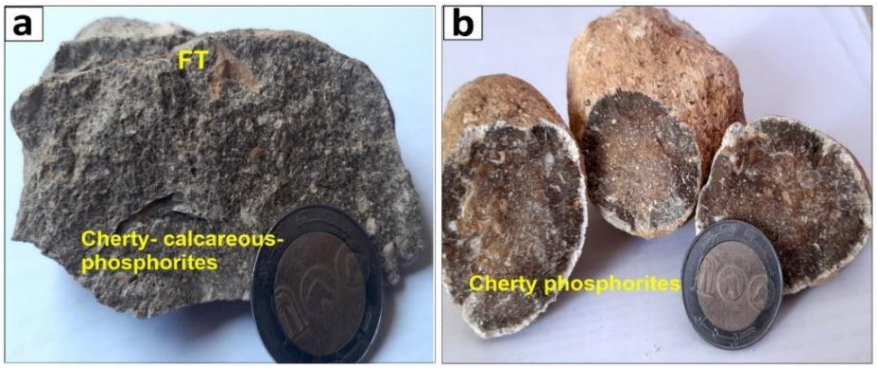

Fig. II. 14. Hand specimens showing: (a) hard, grey, calcareous-cherty phosphorites with abundant medium to coarse-grained phosphatic particles; and (b) hard, grey, cherty phoshorites containing phosphatic particles from Troubia deposit.

At the top of the section, the sedimentary layers are mainly composed of the following units:

Phosphatic dolostone (~ 50 cm thick): Dolostone rock is characterized by a semi-friable to friable, beige to yellow color with an average thickness of about 50 cm (Fig. II. 15a). It is composed of medium- to coarse-grained, poorly sorted phosphatic grains (pellets, **c**oprolites and bioclasts), constituting about 20 % of the rock.

Flint- bearing limestone (~ 2 m thick): The flint-bearing limestone with intercalations of centimetric (10 cm) grey clayey (argillaceous), is typically beige to yellowish in color, soft to medium in hardness (Fig. II. 15b).

Bioclast limestone (~ 3 m thick): It appears as a thick-bedded to massive unit (3 m thick), with a beige to light yellowish color, (Fig. II. 15c). It is composed of a fossiliferous texture visible on fresh surfaces. Broken surfaces reveal an abundance bone fragments, bivalves, and skeletal debris.

Nummulitic limestone (~ 6 m thick): It is characterized by a hard, beige to light grey color, rich in large nummulite fossils, with a medium- to coarse-grained texture. It appears in the upper layers, founding in Ain Troubia and near the Koudiat-Chabor (cf. Figs. II. 6, II. 15d).

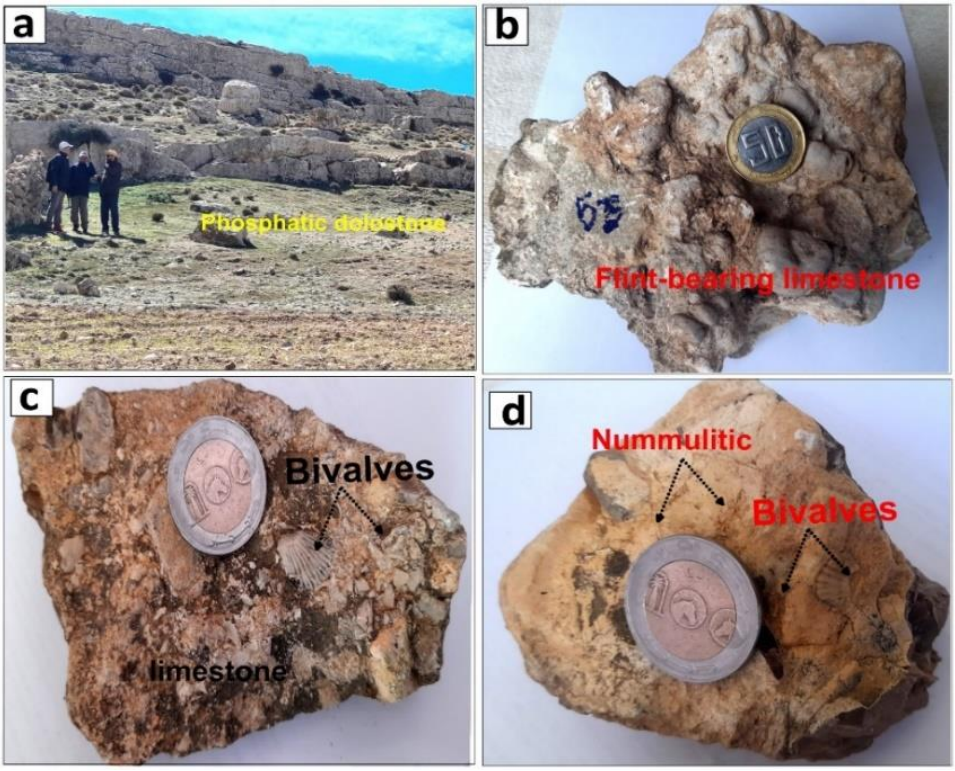

Fig. II. 15. Field photographs and hand specimens taken from the top section of Troubia deposit showing: (a) alternating marly limestones, flint-bearing limestone, bioclasts limestone, and nummulitic limestone ;(b) beige, hard bioclasts limestone; (c) flint-bearing limestone with abundant of bivalves and bioclasts fragments; and (d) beige, nummulitic limestone.

Petrographic investigations show that the **dolostone rock** has a wackestone to packstone texture, and is composed of sub-rounded, brown pellets, and elongated bone fragments within a sparitic matrix and /or cement with rhombohedral dolomite crystal growth (Fig. II. 16a).

Bioclast limestone is characterized by a sparitic matrix containing an abundance of phosphatic particles, bioclasts, and fragments of fish teeth (BFT)), ranging in size from 200 µm to 2 mm., which are occasionally filled with a calcitic matrix (Fig. II. 16b). **The limestone** at the top of the section, is composed of abundant nummulitic fauna (Fig. II. 16c, d), ranging in size from 400 µm to 1 mm.

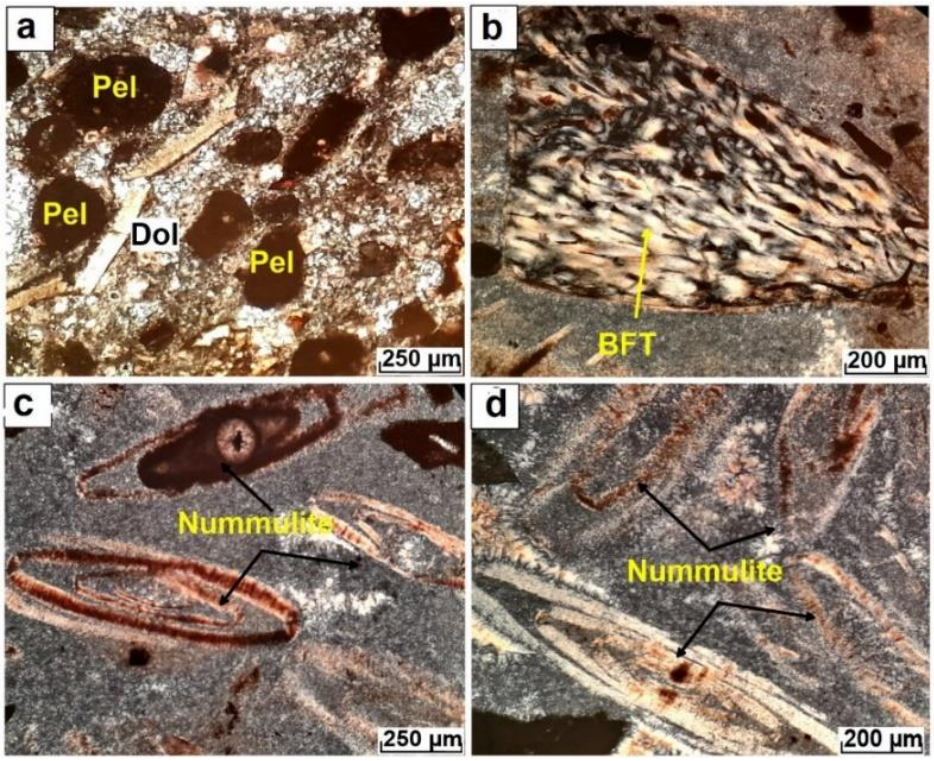

Fig. II. 16. Thin section photomicrographs from the top section of Troubia deposit showing: (a) a dolomitic rock containing abundant sub-rounded, brown pellets (Pel), and rhombohedral dolomite crystal growth (Dol); (b) a sparitic limestone matrix containing abundant of phosphatic particles, bioclasts and fragments of fish teeth (BFT); (c, d) limestone rich in nummulite fauna, ranging in size from 400 µm to 1 mm.

II. 4. 2. The Ain Dibba deposit in the northern basin

In the northern basin, the Ain Dibba phosphorite deposit occurs a few kilometers (10 to 11 km) NNE of the Tebessa town (see Fig. II. 3). In this region, the sedimentary successions are composed of Mesozoic to Cenozoic rocks (see Fig. II. 3). The study of the Thanetian phosphorite layers was carried out through a cross-section taken from the south to the north,

across the Ain Dibba mining area (Fig. II. 17). The coordinates of this cross-section are: 35°27'55" N and 8°9'20" E.

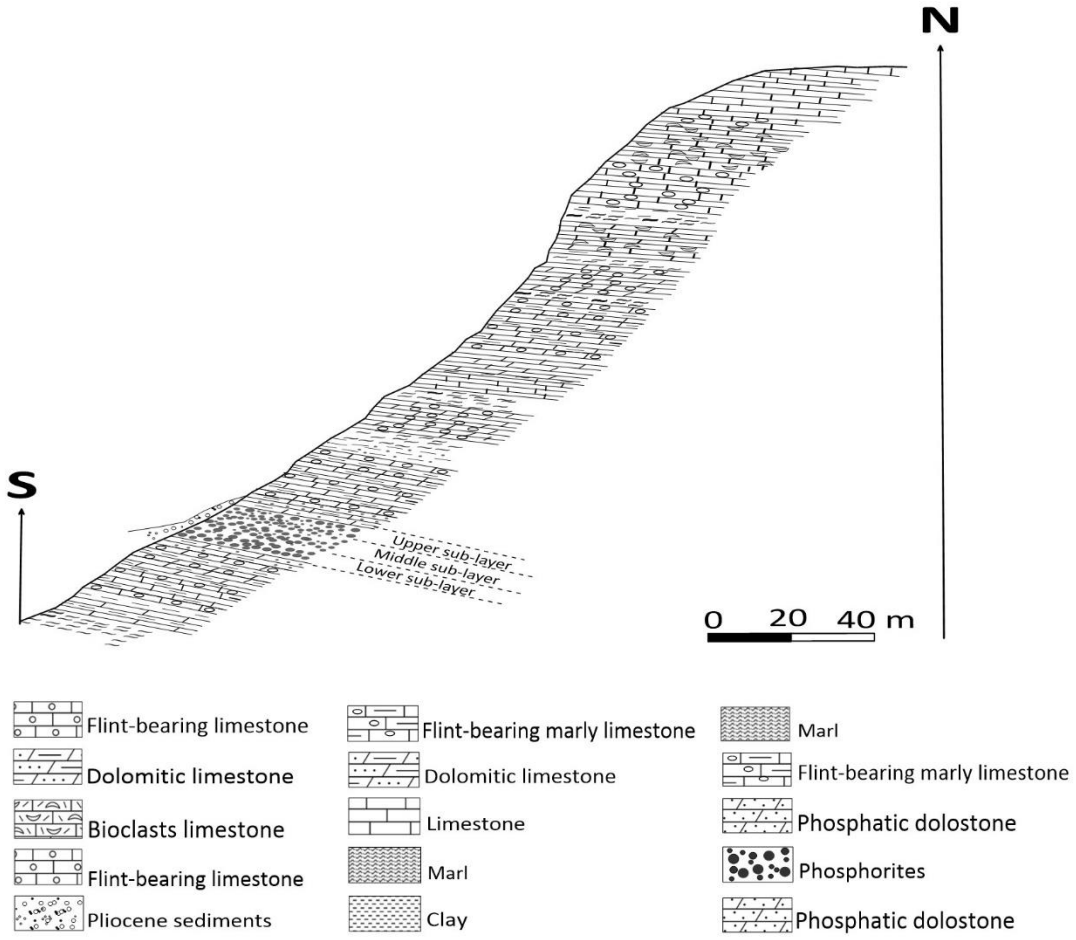

Fig. II. 17. Geological cross-section through Ain Dibba phosphorite deposit.

Based on field observations and detailed descriptions of the different facies encountered in the Ain Dibba deposit, the lithological succession from bottom to top (Fig. II. 18) is as follows:

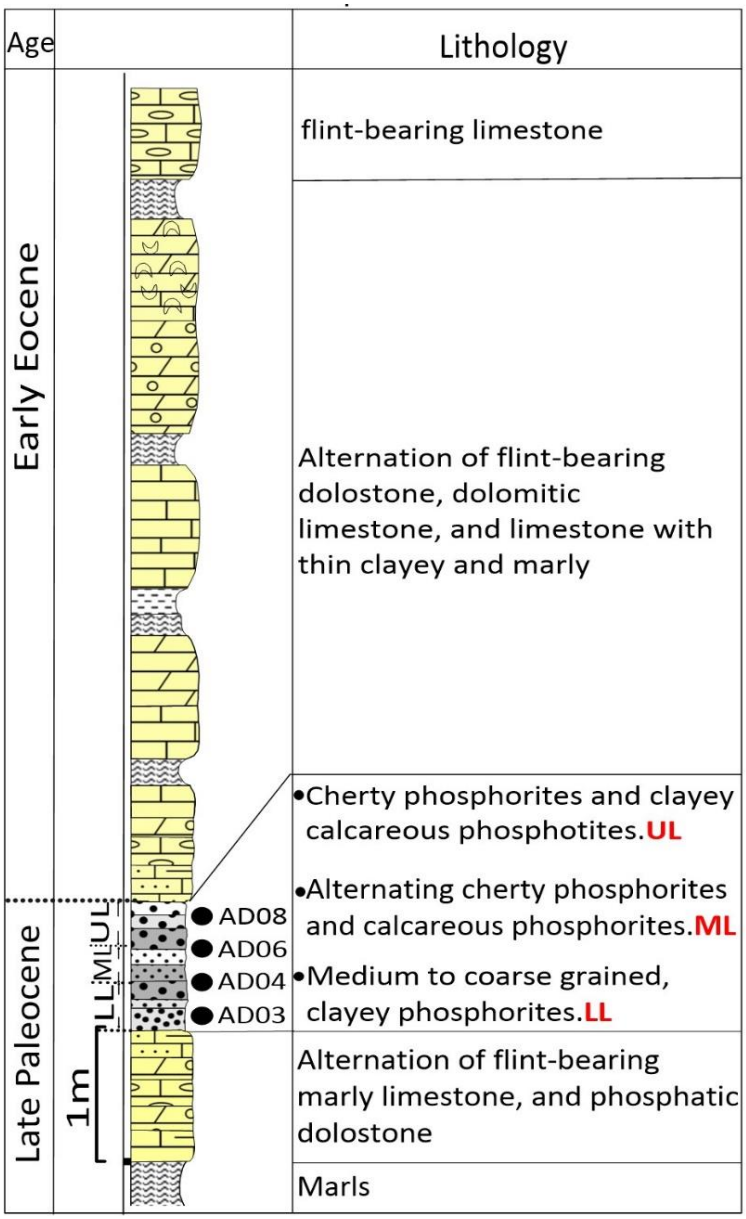

Fig. II. 18. Simplified stratigraphic column of the Ain Dibba deposit showing sample location. LL: Lower Layer, ML: Middle Layer, UL: Upper Layer.

Marls: These sediments are beige to grey in color, and form a thin layer. They are intercalated with centimetric (~10 cm) light grey clay layers (Fig. II. 19a) and form the base of the outcrop. Very thin gypsum veinlets were also noted within these marls.

Flint-bearing marly limestone (~ 20 cm thick): Above the marl sediments lies a layer of flint-bearing marly limestone with intercalations of centimetric (~10 cm) grey clays. It is typically beige to yellowish in color, soft to medium in hardness and contains flint nodules with fractures

filled with dark gray amorphous silica (Fig. II. 19b, c). It is composed of less than 5% of non-coated phosphatic particles: pellets, coprolites, and organic matter (dark color).

Phosphatic dolostone (**~ 30 cm thick):** This unit is characterized by a semi-friable to friable, beige to yellow dolostones with an average thickness of about 30 cm (Fig. II. 19d). It contains medium- to coarse-grained, poorly sorted phosphatic grains (pellets, coprolites and lithoclasts), and exhibits a brownish red color due to the presence of iron oxide and organic matter. Occasionally gypsum crystals are observed within these sediments. A few phosphorite intercalations are observed and the abundance of phosphatic grains increase vertically. These grains are cemented by calcareous cements, mainly calcite and dolomite (Fig. II. 19e). Well preserved, high-diversity benthic foraminiferal assemblages are also recorded (Fig. II19f).

The microscopic observation shows that the **flint-bearing marly limestone** rock has wackstone to packstone textures and is composed of iron oxide filling cracks and pores (Fig. II. 20a). It displays irregularly shaped, black patches dispersed in the exogangue (matrix) as organic matter (OM), and is affected by microcracks containing iron oxides due to the supergene sulfide alteration (Fig. II. 20b). Benthic foraminiferal assemblages are present in both the dolomicrite and the dolomicro-sparite which become abundant towards the top of the layer (Fig. II. 20c, d, e and f). The rhombohedral dolomite crystals show occasionally dark cores that contain some residual organic matter. The dolomitization process displays well-developed growth of rhombohedral dolomite crystals that sometimes fill the cracks and the pores of some lithoslasts, and ostracod fauna fragments (Fig. II. 20g).

Phosphatic dolostone contains less than 10 % of brown to yellowish, sub-rounded to spherical, and irregular non-coated phosphatic particles, including pellets, coprolites, and phosphoclast (lithoslasts), as well as non-phosphatic particles such as gypsum crystals and organic matter (Fig. II. 20h). These components are embedded in a grainstone texture with a sparitic matrix.

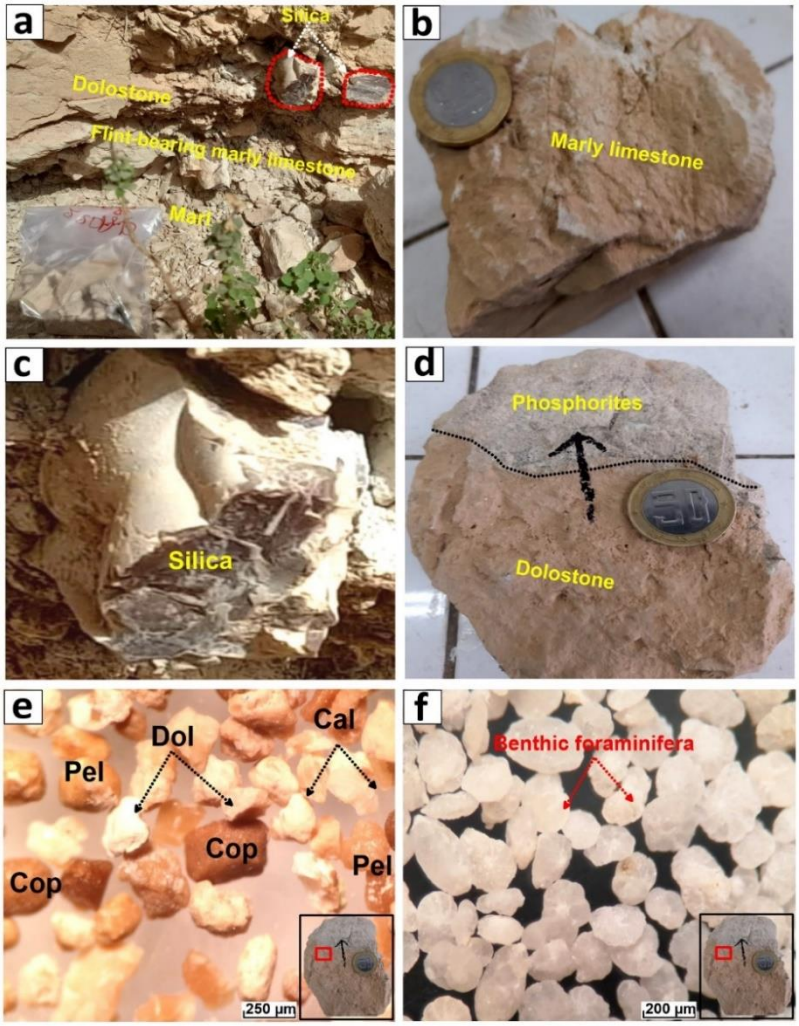

Fig. II. 19. Field photographs of the sedimentary layers at the bottom of the section of Ain Dibba deposit showing: (a) alternating flint-bearing marly limestones, marls and phosphatic dolostones; carbonate hand specimens including: (b) beige, compact marly limestone, (c) kidney-like silica nodules, and (d) contact between phosphatic dolostones and the lower sub-layer phosphorite of Ain Dibba deposit; Photomicrographs showing: (e) abundant dolomite (Dol), calcite (Cal) crystals, benthic foraminifera, and some non-coated-phosphatic particles such as: pellets (Pel), coprolites (Cop) in dolostones.

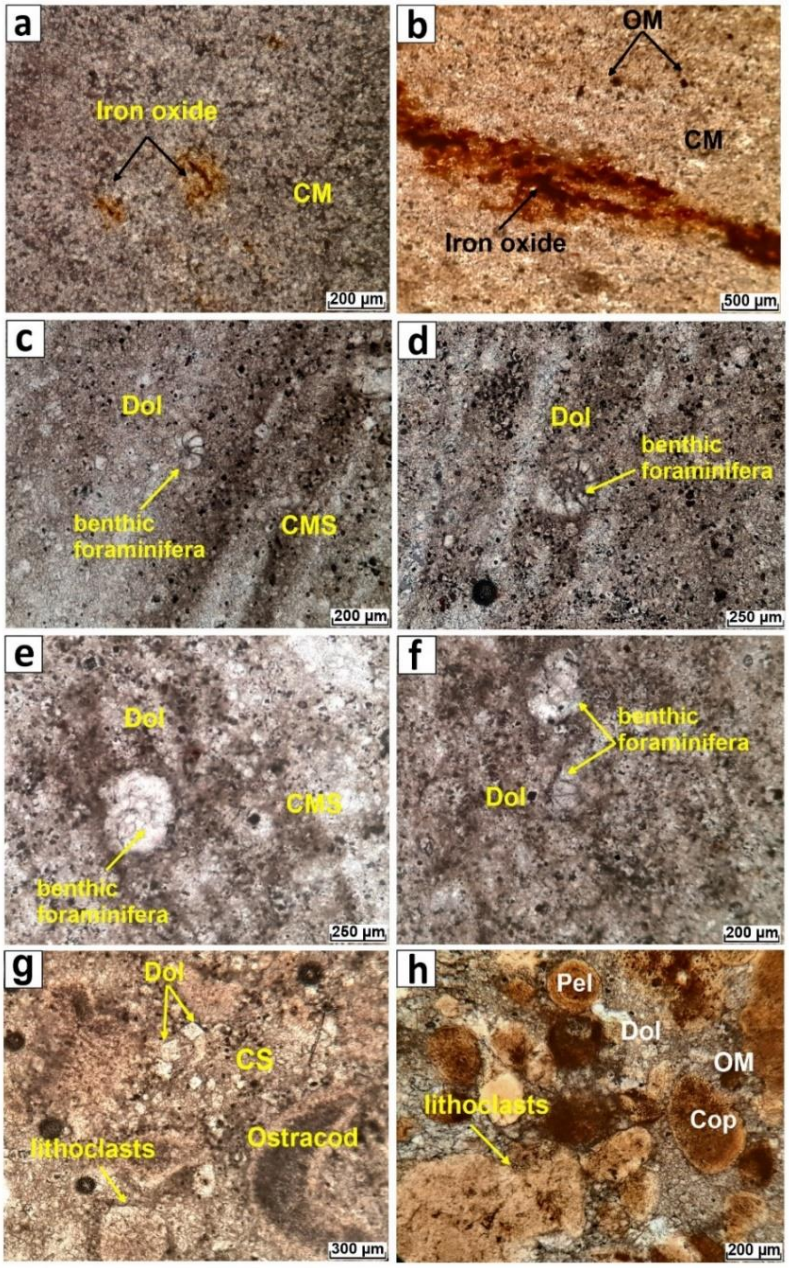

Fig. II. 20. Thin section photomicrographs of the sedimentary layers from the bottom section of Ain Dibba deposit. (a, b) Wackstone dolomicrite (Dol) containing iron oxide and organic matter (OM); (c, d, e, and f) dolomicrite to dolomicro-sparitic cement towards the top with abundant benthic foraminifera; (g) dolomitization process showing rhombohedral dolomite crystals, lithoslasts, and ostracods; (h), non-coated phosphatic particles in a packstone texture: pellets (Pel), coprolites (Cop), organic matter (OM), bioclasts (lithoslasts), and gypsum crystal within dolomitic limestone.

Phosphorite layers: These belong to the Thanetian of the Ain Dibba and consist of thicknesses ranging from 80 cm to 1 m. These phosphorite layers show variations in color, hardness, shape, abundance of the phosphatic particles, and the nature of the cements. They are, therefore, subdivided into three sub-layers: the lower, the middle and the upper sub-layer:

The lower sub-layer (LL) consists of beige to grey, friable to semi-friable, medium to coarse grained, clayey and slightly siliceous phosphorites (Fig. II. 21a, b). It is characterized by significant abundance of phosphatic particles (pellets, coprolites, and glauconites), and bioclasts (fish teeth, bone fragments) that are cemented by clayey matrix (Fig. II. 21c, d). These phosphatic particles make up 75% of the total rock volume, with sizes ranging from 80 µm to a few millimeters.

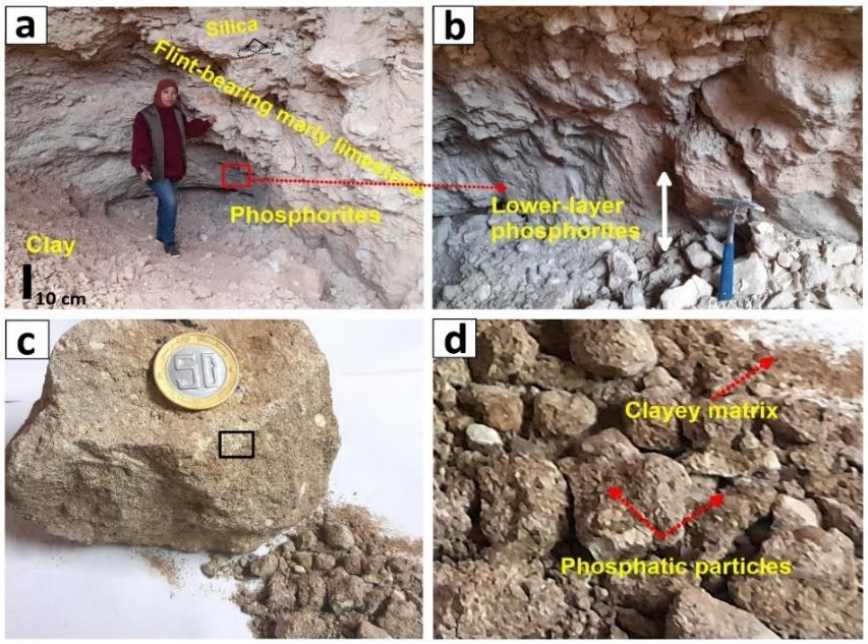

Fig. II. 21. Field photographs of the Ain Dibba deposit showing the lower sub-layer phosphorites (LL). (a) and (b) 20 cm thick clayey and slightly siliceous phosphorite layer is interlayered within decimeter-thick layers of marl, cherty limestone and dolostone; (c) Hand specimen of phosphorite rock taken from the lower sub-layer (LL) showing grey, friable to semi-friable phosphorite, (d) clayey phosphorite containing abundant phosphatic particles.

The middle sub-layer (ML) is composed of grey to dark, compact, much harder phosphorites (cf. Fig. II. 18). It is characterized by an alternation of different phosphorite types: (a) Hard and dark grey ***cherty phosphorites*** with an average thickness of 30 cm (Fig. II. 22a), and contain centimeter-size kidney-like cherty nodules. They consist of abundant poorly sorted, medium to coarse-grained phosphatic particles and bioclasts, accounting for 65% by volume of the total rock. Their sizes range from 50 µm to 2 millimeters (Fig. II. 22b).

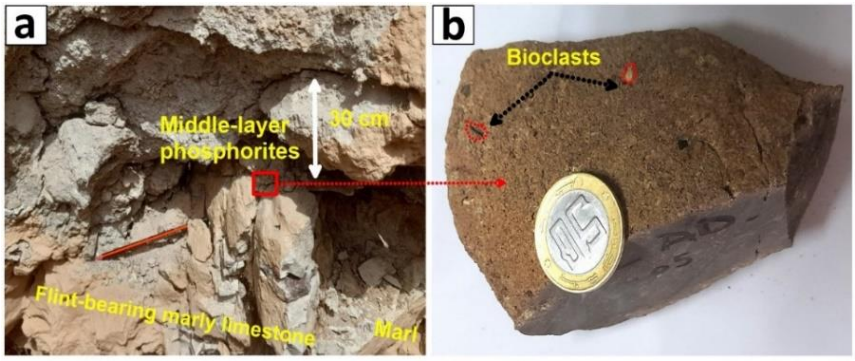

Fig. II. 22. Field photograph showing the middle sub-layer phosphorites (ML) of the Ain Dibba deposit: (a) thin phosphorite layer interlayered within decimeter-thick layers of marl, flint-bearing marly limestone, (b) Hand specimen of phosphorite rock from the middle sub-layer (ML) of Ain Dibba deposit showing hard, dark grey cherty phosphorites, containing abundant of phosphatic particles and bioclasts.

(b) ***Calcareous phosphorites*** consist of semi-friable to hard, beige-grey colored rock, with poorly sorted, medium to coarse grained phosphatic particles (Fig. II. 23a). It contains less abundant phosphatic particles (pellets, coprolites) and bioclasts (fish teeth) compared to other lower and upper phosphorite layers (Fig. II. 23b). These phosphatic particles are cemented by clayey and /or calcareous matrix (calcitic).

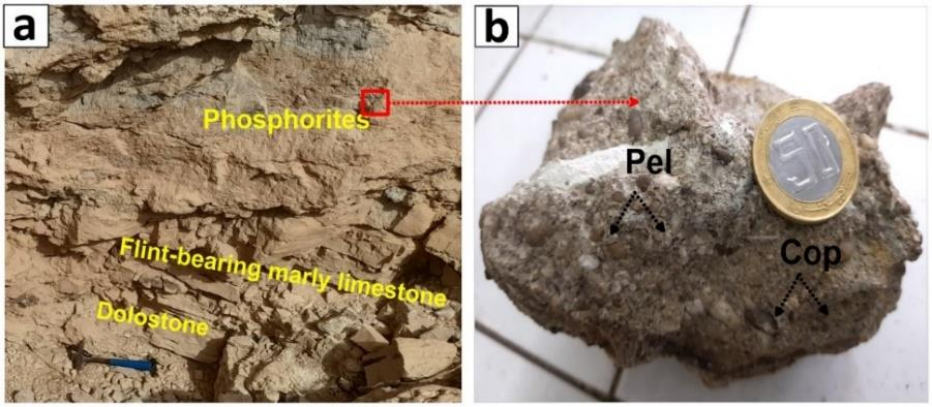

Fig. II. 23. Field photograph of the phosphorite middle sub-layer (ML) of the Ain Dibba deposit showing (a) 30 cm thick phosphorites interlayered within decimeter-thick layers of dolostone and flint-bearing marly limestone; (b) Hand specimen of beige, grey calcareous phosphorites showing abundant coarse grained phosphatic particles and bioclasts particles.

The upper sub-layer (UL), of about 20 to 30 cm thick, is composed of hard cherty phosphorite to hard, slightly semi-friable, beige clayey-calcareous phosphorites with coarse-grained phosphatic particles within a siliceous and /or calcareous cement (see Fig. II. 18 and Fig. II. 24a, b).

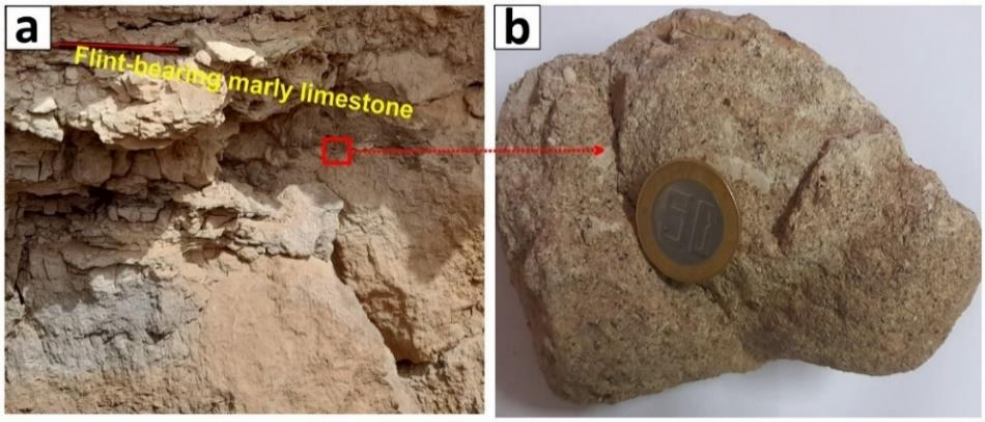

Fig. II. 24. (a) Field photograph showing the phosphorite upper sub-layer (UL) of Ain Dibba deposit that is overlain by a metre-thick flint-bearing marly limestone; (b) Hand specimen of phosphorite taken from the upper sub-layer displaying grey to beige, and hard to semi-friable rock.

Exploitation tailings are located at ~1 km to the west of the studied section of Ain Dibba deposit (Fig. II. 25a), which may be represented the lower layers phosphorites of Ain Dibba deposit. Here, the cherty phosphorites are composed by hard, grey, poorly sorted, coarse phosphatic particles and bioclasts, and beige, slightly hard calcareous phosphorite containing abundant phosphatic particles and bioclasts (Fig. II. 25b, c). These account for 60% of the total rock volume, with particle sizes ranging from 150 µm to 5 mm.

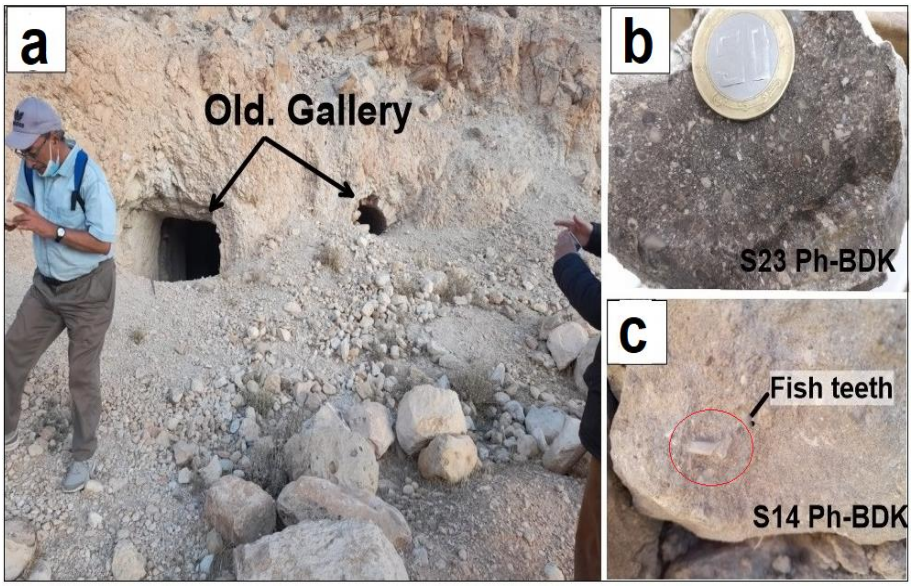

Fig. II. 25. Field photographs from the exploitation tailings at 1 km to the west of the Ain Dibba phosphorites outcrops. (a) exploitation tailings; (b) hand specimen showing grey, coarse-grained cherty phosphorites; (c) hand specimen of beige, semi-friable to hard calcareous phosphorite containing bioclasts (fish teeth).

The upper phosphorite sub-layer is overlain by:

Phosphatic dolostone (~ 30 cm thick): These sediments of about 30 cm thick, consist of semi-friable to hard, yellow to beige color dolostones (see Fig. II. 18, and Fig. II. 26) that contains abundant medium to coarse-grained phosphatic particles.

Fig. II. 26. Field photograph showing beige to grey dolostone containing abundant phosphatic particles.

Flint-bearing marly limestone (~ 80 cm thick): It is a semi-friable to hard, grey to beige rock, characterized by the presence of grey dark kidney-like cherty nodules, and contains some phosphatic particles. The facies display centimeter-thick intercalations of marly limestone, clay and marl levels (Fig. II. 27).

Fig. II. 27. Field photograph showing alternating of beige to grey, flint-bearing marly limestone and marl of Ain Kissa deposit.

Dolomitic limestone (~ 1.2 m thick): These sediments are composed by beige to yellowish, hard dolomitic limestone with marly limestone and marl intercalation levels (Fig. II. 28). The dolostone exhibits reddish-brown surface due to oxidation.

Fig. II. 28. Field photograph showing beige to grey, dolomitic limestone of Ain Kissa deposit.

Limestone with thin clayey and marl layers (~ 1.5 m thick): This layer that is characterized by hard, beige to yellow that may become brownish or reddish in color due to iron oxidation, displays thin intercalations of clayey and marl levels (Fig. II. 29). It contains some fine to medium size phosphatic particles.

The petrographic investigations show that the **dolostone** rock displays wackstone to packstone textures, and contains abundant benthic foraminifera ranging in size from 250 to 500 µm (Fig. II. 30a). **Flint-bearing marly limestone** contains abundant benthic foraminifera and organic matter, which is also present within the micritic to micro-sparitic matrix (Fig. II. 30b). **The dolomicrite** displays a mudstone to wackstone texture, but contains less abundant benthic foraminifera (Fig. II. 30c). The **limestone rock** shows packstone to grainstone textures, and displays abundant of beige, rounded to subrounded pellets, bone fragments, and lithoclasts within a sparitic matrix (Fig. II. 30d).

Fig. II. 29. Field photograph showing beige limestones from the exploitation tailings.

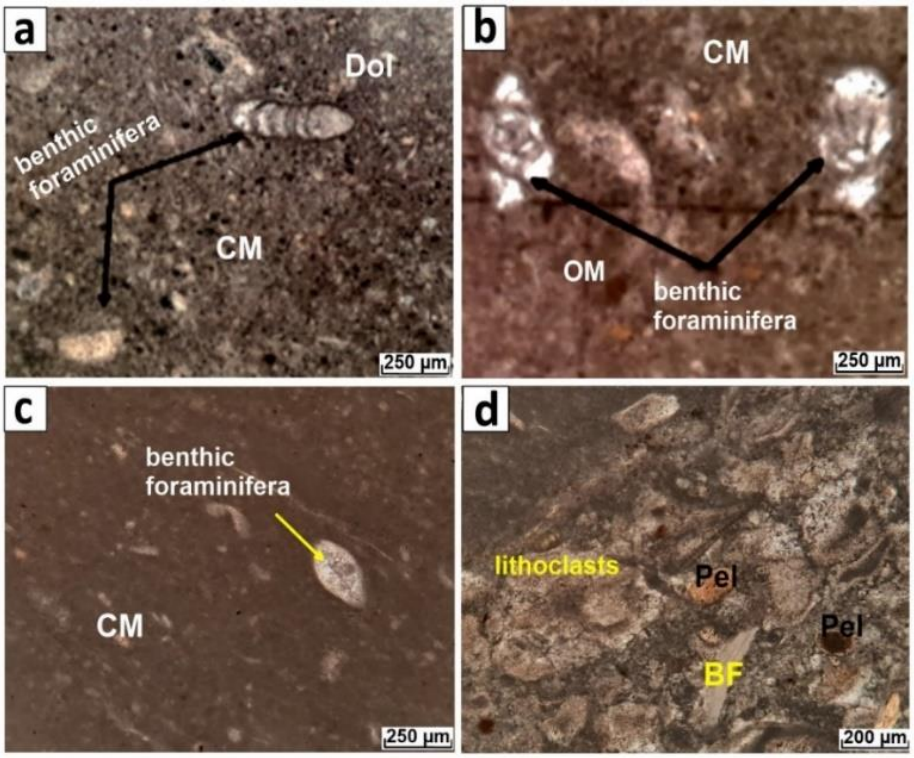

Fig. II. 30. Thin section photomicrographs from Ain Dibba deposit showing: (a) wackstone to packstone dolomitic containing an abundant benthic foraminifera and dolomite crystal (Dol); (b) marly limestone showing micritic to micro-sparitic matrix; (c) dolomicrite matrix (CM) containing benthic foraminifera in a mudstone texture; (d) dolomicro-sparitic cement (CMS) showing abundant phosphoclast (lithoclasts, bioclasts, bone fragmants (BF)), and pellets (Pel).

Flint- bearing dolomitic limestone (~1.5 m thick): This facies is represented by beige color, hard, containing flint nodules (Fig. II. 31a). It is slightly phosphatic and shows a thickness ranging from 1 to 2 meters.

Dolomitic limestone (~1 m thick): The rock is composed of hard, beige to grey in color, and contains abundant bioclacts and bivalve fragments with an average thickness of approximately 1 m (Fig. II. 31b).

Bioclast limestone (~ 1 m thick): It is a beige to light grey facies that may become brownish or reddish on weathered surfaces due to iron oxidation (Fig. II. 31c, d). It is characterized by abundant bone fragments and skeletal debris.

Flint-bearing limestone: This limestone layer appears as thin-bedded to massive rock, characterized by abundant gastropods, some echinoderm fragments, as well as, fragments of ostracod faunas, which sometimes display calcitic filling. The upper most part of the section is composed of centimeter-thick siliceous (flint) levels alternating with limestone layers that contain quartz geodes (Fig. II. 31e, f).

Petrographically, the **dolomitic limestone rock** shows a wackstone to packstone texture, and contains an abundance of rounded to subrounded pellets and cylindrical to elliptical coprolites with rhombohedral dolomite crystals within a micro-sparitic matrix (Fig. II. 32a). The **grainstone limestone** rock is composed of gastropods, some echinoderm fragments (EF), and ostracod fauna (Fig. II. 32b, c). The cracks, micro-fissures and tests of some gastropod fragments are filled with a micro-calcitic matrix (see Fig. II. 32d).

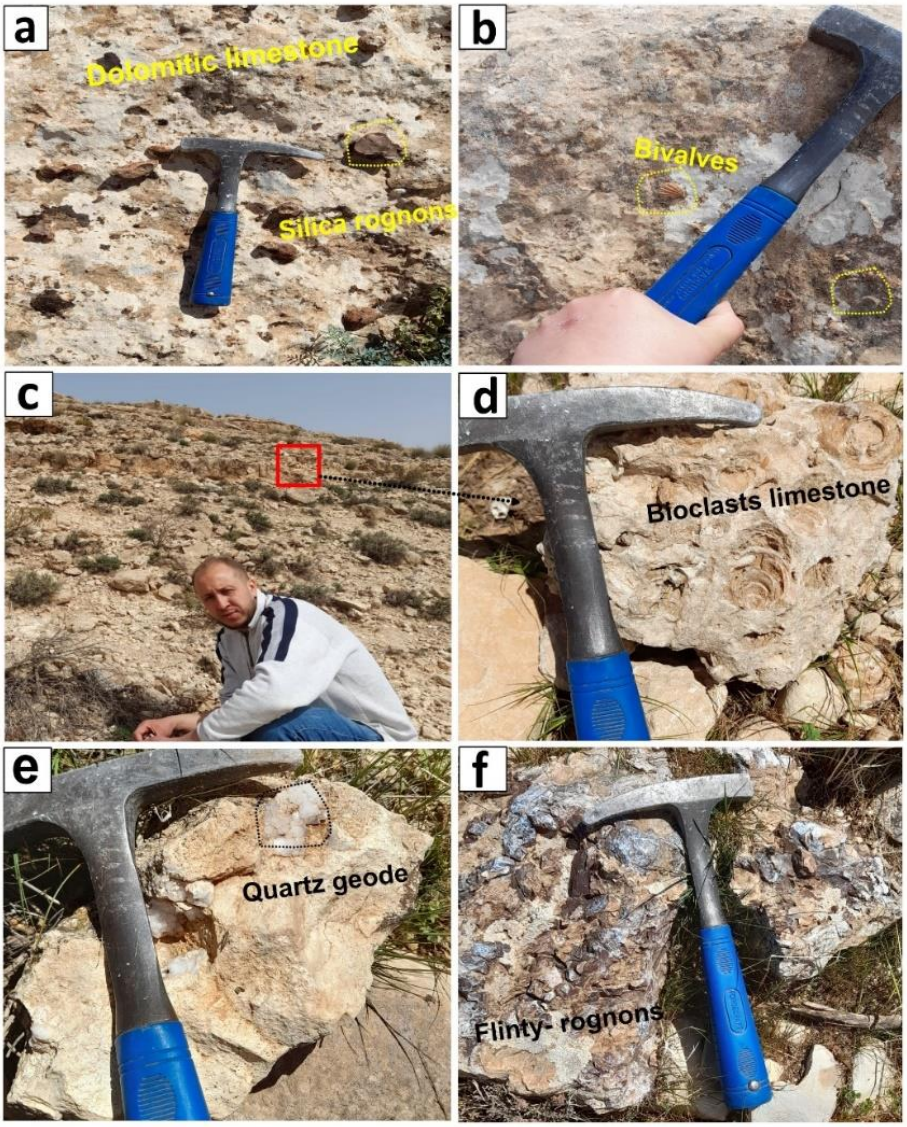

Fig. II. 31. Field photographs from the top section of the Ain Dibba deposit showing: (a) hard, beige flint-bearing dolostone; (b) limestone with abundant bioclasts and bivalves; (c) alternation of bioclast limestone and flint-bearing marly limestone; (d) beige, hard bioclasts limestone; (e) beige limestone with quartz geode; and (f) kidney-like flint.

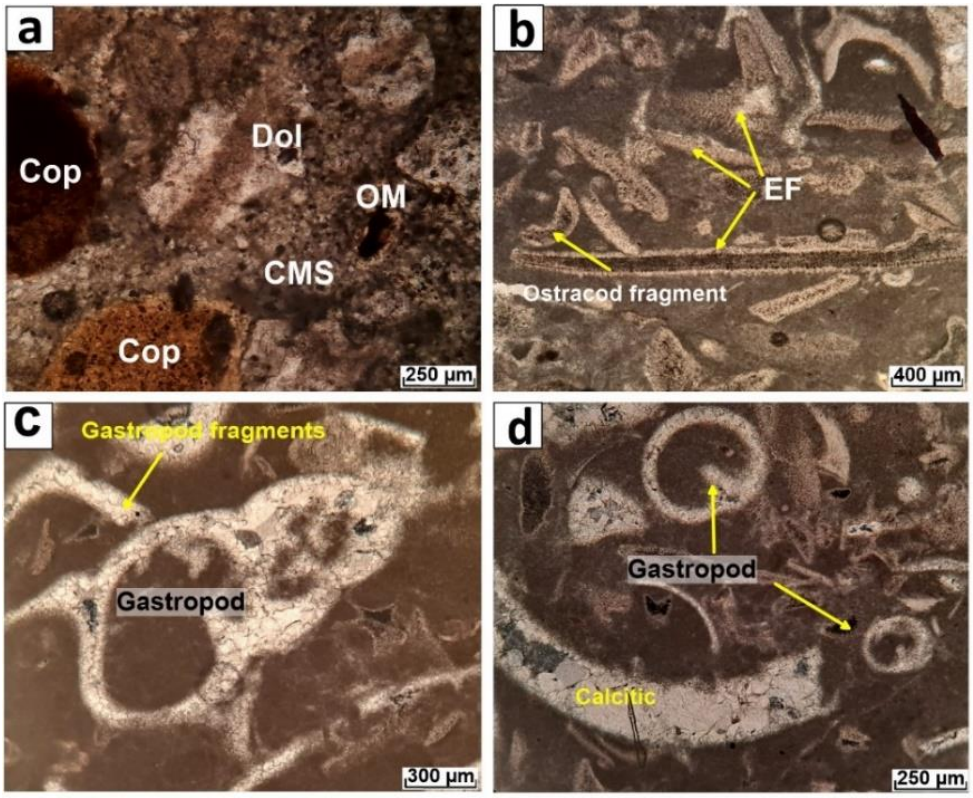

Fig. II. 32. Thin section photomicrographs from the top section of Ain Dibba deposit showing: (a) dolomicro-sparitic cement (CMS) containing abundant phosphatic particles, including pellets (Pel) and coprolites (Cop), dolomite rhombohedra crystal (Dol) and organic matter (OM); (b, c) limestone containing gastropods, some echinoderm fragments (EF) and ostracod fauna; (d) gastropod fragments filled by calcitic matrix.

II. 4. 3. The Ain Kissa deposit in northern basin

The Ain Kissa phosphorite deposit occurs at about10 to 11 km NNW of the Tebessa town (cf. Fig. II. 3) and about 5 km west of Ain Dibba. In this region, the sedimentary successions are geologically similar to those of Ain Dibba (see Fig. II. 3). The study of the Thanetian phosphate-bearing sedimentary layers and associated carbonate layers was based on a cross-section taken from the north-west to the south-east of the Ain Kissa outcrop with the geographical coordinates: Longitude: 8°7'27" E; and Latitude: 35°29'20" N (Fig. II. 33).

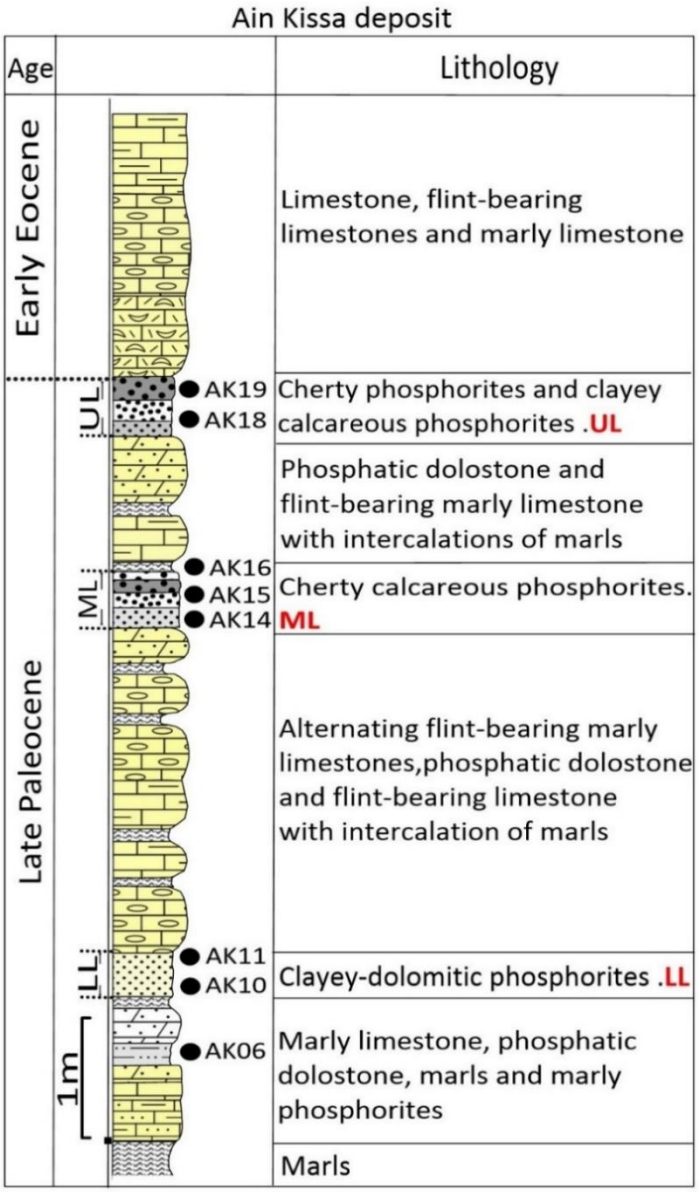

Fig. II. 33. Simplified lithological column of the Ain Kissa deposit showing sample location. LL: Lower Layer, ML: Middle Layer, UL: Upper Layer.

Based on field observations and the detailed description of the different facies encountered in the Ain Kissa deposit (Fig. II. 33), the lithological succession, from bottom to top, is as follows:

Marls: These marls are observed at the lower part of the Ain Kissa outcrop, where they show relatively thin levels (Fig. II. 33). They display some bioclast fragments (Fig. II. 34a).

Marly limestone: (~20 cm thick): It consists of about 20 cm thick, beige to grey, compact**,** semi-friable to hard level that is interlayered within centimeter-thick levels of marls and clayey material (Fig. II. 34a, b). It is characterized by abundant phosphatic particles, including beige to brown pellets, beige coprolites, brown bone fragments, and shark teeth, accompanied by green glauconite grains. They show ovoidal to spheroidal shape and range in size from 100 to 250 µm; some minor dolomite and calcite crysts are also present (Fig. II. 34c). The terrigenous input is represented by angular to sub-angular quartz grains (Fig. II. 34d). These components constitute up to 20 % of the rock.

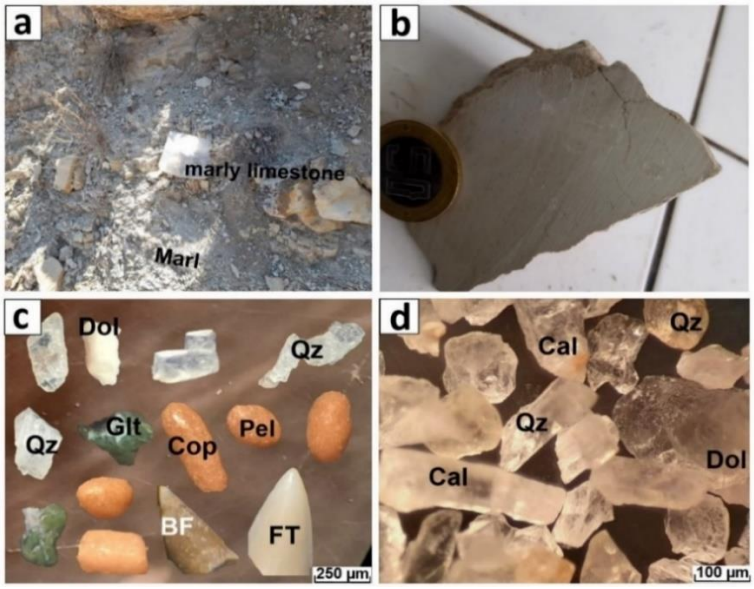

Fig. II. 34. (a) Field photograph from the lower part of Ain Kissa outcrop showing alternation of beige to grey phosphatic marly limestone and marl; (b) hand specimen of beige, compact marly limestone; (c, d) photomicrographs showing: abundant dolomite (Dol), angular to sub-angular quartz grains (Qz) with some phosphatic particles such as: pellets (Pel), coprolites (Cop), glauconites (Glt), bioclasts (fish teeth (FT), bone fragments (BF)) and calcite (Cal).

Microscopically, the marly limestone is characterized by wackstone to packstone textures, and contains abundant planktonic foraminifera, and non-coated phosphatic particles (pellets, coprolites, and glauconites), as well as bioclasts (Fig. II. 35a). Planktonic foraminiferal assemblages *and* pellet particles embedded within the mudstone *to* wackestone textures often exhibit surface oxidation (Fig. II. 35b, c). Sometimes some test fragments are filled with a microsparitic siliceous matrix with abundant organic matter (Fig. II. 35d). Other minor, non-

phosphatic minerals are also recorded, such as green to brown, ovoidal, spheroidal or irregular galuconite, ranging in size from 100 to 350 µm, associated with rhombohedral dolomite crystals, pellets, organic matter, as well as bone fragment particles (Fig. II. 35e, f). Terrigenous supply is represented by angular to sub-angular detrital quartz, ranging in size from 100 to 250 µm, which occurs within the microsparitic matrix, along with abundant dolomite crystals and phosphatic particles (Fig. II. 35g, h).

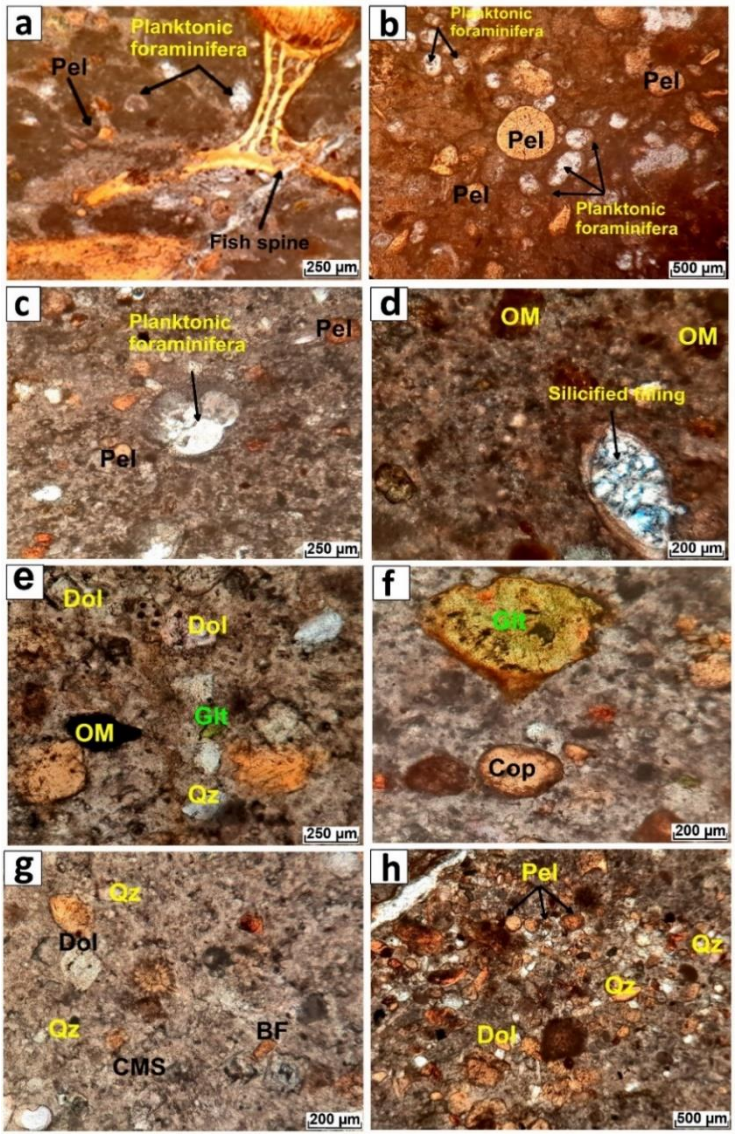

Fig. II. 35. Photomicrographs of the marly limestone rock at the bottom section of Ain Kissa deposit. (a, b, c) wackstone to packstone limestone containing abundant planktonic foraminifera, pellets (Pel), fish spine; (d) sparitic silicified matrix filling in some bioclasts, with organic matter (OM); (e, f) glauconites (Glt), coprolites (Cop), and dolomite crystals (Dol) in mirco-sparitic cement (CMS), with glauconites (Glt) and organic matter (OM); (g, h) limestone showing abundant angular to sub-angular

detrital quartz (Qz), dolomite growth (Dol) in mirco-sparitic cement (CMS), pellets (Pel) and bone fragments (BF).

Marly phosphorites (~ 20 cm thick): This layer consists of about 20 cm thick, beige to yellowish, semi-hard to hard marly phosphorite (see Fig. II. 33, and Fig. II. 36a). It comprises interbedded dark brown, clay-rich levels enriched in disseminated phosphatic material. It is characterized by abundant, poorly sorted, medium to coarse phosphatic particles and bioclasts, accounting for 40% volume of the total rock (Fig. II. 36b). Their size ranges from 50 µm to 2 millimeters.

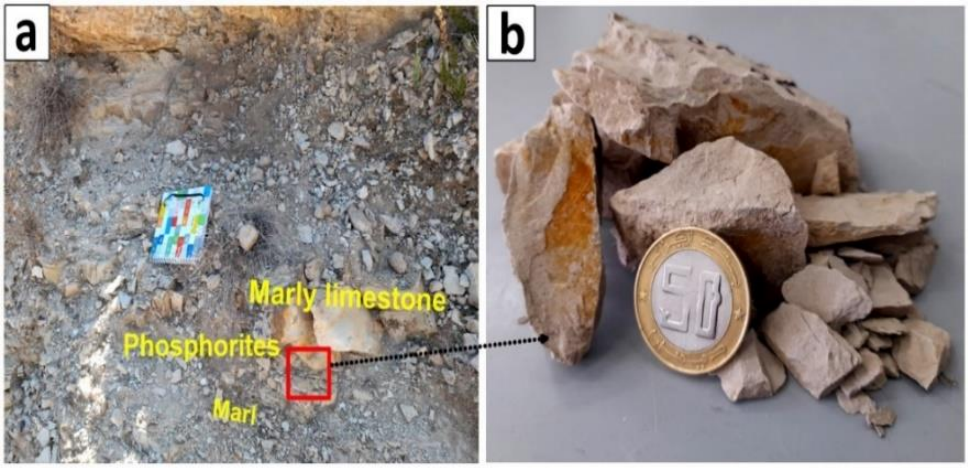

Fig. II. 36. Field photograph of the marly phosphorite rock of Ain Kissa deposit showing: (a) alternating marly limestone, marl, and phosphorite; (b) hand specimen taken from Ain Kissa deposit shows beige, semi-friable to hard marly phosphorite.

Phosphatic dolostone (~ 20 cm thick): This unit consists of a thin (about 20 cm thick) layer of fine-grained, yellow-grey phosphatic dolostone (Fig. II. 37a, b). It contains of fine to medium-grained**,** poorly sorted phosphatic particles (pellets and bone fragments), benthic foraminiferal assemblages, and lithoclasts, with a dolomite and calcite grains matrix (Fig. II. 37c, d). Petrographic investigations show that the dolostone rock has a wackestone to packstone texture and is composed of fine-crystalline dolomite, fine-grained phosphatic particles (pellets), and iron oxides filling cracks and pores within a microsparitic matrix (Fig. II. 38a). Well-developed dolomite rhombohedra are observed growing within a sparitic matrix (Fig. II19b),

which gradually transitions to a dolomicro-sparitic texture toward the top. Reddish-brown oxidation is present along micro-cracks within the rock (Fig. II. 38c). Brown, cylindrical coprolites and benthic foraminiferal assemblages are occasionally filled with dolomicrite (Fig. II. 38d).

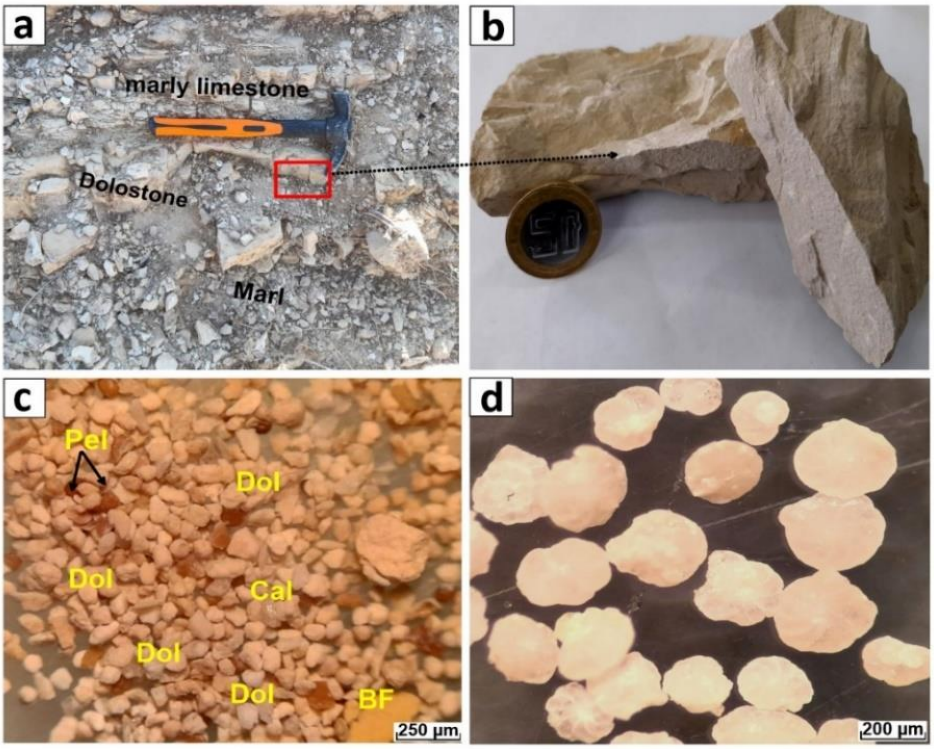

Fig. II. 37. (a) Field photograph of Ain Kissa deposit showing about 20 cm thick of phosphatic dolostone rock alternating with marly limestones and marls; (b) hand specimen of beige, compact dolostone; (c) Photomicrograph showing phosphatic particles: pellets (Pel) and bone fragment (BF) often cemented by calcareous, dolomitic matrix within dolostone; (d) benthic foraminiferal associated in the dolostone rock.

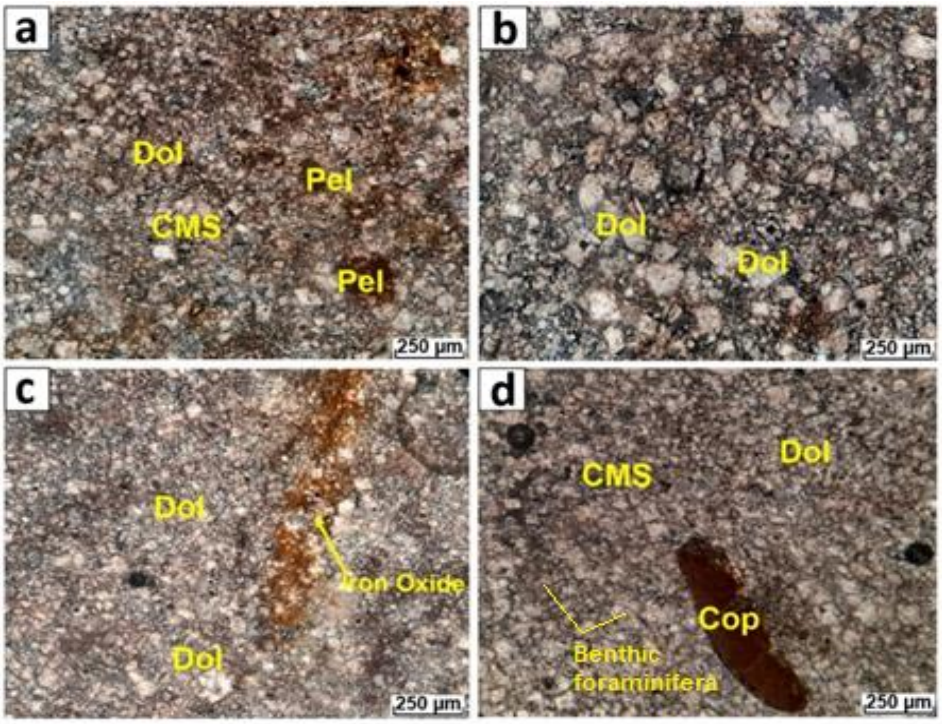

Fig. II. 38. Photomicrographs of the dolostone rock of Ain Kissa deposit. (a) dolomicro-sparitic containing phosphatic particles (Pel) and iron oxides dispersed in the micro-sparitic matrix; (b) well-developed growth of dolomite rhombohedra crystal; (c, d) iron oxide filling the microcracks of the mirco-sparitic matrix (CMS) with coprolites particles (Cop) and benthic foraminiferal assemblages.

Clayey-dolomitic phosphorites (LL; ~ 60 cm thick): These represent ***The lower layer (LL),*** and are about 40–60 cm thick. They are composed of alternating beige to grey dolomites, grey marls, and clayey-dolomitic phosphorites (Fig. II. 39a). Here, the phosphorites are beige to grey, slightly hard, and often dolomitic, sometimes clayey matrix (Fig. II. 39b). They are characterized by abundant medium- to coarse-grained, poorly sorted particles, containing abundant glauconite particles These phosphatic particles range from 80 µm to a few millimeters in size make up 75% of the volume of the total rock.

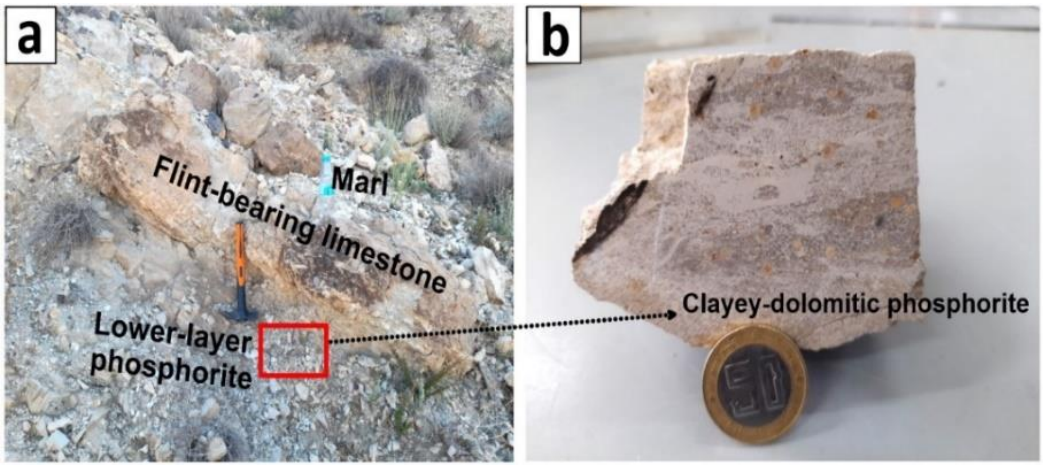

Fig. II. 39. Field photograph of the phosphorite lower layer of Ain Kissa deposit showing: (a) alternating flint-bearing limestone, marl and phosphoite; (b) hand specimen showing beige, clayey-dolomitic phosphorite.

Flint-bearing limestone (~ 1 m thick): This unit is characterized by beige, very hard flint-bearing limestone, with intercalations of marl at the top of the layers (Fig. II. 40). The limestone consists of grey to dark kidney-like silica nodules with thickness reaching up to 1 m.

Fig. II. 40. Field photograph showing beige, hard flint-bearing limestone and grey marl of Ain Kissa deposit.

Flint-bearing marly limestone (~ 2 m thick): This lithology consists of light grey, soft, weathered flint-bearing marly limestone layers with kidney-like silica nodules, intercalations with marly levels (Fig. II. 41). The thickness reaches up to 2 m.

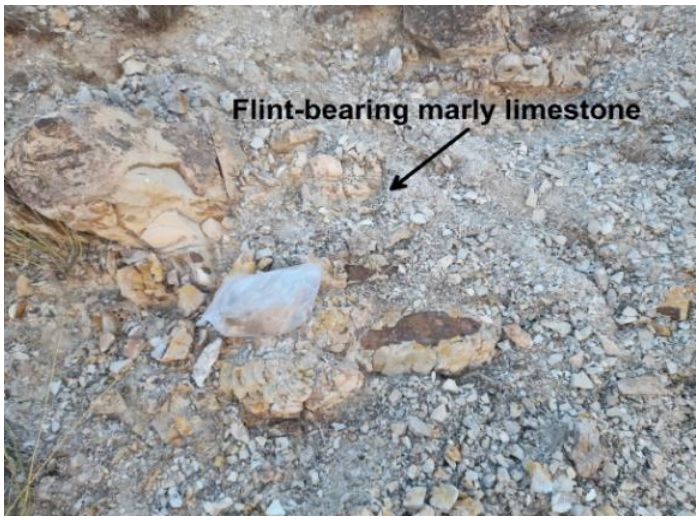

Fig. II. 41. Field photograph showing alternating of beige to grey, flint-bearing marly limestone and marl of Ain Kissa deposit.

Phosphatic dolostone (~ 50 cm thick): This rock is beige to grey, semi-friable to hard, and contains an abundance of medium to coarse-grained phosphatic particles (Fig. II. 42). It is approximately 50 cm thick.

Fig. II. 42. Field photograph showing the phosphatic dolostone rock of Ain Kissa deposit.

Cherty and calcareous phosphorites (ML; ~ 50 cm thick): These represent ***The middle layer (ML),*** of about 40 to 50 cm thick (see Fig. 33, and Fig. II. 43a), and is characterized by alternating different phosphorite types: hard, grey, medium to coarse grained poorly sorted cherty phosphorite and beige, grey fine-to medium grained calcareous phosphorites with

abundant of phosphatic particles (pellets and coprolites), and bioclasts (bioclasts and lithoclasts) (Fig. II. 43 b, c, d).

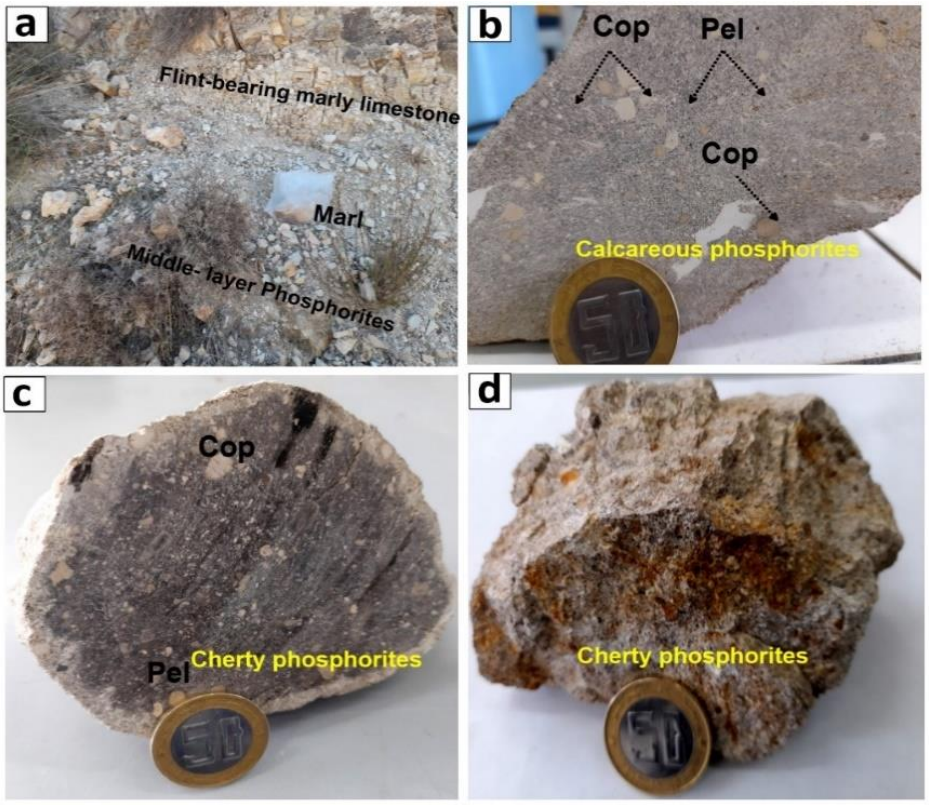

Fig. II. 43. Field photograph of the phosphorite middle layer from Ain Kissa deposit showing: (a) 50 cm thick of phosphorites alternating with flint-bearing marly limestones and marls; Hand specimens showing: (b) beige to grey, slightly hard calcareous phosphorite, (c, d) medium to coarse grained, grey, hard cherty phosphorites.

Flint-bearing marly limestone (~ 60 cm thick): This unit is composed of semi-friable to hard flint-bearing marly limestone with kidney-like silica nodules, and with marl intercalations levels (Fig. II. 44). It exhibits reddish-brown surface oxidation. Microscopically, the limestone has a grainstone texture and is composed of abundant pellets, coprolites, lithoclasts, and iron oxides filling cracks and pores within a sparitic calcitic cement (Fig. II. 45a). The coprolite and lithoclast particles are fissured and fractured, and are surrounded by reddish-brown oxidation that disperses within the matrix (Fig. II. 45b).

Fig. II. 44. Field photograph showing beige, semi-friable, flint-bearing marly limestone of Ain Kissa deposit.

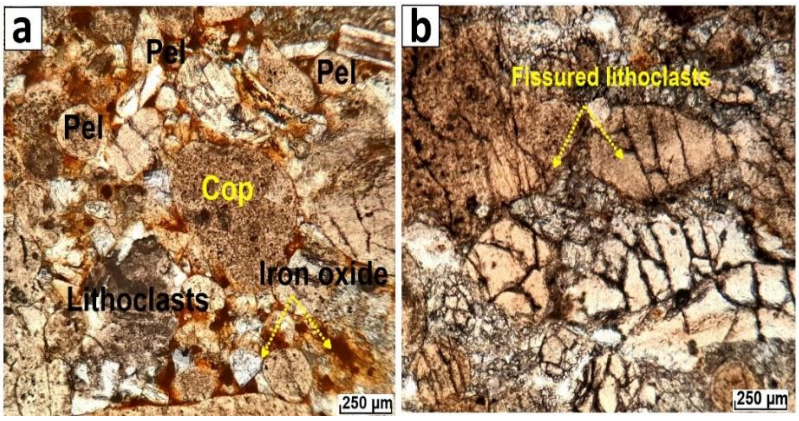

Fig. II. 45. Thin section photomicrographs of the phosphatic limestone of Ain Kissa deposit. (a) pellets (Pel), coprolites (Cop), and lithoclasts, are surrounded by iron oxide; (b) coprolites and lithoclasts particles are mainly fissured.

Phosphatic dolostone (~1.2 m thick): This unit consists of beige phosphatic dolostone with intercalations of beige marl levels (see Fig. II. 33, and Fig. II. 46a). Dolostone rock contains an abundance of medium to coarse-grained phosphatic particles (Fig. II46b). It is approximately 1.2 m thick. This layer is covered by upper layer phosphorites (UL). Microscopically, the dolostone rock shows a dolomicrite to dolomicro-sparitic matrix containing phosphatic particles: rounded pellets and cylindrical to elliptical coprolites, within the micro-sparitic matrix and /or cement (Fig. II. 47a). These phosphatic particles have irregular dark patches (Fig. II. 47b) due to the presence of trapped organic matter inside them, where it occurs either in

concentric micro-layers or in the form of disseminated organic material within dolomitic cement.

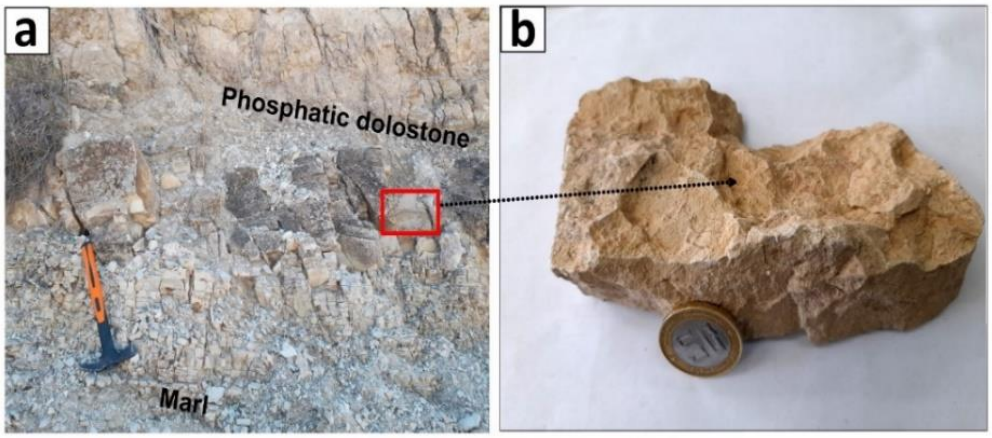

Fig. II. 46. Field photograph and hand specimen of the phosphatic dolostone of Ain Kissa deposit. (a) alternating flint-bearing marly limestone, marl and phosphatic dolostone; (b) beige, slightly hard dolostone.

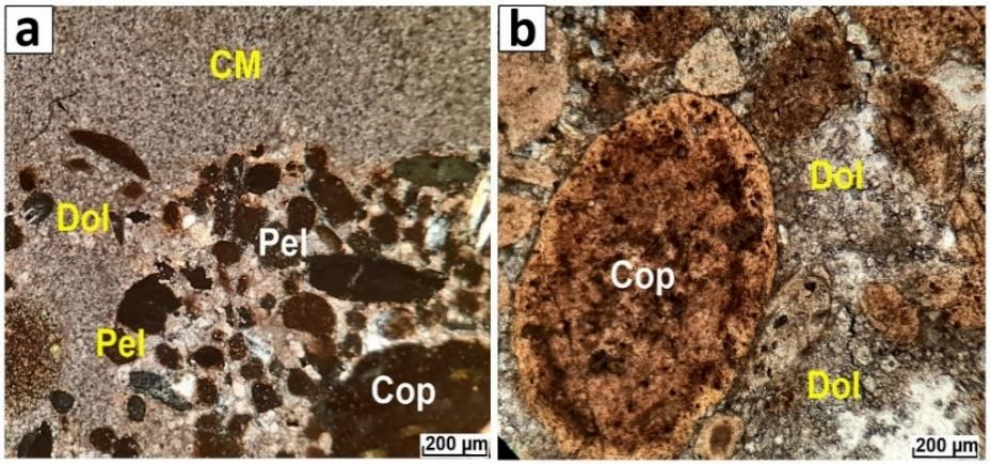

Fig. II. 47. Thin section photomicrographs of the phosphatic dolostone of the Ain Kissa deposit. (a) dolomicro-sparitic (Dol) containing pellets (Pel), coprolites (Cop), and dolomite (Dol); (b) cylindrical, elliptical coprolites within a sparitic cement.

Cherty phosphorites and clayey calcareous phosphorites (UL; ~ 40 cm thick): These represent the ***upper layer (UL)***, which is composed of beige-grey, medium-to coarse-grained and calcareous phosphorites with abundant coprolite particles and fish teeth (Fig. II. 48a, b). This phosphorites become much grey- darker, hard, and display a siliceous cement towards the top forming cherty phosphorite (Fig. II. 48c, d).

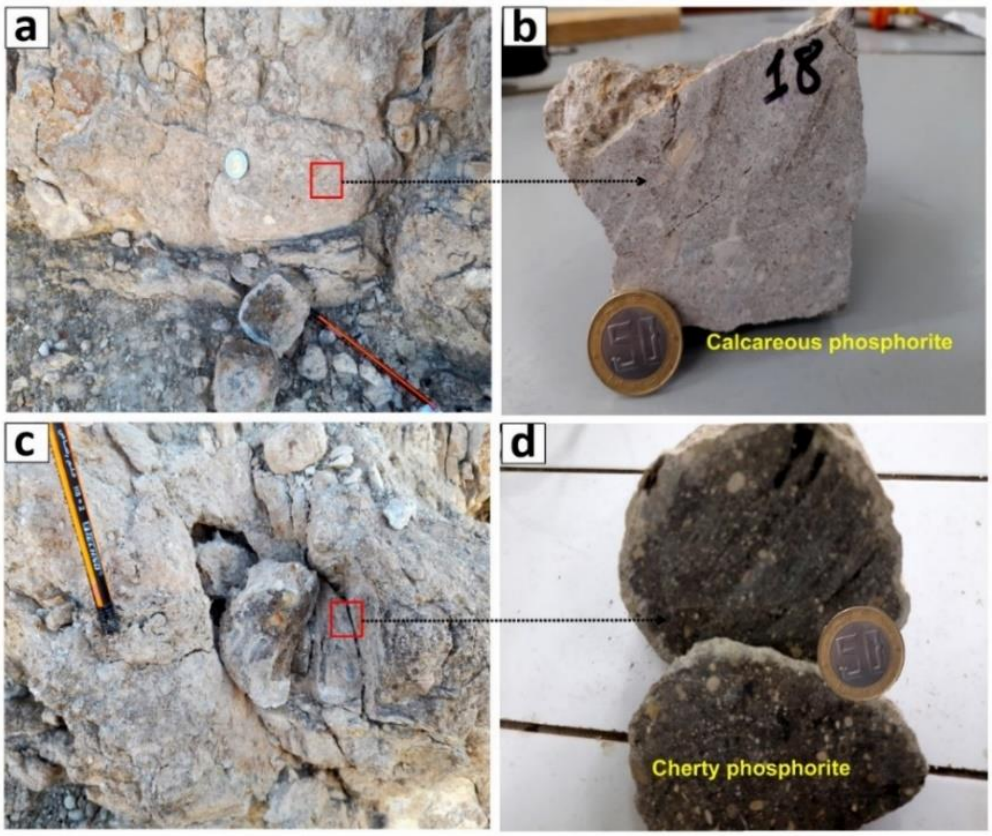

Fig. II. 48. Field photographs and hand specimens of the phosphorites upper layer of the Ain Kissa deposit. (a) alternating flint-bearing marly limestones and calcareous phosphorite;(b) beige, compact calcareous phosphorite; (c, d) hard, grey cherty phosphorite showing abundant of phosphatic particles.

Bioclasts limestone (~ 80 cm thick): This appears as a thin-bedded, massive unit, showing beige to light grey color that may become brownish or reddish on weathered surfaces due to iron oxidation (Fig. II. 49a). The rock is hard to very hard, with fine, fossiliferous texture visible on fresh surfaces. Broken surfaces reveal abundant bone fragments and skeletal debris (Fig. II. 49b). Some levels show well-compacted bioclasts cemented by calcite.

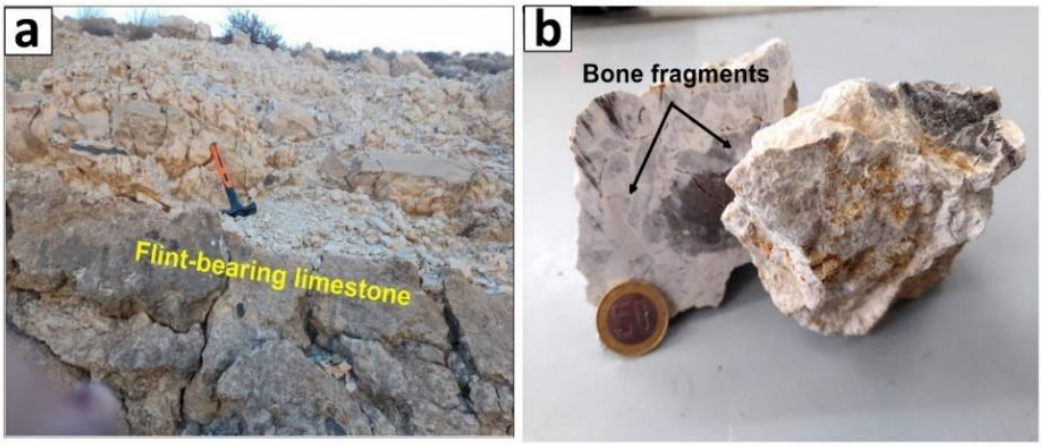

Fig. II. 49. Field photographs of the limestone rock of the Ain Kissa deposit showing: (a) about 1 m thick beige, hard flint-bearing limestone, and (b) beige, hard bioclastic limestone.

Flint-bearing marly limestone (~ 1.5 m thick): This unit is composed by alternating layers of about 1.5 m thick, beige to yellowish, semi-friable to hard flint-bearing marly limestone, yellowish marly limestone, and beige flint-bearing limestone (see Fig. II. 33, and Fig. II. 50).

Fig. II. 50. Field photograph showing alternating of beige flint-bearing limestone, and beige, semi-friable marly limestone of Ain Kissa deposit.

Petrographically, the limestone rock shows a wackstone to packstone texture within a micro-sparitic matrix, and contains an abundance of benthic foraminifera, bone fragments, as well as phosphatic particles (Fig. II. 51a). It is also composed by gastropods fauna and lithoslasts, which are filled by micro-calcitic matrix (Fig. II. 51b). High and various diversity

benthic micro fauna indicate an oxygen-rich open marine environment. Amorphous siliceous cement can recrystallize due to diagenesis, leading to the formation of chalcedony that coexist with a finer-grained amorphous siliceous matrix (Fig. II. 51c), and is represented at the rims and the center of the lithoclasts. Cracks, micro-fissures, and tests of some benthic foraminifera are filled by calcitic cement, forming crystals that act as a cement for phosphatic particles due to high energy during diagenetic processes (Fig. II. 51d). The limestone at the top reveals a micritic to micro-sparitic matrix and/or cement with benthic foraminifera, which sometimes display calcitic filling (Fig. II. 51e, f).

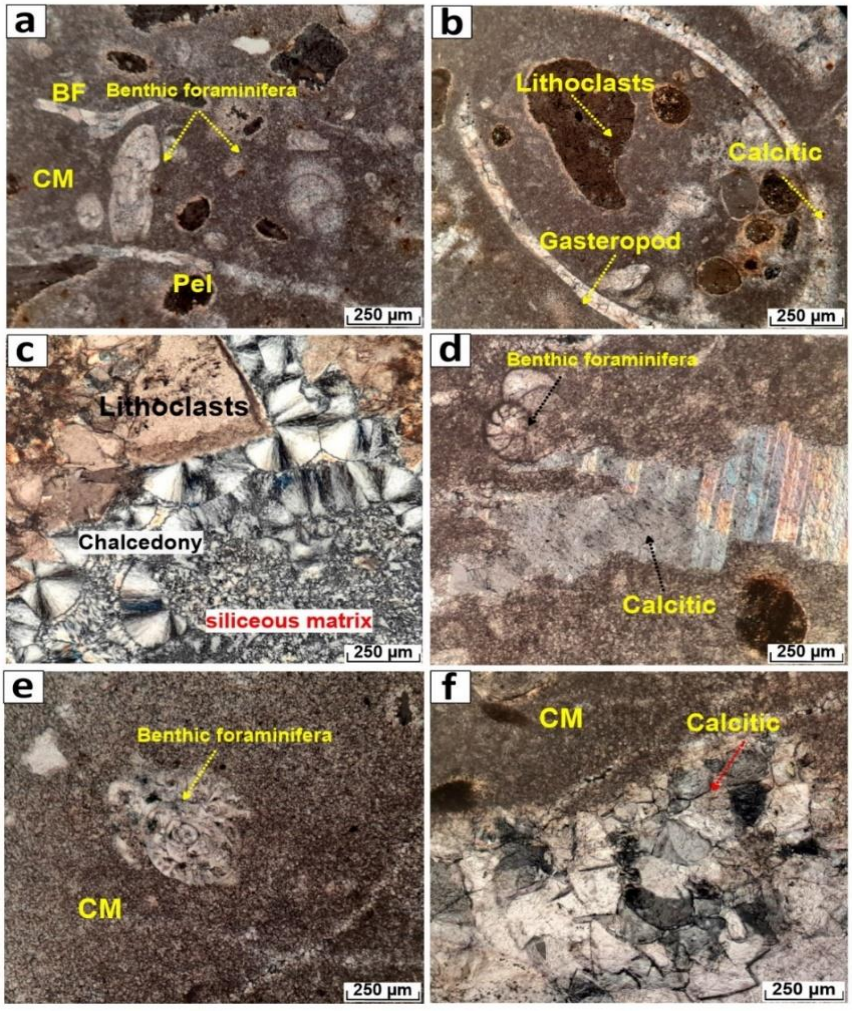

Fig. II. 51. Thin section photomicrographs of the limestone rock of Ain Kissa deposit. (a) limestone containing abundant benthic foraminifera, bone fragments (BF); (b) Bioclast limestone showing abundant gastropods, lithoclasts with calcitic filling; (c) amorphous silica as a matrix is recrystallize to chalcedony as a result of diagenesis, forming sparitic cement; (d) calcitic sparitic cement is filled in fissures; (e, f) benthic foraminifera within micritic matrix (CM) and calcitic filling.

We conclude that the Troubia, Ain Dibba, and Ain Kissa deposits consist of about 40 cm thick of phosphorite layers intercalated within meter- thick of marl, dolostone, flint-bearing marly limestone, marly limestone, bioclasts limestone. The phosphorite layers are characterized by different phosphorite types: cherty phosphorites with centimeter-size kidney-like silica nodules, beige-colored calcareous phosphorites, and clayey-calcareous beige to grey phosphorites showing poorly sorted, medium to coarse phosphatic particles. These layers are semi-friable to hard at the bottom of the sections compared to the top, which are harder, indicating more siliceous matrix and/ or cement. In addition, the phosphorites in the Ain Kissa deposit are more composed by calcareous cement in the bottom (dolomitic) than in other sections. However, the Troubia deposit shows more hard, grey cherty phosphorites.

Chapter III

Sedimentological study of the Troubia, Ain Dibba, and Ain Kissa phosphorites

Chapter III

Sedimentological study of the Troubia, Ain Dibba, and Ain Kissa phosphorites

Particle size analysis is a useful tool used to obtain a detailed understanding of the hydrodynamic condition, transport mode, sediment provenance, sorting, and paleo-environmental features, as well as reconstruction of past phosphorite sedimentological processes (e.g. Folk and Ward, 1957; Visher, 1969; Riggs, 1984; Cook and Shergold ,1986; Cook et al., 1986; Glenn et al., 1994; Bezzi et al., 2012; Dassamiour et al., 2021; Ferhaoui et al., 2022). Particle size fraction analysis results have mostly been used to highlight the rare earth elements plus yttrium (REY) contents in phosphorite ores of various sizes, thus assessing their economic potential (e.g., Bezzi et al., 2012; Ferhaoui et al., 2022). Recently, the studies were focused on the potentially hazardous elements (PHE) contents in phosphorite ores and their wastes (e.g., Ferreira da Silva et al., 2010; Bezzi et al., 2012; Boumaza et al., 2021, and 2023; Saouli et al., 2025), allowing for the evaluation of environmental impacts which pose environmental and health risks (Khelifi et al., 2020, 2021). On the other hand, particle size analysis has been able to assess the environmental impact on farmland and surrounding sediments and soils (e.g., Khelifi et al., 2020; Boumaza et al., 2024). The aim of this study is to investigate and give a comprehensive model that describes the depositional hydrodynamic conditions of the Ain Dibba and Ain Kissa deposits. The friable collected phosphorite samples were subject to detailed morphoscopic and granulometric analysis.

III. 1. Morphological characteristics of isolated phosphatic particles

Based on field observations and lithological descriptions, the samples were selected on the basis of their friability with a generally clayey matrix, which made them suitable for the various particle morphological and size treatments. The phosphate particles: pellets, coprolites, bioclasts, and glauconite were separated from their matrix through sample smooth crushing and wet sieving with distilled water. Particle separation was performed using hand-picking technique under a binocular microscope. Unlike the Ain Dibba and Ain Kissa phosphorites, the Troubia deposit shows hard cherty phosphorite rocks which are difficult to separate the phosphatic particles.

III. 1. 1. The Ain Dibba phosphorites

Lower sub-layer phosphorite (LL)

This sub-layer consists of well-developed phosphatic grains up to 70% and sized from 100 µm to up to 2 mm, with the dominance of the 400 µm grain size. The isolated particles observed under the binocular microscope, which are mainly pellets, coprolites, glauconites, microfossil, and phosphatic bioclasts, show predominantly smooth and polished surfaces, and are medium to coarse-grained with poor sorting (Fig. III. 1). Thess particles display sometimes cracks, intense abrasion, and pores at their surfaces. The pellets are brown to yellowish, rounded to subrounded, spherical to oval particles, and display grain size ranging from 80 µm to 300 µm (Fig. III. 1a). The coprolites (fossil fecal) are recognized by their wide variety of shapes, which can be divided into: (1) cylindrical, rounded, (2) ovoid or oval, (3) spiral, (4), elliptical, (5) elongated, and irregularly shaped, and display yellow to brownish color, and may reach 1 to 2 mm in diameter (Fig. III. 1b). Glauconites display green to light green color, irregular shapes, and range in size from 100 µm to 300 µm (Fig. III. 1c). The bioclasts particles are represented by vertebrate fragments (bones and teeth, up to 25% of the rock) of different sizes

(0.2-2mm), gastropod and ostracod fragments, and are in most cases completely phosphatized, and often associated with quartz and dolomite crystals in the matrix (Fig. III. 1d).

Interpretation: The occurrence of smooth and polished surfaces on phosphatic grains reflects a history of remobilization from depths, reworking and transport under high hydrodynamic conditions by marine currents before deposition and diagenesis. The fractured particles are probably due to burial compaction effects, fragmentation by marine wave action during reworking process. Poorly sorted and heterogeneity in their shapes, sizes, and morphologies indicate agitated environment, fast sedimentation during early diagenesis. The pellets and coprolites color varies from light yellow to very dark brown or opaque, is probably related to the presence of organic, argillaceous, or ferruginous impurities. The pellets are thought to result from organic matter phosphatization as well as the fragmentation of preexisting coprolites during reworking events. The abundance of bone fragments, fish teeth, ostracods, and gastropods fragments are consistent with a high energy, more oxygenated, and high productivity environment. The presence of glauconites, believed to be formed in oxygenated to semi-reduced environments.

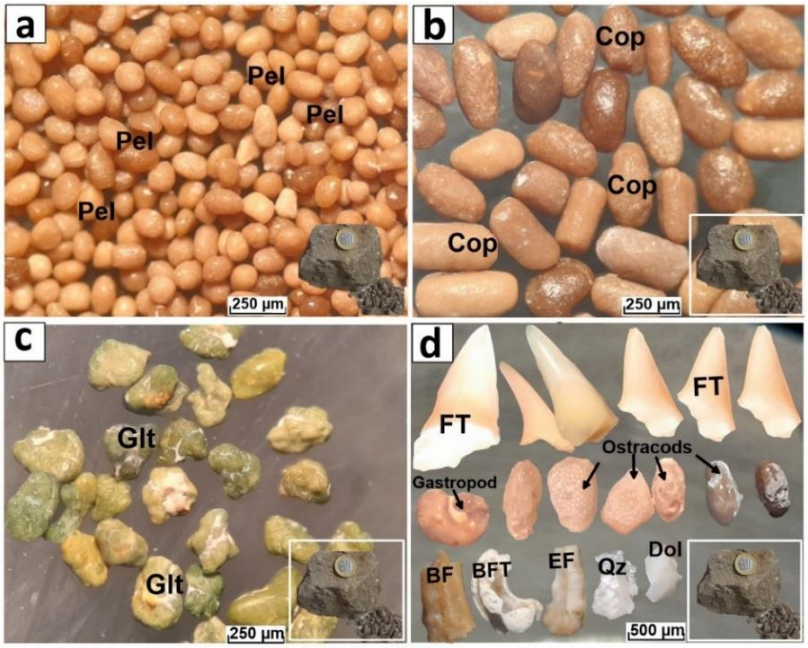

Fig. III. 1. Photomicrographs showing phosphatic particle separates. (a) Pellets (Pel); (b) coprolites (Cop); (c) glauconites (Glt); (d) fish teeth (FT), bone fragments (BF), quartz particles (Qz), Dolomite (Dol), gastropod, some echinoderm fragment (EF), and ostracods.

Middle sub-layer phoshorites (ML)

The isolated fractions of the phosphorites show that they are composed of poorly sorted, medium to coarse grained with abundant of pellets, coprolites, bone fragments, and fish teeth that are cemented by a calcitic matrix (Fig. III. 2). They show, however, smooth polished surfaces, and are heterogeneous in their shapes, colors, morphologies (the rock is poorly sorted) and proportions which vary from about 60% of the rock. Their sizes range from 100 µm to 2 mm. The pellets display rounded to subrounded shapes, brown to yellow colors with smooth and polished surfaces (Fig. III. 2a). Coprolites display irregular shape and micro-cracks on their surfaces. They are associated with bone fragments and fish teeth within a calcitic matrix (Fig. III. 2b).

Interpretation: The occurrence of smooth and polished surfaces on phosphatic grains reflects the remobilization from depths, reworking and transport under high hydrodynamic conditions by marine currents before deposition and diagenesis**.** The cracks, micro-cracks, and

fissures on their surfaces may be due to the burial compaction effects, fragmentation by marine wave action during reworking process. The abundance of bone fragments and fish teeth indicate biogenic origin with a high productivity environment in upwelling currents zone rich in (P) and (Si). The pellets are thought to result from organic matter phosphatization as well as the fragmentation of preexisting coprolites during reworking events. The color of the pellets depends on the presence of organic, argillaceous, or ferruginous impurities.

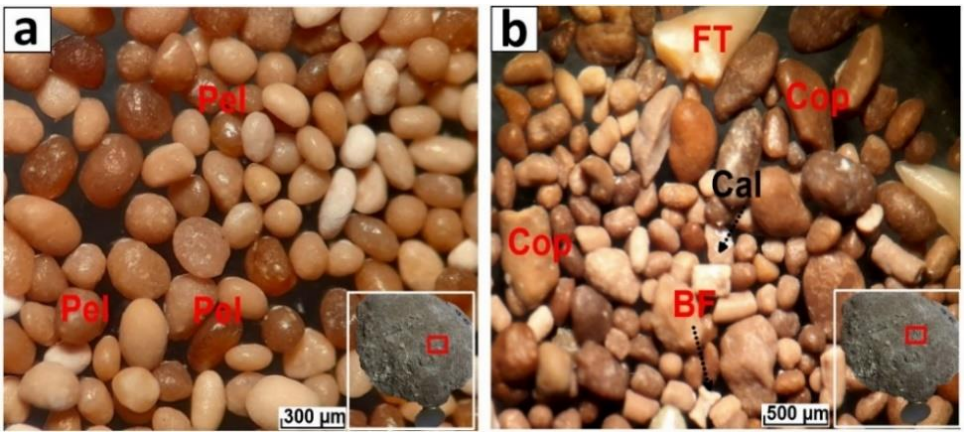

Fig. III. 2. Photomicrographs showing phosphatic particle separates. (a) Rounded to subrounded pellets (Pel), (b) cylindrical to irregular coprolites (Cop), bone fragments (BF), and fish teeth (FT), within calcite as cement (Cal).

Upper sub-layer phosphorites (UL)

In this sub-layer, the phosphorites are composed of sub-rounded to spherical pellets and coprolites, exhibiting yellow to brown coloration, and are cemented by calcareous cement (Fig. III. 3a). The coprolites are coarse-grained, light brownish to dark in color, and range in size from 400 µm to a few millimeters, whereas the bone fragments and fish teeth (Fig. III. 3b) show platy, angular to sub-angular, prismatic or irregular shapes, with grain sizes ranging from 500 µm to up 2 mm.

Interpretation: The phosphatic particles sizes range from 100 µm to up to 3 mm, suggesting that they deposited in agitated and high-energy environments. Poorly sorted and

heterogeneous in their shapes are most likely attributed to high-energy environment. The phosphate particles were intensively reworked, causing the grains to become closer together. The cracks, micro-cracks, and fissures on their surfaces may be due to the burial compaction effects, fragmentation by marine wave action during reworking process. The abundance of bone fragments and fish teeth indicate biogenic origin with a high productivity environment in upwelling currents zone rich in (P) and (Si). This results indicate high energy and more shallow depositional environment, connected to the open ocean during diagenetic processes.

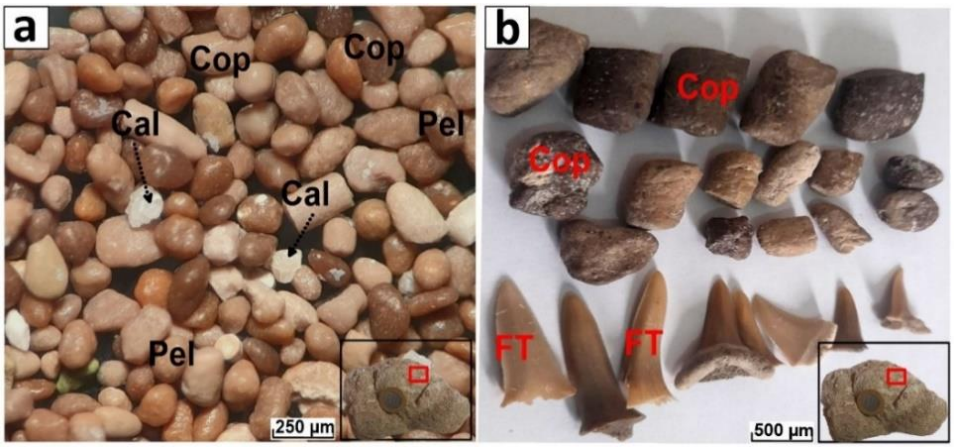

Fig. III. 3. Photomicrographs showing phosphatic particle separates: (a) abundant of various shapes of pellets (Pel), and coprolites (Cop), as well as, calcite as cement, (b) abundant coarse-grained of coprolites (Cop) and fish teeth (FT).

III. 1. 2. The Ain Kissa phosphorites

At the bottom of the studied section, the marly phosphorite rock contain smooth polished pellets, coprolites, rare glauconites, fish teeth, and detrital quartz grains (Fig. III. 4). These phosphatic particles reveal heterogeneity in their shapes, colors, and morphologies, with grain sizes ranging from 50 µm to several millimeters. Pellets show rounded to sub-rounded shape, yellow to beige color, ranging in sizes from 80 to 200 µm, whereas greenish glauconite particles are rare and show irregular shapes, oxidized surfaces and ranging in size from 150 to 250 µm (Fig. III. 4a). Coprolites show cylindrical, elongated, or irregular shapes and display a light

whitish, brownish to dark color, and variable sizes that generally exceeds 250 μm, up to 1 mm (Fig. III. 4b). Other minor, non-phosphatic minerals, such as detrital quartz, may also occur within the phosphorites. Detrital quartz grains show angular to subangular shapes and range in size from 60 to 200 m (Fig. III. 4c). The amount of quartz grains decreases upward. The bioclasts are mainly fish teeth and bone fragments (Fig. III. 4d), elongated, and angular to sub-angular in shape, ranging in size from 400 μm to 2 mm.

Interpretation: The occurrence of smooth and polished surfaces on phosphatic grains reflects the remobilization from depths, reworking and transport under high hydrodynamic conditions by marine currents before deposition and diagenesis. The fractured particles are probably due to the compaction effects. Moderately sorted and heterogeneous in their shapes, sizes, and morphologies indicate slightly to agitated environment, fast sedimentation during early diagenesis. The pellets and coprolites color varies from light yellow to very dark brown or opaque, is probably related to the presence of organic, argillaceous, or ferruginous impurities. The abundance of bone fragments, fish teeth indicate agitated, high energy, more oxygenated, and high productivity environment. The abundant presence of angular detrital quartz most likely derived from an adjacent continental terrigenous source probably during the PETM events and little transport. The presence of glauconites, believed to be formed in oxygenated to semi-reduced environments.

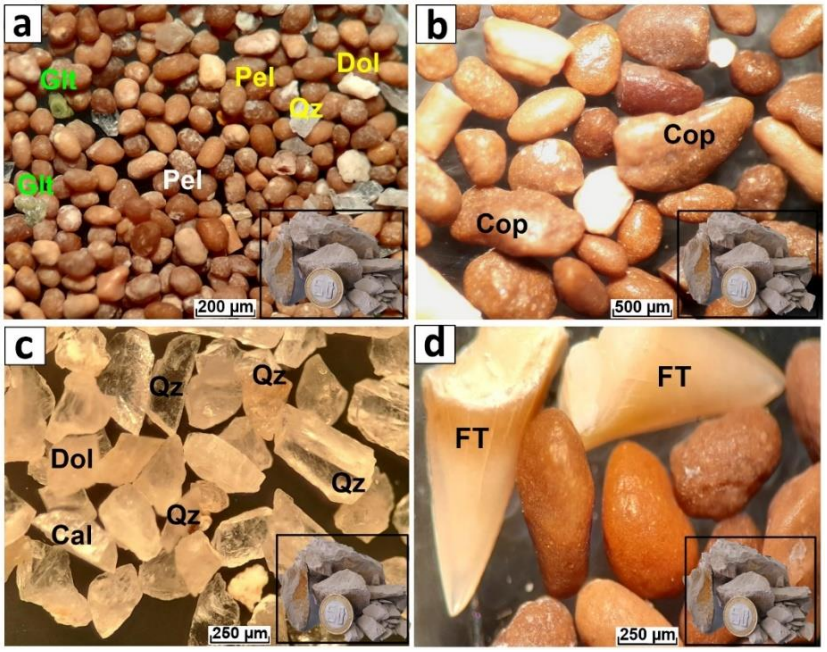

Fig. III. 4. Photomicrographs showing phosphatic particle separates from marly phosphorite of Ain Kissa deposit. (a) Abundant of phosphochems such as: pellets (Pel), glauconites (Glt), and quartz (Qz), dolomite (Dol), (b) brown to dark various shapes of coprolites; (c) angular to sub-angular of detrital quartz (Qz); (d) fish teeth with sizes ranging from 500 to 2 mm (FT).

Lower layer phosphorite (LL)

The lower phosphorite layer (LL) is characterized by abundant medium- to coarse-grained, poorly sorted particles, which make up about 75% of the volume of the total rock, with sizes ranging from 80 µm to a few millimeters (Fig. III. 5). The isolated fraction shows a relative heterogeneity in the shapes and colors. The pellets show rounded to sub-rounded, or spherical to oval in shape, yellowish to brown in colors, and ranging in size from 80 µm to 400 µm (Fig. III. 5a). Occasionally, the cylindrical coprolites exhibit brownish to red external colors, and show cracks and pores on their surfaces (Fig. III. 5b). In contrast, greenish glauconite particles are less abundance and represent less than 3% of the total grains, and reveal irregular shapes, with sizes in the range 150–250 µm (Fig. III. 5c). The bioclasts are mainly bone fragments and fish bones, naturally colorless, elongated, and angular to sub-angular in shape (Fig. III. 5d). Also, angular to sub-angular quartz are frequently observed, along with dolomite particles as a cement (Fig. III. 5d).

Interpretation: The phosphatic particles sizes range from 100 µm to up to 3 mm, suggesting that they deposited in agitated and high-energy environments. Poorly sorted and heterogeneous in their shapes are most likely attributed to high-energy environment. The phosphate particles were intensively reworked, causing the grains to become closer together. The pellets are thought to result from organic matter phosphatization as well as the fragmentation of preexisting coprolites during reworking events. The color of the pellets depends on the presence of organic, argillaceous, or ferruginous impurities. The cracks, micro-cracks, and fissures on their surfaces may be due to the burial compaction effects, fragmentation by marine wave action during reworking process. The abundant detrital quartz most likely derived from an adjacent continental terrigenous source probably during the PETM events. The abundance of bone fragments and fish teeth indicate biogenic origin with a high productivity environment in upwelling currents zone rich in (P) and (Si). The presence of glauconites, believed to be formed in oxygenated to semi-reduced environments. This results indicate high energy and slightly reducing to more shallow depositional environment, connected to the open ocean during diagenetic processes.

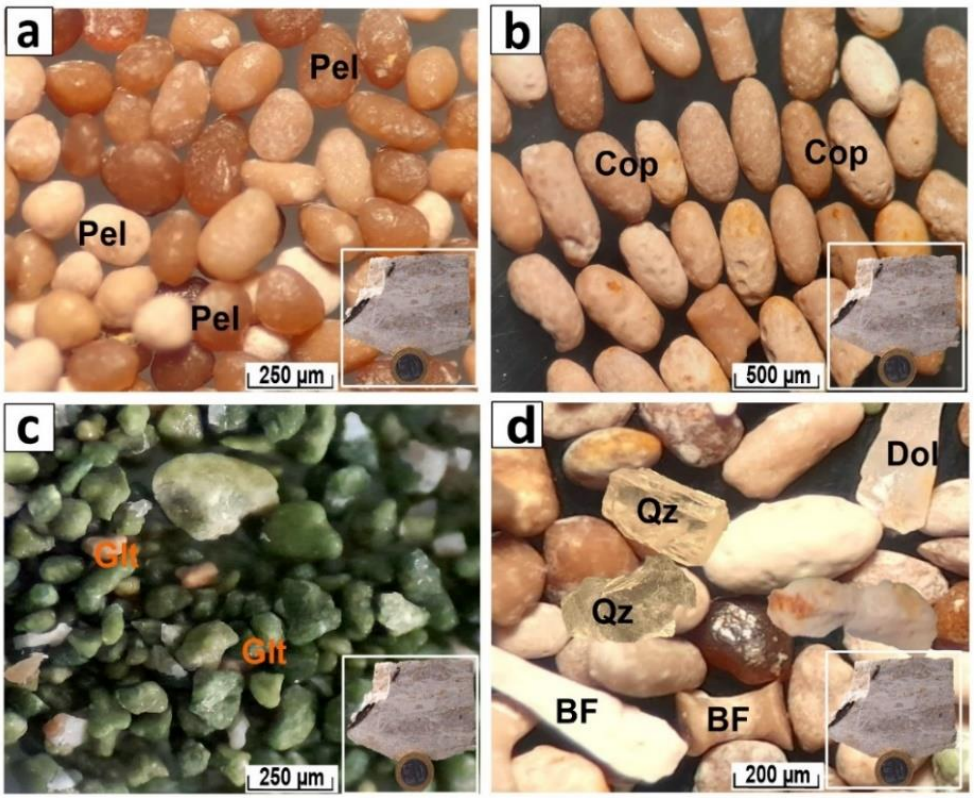

Fig. III. 5. Photomicrographs showing phosphatic particle separates of the lower layer phosphorite from Ain Kissa deposit. (a) Abundant rounded to sub-rounded, yellowish to brown pellets (Pel), (b) whitish, brownish to dark color coprolithes (Cop) with cracks and fissures on their surfaces, (c) abundant of greenish, irregular, and sizes ranging from 100 to 250 µm of glauconite particles (Glt), (d) elongated bone fragments (BF) with angular to sub-angular quartz (Qz) and dolomite (Dol) particles as a cement.

Middle-layer phosphorite (ML)

The isolated fractions of the phosphorites show that they are composed of poorly sorted, medium to coarse grained with abundant of pellets and coprolites. They are heterogeneous in their shapes, colors, morphologies (the rock is poorly sorted) and proportions which vary from about 70% of the rock, similar abundance phosphatic particles to the lower and upper layers (Fig. III. 6). They show smooth polished surfaces, and sometimes display cracks and pores at their surfaces, probably due to the compaction effects. The pellets, which are the most abundant phosphatic particles (40–45% of the total grains), are often rounded, sub-rounded, spherical to oval in shape, brown to yellowish in color, and display grain size from 80 µm to 400 µm (Fig. III. 6a). Coprolites, which represent up to about 30 % of the phosphatic particles, reveal

cylindrical, elliptical, elongated or irregular shapes, with whitish, brownish to dark color (Fig. III. 6b).

Interpretation: The pellets are thought to result from organic matter phosphatization as well as the fragmentation of preexisting coprolites during reworking events. The color of the pellets depends on the presence of organic, argillaceous, or ferruginous impurities. The cracks, micro-cracks, and fissures on their surfaces may be due to the burial compaction effects, fragmentation by marine wave action during reworking process. The poorly sorted suggest agitated and high energy environment. The smooth polished surfaces most likely due to remobilization from depths and transport before deposition and diagenesis. This indicate high energy environment during early diagenesis process in Ain Kissa deposit.

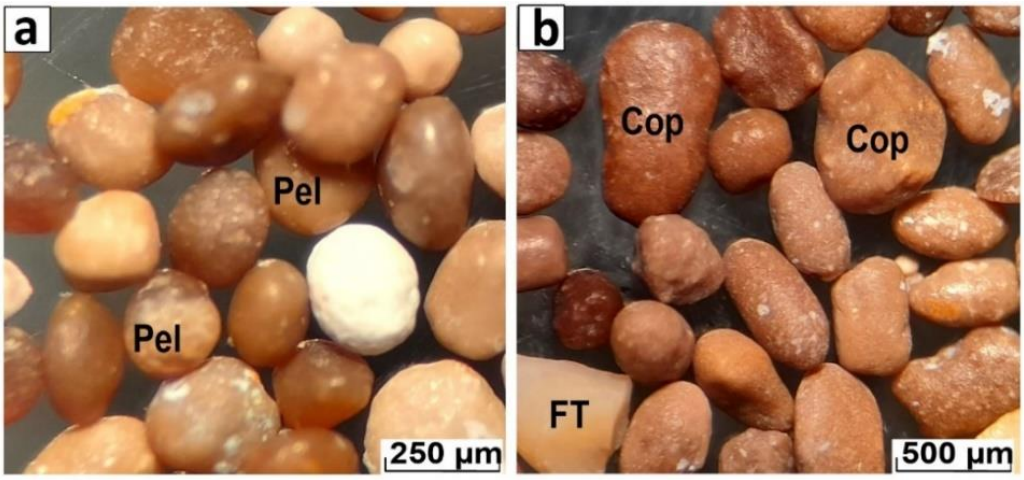

Fig. III. 6. Photomicrographs showing phosphatic particle separates of the middle layer phosphorite from Ain Kissa deposit. (a) An abundant of yellow to brown pellets (Pel) with sizes ranging from 80 to 300 µm, (b) coprolites (Cop) with various color, shapes and have cracks on their surfaces.

Upper-layer phosphorite (UL)

The upper layer (UL) consists of medium to coarse-grained phosphorites with abundant pellets, coprolite and fragments of bones and fish teeth. The phosphatic particles are heterogeneous in their shapes, colors, morphologies (the rock is poorly sorted) and proportions which vary from about 60 to 75% of the rock (Fig. III. 7). The pellets show rounded to subrounded shapes and a brown color, whereas coprolites display cylindrical to irregular

shapes, and are cemented by calcareous and siliceous matrix (Fig. III. 7a). Occasionally, they exhibit brownish.to red external colors, and have cracks and pores on their surfaces (Fig. III. 7b).

Interpretation: The phosphatic particles have smooth, polished surfaces, which are probably the result of transport and remobilization from depths prior to deposition and diagenesis. The color of the pellets depends on the presence of organic, argillaceous, or ferruginous impurities. The fractured and cracked surfaces are most likely caused by compaction effects. The poorly sorted heterogeneous in their shapes are most likely attributed to high-energy environment of phosphorites of Ain Kissa deposits in upper section.

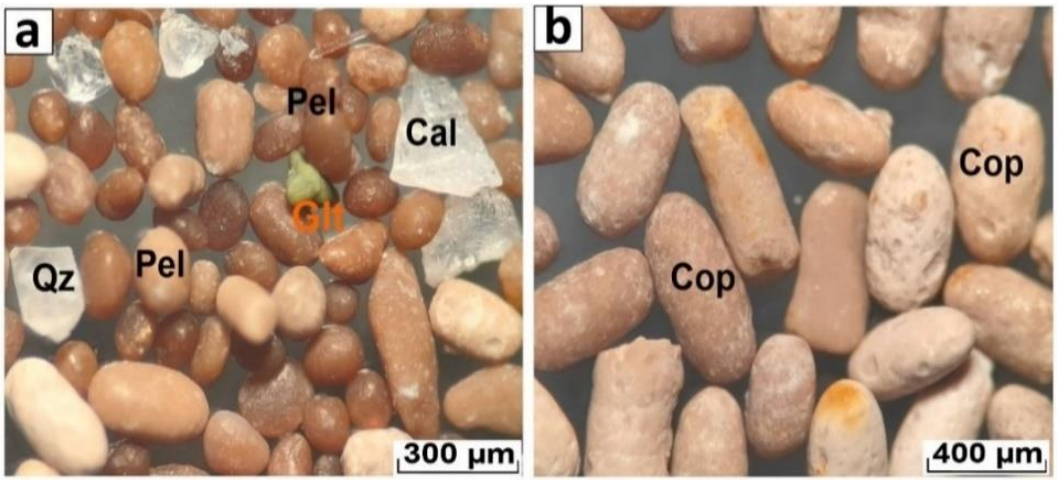

Fig. III. 7. Photomicrographs showing phosphatic particle separates from the upper phosphorites layer of Ain Kissa deposit. (a) Dark to brown, rounded to sub-rounded pellets (Pel) occur within calcitic (Cal) and/or siliceous (Qz); (b) cylindrical to elongated, yellow coprolites (Cop) are cracked and fissured.

III. 2. Particle size distribution and characterization

The collected phosphorite samples were subject to detailed granulometric analysis, where two approaches were adopted:

Methods

The particle size analysis was carried out on sixteen (06) phosphorite samples collected from the studied deposits. These samples were selected on the basis of their friability with a

generally clayey matrix, which made them suitable for the various particle size treatments. They were sieved at a 3 mm-size mesh, and dried at a temperature less than 40°C. These samples are checked under a binocular microscope to remove the coarse matrix, such as dolomite, calcite and quartz particles. Particle size analysis was performed on samples using a Mastersizer 3000 laser diffraction particle size analyzer at the University of Sfax, Tunisia, using wet methods. The samples were analyzed in water suspension. In order to obtain good particle dispersions, a suitable ultrasonic sound time has been applied (120s). In order to compare the granulometric parameters from different samples, medium diameter (MMD) has been calculated. D (v; 0.5) corresponds to the particle caliber for that 50% of the sample having a lower size and 50% of sample having a higher size. This laser diffraction is designed for measuring particle sizes ranging from 0.02 to 3000 μm.

Statistical treatment

Cumulative frequency curves were produced from the cumulative weight percent of particle size data of each section. The frequency curves were drawn to define the modes, asymmetry frequency curve, angularity curve and cumulative particle size (μm) curves. The main statistical parameters calculated include the mean (Mz): standard deviation, (sorting, δi), asymmetry: skewness (SKi), graphic kurtosis (KG). Particle size parameters were calculated according to Folk and Ward (1957) as shown in Table 1, and formula using GRADISTAT v8 (Blott and Pye, 2001). Additionally, the uniformity coefficient (Uc) and the curvature coefficient (Cc) parameters were calculated using the following formulas: Uc: uniformity coefficient = (D60/D10); Cc: curvature coefficient = ($D30^2$ /(D60*D10)); and specific surface area (SSA).

Table III. 1. Statistical formulas used for calculating particle size parameters of Ain Dibba and Ain Kissa phosphorites (Folk and Ward, 1957)**.** Mz mean particle size; σi standard deviation (sorting); Skf skewness coefficient; Kg kurtosis coefficient; n number of samples.

Particle size indices	**Interpretation**
Mean Particle Size (Mz): $Mz = (\varphi 16 + \varphi 50 + \varphi 84) \div 3$	Mz < 1 φ: Coarse sands and gravels. 1 φ < Mz < 2 φ: Medium sands. 2 φ < Mz < 3 φ: Fine sands. 3 φ < Mz < 4 φ: Very fine sands. Mz > 4 φ: Silts and clays.
Skewness Index (Ski): $Ski = [(\varphi 16 + \varphi 84 - 2\varphi 50) \div 2(\varphi 84 - \varphi 16)] +$ $[(\varphi 95 + \varphi 5 - 2\varphi 50) \div 2(\varphi 95 - \varphi 5)]$	-1 < Ski < -0.3: Strongly coarse-skewed curve. -0.3 < Ski < -0.1: Coarse-skewed curve. -0.1 < Ski < +0.1: Nearly symmetrical curve. +0.1 < Ski < +0.3: Fine-skewed curve. +0.3 < Ski < +1.0: Strongly fine-skewed curve.
Sorting Index (σ) : $\sigma = [(\varphi 84 - \varphi 16) \div 4] + [(\varphi 95 - \varphi 5) \div 6.6]$	σ < 0.35 φ: Very well sorted sand. 0.35 φ < σ < 0.5 φ: Well sorted sand. 0.5 φ < σ < 0.7 φ: Moderately well sorted sand. 0.7 φ < σ < 1 φ: Moderately sorted sand. 1 φ < σ < 2 φ: Poorly sorted sand. 2 φ < σ < 4 φ: Very poorly sorted sand. σ > 4 φ: Extremely poorly sorted sand.
Kurtosis (KG) : $KG = (\varphi 95 - \varphi 5) \div [2.44(\varphi 75 - \varphi 25)]$	KG < 0.67: Very platykurtic curve (very flat). 0.67 < KG < 0.90: Platykurtic curve (flat). 0.90 < KG < 1.11: Mesokurtic curve (normal peak). 1.11 < KG < 1.50: Leptokurtic curve (peaked). 1.50 < KG < 3: Very leptokurtic curve (very peaked). KG > 3: Extremely leptokurtic curve (extremely peaked).

III. 2. 1. Results and interpretation

The different particle size distribution patterns and data on particle size, and particle size parameters were obtained for the phosphorite deposits as considered in Fig. III. 9 and Table III. 3.

III. 2. 1.1. Particle size distribution curves

The particle size ***frequency*** of the analyzed samples exhibits various distribution patterns, including unimodal, bimodal, and polymodal types (Fig. III. 8a). These variations in particle size distribution reflect differences in the paleo-hydrodynamic conditions during phosphorites deposition. The vertical succession of the Ain Dibba phosphorite samples from ADD03 at the bottom to ADD08 at the top reveals an evolution in depositional energy and hydrodynamic conditions. Phosphorite sample (ADD03) shows a polymodal particle size distribution, ranging from 50 µm to 2 mm, with a dominant mode around 100–250 µm**.** This pattern suggests the presence of multiple grain populations, complex depositional setting. It may reflect the influence of relatively agitated and high-energy conditions, mixed sediment sources, or possibly varying modes of transport. Phosphorite sample (ADD06) displays a bimodal distribution, with particle sizes ranging from 40 µm to 2 mm. This pattern suggests a mixed depositional environment characterized by alternating moderly- and high-energy conditions, able of transporting and depositing both fine and coarse particles. A bimodal distribution is observed in the phosphorite sample ADD08, located at the top of the section, with grain sizes ranging from 50 µm to 800 µm. This distribution reflects a transition from high-energy to moderate-energy depositional conditions, likely associated with reduced upwelling activity and more uniform sedimentation. In contrast, some friable samples at bottom of Ain Kissa deposit show a change in depositional energy and hydrodynamic conditions. Phosphorite sample (AKD6) exhibits a unimodal grain size distribution, with a sharp peak around 200 µm, indicating a little mixing of clay and depositional environment under more stable, and

moderate-energy environment. Phosphorite samples (AKD10 and AKD12) show a more biomodal distribution, with particle sizes ranging from 40 µm to 800 µm, suggesting more variable, agitated and high energy conditions with poorly sorting. This indicates an increasingly complex depositional environment during early diagenesis. As whole, the particle sizes range from 1 to 100 µm comprises fine well-rounded pellets and exo-gangue, such as calcite, dolomite, glauconite, and quartz; the range 100 to 250 µm size essentially includes sub-rounded pellets; the range from 250 to 500 µm size is represented mostly by nucleated pellets (pseudo-oolites), coprolites, coprolites fragments, and lithoclasts; 500 µm to few millimeters represented by fish teeth, bioclastic debris, coprolites and phosphatic lithoclasts. These results indicate that the phosphatic particles of the studied deposits are poorly sorted, and were deposited in high energy depositional environment.

The cumulative frequency curve displays an S-shaped curve, where the gradient of the cumulative frequency curves at the middle part reflects the sorting of particles (Fig. III. 8b). The cumulative frequency curve provides insight into the sorting and energy of the depositional environment. In Ain Dibba phosphorites, the samples in order (ADD03, ADD06, and ADD08) show that the cumulative frequency curves are medium to very gentle slope (Fig. III. 8b), indicating evolution from moderate to poor sorting of phosphatic particles size distribution**.** This suggests moderate or agitated and fluctuating hydrodynamic energy, allowing grains of many different sizes to deposit together such as: fine, medium, and coarse particles. By contrast, samples from Ain Kissa phosphorite in order (AKD06, AKD10, and AKD12) display very steep slope of the cumulative frequency curve at the bottom, which indicates that the phosphatic particles are well sorted. This implies deposition under moderate, calm, and more consistent energy conditions**.** The cumulative frequency curves for samples AKD10 and AKD12 show a relatively steep slope. This suggests that phosphatic particles were moderately sorted during deposition in agitated conditions, and that the depositional environment experienced moderate

energy due to upwelling currents and marine wave action. This data indicates that the fractions smaller than 100 µm which represent 20% of the particles, are composed of the clayey matrix and/or calcareous cement as well as the fine particles (glauconites, fine phosphatic particles). The fractions ranging from 100 to 500 µm represent 52% (e.g. pellets and some coprolite fragments), while the fractions larger than 500 µm represent 28% and consist of coprolites, lithoclasts, and bioclasts. However, only one phosphorite sample in the Ain Kissa deposit (AKD10) shows abundant pellets and finer fraction particles sizes about 40 %, moderately well sorted particles.

Based on ***the probability cumulative curves*** for grain size distributions, the data indicate the transportation mode of the phosphatic particles to the depositional environment (Fig. III. 8c; Visher, 1969). They show three straight line segments. Each segment of the curve is interpreted to show different sub-populations of particles that were transported simultaneously but by different pathways: suspension, saltation and rolling. The phosphorite samples plotted in the probability curve show that most of the particles are transported mainly by suspension and saltation (Fig. III. 8c). These plots also show that most grains are moderately poorly-sorted, probably due to transport and high energy environment during the deposition processes.

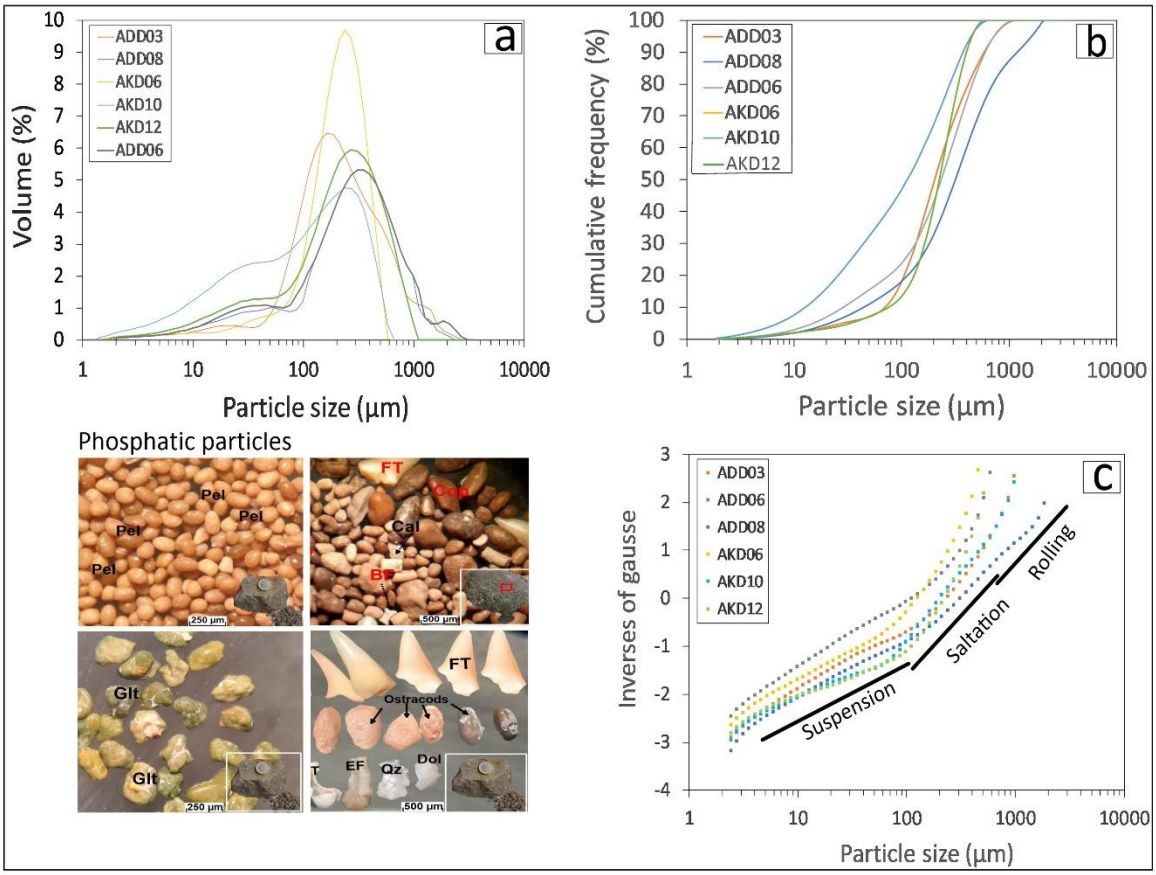

Fig. III. 8. Granulometric representative samples of the Ain Dibba (ADD samples) and Ain Kissa (AKD samples) phosphorites deposits. (a) Particle size distribution frequency curves; (b) Graphical representation of the cumulative particle size frequencies. (c) Probability curve after Visher (1969) reflecting models of the transportation.

III. 2.1.2. Physical and particle size characteristics of the phosphorites

The use of statistical parameters obtained from particle size analysis for environmental reconstruction help to distinguish past depositional conditions. Particle size parameter such as skewness (Skf), kurtosis (Kg), mean particles size (Mz), and standard deviation (σi, sorting), uniformity coefficient (Uc), curvature coefficient (Cc) and surface area (SSA) are key indicators of particles sorting, transport conditions, and the depositional environment, aiding in the analysis of particles characteristics and their potential uses (see Tabs. III. 1 and III. 2; Folk and Ward, 1957). The mean size (Mz) gives the transport energy in depositional environment, with coarser grains indicating higher energy and finer grains lower energy. Sorting (σi)

measures the uniformity of grain sizes; well-sorted sediments suggest stable energy, while poor sorting indicates fluctuating conditions. Skewness (Skf) reveals the dominance of fine or coarse particles, where positive skewness points to finer material and calm settings, and negative skewness indicates coarser material and stronger energy. Kurtosis (Kg) reflects the uniformity or mixing of particle sizes curve, with high kurtosis suggesting uniform sediment deposition and low kurtosis indicating mixed, variable environments. Also, uniformity coefficient (Uc) measures the range of particle sizes, curvature coefficient (Cc) reveals the shape of the grain size distribution curve (Fetter, 2001). Specific surface area (SSA) parameter allow to reflecting the grain fineness and surface exposure, providing insights into chemical properties and particles reworking (Boumaza et al., 2021). All data on particle size and the calculated granulometric parameters of phosphorites studied in Ain Dibba and Ain Kissa deposits are shown in Table III. 2.

Different patterns of particle size distribution were obtained for the considered P-bearing deposits. The particles size in Ain Dibba samples show that the mean particles (Mz) ranges from 2 to 2.18 φ (see Table III. 2), indicating a medium to coarse grained. Their particles size distributions are nearly symmetrical- skewed towards fine-skewed (skewness ranging from 0.07 to 0.28), which may be related to the predominance of the pellets, coprolites particles and bioclasts fragments. The kurtosis coefficient (Kg) displays high values ranging from 1.21 to 1.24 φ, suggesting leptokurtic curves. The sorting (σ_i) parameter reveals values that vary between 1.31 and 1.66 φ, indicating poorly sorted phosphatic particles. This data indicates that the phosphatic particles in Ain Dibba deposit are deposited in an agitated environment and under high-energy conditions. Conversely, the particles size parameters in Ain Kissa deposit show mean particles (Mz) ranges from 2.26 to 3.48 φ (see Table III. 2), suggesting fine to medium grained. The skewness (Skf) reveals values ranging from 0.29 to -0.37 φ, as a strong fine-skewed to strong fine-skewed curves, which are attributed the dominance of fine and

medium particles such as: pellets, glauconites, organic matter, matrix /or and cement, fine phosphatic particles. The kurtosis coefficient (Kg) displays values between 0.85 and 1.41 φ, pointing leptokurtic, but only phosphorite sample in Ain Kissa deposit shows Platykurtic (Kg = 0.85 φ). The sorting (σ_i) parameter reveals values that vary between 0.98 and 1.88 φ, indicating change from moderately to poorly sorted phosphatic particles. They can be classified as poorly sorted, medium to fine phosphatic particles. This result indicate that the deposition occurred in more stable, calm hydrodynamic energy and well sorting with reworking processes towards a slightly agitated environment and under moderate-energy conditions.

The Ain Dibba phosphorites are characterized by a specific surface area (SSA) ranging from 67 to 193, a uniformity coefficient (UC) ranging from 8.5 to 12.5 and a curvature coefficient (Cc) ranging from 0.97 to 2.16 (see Table III. 2). Based on these parameters, the phosphatic particles are mostly very poorly sorted, with abundance of finer particles such as organic matter, glauconites, as well as a clay matrix, suggesting moderate to high energy depositional environments during diagenesis process. In contrast, the Ain Kissa phosphorites display specific surface area (SSA) values between 69.75 and 134 (see Table III. 2). The highest SSA are recorded in ADK06, which indicates a greater abundance of fine particles, including organic matter and glauconite, as well as a clay matrix. The uniformity coefficient (UC) and curvature coefficient (Cc) show values ranging from (3.38 to 6.89; and 1.05 to 1.82; respectively, see Table 3), which are attributed to poorly sorting particles. This results indicate that the phosphatic particles are deposited in agitated environment. As whole, the particle size characteristics of Ain Dibba and Ain Kissa phosphorites are similar to those that recorded in Northern basin (σ g = 2.89) such as at Djebel El Kouif and Djebel Dyr (Kechiched et al., 2018; Kechiched et al., 2020; Ferhaoui et al., 2022). However, they are compared to those from the Kef Essenoun deposit which are moderately sorted (σ g = 1.85–1.96) and exhibits a normal distribution with a mean grain size of 0.27 mm (σ g = 1.85–1.96; Ferhaoui et al. 2022).

III. 2.1.3. The C–M pattern (Passega diagram)

The C–M plot was initiated by Passega, (1957, 1964) to interpret the hydrodynamic conditions that prevail during the deposition of sediments. The C–M is a bivariate plot of the median value (M, D_{50}) in micron vs coarser one-percentile value (C, D_{99}) in micron on a log–probability scale (Table III. 2). The connection between C and M is related to the energy of the transportation medium as well as the nature and type of the sediment (Visher, 1969). The Passega diagram illustrated in Figure III. 9 revealed quite a few fields of rolling and suspension, corresponding to the different transportation and sedimentation conditions in the shallow marine environments. The binary plot of C against M values (Table III. 2) on the Passega diagram suggests that samples from Ain Dibba phosphorites plotted in both rolling and suspension (OP), and suspension and rolling (PQ), whereas most of the phosphorite samples from Ain Kissa deposit are scattered in the suspension and rolling (PQ). This result indicates that the deposition occurred in an agitated environment and high-energy conditions.

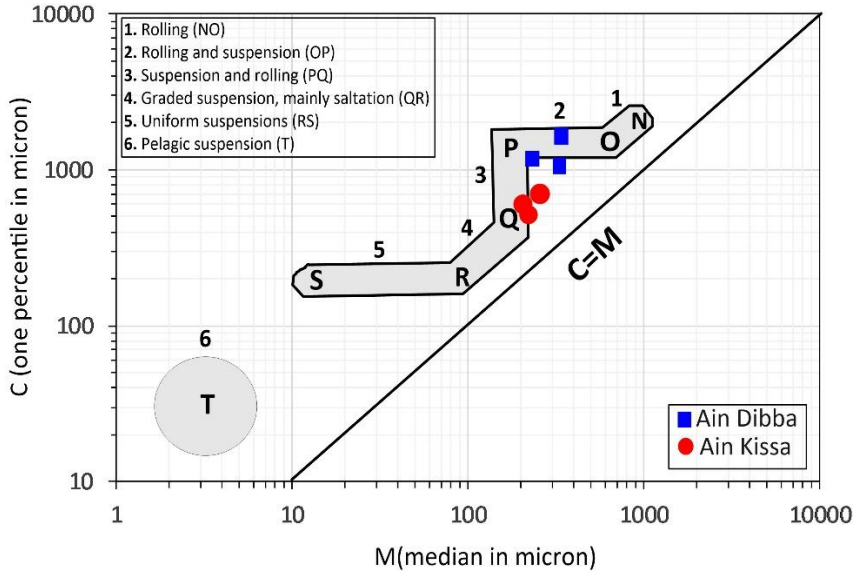

Fig. III. 9. Binary plot of C–M values on the Passega diagram, showing the mode of transportation and depositional process.

Table. III. 2. Results of particles size parameters of phosphorites studied in Ain Dibba and Ain Kissa deposits. Mz mean particles size; σi standard deviation (sorting); Skf skewness coefficient; Kg kurtosis coefficient; n number of samples, Uc: uniformity coefficient; Cc: curvature coefficient; SSA: Specific Surface Area.

Sample	Particles size parameters (in φ)				Results	Interpretation
(n = 06)	Mz	Skf	Kg	σ_i	Studied phosphorites	
ADD03	2.18	0.07	1.21	1.31	Medium to coarse grained, nearly symmetrical, leptokurtic curve, poorly sorted .	
ADD06	2	0.28	1.24	1.66	Medium grained, fine-skewed, leptokurtic curve, poorly sorted	The deposition occurred in an agitated environment and high-energy conditions, more moderately towards the top, with reworking processes.
ADD08	2.01	0.14	1.23	1.65	Medium to coarse grained, nearly symmetrical , leptokurtic curve, poorly sorted	
AKD06	2.26	0.32	1.41	0.98	Fine grained, strong fine-skewed, leptokurtic curve, well to moderately sorted	More stable, calm hydrodynamic energy and well sorting.
AKD10	3.48	0.29	0.85	1.88	Fine to medium grained, fine-skewed , platykurtic curve, slightly poorly sorted	The deposition occurred in an slightly agitated environment and under moderate-energy environments, with reworking processes.
AKD12	2.45	0.37	1.19	1.66	Fine to medium grained, fine-skewed, leptokurtic curve, poorly sorted	

Sample	Particles size parameters								Results	Interpretation
(n = 06)	SSA	Uc	Cc	D10(µm)	D30 (µm)	D50 (µm)	D60 (µm)	D90 (µm)	Studied phosphorites	
ADD03	92.7	10.1	2.16	28.7	134	233	290	599	Medium-high surface area (coarser to finer particle size), very poorly sorted, relatively poorly graded.	The abundance of finer particles and poorly sorted particles suggests deposition in high to moderate hydrodynamic energy.
ADD06	192.5	12.52	0.97	12.7	44.2	200	159	372		
ADD08	66.69	8.52	1.91	44.6	180	315	380	1180		
AKD06	134.2	6.89	1.82	22.2	78.6	127	153	286	High surface area (finer particles size), well sorting, well-graded.	Low-energy during depositional environment with stable transport in shallow marine basin by upwelling currents
AKD10	69.75	3.56	1.05	69.9	135	202	249	585	Medium surface area (slightly fine, medium, particles), moderately sorted, well-graded.	Less abundance of finer particles with moderately sorted indicating deposition in a slightly agitated environment.
AKD12	70.09	3.38	1.4	75.5	164	223	255	400		

Conclusion

The isolated phosphatic particles in Ain Dibba and Ain Kissa deposits are heterogeneous in their shapes, colors, morphologies (the rock is poorly sorted) and proportions which vary from about 50 to 75% of the rock. They show, however, smooth polished surfaces, most likely due to remobilization from depths and transport before deposition and diagenesis. The particle size analysis and calculated granulometric parameters suggest that the phosphorites were deposited in Ain Dibba deposit in an agitated environment and under high-energy conditions, likely associated with increases upwelling activity (rich on P and Si). The particles have a bimodal to polymodal distribution, and are poorly sorted, coarse to medium in size, with a mean grain size of 0.27 mm, indicating sandy phosphorites. However, the Ain Kissa deposit shows a high-energy, slightly agitated environment with a unimodal to binomodal particle size distribution, and moderately sorted, well-graded, slightly fine and more medium particles.

Chapter IV

Petrography and mineralogy of the Troubia, Ain Dibba and Ain Kissa phosphorites

Chapter IV

Petrography and mineralogy of the Troubia, Ain Dibba and Ain Kissa phosphorites

The petrographic and mineralogical studies of the Algerian phosphorites have been extensively studied by many authors (e.g., Kechiched et al., 2018, 2020; Boulemia et al., 2021; Dassamiour et al., 2021; Ferhaoui et al., 2022; Laouar et al., 2024; Saouli et al., 2025). These studies have enabled to determine the morphology, texture, and mineralogical composition, providing insights into their depositional environment, diagenetic evolution, and post-depositional alterations. On other hand, these studies were useful for unraveling the features of each mineral phase, which allows to tracking their source, content, and the enrichment of rare earth elements (REE), as well as to identifying the specific mineral phases that host these critical elements. Additionally, the nature of clay minerals provides valuable indicators for interpreting upwelling intensity, paleo-environmental conditions, and paleo-climatic settings (Sassi 1974; Chabou-Mostefai, 1987; Felhi et al. 2008; Tlili et al. 2010, 2011; Haj Ahmed et al., 2014). This chapter aims to present the detailed petrographic features and mineralogical assemblages of the Troubia, Ain Dibba, and Ain Kissa deposits, and, on the other hand, to help us to better understand their paleo-depositional environment. The results were obtained from sampling preparation through optical microscope observations, XRD, FTIR, and SEM-EDS analyses.

IV. 1. Petrography

The petrographic study is carried out through the observation of prepared thin sections from phosphorite samples under an optical microscope. About 80 samples were collected from the Troubia, Ain Dibba, and Ain Kissa phosphorite. From these, more than 60 thin sections

were prepared at the Thin Section Laboratory, Department of Geology, Badji Mokhtar University-Annaba, and examined using a transmitted and reflected light optical microscope. Although the phosphorite rocks studied are semi-friable to hard, some of them required specific protocol due to their friability. These samples were dried at 100 °C to remove moisture and impregnated with resin under vacuum to remove air bubbles. The resin was then hardened by heating at ~80 °C for about 1.5 hours. The hardened samples were subsequently cut, polished, and mounted following standard thin-section preparation procedures.

IV.1. 1. The phosphatic particles:

Microscopic observation shows that the phosphorites of Troubia, Ain Dibba and Ain Kissa deposits are mainly composed of phosphatic particles: pellets, coprolites, bioclasts (bone fragments and fish teeth) and glauconites that are mostly cemented by a calcareous (calcitic/dolomitic), clayey and/or siliceous matrix. Other minor, non-phosphatic minerals, such as detrital quartz and gypsum, may also occur within the phosphorites. The proportion of these particles varies from 50 to 75% of the rock.

Pellets

The pellets, which are the most abundant phosphatic particles (40–45% of the total grains), are often rounded, subrounded, spherical to oval in shape, brown to yellowish in color, and display grain size from 80 µm to 400 µm (Fig. IV. 1). The color of the pellets depends on the presence of organic, argillaceous, or ferruginous impurities. They are similar to many of the Algerian-Tunisian deposits, which are thought to result from organic matter phosphatization as well as the fragmentation of preexisting coprolites during reworking events. The rounded to subrounded pellets typically exhibit high porous structure, micro-cracks, minerals inclusions, and fractured surfaces (Fig. IV. 1a, b), may be related to transport, burial and sediment accumulation and compaction (see Chapter III). The spherical and ovoid pellet particles are

commonly coated with micritic and/or patches organic material that makes sharp contacts with the matrix (Fig. IV. 1c, d).

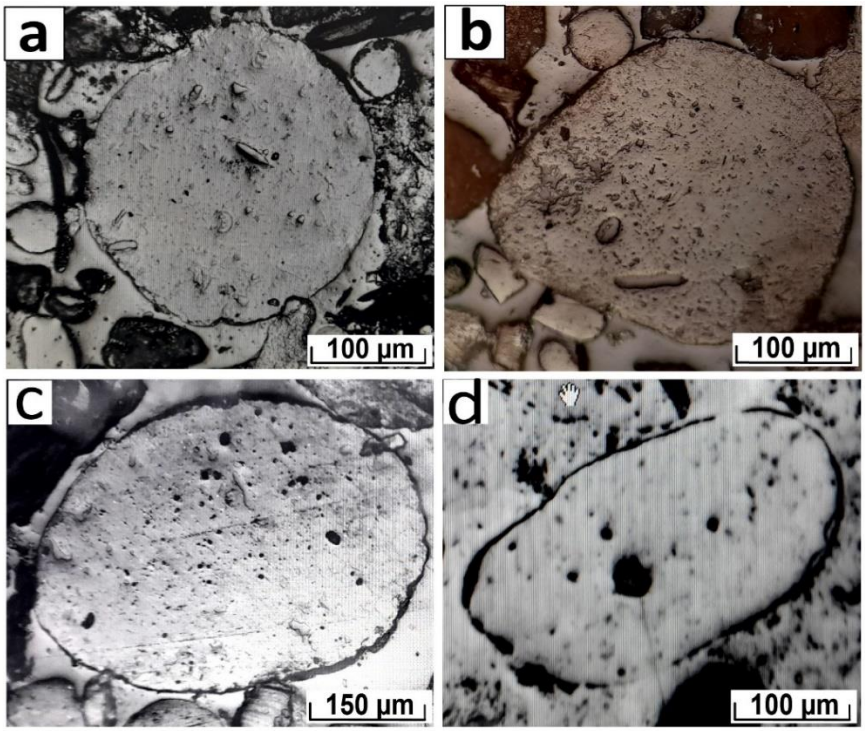

Fig. IV. 1: Thin section photomicrographs showing pellet particles of different shapes (a, b, c and d) containing microcracks and fractured surfaces, as well as being coated with micritic organic materials (in black).

The pellets are characterized by variations in the content of organic materials, which occur in the following forms: (1) filling the majority of the particle; (2) randomly disseminated organic material in the form of patches; (3) in the form of concentric micro-layers; or (4) concentrated in the central part of the pellet (Figs. IV. 2a, b, c, and d).

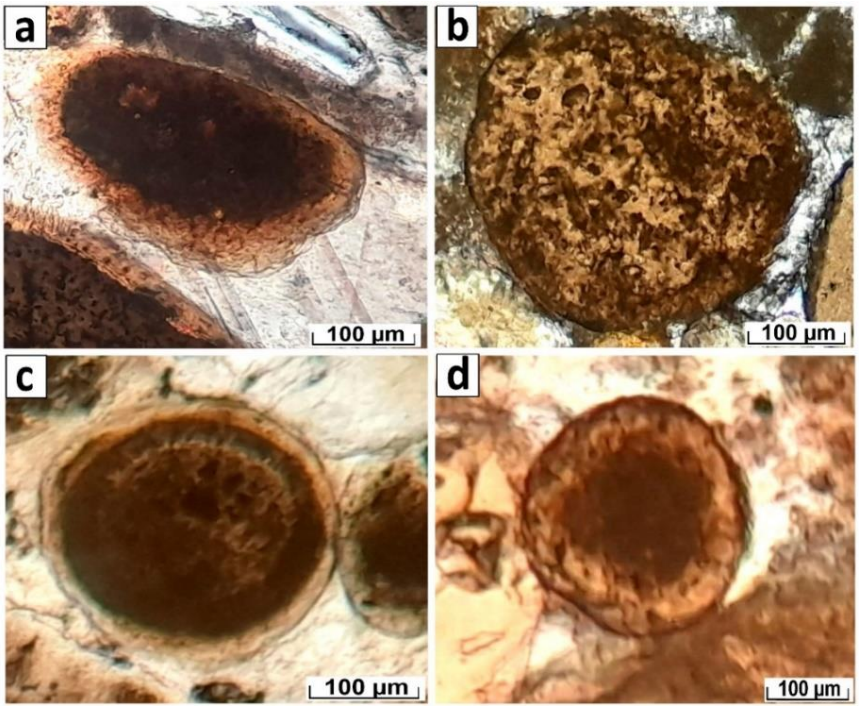

Fig. IV. 2. Thin section photomicrographs showing distribution of organic matter in pellets particles. (a) Ovoid pellets are filled with dark organic matter and initial corrosion is discernible on the outer rim of the grain.; (b) spherical pellet containing organic materials randomly scattered as patches; (c) subrounded pellet showing concentric micro-layers of organic materials; (d) rounded pellet displaying organic materials concentrated in the central part.

The pellets that show concentric structures (~5% of the total particles) are composed of a nucleus, often quartz grain or fossil and bone fragments, surrounded by thin, dark brownish to black concentric phosphatic material (cortex) forming nucleated grains (Fig. IV. 3a-d). They are usually spherical, oval or elongated in shape and range in size from 100 to 250 µm. Here, the nucleated pellets are formed by the phospho-micritization process of bone fragments and fossils. This started first by the development of a brown envelope formed by successive perforations of the edges of the bone fragment, then the phosphatization progressively spreads towards the center during diagenetic processes. The phosphatization is usually accompanied by a dulling of the edges and around the fragments due to mechanical abrasion. These results are interpreted to represent multi-stage phosphatization at highly agitated conditions.

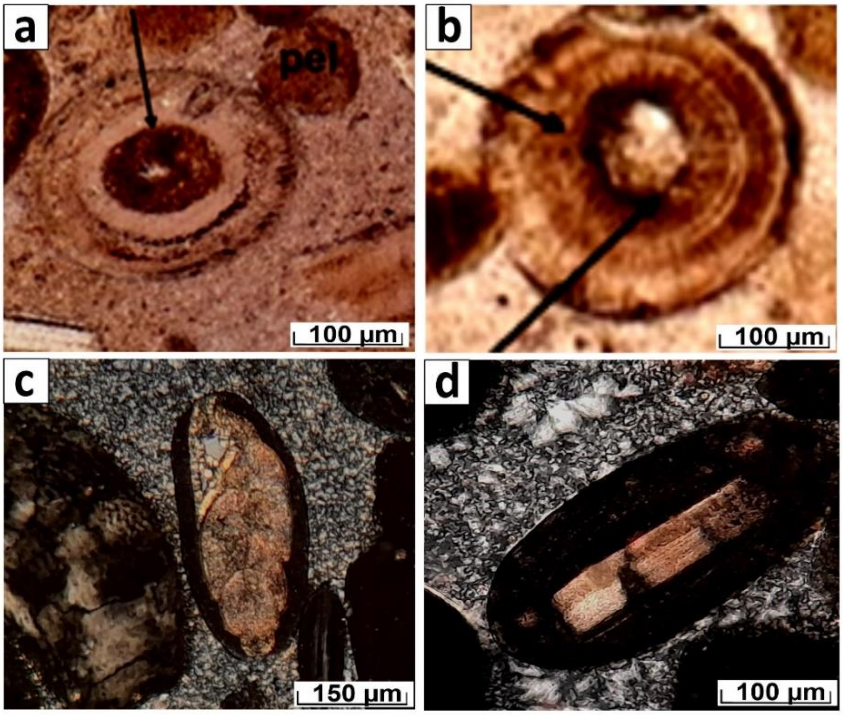

Fig. IV. 3. Thin section photomicrographs showing: (a, b) rounded to subrounded pellets with concentric structures containing quartz nuclei, (c, d) oval to elongated nucleated pellets showing bone fragment and fossil nucleus surrounded by thin, dark brownish to black concentric phosphatic material (cortex).

Coprolites

Coprolites are heterogeneous in their shapes, colors and morphologies (the rock is poorly sorted), and their proportions vary from about 30 to 35 % of the rock. They also display cracks, fractured and pores at their surfaces, probably due to the compaction effects (Fig. IV. 4a-f). They typically exhibit cylindrical to irregular shapes, with colors ranging from white, brown to grey and varying in size from 500 µm to several millimeters. Coprolites often contain inclusions of organic matter, tiny quartz crystals calcareous materials (mainly dolomite and/or calcite crystals), siliceous minerals, and bone fragments (see red arrows, Fig. IV. 5a). Later silicification processes are observed by the development of amorphous silica (opal-CT), which occurs either as veins cross-catting and replacing the central part of the coprolite particles, or at their rims (red arrows; Fig. IV. 5b), showing diffuse contours of the particles with the siliceous matrix. This may originate from the precipitation of dissolved silica, and incorporation

of radiolarian tests, diatom frustules and siliceous algae in the depositional environment (Tlili et al., 2010, 2011).

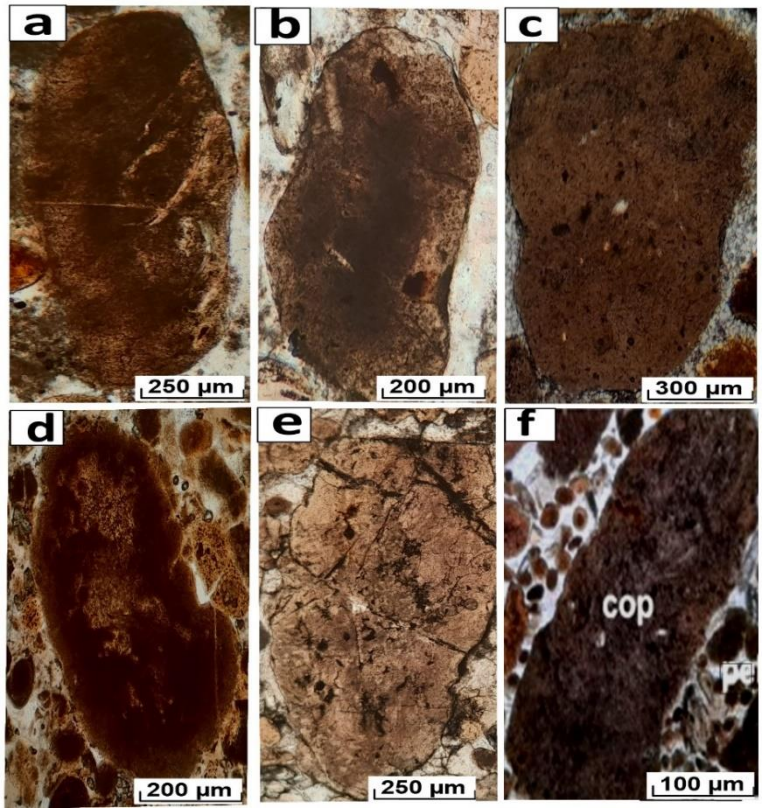

Fig. IV. 4. Photomicrographs showing coprolites particles in studied phosphorites deposits. (a, b) Coprolites particles (Cop) showing smooth polished surfaces, cylindrical to irregular shapes; ranging from white, brown to grey in color; (c-f) phosphatic coprolites displaying cracks, pores, organic material patches on their surfaces.

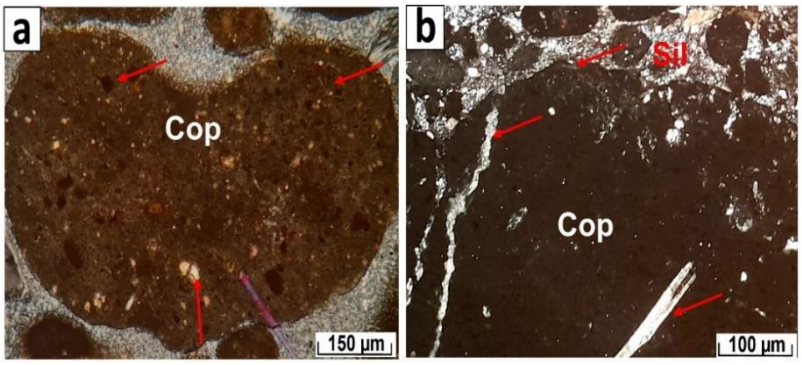

Fig. IV. 5. Thin section photomicrographs of coprolite particles showing: (a) various types of inclusions in coprolites (Cop); (b) coprolites (Cop) with occasionally siliceous fillings of amorphous silica (opal-CT).

Glauconites

Glauconite particles represent less than 3% of the total grains, and show dark to light green color, oxidized surfaces, and elongated to irregular shapes, with sizes in the range 150–250 μm (Fig. IV. 6). Greenish glauconite particles show a dark core and green rim, suggesting an early maturation stage (weak glauconitization processes), and may be related to glauconitization of phosphatic material (Fig. IV. 6a, b). Unlike pellets and coprolites, glauconites are less abundant in the studied phosphorites, with a higher concentration found in the lower layers (Fig. IV. 6c).

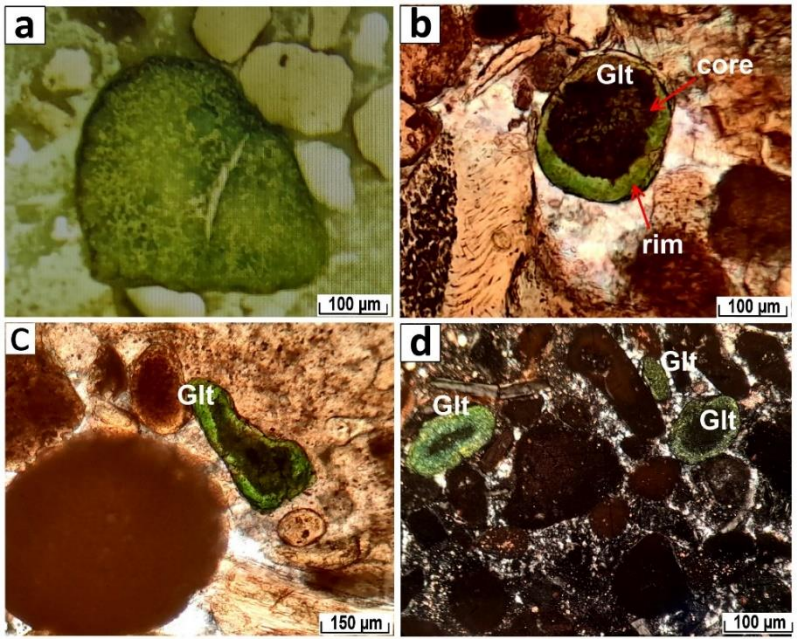

Fig. IV. 6. Thin section photomicrographs of glauconite particles in phosphorites deposits. (a, b) Greenish glauconites (Glt) showing dark core and green rim; (c) an abundance of glauconites within siliceous matrix (Glt).

Bioclasts

The bioclasts that compose about 10% of the phosphatic particles, are mainly fish teeth, fragment of fish teeth, bone fragments, lamellibranch fragments, gastropod, with size ranging from 150 μm to 4 mm in size (Fig. IV. 7). The fish teeth (Fig. IV. 7a) and bone fragments (Fig. IV. 7b) show platy, angular to subangular, prismatic or irregular shapes, with grain sizes ranging

from 100 μm up to 2 mm. They often show various shades of yellow to grey colors, and are usually surrounded by calcareous, clayey or siliceous material (red arrows, Fig. IV. 7c, d). Elongated bone fragments and lamellibranch fragments (Fig IV. 7e, f) show a beginning of phospho-micritization with dark to grey micritic envelope that makes enclosed within the siliceous and argillaceous (Arg) matrix (see red arrows). The replacement of phosphate grains by cementing siliceous material (amorphous silica) reflects the late silicification diagenetic process effect.

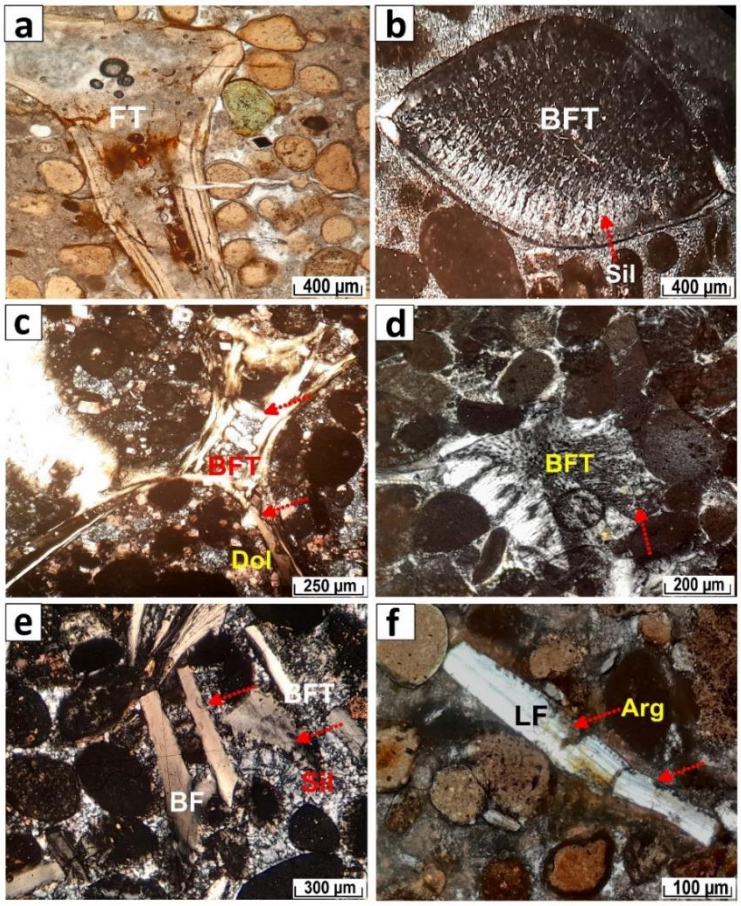

Fig. IV. 7. Thin section photomicrographs showing the main types of bioclasts in phosphorite deposits. (a) Fish teeth (FT) showing a size up to 3 mm with pellets and glauconite; (b) outer micrite rims of fragments of fish teeth (BFT) are filled with amorphous silica material; (c) spines of fish teeth (BFT) showing pore-filling dolomite crystals (Dol) in a sparitic matrix; (d) bone fragments (BFT) coated with micritic and/or organic material that makes sharp contacts with the matrix (see red arrow); (e, f) elongated bone fragments (BF) and lamellibranch fragments (LF) showing dark to grey micritic envelopes that makes enclosed within the siliceous and argillaceous (Arg) matrix (see red arrows).

Non-phosphatic minerals

Other minor, non-phosphatic minerals, such as detrital quartz and gypsum, are also observed within the phosphorites. Detrital quartz grains show angular to subangular shapes and range in size from 60 to 100 m (Fig. IV. 8a), while gypsum grain ranges in size from 100 to 200 µm (Fig. IV. 8b). Here, the crystalline silica is represented by quartz grains.

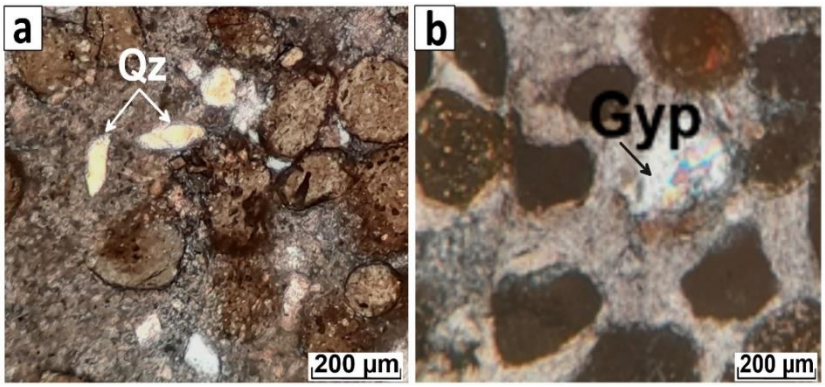

Fig. IV. 8. Thin section photomicrographs showing (a) angular to subangular quartz detrital (Qz) within phosphatic particles and (b) gypsum mineral (Gyp).

Iron oxides

Iron hydroxides are also observed within the microcracks and interstices of the phosphatic particles (Fig. IV. 9a, b). This may be attributed to the post deposition oxidation of iron-rich material.

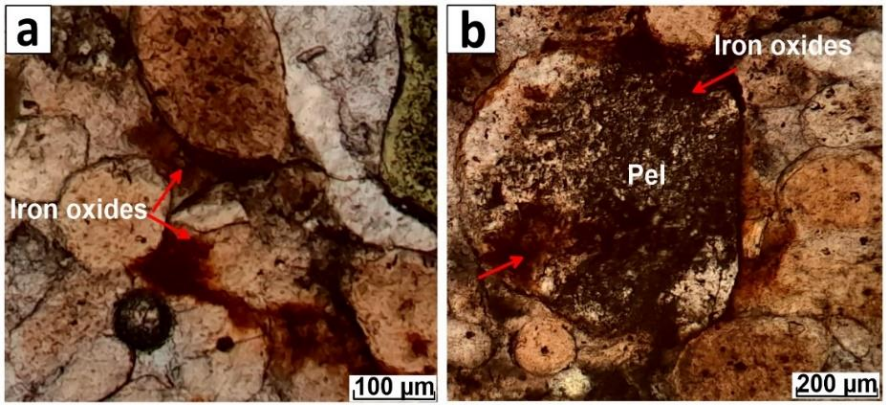

Fig. IV. 9. Thin section photomicrographs showing iron oxides: (a) filling pores and microcracks; (b) interstitial material.

Matrix/Cement

The phosphatic particles are often cemented by calcareous, often dolomitic matrix, rarely clayey (argillaceous) and/or more siliceous matrix. (Fig. IV. 10). As whole, the phosphatic particles are commonly coated with argillaceous micritic and/or organic material that makes sharp contacts with the matrix (Fig. IV. 10a). The dolomite matrix can be occurred in different forms: disseminated rhomboidal dolomite crystals with fine to medium size surrounding the particles (euhedral dolomite crystals), dolomite inclusions within the phosphate particles, and dolomite-filled voids in some phosphatic particles (see yellow arrows, Fig. IV. 10b). This suggests that the development of dolomite can be attributed to high-MgO pore water during early diagenesis processes. The calcitic cement typically are composed of sparitic microcrystalline calcareous material, with sizes exceeding 10 μm surrounded the phosphatic particles (Fig. IV. 10c). Later silicification processes are also observed by the development of amorphous silica (opal-CT) at the rims and sometimes at the center of the phosphatic particles (see red arrow, Fig. IV. 10d), showing diffuse contours of the particles with the sparitic matrix within grainstone texture. The siliceous material may be originated from fragmented fossils of siliceous tests, and precipitated silica.

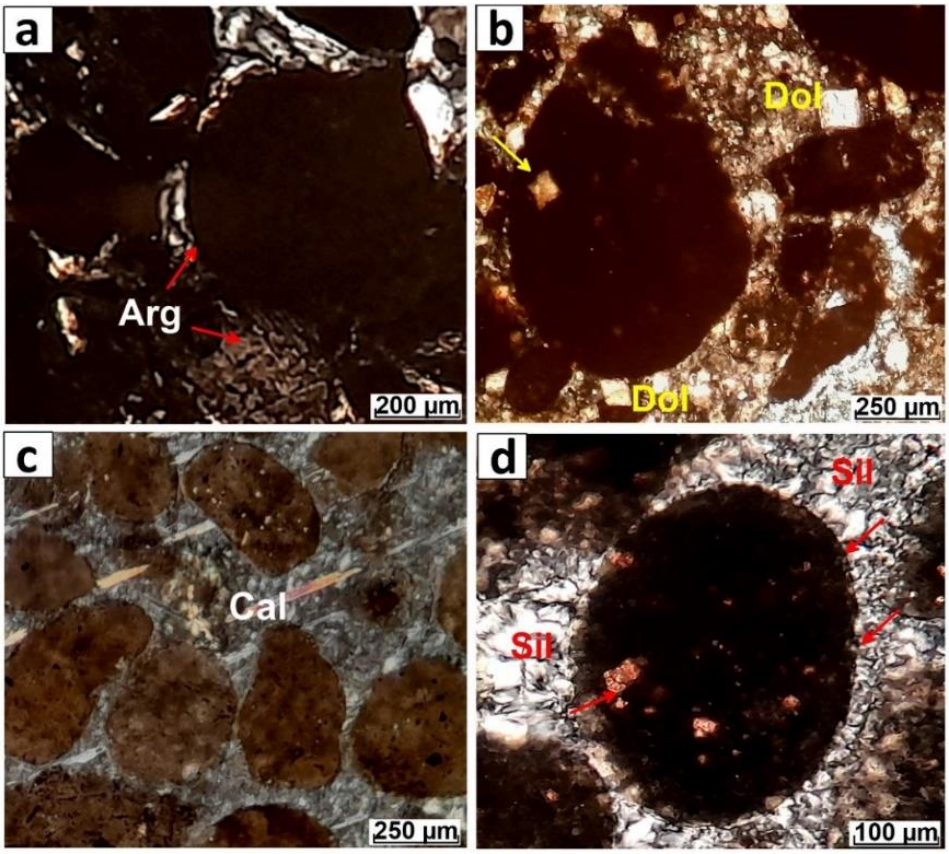

Fig. IV. 10. Thin section photomicrographs showing the different forms of matrix and /or cement that occur in phosphorite deposits. (a) Pellet particles cemented by an argillaceous (Arg) matrix (clayey, red arrows); (b) a dolomitic matrix showing well-crystallized dolomite rhomb crystals (euhedral dolomite) ranging in size from 50 to 100 µm (Dol); (c) phosphatic particles cemented by sparitic calcitic cement within grainstone texture (Cal); (d) the pellet particles are surrounded by an amorphous silica matrix (Sil), and have patches of this matrix dispersed on their surfaces as inclusions (see red arrows).

IV. 1. 2. The phosphorite sub-layers

IV. 1. 2. 1. The Troubia phosphorites

Based on field and petrographic observations, the phosphatic rocks types in Troubia deposit are dolomitic-cherty and cherty phosphorites (see Fig. II. 6). These rocks contain higher abundances of phosphatic particles than the Ain Dibba and Ain Kissa deposits, and are also harder due to being cemented by a dolomitic and /or more siliceous matrix. They are composed of phosphatic particles: pellets, coprolites, bioclasts (bone fragments and fish teeth) and glauconites that are cemented by calcareous (dolomitic), and/or siliceous matrix. The microscopic observation of these particles (Figs. IV. 11 and IV. 12) shows that they are

heterogeneous in their shapes, colors, morphologies, and proportions which vary from about 60 to 80% of the rock.

In cherty phosphorites, the pellets (40–45% of the total grains) are often rounded, subrounded, spherical to oval in shape, brown to yellowish in color, and range in size from 80 to 400 µm, and they are commonly coated with micritic and/or organic material that forms a sharp contact with the sparitic siliceous matrix in a grainstone texture (red arrows, Fig. IV. 11a). However, later silicification processes are observed by the development of amorphous silica (opal-CT), which occurs either as veins cross-catting replacing the central part of the irregular coprolite particles, or at their rims (red arrows; Fig. IV. 11b), showing diffuse contours of the particles with the sparitic siliceous matrix. Greenish glauconites represent more than 5% of the total grains in the Troubia phosphorites compared to those of Ain Dibba and Ain Kissa phopshorite layers, and occurs as irregularly shaped grains with dark cores and green rims within a siliceous matrix (Fig. IV. 11c). Their size ranges from 150 µm to 400 µm. The bone fragments and fish teeth (10–15% of the phosphatic particles) often show platy, angular to sub-angular, prismatic or irregular shapes, yellow to grey colors with grain sizes ranging from 100 µm up to 1 mm, and are usually phosphatized or partially/completely silicified by sparitic siliceous material (red arrows; Fig. IV. 11d). These results indicate that the absence of concentric growth structures within the phosphatic particles support the reworked origin of the phosphatic grains, whereas the abundance of bone fragments and fish teeth are consistent with a high energy environment, origin related to the presence of an active upwelling system during diagenesis process (Ahmad et al., 2019). The phosphorites show grainstone texture in a sparitic matrix, suggesting also high energy and shallow depositional environment, connected to the open ocean during diagenetic processes. The silicified coprolites and bone fragments are likely of reworked origin from silica-rich phosphatic sediments, as indicated by their internal silica infill and the compositional similarity to surrounding siliceous matrix in environment

supersaturated with dissolved silica. The presence of glauconites in an early stage of maturation (weak glauconitization processes), may be related to glauconitization of phosphatic particles (Laouar et al., 2024; Kechiched et al., 2018).

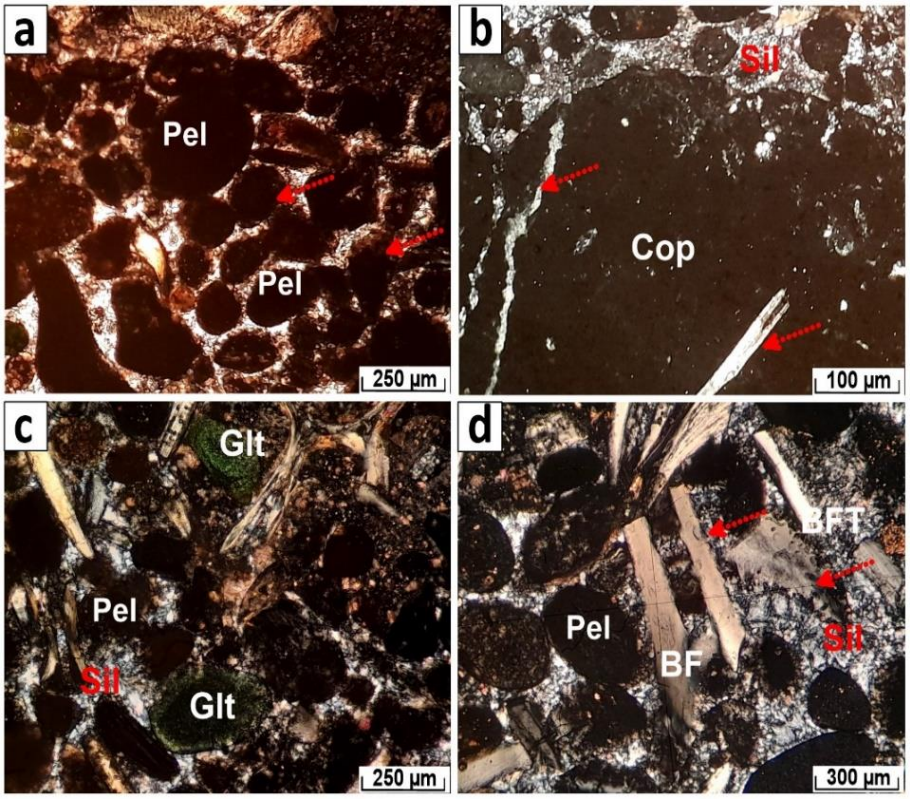

Fig. IV. 11. Thin section photomicrographs of cherty phosphorites from Troubia deposit. (a) Dark pellets (Pel within grainstone texture cemented by siliceous matrix; (b) coprolites particles (Cop) silicified by veins siliceous cross-cutting during early diagenesis conditions, (c) green glauconites (Glt) showing irregular shape with dark core and green rim within exo-matrix siliceous; (d) angular to sub-angular, prismatic bone fragments (BF) and fish teeth (BFT) filled by the matrix where their diffuse contours with the siliceous matrix.

Dolomitic-cherty phosphorite

This phosphorite is characterized by an abundance of rounded to sub-rounded, spherical to oval pellets with yellow to brown color, ranging in size from 60 to 300 µm, and surrounded by a sparitic siliceous matrix (amorphous silica as opal-CT) in a grainstone texture (Fig. IV. 12a). These phosphatic particles are cemented by a sparitic dolomite matrix, which can be occurred in different forms: disseminated rhomboidal dolomite crystals with fine to medium size (5 µm to 150 µm size) surrounding the particles (euhedral dolomite crystals); dolomite

inclusions within the phosphate particles; and dolomite-filled voids within some phosphatic particles (Fig. IV. 12b). This suggests that the development of dolomite can be attributed to high-MgO pore water during early diagenesis processes. Coprolites, which represent up to about 35 % of the phosphatic particles, show typical cylindrical, elliptical, elongated or irregular shapes, with whitish, brownish to dark color, and contain dolomite inclusions (Fig. IV. 12c). The grain size may exceed 250 µ m and occasionally reaches few millimeters. This suggests fragmentation by marine wave action and burial compaction, and growth of dolomite crystals during diagenetic processes. The bone fragments and fish teeth (up to 20 % of the total rock grains) which often show platy, angular to sub-angular, prismatic or irregular shapes, ranging in size from 100 µm to 2 mm, are usually phosphatized or partially/completely silicified by sparitic dolomitic-siliceous material (red arrows, Fig. IV. 12d). They which often show various shades of yellow to grey colors, are coated with phospho-micritic and/or dolomitic rhomboids crystals material that makes sharp contacts with the matrix (Fig. IV. 12e). Greenish glauconites are enriched in the phosphorite rocks, comprising up to 4 % of the total rock grains, and display irregularly shapes with irregular internal structures varies between dark and green, with size ranging from 100 µm to 400 µm (Fig. IV. 12f), may be related to degree stage of glauconitization processes.

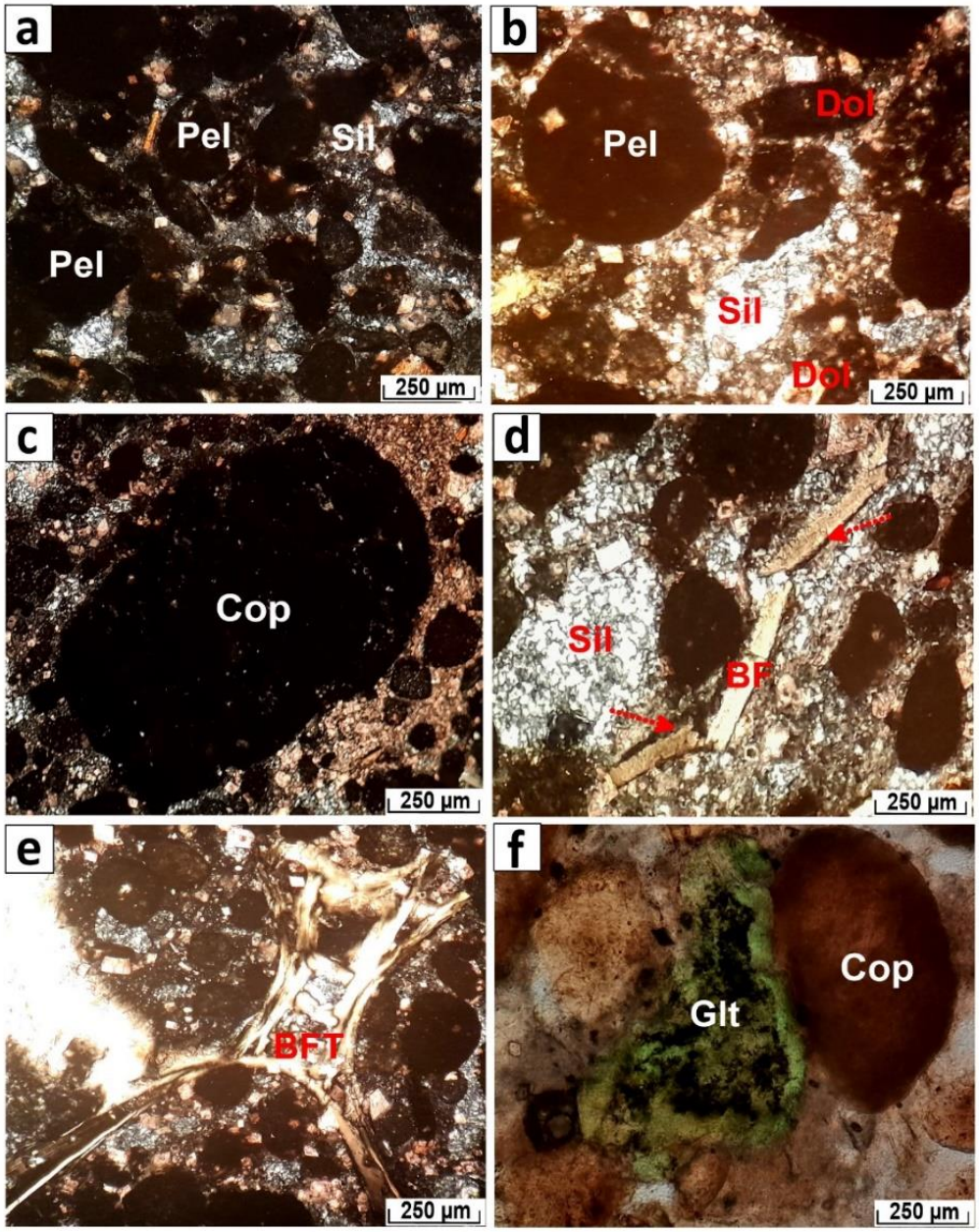

Fig. IV. 12. Thin section photomicrographs of dolomitic-cherty phosphorites from Troubia deposit. (a, b) Rounded to sub-rounded pellets (Pel) showing filled by rhombs dolomite (Dol) within siliceous matrix (Sil); (c) coprolites (Cop) coated on their surfaces by dolomite crystal; (d, e) fragments of spine fish (BFT) and bones (BF) showing dolomite matrix are diffuse on their surfaces within exo-matrix siliceous nature (Sil); (f) irregular green glauconites (Glt) showing dark core and green rim.

IV. 1. 2. 2. The Ain Dibba phosphorites

Lower sub- layer phosphorite (LL)

The microscopic observation of the phosphatic particles (Fig. IV. 13) reveals heterogeneity in their shapes, colors, and morphologies, indicating that the rock is poorly sorted. These constituents represent approximately 75% of the total rock volume, with grain sizes ranging from 80 µm to several millimeters. They are composed predominantly of medium-to coarse-grained, and poorly sorted phosphatic components (phosphochems and phosphoclasts). The pellets, which constitute 40–45% of the total phosphatic particles, are often rounded, sub-rounded, spherical to oval in shape, brown to yellowish in color, occasionally nearly black reflecting variations in organic matter (OM) content (Fig. IV. 13a) that occurs either in concentric micro-layer (red arrow) or in the form of disseminated organic material (TOC; Ben Hassen et al., 2010). Their size ranges from 80 µm to 400 µm. However, the contents of some particles were diffused and embedded in the matrix (exo-gangue), which indicates that the matrix is also enriched in phosphorus and organic matter (Ben Hassen et al., 2010, Saouli et al., 2025; Aouachria et al., 2025). Coprolites, representing up to about 30% of the total phosphatic particles, are fossilized excrement originating from fecal matter and exhibit cylindrical, elliptical, elongated, or irregular shapes, with colors varying from whitish to brownish or dark (Fig. IV. 13b). The fractured coprolites were dispersed and embedded makes sharp contacts with a matrix, causing by marine wave action, burial compaction, and fragmentation during reworking process (Fig. IV. 13c). The bone fragments and fish teeth, which compose about 10% of the phosphatic particles, display platy, angular to sub-angular, prismatic, or irregular shapes, and occasionally show siliceous and/or clayey matrix fillings, with sizes ranging from 100 µm to 1 mm (Fig. IV. 13d). Greenish glauconite particles are rare, accounting for about 2% of the total particles, and show a dark core and green rim, suggesting an early maturation stage (weak glauconitization processes), and may be related to glauconitization of phosphatic

material (Fig. IV. 13e). Lithoclasts are also observed (Fig. IV. 13f) within a clayey (argillaceous) matrix.

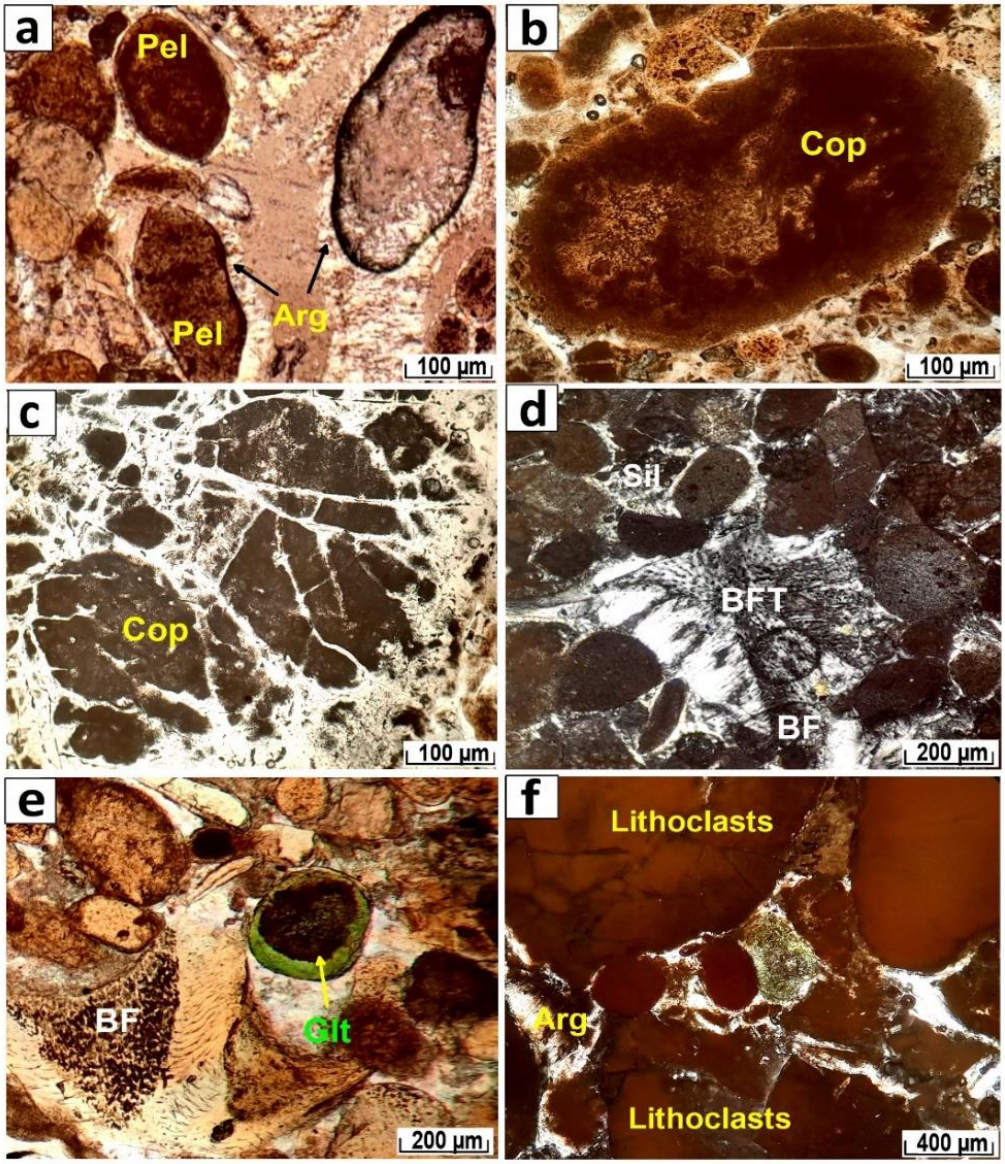

Fig. IV. 13. Thin section photomicrographs of phosphorites from Ain Dibba deposit. (a, b) Dark pellets (Pel) and brown coprolites (Cop) containing organic matter (OM), and embedded in the argillaceous matrix with diffuse rims; (c) fractured coprolites dispersed within the matrix; (d) abundant bone fragments within sparitic siliceous matrix in a grainstone texture; (e) glauconite particles (Glt) showing dark core and green rim; (f) irregular lithoclasts, coprolites (Cop), and glauconites (Glt) are cemented by a clayey (argillaceous) matrix.

Middle sub-layer phoshorites (ML)

Cherty phosphorites are composed predominantly of medium- to coarse-grained, and poorly sorted phosphatic components (phosphochems) and phosphoclasts, which together account for approximately 65% of the total rock volume (Fig. IV. 14). Their size ranges from 50 μm to 2 millimeters. These phosphatic particles in sparitic cement were intensively reworked, causing the grains to become closer together showing grainstone texture (Fig. IV. 14), before being cemented by a siliceous matrix; suggesting burial compaction, and rapid sedimentation under high-energy conditions. The pellet particles (40–45% of the total grains) are often rounded, subrounded, spherical to oval in shape, brown to yellowish in color, and range in size from 80 to 400 μm (Fig. IV. 14a). The pellets that show concentric structures (~5% of the total particles) are composed of a nucleus, often quartz grain or fossil and bone fragments, surrounded by thin, dark brownish to black concentric phosphatic material (cortex). They are usually spherical, oval or elongated in shape and range in size from 100 to 250 μ m in size (Fig. IV. 14b). Coprolites (~ 35% of the total grains) are cylindrical to irregular in shape, whitish to dark brown, and may exceed 250 μm reaching a few millimeters, and have cracks and micro-inclusions on their surfaces (Fig. IV. 14c), indicating the affected by the diagenesis processes. Sometimes, the fish teeth fragments are partially and / or completely silicified by amorphous silica (Fig. IV. 14d), causing late silicification in post-deposited conditions. The bone fragments and lithoclasts show platy, angular to subangular, prismatic or irregular shapes, and range in size from 100 μm up to 1 mm surrounded by siliceous material (Fig. IV. 14e). They often show various shades of yellow to grey colors, and are commonly coated with micritic and/or organic material that makes sharp contacts with the matrix (Fig. IV. 14f), showing diffuse contours of the particles with the siliceous matrix. Silicification represented by opal-CT in the matrix of some phosphorites (cherty phosphorites) may originate from precipitation of dissolved silica,

and incorporation of radiolarian tests, diatom frustules and siliceous algae in the depositional environment (Ben Hassen et al., 2010; Henchiri, 2007).

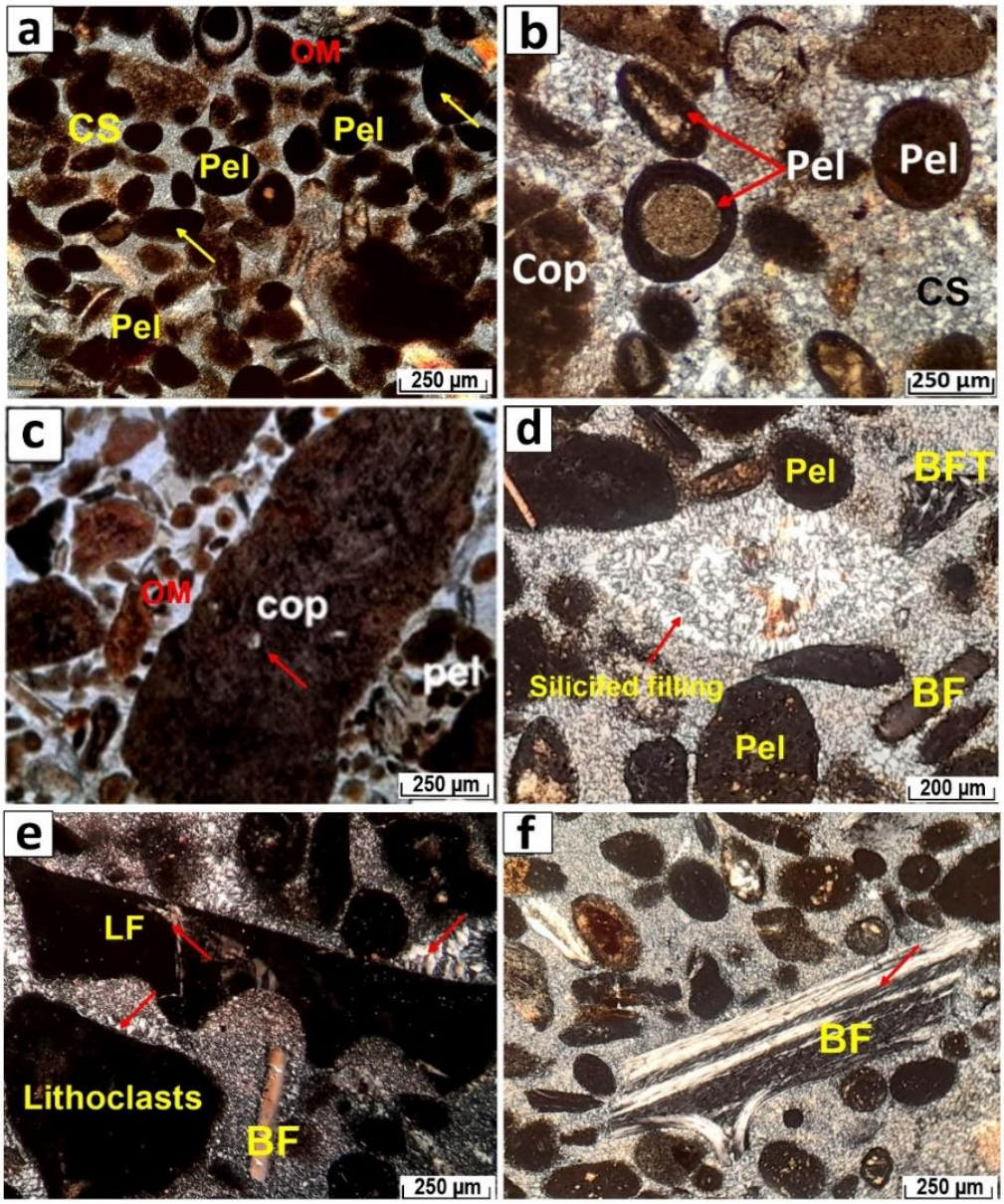

Fig. IV. 14. Thin section photomicrographs of phosphorites from Ain Dibba deposit. (a) brown, rounded to sub-rounded pellets with abundant organic matter (OM) within micro-sparitic siliceous cement (CS); (b) rounded to sub-rounded pellets with concentric structures (Pel) showing bone fragments and fossil nuclei, along with sub-rounded pellets (Pel) and irregular-shaped coprolite particles (Cop) within siliceous cement; (c) coprolites are filled by siliceous inclusions (Cop); (d), tests of foraminifera and fish teeth (BFT) are filled by siliceous cement; (e) bone fragments and lithoclasts cemented by siliceous matrix (red arrow); (f) grey, elongated bone fragments (BF) filled by siliceous matrix (red arrow).

- **Calcareous phosphorites**

The phosphatic particles in the phosphorite are heterogeneous in their shapes, colors, morphologies heterogeneous in their shapes, colors, morphologies (the rock is poorly sorted) and proportions which vary from about 60 to 75% of the rock. They are composed of pellets and coprolites, bone fragments and fish teeth, and are more prominent compared to the middle phosphorite layers (Fig. IV. 15). Their sizes range from 100 µm to 1 mm. The pellets, which are the most abundant phosphatic particles (40–45% of the total grains), show rounded, subrounded, spherical to oval in shape, brown to yellowish in color, and display grain size from 80 µm to 400 µm within spary calcite matrix in the grainstone texture (Fig. IV. 15a). Although concentric growth structures are absent within the phosphatic particles, the pellets display cracks, and their contents (see red arrows) were dispersed and embedded in a calcareous (calcitic) matrix (exogangue) (Fig. IV. 15b), indicating the high organic content (TOC) phosphorus (P) in the matrix. The coprolites (30-35 % of the total grains) are fractured (see red arrow) within a sparitic calcitic cement (Fig. IV. 15c), may be influenced by marine wave action, burial compaction and reworking processes. The particles display clayey and / or calcitic filling material at their rims and occasionally at their centers (Fig. IV. 15d), revealing dispersed contours of the particles with the matrix during diagenesis processes. The bone fragments and fish teeth (up to 20 %) display platy, angular to subangular, prismatic or irregular shapes, with grain sizes ranging from 100 µm up to 2 mm (Fig. IV. 15e). They often display a variety of colours ranging from yellow to grey, and are typically surrounded by calcareous material, suggesting high energy and shallow depositional environment (Fig. IV. 15 f).

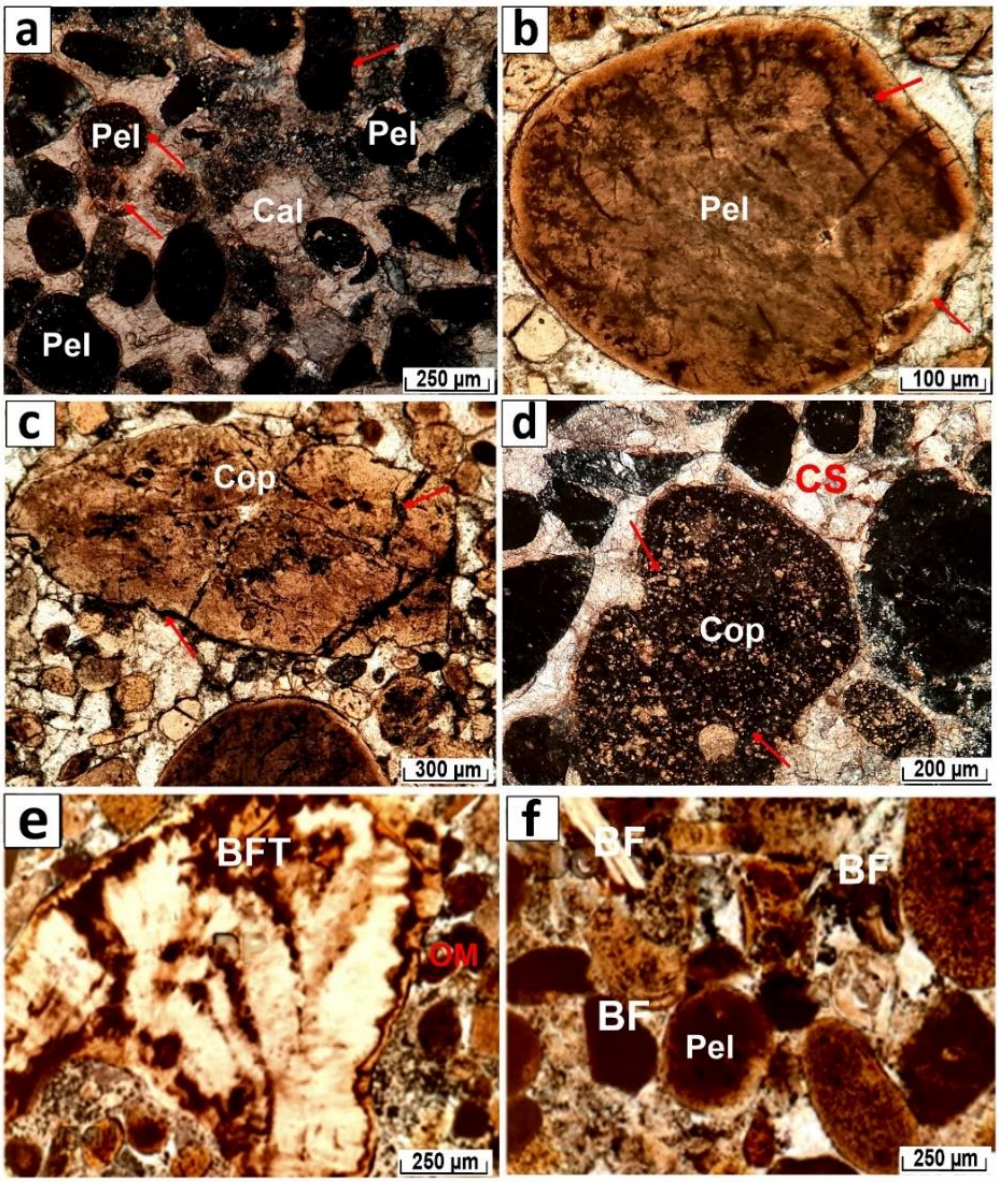

Fig. IV. 15. Thin section photomicrographs of phosphorites from the Ain Dibba deposit. (a) abundant brown, rounded to subrounded pellets (Pel) are surrounded by spary calcite matrix (red arrows) in the grainstone texture; (b) the contents of some pellets particles (Pel, red arrow) were dispersed and embedded in a calcareous matrix as known exogangue; (c) fractured coprolites (Cop) (red arrow); (d) coprolites (Cop) filled with sparitic calcareous cement (CS); (e) larger bone of fish teeth (BFT) with presence of organic matter (OM); (f) angular to subangular, prismatic bone fragments (BF).

Upper sub-layer phosphorites (UL)

The phosphorites are composed of sub-rounded to spherical pellets and cylindrical coprolites, bioclasts particles, and are cemented by calcitic-siliceous cement (Fig. IV. 16). Their size ranges from 50 µm to a 2 millimeters and proportions which vary from about 50 to 60% of the rock. The pellets, which are often dark in color due to their high organic matter content,

display rounded to subrounded shapes, and contain inclusions of calcite and siliceous minerals (Fig. IV. 16a). The calcitization processes are known by the development of micrite to sparry calcite envelopes and calcite-infilling at the rims and sometimes at the center of the pellets and coprolites phosphatic particles (see red arrows; Fig. IV. 16b, c). The bone fragments (Fig. IV. 16d) show platy, angular to sub-angular, prismatic or irregular shapes, with grain sizes ranging from 100 µm to up 1 mm. They show various shades of yellow to grey colors, and are enclosed by calcareous, clayey or siliceous material. These results indicate increasing in environment energy in the top and more shallow depositional environment, connected to the open ocean during diagenetic processes.

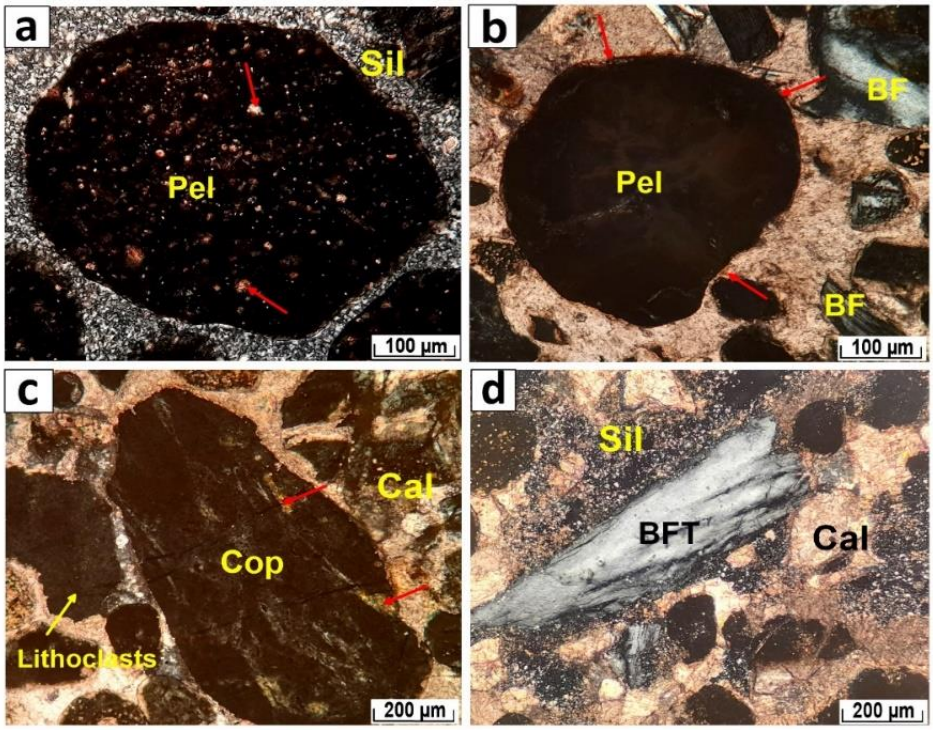

Fig. IV. 16. Thin section photomicrographs of phosphorites from Ain Dibba deposit. (a) rounded to subrounded pellets showing silicified filling within micro-sparitic siliceous matrix (red arrow); (b) pellets particles (Pel) showing dark in color due to high organic matter contain, surrounded by oxidation (red arrow) with bone fragments (BF); (c) coprolites partilces (Cop) surrounded by glauconite material (red arrow) with lithoclasts within calcareous cement; (d) grey, elongated bone fragments (BFT) coated by sparitic calcareous cement (Cal) or/ and siliceous matrix (Sil).

IV. 1. 2. 3. The Ain Kissa phosphorites

At the bottom of Ain Kissa deposit, the marly phosphorite is characterized by low proportion of phosphatic particles (40-50 % of the total rock volume) compared to those observed in the lower and middle sub-layers, while the matrix predominates, reaching nearly 20% of the total volume. These phosphatic particles reveal homogeneity in their shapes, colors, and morphologies (Fig. IV. 17), with grain sizes ranging from 50 µm to 500 µm. The pellets are sub-rounded and bordered by a thin, light envelope (Fig. IV. 17a), which suggests that these envelopes are most likely fine-grained apatite coatings formed during the early stages of diagenesis under phosphate-rich conditions (Ben Hassen et al., 2010; Slansky, 1980). The micro-sparitic siliceous matrix are observed in the phosphorite, either altered the rims of the phosphatic particles and replaced the outer cortex or coating on the surface as inclusions (red arrow; Fig. IV. 17b), are most likely developed during post-depositional process. The sparitic silica occurs either veins cross-cutting the phosphatic particles, and dispersed silica patches within particles, or pore-filling cement (see arrow; Fig. IV. 17c), which is explained as the result of diagenetic alteration process (Soudry, 1985). The bone fragments and fish bones, often show naturally colorless and elongated to sub-angular in shape, and are usually enclosed in a dark to brown envelope coated with micritic matrix, (Fig. IV. 17d), may be related to the beginning of phospho-micritization and fragmentation during reworking process. Glauconite particles reveal irregular shapes with a dark core and green rim, coated by an argillaceous micritic matrix (Fig. IV. 17e). They range in size from 150 µm to 300 µm. Other minor non-phosphatic constituents, such as angular to subangular detrital quartz, were also observed, ranging in size from 60 to 100 m (Fig. IV. 17f).

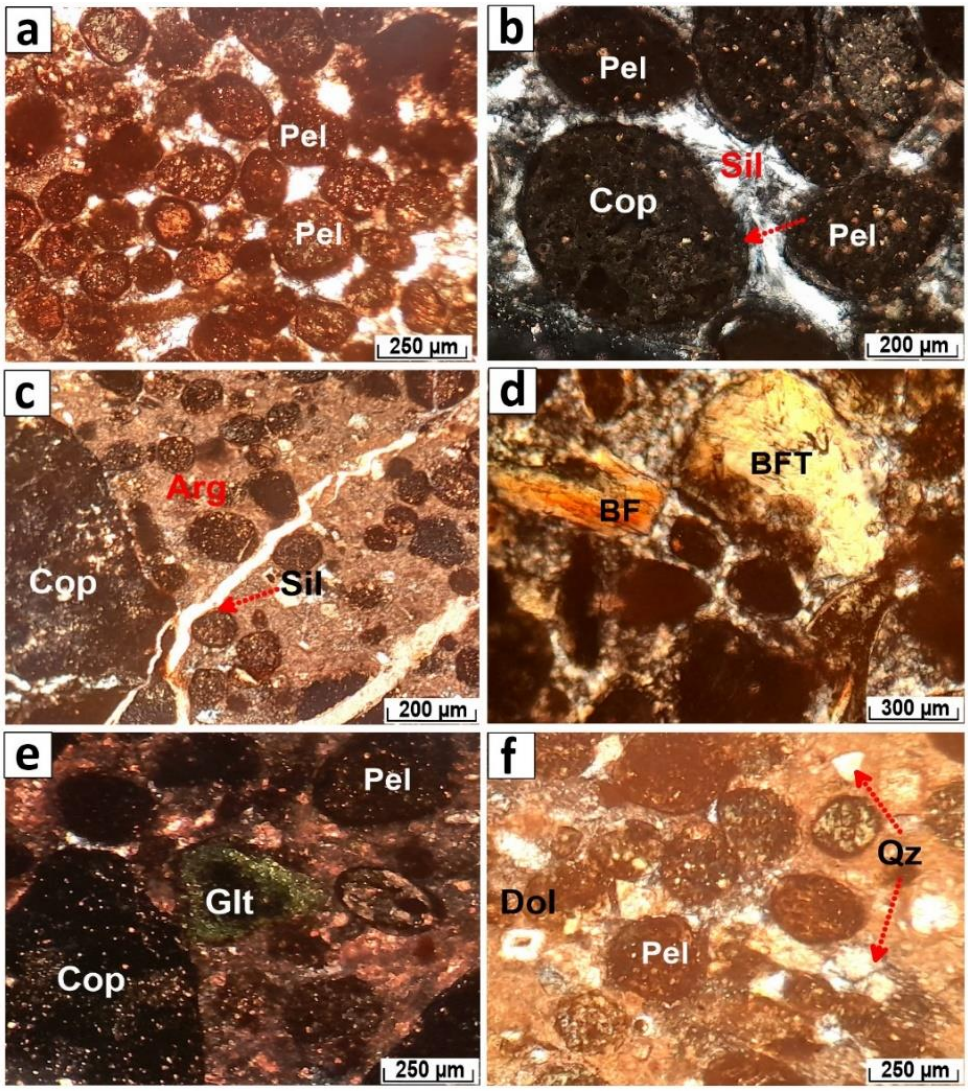

Fig. IV. 17. Thin section photomicrographs of marly phosphorites at the bottom section from Ain Kissa deposit. (a) Abundant pellets particle (Pel) coated with micritic and/or organic material that makes sharp contacts with the dolomitic siliceous and/or clayey matrix; (b, c) the development of silica (Sil; opal-CT) at the rims and sometimes at the center of the phosphatic particles (red arrows); (c) and cemented by argillaceous (Arg) (clayey); (d) fragments of bones (BF) and fish teeth (BFT) showing platy, angular to subangular, prismatic or irregular shapes, surrounded by calcareous, clayey or siliceous material; (e) glauconites particles (Glt) with pellets and coprolites cemented by siliceous matrix from the Ain Kissa phosphorites; (f) angular to subangular detrital quartz (Qz) particles in Ain Kissa phosphorites with dolomitic matrix (Dol).

Lower layer phosphorite (LL)

This phosphorites are composed by an abundance of medium-to coarse-grained, poorly sorted, and glauconite particles which make up 75% of the volume of the total rock, with sizes ranging from 80 µm to a few millimeters (Fig. IV. 18 and IV. 19). The pellets are sub-rounded and also bordered by a thin, light envelope (see arrows; Fig. IV. 18a). These pellets are

characterized by variations in the content of organic materials (see arrows; Fig. IV. 18b), which occur in the following forms: (1) filling the majority of the particle; (2) randomly disseminated organic material in the form of patches; (3) in the form of concentric micro-layers; or (4) concentrated in the central part of the pellet. Sometimes the phosphatic particles with patches of dark organic material, shows initial alteration and corrosion which is discernable on outer rim of particles (red arrows) as shown in Fig. IV. 18c, indicating very high porosity of these particles. The absence of concentric growth structures within the phosphatic particles support the inferred reworked origin of the phosphatic grains. On the other hand, the organic material has been dispersed within the clayey-dolomitic matrix (exogangue) as shown in Fig. IV. 18d, indicating the high content of TOC and P_2O_5. The oxidation of organic material associated with the matrix are more rapidly than that entrapped within the particle, may be related to reworking processes (Dassamiour et al., 2013).

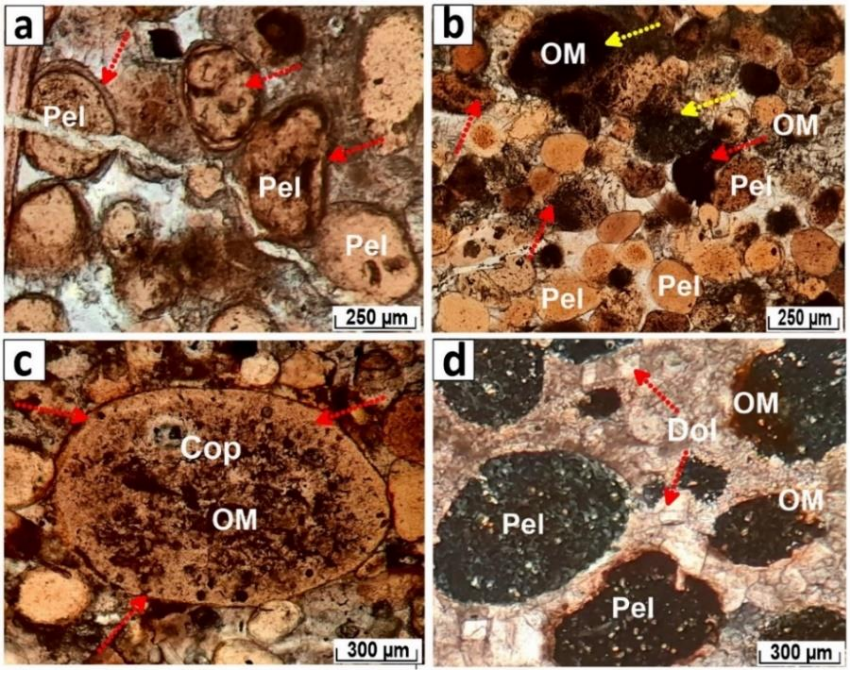

Fig. IV. 18. Thin section photomicrographs of phosphorites from lower layer phosphorite of Ain Kissa deposit. (a) The pellets (Pel) are bordered by a thin and clear to beige envelop; (b) irregular distribution of the organic matter(OM) within pellets phosphatic and also diffuse as a matrix; (c) coprolites (Cop) have patches of dark organic matter (OM), either outer of the particles or in the center; (d) organic matter (OM) occurs as exomatrix of phosphorites deposit (exo-gangue) with dolomite crystals as cement (Dol).

The bioclasts (fish teeth and bone fragments) that compose about 10% of the phosphatic particles, are commonly coated with micritic and/or organic material that makes sharp contacts with the matrix (e.g., Fig. IV. 19a). However, later silicification processes are shown by the development of silica (opal-CT) at the rims and sometimes at the center of the phosphatic particles (Fig. IV. 19b), showing diffuse contours of the particles with the matrix. The sparitic calcite and micro-sparitic siliceous matrix are observed in the phosphorite, either altered the rims of the phosphatic particles and replaced the outer cortex or coating on the surface as inclusions (Fig. IV. 19c). This result suggests that the degraded phosphatic materials are related to post-depositional alteration processes. Greenish glauconite particles show dark core and green rim (Fig. IV. 19d), suggesting that they are in an early stage of maturation (weak glauconitization processes). Other minor non-phosphatic constituents, such as angular to sub-angular detrital quartz, were also observed within a dolomitic-siliceous matrix (Fig. IV. 19e). It should be noted that glauconite particles and detrital quartz are more abundant in the phosphorite layers of the Ain Kissa deposit than in those of the Ain Dibba deposit. Dark to brown lithoclasts surrounded by a clayey-siliceous matrix were also observed in the phosphorites (Fig. IV. 19f). These may be related to the high energy of the depositional environment.

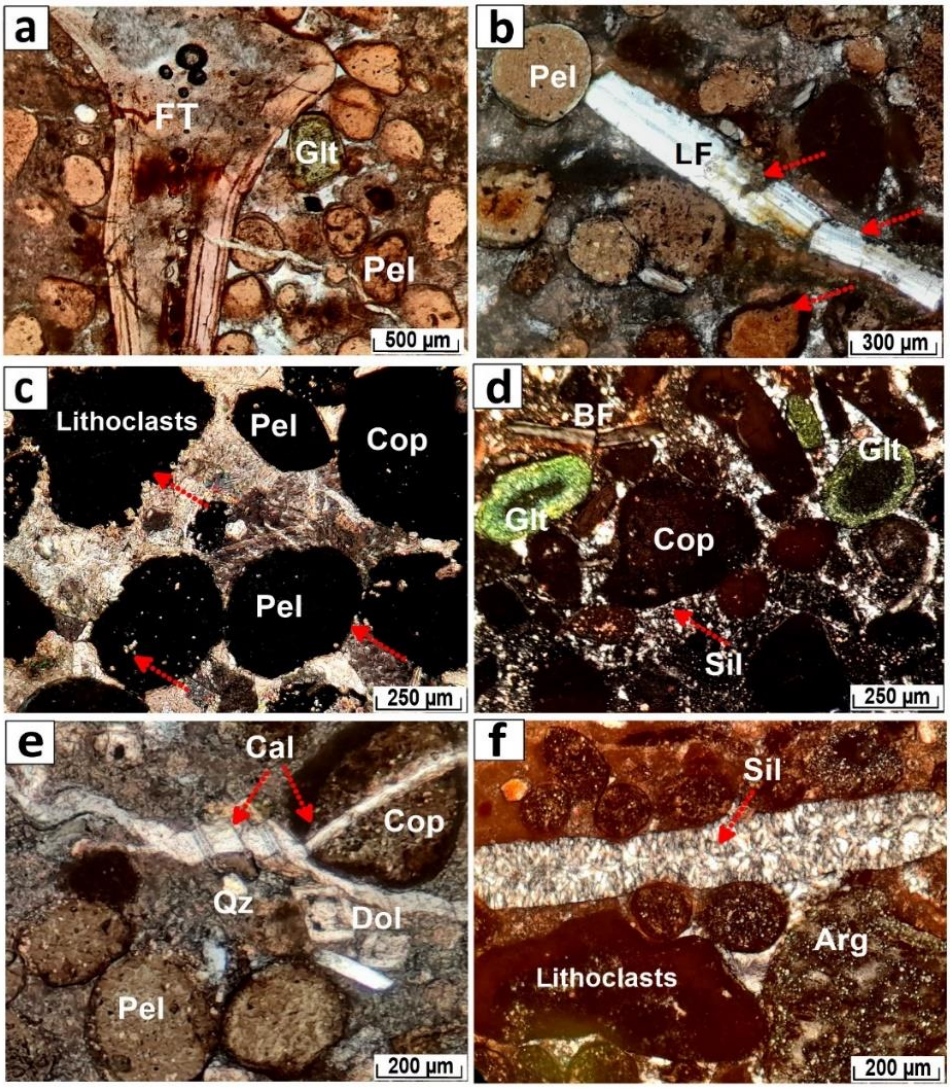

Fig. IV. 19. Thin section photomicrographs of phosphorites from lower layer phosphorites from Ain Kissa deposit. (a, b) Fish teeth (FT), bone fragments (BF), and lamellibranch fragments (LF) with size extending 1 mm, are coated with micritic and/or organic material; (c) phosphatic particles within calcitic and/ or siliceous matrix; (d) green glauconite particles (Glt) showing dark cores and green rims; (e) angular to sub-angular detrital quartz (Qz) with dolomite crystals (Dol) as a matrix; (f) phosphatic and the lithoclasts are cemented by clayey (argillaceous, Arg) and /or siliceous matrix (Sil, Opal-CT).

Middle-layer phosphorite (ML)

This layer is composed by alternating different phosphorite types: fine-to medium grained calcareous phosphorite, and poorly sorted, medium to coarse grained, cherty phosphorite with abundant of phosphochems (pellets and coprolites), and phosphoclasts (bioclasts and lithoclasts). The microscopic observation of these phosphatic particles shows that they are heterogeneous in their shapes, colors, morphologies (the rock is poorly sorted) and

proportions which vary from about 75% of the rock (Fig. IV. 20), similar abundance phosphatic particles to the lower and upper layers. The pellets, which are the most abundant phosphatic particles (40–45% of the total grains), are often rounded, sub-rounded, spherical to oval in shape, brown to yellowish in color, and display grain size from 80 μm to 400 μm within sparitic calcareous matrix often calcitic (Fig. IV. 20a). The calcitization processes are well represented by the development of micrite envelopes and calcite-infilling producing micritized or calcitized phosphatic grains, occurring in different forms: micrite to sparry calcite rims around degraded phosphatic grains; irregular calcite patches, calcite veins cross-cutting the matrix and particles (Fig. IV. 20b). In contrast, the phosphatic particles (coprolites, bone fragments, and fish teeth) are cemented by siliceous matrix (Fig. IV. 20c, d, e, and f), and the later silicification processes are shown by the development of silica (opal-CT) at the rims and sometimes at the center of the phosphatic particles, showing diffuse contours of the particles with the matrix.

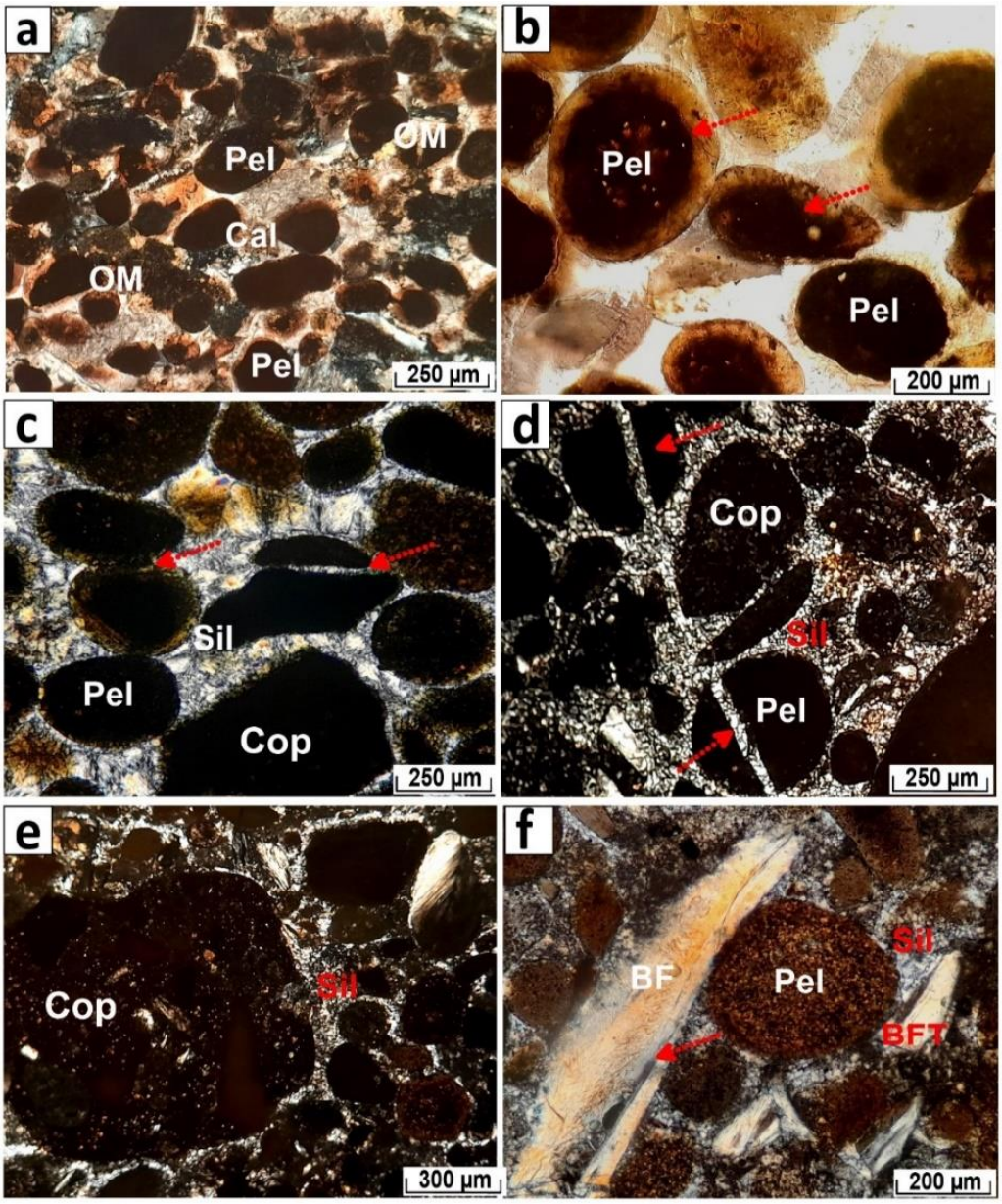

Fig. IV. 20. Thin section photomicrographs of middle layer phosphorites from Ain Kissa deposit. (a) Dark pellets (Pel) are cemented by sparitic calcareous matrix (calcitic, Cal) (b) pellets (Pel) showing calcite-infilling; (c) the phosphatic particles silicified by siliceous materials (Sil); (e) coprolites (Cop) containing various materials; (f) elongated bone fragments (BF) showing partial and/or complete silicification (red arrow) at their rims and counter.

Upper-layer phosphorite (UL)

The upper layer (UL) consists of medium to coarse-grained calcareous phosphorites with abundant pellets, coprolite and fragments of bones and fish teeth, that become much grey-darker, hard, and display a siliceous cement towards the top forming cherty phosphorite. The phosphatic particles are heterogeneous in their shapes, colors, morphologies (the rock is

poorlysorted) and proportions which vary from about 60 to 70% of the rock (Fig. IV. 21). Occasionally, they exhibit cracks and pores on their surfaces, which are most likely caused by compaction effects. The pellets (40–45% of the total grains) are often rounded, subrounded, spherical to oval in shape, brown to yellowish in color, and range in size from 80 to 400 μm, and they are commonly coated with the sparitic calcareous matrix in grainstone texture (Fig. IV. 21a). The fractured coprolites were dispersed and embedded makes sharp contacts with a siliceous matrix (Fig. IV. 21b), causing by marine wave action, burial compaction, and fragmentation during reworking process. However, other pellets particles which show concentric growth structures (~5% of the total particles) are composed of a nucleus, often quartz grain or fossil and bone fragments (red arrows, Fig. IV. 21c, d), surrounded by thin, dark brownish to black concentric phosphatic material (cortex). They are usually spherical, oval or elongated in shape and range in size from 100 to 250 μm in size. It is worth noting that the nucleated pellets (concentric structure) particles as called coated phosphochems, are enriched in the upper phosphorite layers of the Ain Kissa deposit compared to those from lower and middle layers, and are attributable to represent multi-stage displacement and highly agitated conditions (Ahmed et al., 2022). The packstone to grainstone texture in a micro-sparitic to sparitic siliceous matrix (Opal-CT silica) are observed as well developed in the phosphorite (red arrows; Fig. IV. 21e, f), either altered the rims of the bone fragments and pellets, and replaced the outer cortex or coating on the surface as inclusions.

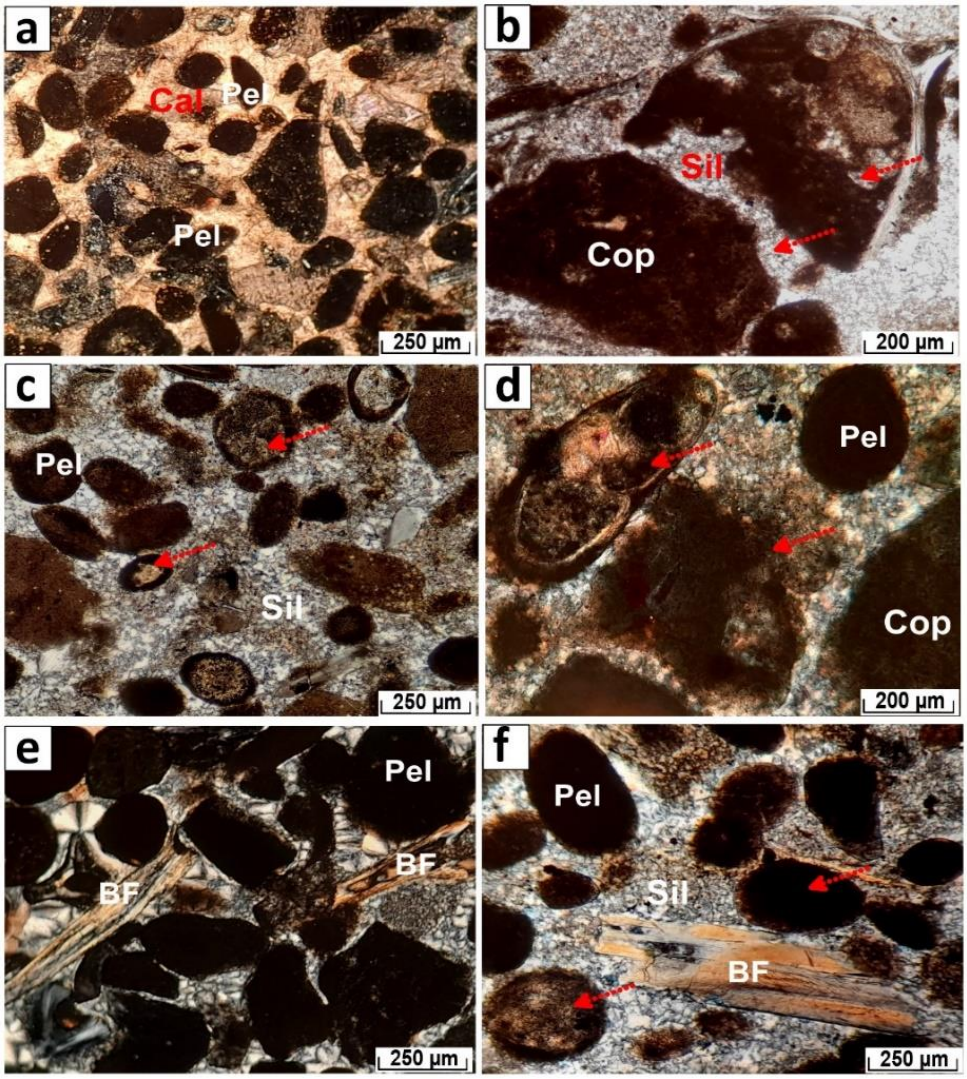

Fig. IV. 21. Thin section photomicrographs of upper layer phosphorites from Ain Kissa deposit. (a) Dark pellets (Pel) within calcitic matrix (Cal) and calcitization has to replace the whole periphery of phosphatic phosphorite ; (b) fractured coprolites (Cop) showing siliceous matrix (Sil) disseminate in rims and sometimes at the center; (c, d) rounded to sub-rounded pellets with concentric structures (Pel) showing bone fragment and fossil nuclei; (e, f) elongated bone fragments (BF) with pellets within micro-sparitic to sparitic siliceous matrix (Sil), showing diffuse contours of the particles with the matrix.

IV. 2. Mineralogy

IV. 2. 1. X-ray diffraction (XRD) analysis

07 representative samples were selected from the Troubia, Ain Dibba, and Ain Kissa deposits for X-ray diffraction (XRD) analysis. This was performed using a Bruker two-circle machine, type D8 Advance, at the Laboratory of the Crystallography and Applied Thermodynamics, Faculty of Science, Tunis El Manar, Tunisia. XRD characteristics were: radiation source (CuKα1/α2) with a wavelength λ of 1,54060/1,54439Å (Iα1/Iα2=2), acceleration voltage of 35 kV. Measurements were recorded in the angular range of 5-70° (2θ). The diffraction data were interpreted using the X'pert HighScoreplus software package (PANalytical_2004) and PDF-2 (2019) database.

IV. 2.1. 1. Results

The XRD analytical results show that the phosphorites are mainly composed of a carbonate fluor-apatite (CFA), known as francolite, while calcite, dolomite, opal-CT are present as they constitute the matrix and /or cement of the phosphorite grains, as shown by petrographic observations (see Fig. IV. 22). Other minor accessory minerals, such as gypsum, detrital quartz and diagenetic zeolites (clinoptilolite-heulandite) are also detected. CFA with the generalized chemical formula: $(Ca, Na, Mg, Sr)_{10}$ $(PO_4, CO_3, SO_4)_6$ F_2 (e.g., McArthur et al., 1986) is also reported in Algerian-Tunisian phosphorites (Chabou-Mostefai, 1987; Bezzi et al., 2012; Garnit et al., 2012; Kechiched et al., 2020). Siliceous material as amorphous silica (opal-CT) are dominant in the lower and middle phosphorite layers of Ain Kissa and Troubia deposits, whereas gypsum is recorded in the upper layer of Ain Dibba phosphorites. Although the glauconite enrichment, observed in many samples through petrography and SEM techniques, this mineral was not detected by XRD and was not reported in any XRD data of the Algerian and Tunisian phosphorites, even in glauconite-rich types, probably because it is the result of

the glauconitization process which often produces structurally immature glauconite minerals (see Laouar et al., 2024).

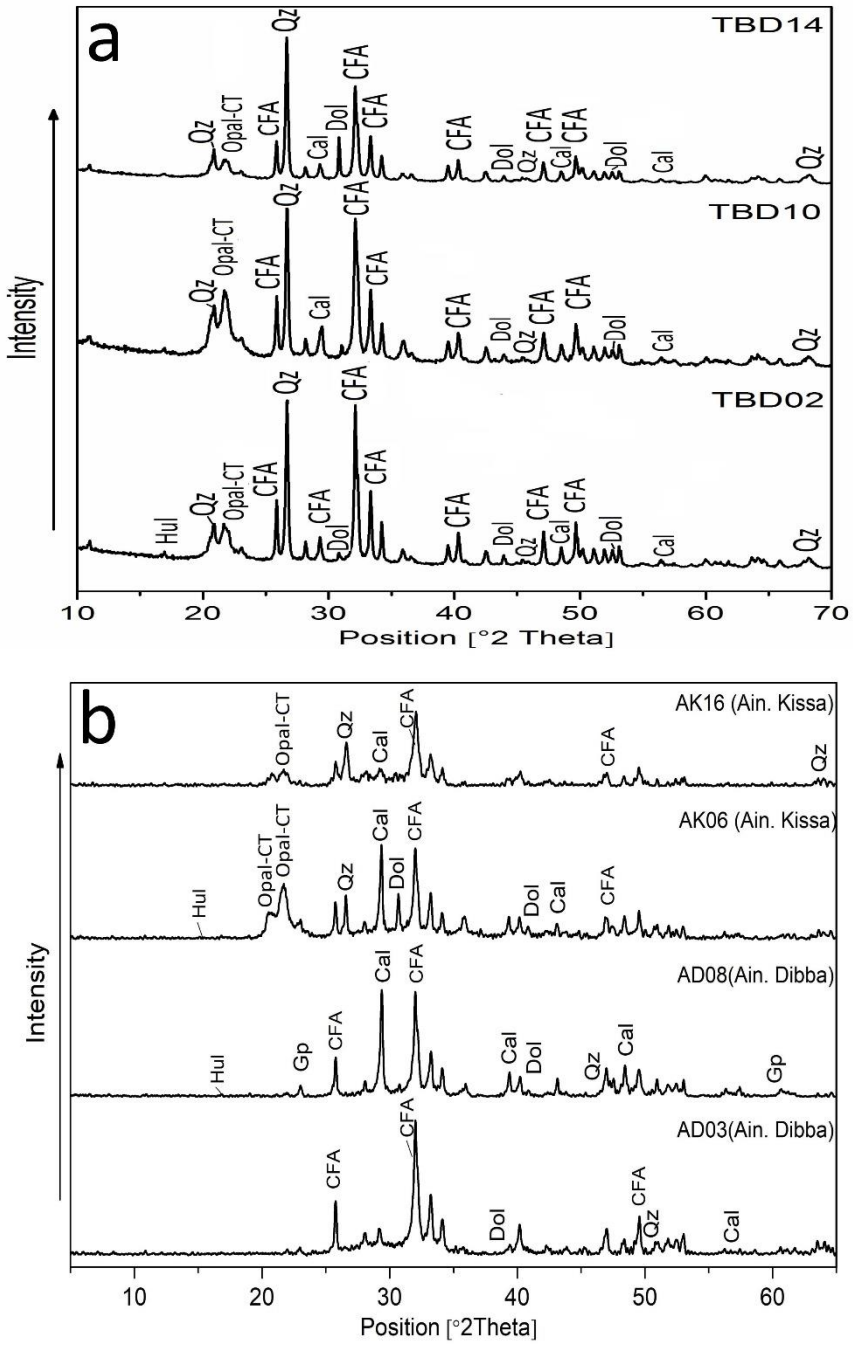

Fig. IV. 22. XRD patterns of phosphorite samples showing the mineralogical composition of studied phopshorites: carbonate fluor-apatite (CFA), dolomite (Dol), calcite (Cal), quartz (Qz), opal-CT, gypsum (Gp), zeolites (clinoptilolite-heulandite) (Hul).

IV.2.1.2. Interpretation and discussion

The investigated phosphorites from Troubia, Ain Dibba, and Ain Kissa deposits indicate that phosphorites are composed of CFA, Opal-CT, quartz, dolomite, and calcite, gypsum, and zeolites, similar to the majority of Algerian and Tunisian phosphorite composition (kechiched et al., 2020; Garnit et al., 2017). High silica content characterizes phosphorites that contain a large fraction of detrital quartz grains delivered from an adjacent continental terrigenous source (i.e., Ile Kasserine). In addition to the detrital-derived silica, a significant portion of the amorphous silica content (opal-CT) as matrix in the phosphorites, is likely attributed to upwelling processes that bring P and Si from the deep oceanic to surface water followed by sedimentation (e.g., Abed, 2013), or dissolved silica in the depositional environment, derived from seawater and pore water, as well as biogenic input from siliceous microfossils, mainly diatoms and radiolarians (Sassi 1974; Prévôt, 1988; Felhi 2010; Tlili et al., 2010, 2012; Maldonado et al., 2011; Henchiri and Fattah, 2013; El Haddi et al., 2014).

IV. 2. 2. Infrared spectroscopic analysis

In addition to XRD analysis, the mineral phases in the phosphorite samples were identified using representative data of Infrared spectrometry analysis (FTIR: Fourier Transform Infrared Spectroscopy) in powder samples. Representative phosphorites samples were also selected from the Troubia, Ain Dibba, and Ain Kissa deposits for Infrared spectrum analysis (FTIR). This was carried out at the laboratory of the Physical Department, Faculty of Sciences of Sfax, using a Two- FTIR Spectrometer, scanning with the frequency range of 4000-400 cm^{-1} of the electromagnetic spectrum.

IV. 2. 2. 1. Results

FTIR analysis reveals that the main bands are entirely attributable to the phosphate and carbonate components (PO_4^{3-} and PO_4^{2-}, CO_3^{2-} and OH groups; Fig. IV. 23a, b). The spectra are

dominated by four characteristic PO_4^{3-} absorption bands, observed in 1200–960 cm^{-1} and 600–450 cm^{-1} regions (e.g., 1200-400 cm^{-1}), which are typical of crystalline apatite. The symmetric stretching (ν_1) and bending (ν_2) modes of PO_4^{2-} are represented by weak singlet bands at 964 cm^{-1} and 472 cm^{-1}, respectively. Additionally, broader bands of higher intensity are attributed to the asymmetric stretching (ν_3) and bending (ν_4) modes of PO_4^{3-} and PO_4^{2-}, respectively. The ν_3 mode appears as a strong singlet band at 1030 cm^{-1}, while the relatively low-intensity ν_4 bending mode is represented by two main bands in the range of 565–605 cm^{-1} range. The presence of hydrogen phosphate ions (HPO_4^{2-}) in our IR spectra data is not very obvious in our IR spectra data due to their overlap with the ν_2 carbonate (CO_3^{2-}) bands and the broad shoulder centered around 1200 cm^{-1}, where HPO_4^{2-} vibrations are typically expected (1216–1222 cm^{-1}). Nevertheless, they can be identified by the weak absorption bands observed at 526 cm^{-1}, 798 cm^{-1}, and within the range of 1148–1090 cm^{-1}. In addition to the phosphate ion vibrations, the carbonate ions (CO_3^{2-}) may occur in two different environments, resulting from two types of carbonate substitution mechanisms. CO_3^{2-}ions can substitute for both OH^- (F^-, Cl^-) at the channel sites (A-type substitution), or they may replace phosphate ions (B-type substitution). These substitutions involve complex mechanisms of structural incorporation and charge compensation (Elliott, 1994). The IR spectra reveal a notable presence of carbonate ions (CO_3^{2-}), as evidenced by the strong absorption in the 1454–1425 cm^{-1} range (asymmetric stretching vibrations of CO_3^{2-}, V_3) and in the 866 cm^{-1} range (bending vibrations of CO_3^2, V_2).

These ν_3 and ν_2 vibrations are characteristic of carbonate groups occupying the B-type substitution site in the apatite structure, where carbonate ions replace phosphate groups (Fleet, 2009). The bands at 1635 and 866 cm^{-1} may indicate the presence of carbonate gangue, which appears more intense in these samples due to the abundance of carbonate minerals such as calcite and dolomite (El-Feki et al., 1991). The band at 1636 cm^{-1} corresponds to bending vibrations of H_2O, reflecting the presence of molecular water. The presence of calcite is

supported by a weak CO_3^{2-} absorption band at 713 cm^{-1}, which is attributed to the calcite ν_4 mode (Liu, 2002) and is consistent with samples that are enriched in calcareous cement.

On the other hand, the OH^- group (v(OH)) is characterized by absorption bands at significantly lower and higher wavenumbers. A distinct band at 649 cm^{-1} and a broad band at 3501 cm^{-1} are observed, both indicative of structural water and hydroxyl presence within apatite minerals, such as hydroxyapatite. The doublet at 800-780 cm^{-1}, which is related to the Si–O–Si bending vibrations, is attributed to amorphous silica and detrital quartz (Szilas et al., 2008).

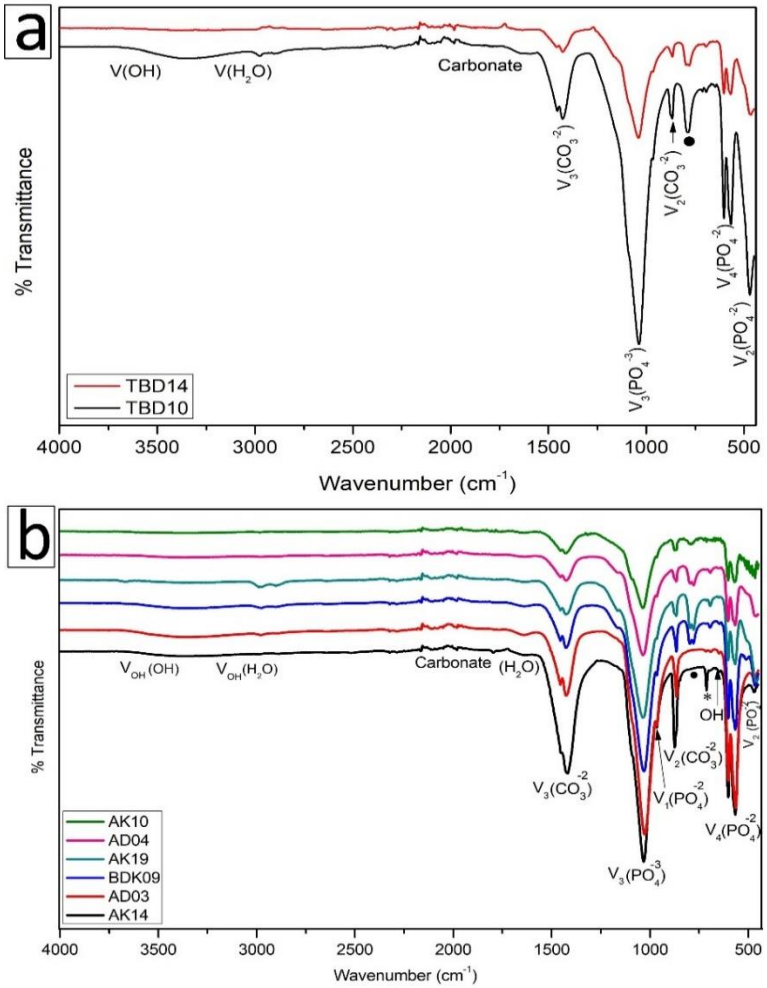

Fig. IV. 23. FT-IR spectrum of studied phosphorite in the region of 4000–400 cm−1. (*calcite V_4 band at 713 cm^{-1}; (•) quartz band).

IV. 2.2. 2. Interpretation and discussion

The infrared spectra characteristic of the studied phosphorites display distinct absorption bands corresponding to carbonate-fluorapatite (CFA), with high intensities of carbonate gangue (calcite and dolomite), indicating the presence of calcareous phosphorites. In contrast, the strongest silica intensities (amorphous silica as opal-CT siliceous cement) are recorded in cherty phosphorites. The peak at 1030 cm^{-1} is attributed to PO_4^{3-} stretching vibrations and exhibits the strongest intensity in phosphorite samples enriched in phosphatic particles such as coprolites, pellets, and bioclasts, in contrast to samples dominated by glauconites.

The presence of quartz (SiO_2) absorption bands is attributed to the reflected detrital input during the phosphorite deposition. The highest band intensities are observed in phosphorite samples with a high proportion of detrital quartz, glauconite minerals, and amorphous silica as opal- CT (siliceous matrix). Although the glauconite enrichment, was observed through petrography and SEM techniques, FTIR data do not clearly show the presence of (Fe^{3+}OH Fe^{3+}), (Si-O), and Al (Al OH Al) peaks. This may be related to the weak stage degree of maturation of the glauconites (weak glauconitization processes) in the phosphorite samples. This is consistent with our mineralogical results, as well as with reported (IR) data from Algerian-Tunisian phosphorites (e.g. Kolevaa and Petkova,2012, Elgharbi et al., 2014, Boumaza et al, 2021). These data are also similar to those reported for typical phosphate modes in synthetic and natural apatites: francolite (e.g. Gulbrandsen et al., 1966; LeGeros et al., 1967; Regnier et al., 1994; Antonakos et al., 2007).

IV. 2. 3. SEM and EDS observations

Scanning Electron Microscopy and Energy Dispersive Spectroscopy (SEM-EDS) analyses were performed on both selected polished sections, matrix and particle separates (pellets, coprolites, fish teeth, bone fragment and glauconite) to better show morphology, textural and semi-quantitative chemical compositions of these phosphatic particles. These

phosphatic particles (pellets, coprolites, fish teeth, bone fragment and glauconite) were separated from their matrix through sample crushing, wet sieving with distilled water and then washing thoroughly. They were then checked and separated using hand-picking techniques under a binocular microscope. Broken particles were also studied to determine their internal texture and composition. Polished sections were prepared and examined carefully under a metallographic microscope to investigate any variations in the texture and chemical composition characteristics within individual particles and in the matrix. The cherty phosphorite samples were sieved without pre-treatment to obtain sub-samples of grain size fractions: <45 μm. SEM-EDS analyses were carried out using a VEGA3 TESCAN SEM with an acceleration voltage of 20 kV and X-flash 6/10 detector for the energy dispersive spectroscopy analyses (EDS) at the Institute of Applied Science and Technology, University Larbi Ben M'hidi Oum El Bouaghi, Algeria. Some supplementary analyses were performed at the SEM-EDS laboratory, School of Mines, Annaba.

IV. 2. 3.1. Results

SEM and EDS techniques were performed on **particles separates** (pellets, coprolites, glauconite and fish teeth) to better show textural and semi-quantitative chemical compositions of these phosphoric particles. The results show that the pellets display rounded to sub-rounded shapes, with light phosphatic rims and dark cores, most likely due to the presence of organic matter (OM) (Fig. IV. 24a; yellow arrow). They also show a higher porosity than coprolites, which increases towards the particle rims (Fig. IV. 24a). Porosity, micro-cracks and fractures are also characteristics of all studied particles (Fig. IV. 24b, c, d, e). The surfaces of the particles showing a heterogeneous structure and have cavities with apatite crystals (Fig. IV. 24f). Apatite phases show hexagonal crystals that may contain inclusions of tiny quartz and dolomite crystals (Fig. IV. 24g, h, i, and j). Although pellets and coprolites differ in size and shape, their EDS analysis results often show enrichment in Ca, P and F, which have similar contents in both

particles. These elements, along with Al, exhibit also relatively high contents in bone fragments and the fish teeth (Fig. IV. 24f–k). However, the glauconites are rather enriched in Fe, Al, K, and Si, but are depleted in Ca, P and F when compared to phosphate particles (Fig. IV. 24g–k). Also, EDS results of the pellet, coprolite, and bioclast particles show an enrichment in P content which represented the apatite mineral, while other elements such as: Al, K, Fe, Si, and K are not homogeneous distributed, showing lower contents; reflects diagenetic processes during deposition and may be indicate the initial stages of glauconitization processes. However, the glauconites are rather enriched in Fe, Al, K, and Si elements, but are less enriched in in Ca, P when compared to phosphate particles, indicating that phosphatization process of fecal particles predates the glauconitization process.

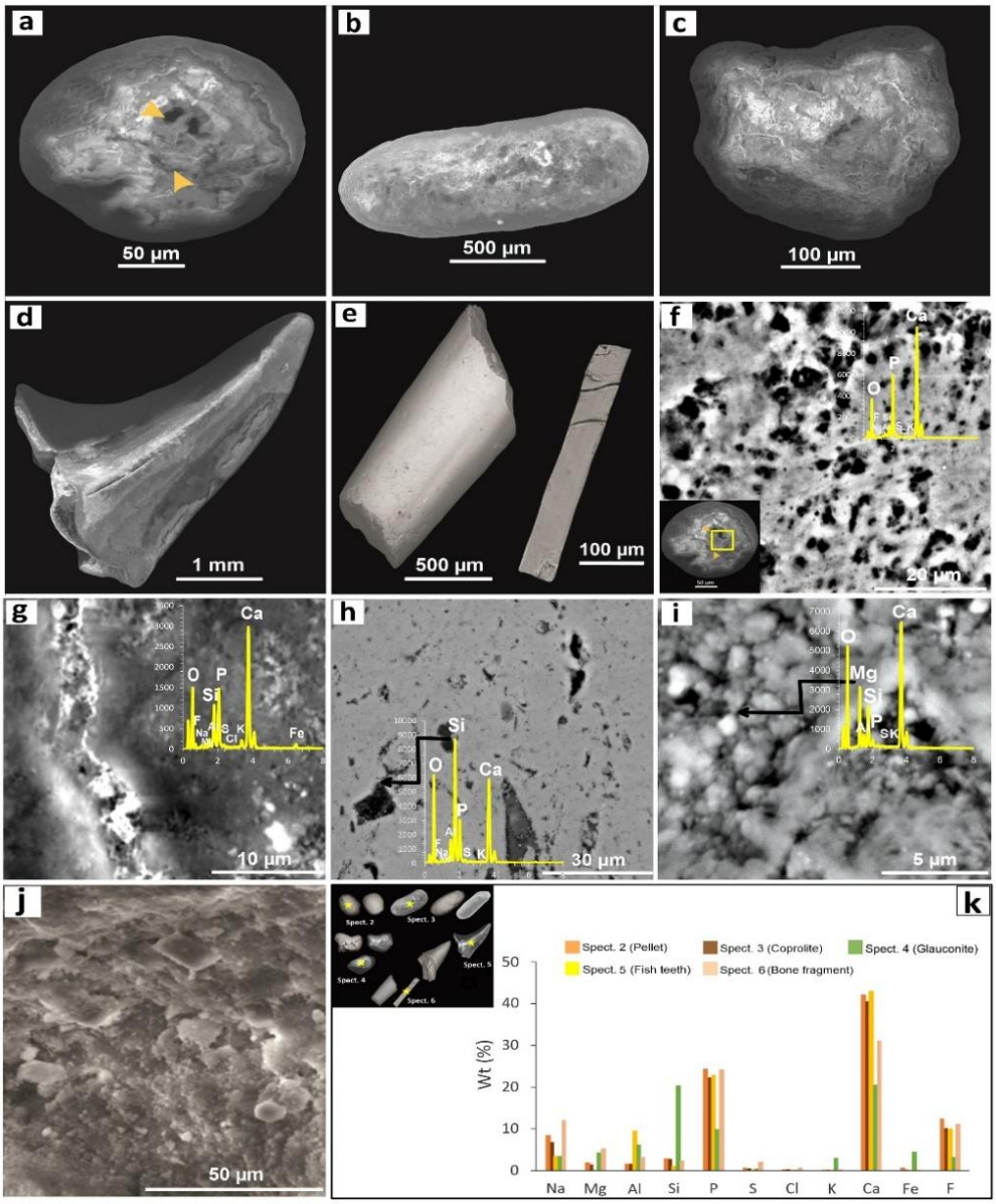

Fig. IV. 24. SEM images and EDS analytical data of phosphorite particles from Troubia, Ain Dibba, and Ain Kissa deposits. (a) pellet particle exhibiting a white rim and dark core (yellow arrows), with high internal porosity; (b, c, d, e) phosphatic particles: pellet (b), coprolite (c), tooth fish (d), and bone fragments (BF) with porous surfaces, microcracks and fractures; (f) The surfaces of the particles showing a heterogeneous structure, highly porous and have cavities with chemical composition of apatite mineral; (g, h) magnification of glauconite with chemical composition showing porous surface and quartz inclusion; (i, j) magnification of a pellet particle showing hexagonal apatite crystallites (~9 µm) and a dolomitic crystal inclusion; (k) SEM images of selected particles and EDS qualitative analysis showing Ca, P and F abundance in phosphate particles, Ca, P, F and Al enrichment in fish teeth and bone fragments, and Fe, Al, K, and Si enrichment in glauconite.

SEM and EDS techniques were also performed on ***polished sections.*** The sub-rounded to spherical pellets phosphatic particles are characterized by a homogeneous surface texture,

weak porosity, and the presence of dark patches distributed on their surface, embedded within a clayey-siliceous matrix (Fig. IV. 25a). They exhibit an internal structure characterized by the presence of pores and dark cavities surrounding the central porous structure, most likely due to the presence of organic matter (OM) (Fig. IV. 25b). The larger magnification image of the internal structure of the phosphatic particles (Fig. IV. 25c, d), observed through the pore shown in Fig. IV. 25b, reveals organic particles coated with phosphates and trapped within clusters of hexagonal apatite crystals (CFA). EDS analysis shows compositional variations: carbon (C) and oxygen (O) dominate in the pores and cavities, indicating an organic phase, while phosphorus (P) and calcium (Ca) prevail in surrounding areas, reflecting a apatitic phase (CFA). Organic matter (OM) is generally dispersed within the pellets either homogeneously distributed or concentrated in specific areas (Fig. IV. 25d), appearing as flat, broad particles (patches) or as small particles (~100 nm in size), often linked by organic bridges. These organic films are associated with the hexagonal apatite crystals within the phosphatic particles (CFA, Fig. IV. 25d).

Pellets particles are observed embedded within a siliceous matrix and associated with altered dolomite crystal (Fig. IV. 26a). The rhombohedral dolomite crystal inclusions within the phosphate particles indicate the development of dolomite during diagenetic processes, and their EDS qualitative analysis reveals elevated concentrations of: Mg, and Ca (Fig. IV. 26b). The rhombohedral dolomite crystal exhibits a variety of morphologies, which are often characterized by the presence of cavities, dark cores and grey rims, mostly related to de-dolomitization process (Fig. IV. 26c). At higher magnification, the internal structure of dolomite revealed may be the presence of rod-shaped bacterial forms resembling microorganisms associated with OM, with their EDS qualitative analysis reveals elevated concentrations of: C, and O (Fig. IV. 26d).

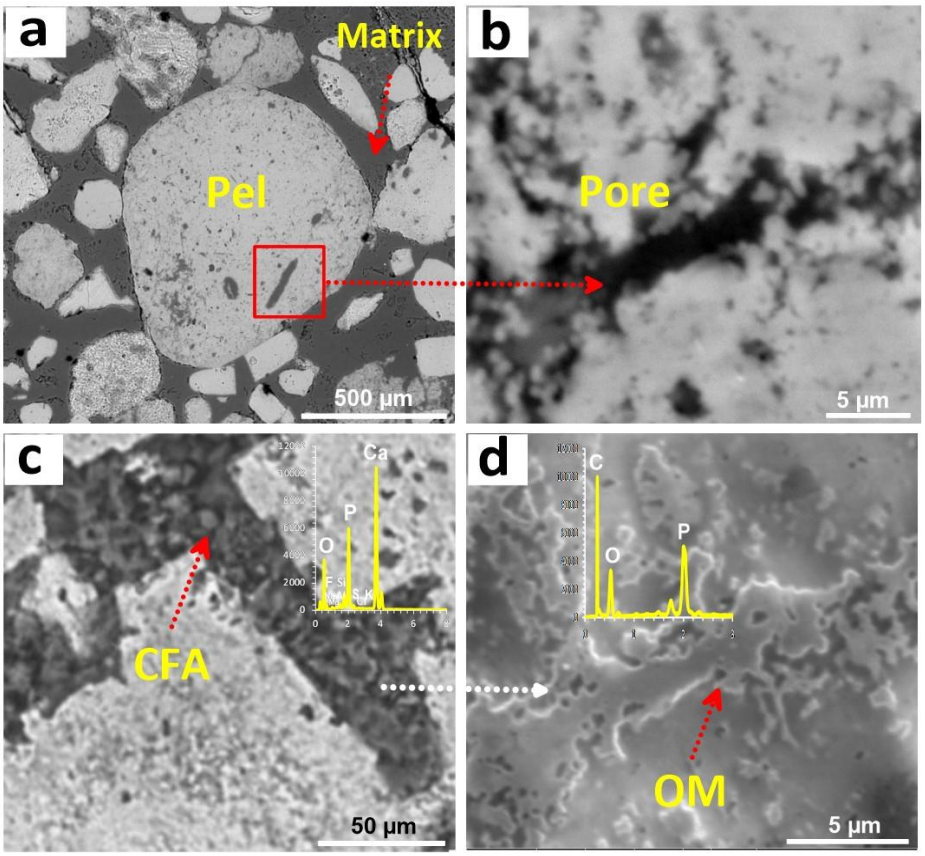

Fig. IV. 25. SEM images and EDS analytical data illustrating the internal structure of phosphorite particles from Troubia, Ain Dibba, and Ain Kissa deposits. (a) A spherical pellet particle (Pel) with a homogeneous surface structure, surrounded by a clayey-siliceous matrix, and exhibiting weak porosity; (b) an internal pore and dark bands within the pellet particles (Pel), corresponding to organic matter (OM); (c) larger magnification image of micro-cavity hosting hexagonal apatite crystals (CFA); (d) presence of organic matter (organic bridges) inside phosphate particles, with EDS qualitative analysis indicating abundant C and O; and associated with hexagonal apatite crystals (CFA).

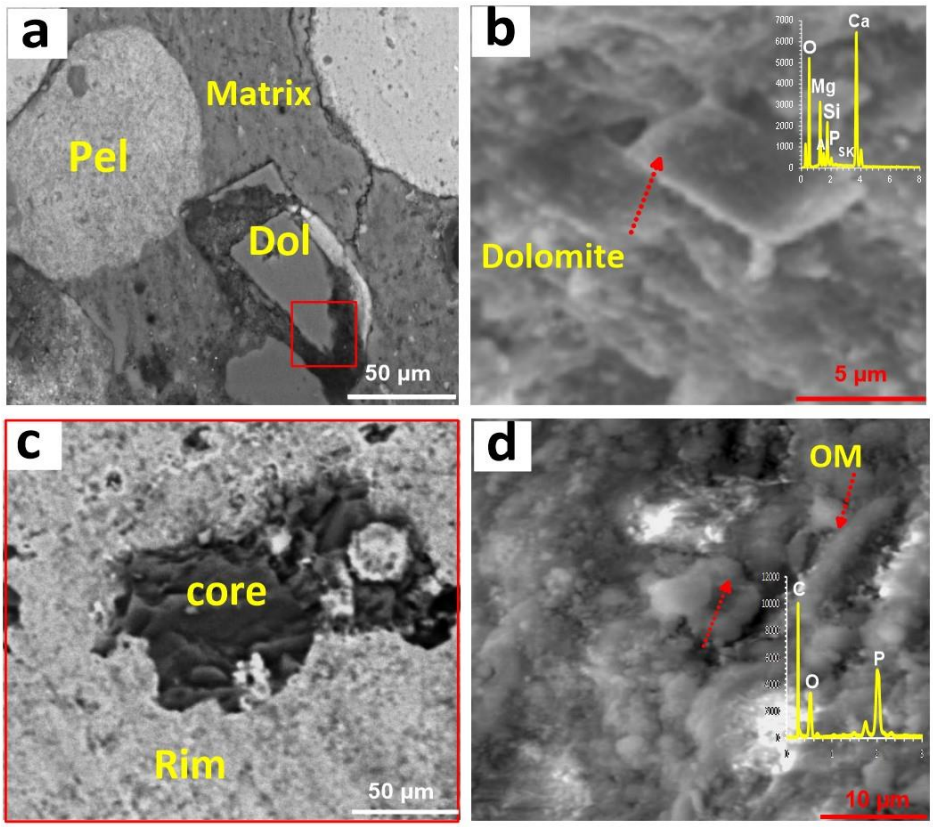

Fig. IV. 26. SEM images and EDS analytical data of cement surrounding the phosphatic particles from Troubia, Ain Dibba, and Ain Kissa deposits. (a) phosphatic particles (Pel) embedded within a siliceous matrix and associated rhombohedral dolomite crystals (Dol); (b) well crystallized- rhombohedral dolomite crystals (Dol) inclusions within the phosphate particles; (c) rhombohedral dolomite displaying a central cavity; (d) higher magnification of (c), showing micro-organisms hosted within the dolomite crystal, with EDS qualitative analysis indicating elevated C and O contents (OM).

In the upper layers, the studied phosphorites are mainly cemented by a siliceous matrix, forming cherty phosphorites. SEM analysis show that their matrix is composed by amorphous silica as spheres-shaped opal associated with dolomite crystal (yellow arrow, Fig. IV. 27a). This opal spheres are composed of cross silica fibers with about 4 µm length, and their EDX analysis show that they are mostly constituted of Si (Fig. IV. 27b). The zeolites crystal (clinoptilolite-heulandite) are also observed within cherty phosphorites (Fig. IV. 27c), and their EDX qualitative analysis showing an abundance Si, Al, Mg, Na, Ca and less K (Fig. IV. 27d).

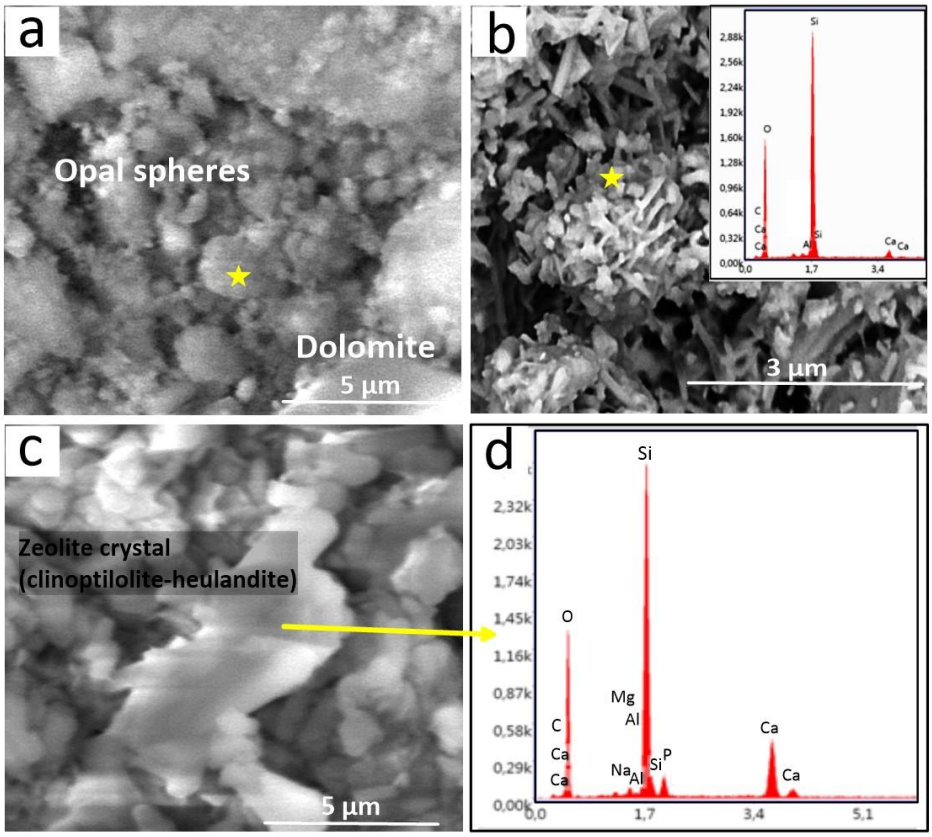

Fig. IV. 27. SEM images and EDS analytical data illustrating textural features of the matrix in cherty phosphorites from Troubia, Ain Dibba, and Ain Kissa deposits. (a) spheres Opal occurring on thin fibers (yellow arrow); (b) high-magnification SEM image of (a), with EDX microanalyses indicating that the spherical shape opal is mainly composed of Si element; (c) presence of zeolites crystal (clinoptilolite-heulandite) within cherty phosphorites, (d) EDX qualitative analysis showing an abundance Si, Al, Mg, Na, Ca and less K elements in zeolites crystal (clinoptilolite-heulandite).

IV. 2. 3. 2. Interpretation and discussion

The high porous structure, cracks, fractured and smooth surfaces of phosphatic particles may be related to burial, remobilization and transport from depth before deposition, sediment accumulation and compaction. This process allows chemical elements such as rare earth elements (REE) to become enriched through adsorption from seawater and pore water during early diagenesis (e.g., Reynard et al., 1999; Lecuyer et al., 2004). Silicification represented by opal-CT in the matrix of some phosphorites (cherty phosphorites) may originate from precipitation of dissolved silica, or incorporation of radiolarian tests, diatom frustules and siliceous algae in the depositional environment, causing upwelling processes which bring P and Si to surface water (e.g., Sassi, 1974; Henchiri, 2007; Ben Hassen et al., 2010; Felhi, 2010; Tlili

et al., 2010, 2012; Abed, 2013; Henchiri and Fattah, 2013; Kechiched et al., 2020). Dolomite inclusions within the phosphate particles indicate the development of dolomite during diagenetic processes, whereas zeolites can be derived from silica, especially in cherty phosphorites (Kechiched et al., 2020). The dolomite is observed with opal- CT determined that dolomitization is frequently associated with biogenic silica (Bernoullia and Gunzenhauser, 2001). The well-crystallized dolomite rhombs with developed crystal faces (euhedral dolomite crystals) is an indicator of in-situ growth during diagenesis with high MgO seawater (Henchiri, 2007). The presence of organic matter (OM) within phosphatic particles in studied phosphorites suggest an associated *organo-apatitic* composant during early diagenesis (Dassamiour et al., 2011; Ben Hassen et al., 2010).

The petrographic features and mineralogical assemblages of Troubia, Ain Dibba, and Ain Kissa phosphorites are summarized in Table IV. 1.

Conclusion

Petrographic data show that the phosphorites of Troubia, Ain Dibba, and Ain Kissa deposits are mainly composed of pellets, coprolites, bioclasts, rare glauconite, gypsum, and detrital quartz grains, which are cemented by calcareous, siliceous or rarely clayey matrix. XRD and FTIR data reveal that these phosphorites are composed of CFA, Opal-CT, quartz, dolomite, calcite, gypsum, and diagenetic zeolites (clinoptilolite-heulandite). The occurrence of siliceous materials is represented by an amorphous silica forming the matrix that surrounds the phosphatic particles (opal-CT), whereas the crystalline silica is represented by detrital quartz. The presence of organic matter (OM) within phosphatic particles in studied phosphorites suggest an associated *organo-apatitic* composant during early diagenesis. The development of dolomite can be attributed to high-MgO pore water.

Table IV.1. The petrographic features and mineralogical assemblages of Troubia, Ain Dibba, and Ain Kissa phosphorites.

Locality			Ain Dibba deposit		Ain Kissa deposit			Toubia deposit		Diagenetic conditions
Petrographic features										
Phosphatic particles			**Abundance (%)**	**Morphology**	**Shape**	**Size**	**Color**	**OM content**		**Diagenetic conditions**
Phosphatic particles (50 to 75% vol of the total rock)	Pellets	Without nuclei	30 to 40 % of the total particles	Polished and smooth, poorly sorted	Rounded, sub-rounded, spherical to oval	80 µm - 400 µm	Brown to yellowish	Trapped within pellets in the cores		High energy environment, high organic content, the inferred reworked origin, contact one with other, during reworking
		Nucleated (concentric structure)	10 to 20% of the total particles	Polished and smooth, poorly sorted	Spherical, oval or elongated depending the nature of nucleus (quartz grain or fossil and bone fragments	100 - 250 µm	Brown to dark	Surrounding the cores organic or inorganic as rimes		Multi-stage displacement during growth structures of pellet and highly agitated conditions
								Rare		
	Coprolites		30 % of the total particles	polished and smooth, heterogeneous,cracks and micro-inclusions.	Cylindrical, elliptical, elongated or irregular	250 µm to few millimeters	Whitish, brownish to dark	Dispersed irregular patches, often homogeneous in internal structure		Fragmentation of the coprolites by marine wave action and burial compaction; reworking processes. Dolomite growth during diagenesis
	Bioclasts (fish teeth and bone fragments)		10% of the total partilces	Cracks, fissured and micro-inclusions	Angular to subangular, prismatic or irregular	150 µm to 4 mm	Yellow to gray	Sometimes embedded within matrix rich on OM		High productivity environment, high energy environment, alteration process during early diagenesis conditions
	Glauconites		1% of the total particles, irregular shapes; green to light green color, 150 to 300 µm		3% of the total particles; irregular shapes, Greenish color,			4% of the total particles; irregular shapes, Greenish		Sub-reduced to sub-oxic environments with slow sedimentation rate
Non- Phosphatic minerals	Detrital quartz		3% of the total particles, angular to sub-angular shapes, colorless to pale gray, 60 to 100 µm in size					1% of the total particles, angular to sub-angular shapes, colorless to pale gray, 60 to 100 µm in size		Detrital inputs from the continental shelf,
	Gypsum		2% of the total particles		Rare					
Cements			Clayey (argillaceous), and/or siliceous matrix, calcitic matrix.		Calcareous matrix (dolomitic, calcitic) , siliceous matrix.			Dolomitic- siliceous matrix with rich in organic		Incorporation of radiolarian tests and siliceous algae, upwelling processes
Texture			Packstone to grainstone texture in a sparitic matrix							High energy and shallow depositional environment
Mineralogical assemblages										
Main mineralogical phases			Carbonate fluor-apatite (CFA)							
Accessory phases			Calcite, dolomite, quartz, gypsum, zeolites (clinoptilolite-heulandite)		Calcite, dolomite, quartz, opal-CT, zeolites (clinoptilolite-heulandite)					

Chapter V

Geochemistry of the Troubia, Ain Dibba and Ain Kissa phosphorites

Chapter V

Geochemistry of the Troubia, Ain Dibba and Ain Kissa phosphorites

The geochemical investigations of major, trace, and REE elements in Algerian sedimentary phosphorites have been extensively evoked recently across various scales, such as whole-rock, separate particles, matrix, grain-size fractions (e.g. Bezzi et al., 2012; Kechiched et al., 2018, 2020; Tahri et al., 2019; Dassamiour et al., 2021; Ferhaoui et al., 2022; Laouar et al., 2024; Aouachria et al., 2025). These previous geochemical investigations were mostly used to reconstruct paleoenvironment conditions of their deposition, and on other hand to highlight the P_2O_5, trace, and rare earth elements plus yttrium (REY) contents in phosphorite ores, thus assessing their economic potential. Besides, other studies were focused on the potentially hazardous elements (PHE) contents in phosphorite ores and their wastes across various sizes (Bezzi et al., 2012; Boumaza et al., 2021, 2023; Saouli et al., 2025), allowing for the evaluation of environmental impacts which pose environmental and health risks. These phosphorites deposits coincide well with the Paleocene-Eocene Thermal Maximum (PETM) and other pre-PETM excursions (Zachos et al., 2001; Ounis et al., 2008; Hessler et al., 2017; Kocsis et al., 2014; Buccione et al., 2021; Dong et al., 2024; Saouli et al., 2025), a period characterized by a warm and humid climate that increases the availability of organic matter deposition and biogenic activity, dissolved potentially hazardous elements (PHE) and REE ions in seawater, and pore water. On the other hand, the Paleocene-Eocene transition, which are attributed to Large Igneous Provinces as major driver (LIPs; Storey et al., 2007; Jones et al., 2019) played a critical role in recycling P and Si between the deep ocean and surface waters, most likely associated with nutrient-rich upwelling currents after OM burial in deep zones, associated with the PETM events.

From the previous geochemical data, high REE and some trace elements contents were recorded, mainly in the giant Bled El Hadba and Kef Essenoun deposits in the southern basin, and Dj. El Kouif phosphorites in the northern basin (Kechiched et al., 2016, 2020; Ferhaoui et al., 2022; Laouar et al., 2024). In-depth and comprehensive detailed geochemical studies on these phosphorites, it was shown that glauconite is the most REE-enriched mineral, with contents that may reach up to 2050 ppm among the phosphatized particles (pellets, coprolites and bioclasts) in southern basin (Kechiched et al., 2018; Laouar et al., 2024). However, the northern basin shows the ΣREE contents drop to 470 ppm at El Kouif and Djebel Dyr (Kechiched et al., 2020). From these studies, it was also believed that phosphorites of the southern basin were more enriched in REE because of their favorable paleo-environmental conditions to REE uptake from both seawater and pore-water reservoirs within reducing conditions during early diagenesis (Laouar et al., 2024). The Troubia, Ain Dibba, and Ain Kissa phosphorites, which are located at about 10 km north of the Tebessa town, have never been subject to detailed geochemical investigations in terms of P_2O_5 and REE contents.

The aim of this chapter is to present the detailed major, trace and REE geochemical investigations of the Troubia, Ain Dibba, and Ain Kissa deposits. The results were obtained through the preparation of whole rock samples using XRF and ICP-MS analyses. Although they are not yet economically very important in terms phosphorite reserves, the present geochemical study will contribute highly to the knowledge of their critical trace and REE contents, as well as to better understand their paleo-depositional environment. The comparison of the present data with those of the most economically significant North African phosphorite deposits located in the southern and northern basins of the Kasserine Paleo-Island (e.g. Kef Essenoun (Kechiched et al., 2018, 2020), Bled El Hadba (Laouar et al., 2024) in Algeria will provide insights into paleo-environmental factors set that contribute to the enrichments in both P_2O_5 and REE contents of these phosphorite.

V. 1. Sampling, analytical techniques and methods

In the analysis of major, trace, and rare earth elements, 23 phosphorite samples were selected from three different deposits: 7 from the Troubia deposit, 8 from Ain Dibba (including 4 samples from the studied geological section shown in chapter II, Fig. II. 6 and Fig. II. 18, and another 4 samples from the exploitation tailings at ~1 km to the west of the studied section), and 8 samples from the Ain Kissa deposit (cf. chapter II, Fig. II. 33). 13 whole-rock samples were analyzed using X-Ray Fluorescence method at the Mineralogical Laboratory within the Faculty of Sciences at Sfax University, while 10 samples were examined using an ICP-MS at University of Montpellier, France. The XRF analytical method used a ThermoScientific device Niton FXL FM-XRF analyzer with a 50 kV, 200 μA x-ray tube and a CDD GOLDD drift detector technology. This generates fast and reliable elemental results (1–3 min/sample) using mining program, which allows the analysis of 38 major and trace elements (Sb, Sn, Cd, Ag, Mo, Nb, Th, Zr, Y, Sr, U, Rb, Bi, As, Au, Se, Hg, Ga, Pb, W, Zn, Cu, Ni, Co, Fe, Mn, Cr, V, Ti, Ca, K, Ba, Al, P, Si, Cl, S, Mg). The samples were finely ground and then steamed at 50 ◦C overnight. The powder was, then, recovered in the plastic XRF double-ended cup (diameter 32 mm), the one end was previously covered by a thin exchangeable Polypropylene film TF-240-255. Moroccan and Tunisian phosphate standards were used for the calibration of major elements, especially phosphorus and calcium. For ICP-MS analytical method, an Inductively Coupled Plasma Mass Spectrometer (Agilent 7700x ICP-MS) was used at the ICP-MS Laboratory, Plateforme AETE-ISO, OSU OREME, University of Montpellier, France. Whole-rock samples were powdered using an agate mortar, and about 50 mg of each sample were dissolved twice in a mixture of hydrofluoric acid (0.5 m HF) and nitric acid (1 ml HNO3) on a hot plate at 110 ◦C for 48h. After dissolution, the solution was evaporated to dryness and diluted shortly before analysis in HNO3 2%. The overall analytical reproducibility of internal laboratory standards (BEN, UBN and ACI), based on repeated analyses is better than ±5%.

Principal Component Analysis (PCA) was applied to interpret the relationship between the analyzed elements and to determine the associations of both variables and individuals. In this PCA, samples with missing variables were removed prior to the treatment. This analysis was carried out using XLSTAT software (Addinsoft, 2021).

V. 2. Results and interpretation

The whole-rock chemical analysis results for the phosphorite samples from the Troubia, Ain Dibba, and Ain Kissa deposits are presented in Tables V.1 and V. 2 for major elements, and in Tables V3 and V4 for trace elements. The rare earth element (REE) data from both Ain Dibba and Ain Kissa deposits are listed in Table V. 5. The compiled dataset is provided separately in Appendices 1 and 2, and is presented as Supplementary Material 1 and 2.

Geochemical data have revealed significant variations in the concentrations of major, trace, and REEs elements across all deposits. The distribution of major, trace, and rare earth elements (REE) in phosphorite are controlled by many factors, including the abundance of phosphatic particles, the nature of the matrix/cement, the presence of glauconite minerals, and the paleogeographic/paleoenvironmental conditions. PAAS-normalized geochemical data of trace elements of samples from studied phosphorites according to Taylor and McLennan, (1985), are compared to the average values of global phosphorites (Li, 2000).

V. 2. 1. Major elements

The major oxides composition of the phosphorite samples from Troubia, Ain Dibba, and Ain Kissa deposits are generally dominated by high CaO, P_2O_5, and SiO_2 contents. MgO, Na_2O and SO_3 are less abundant elements, while the Fe_2O_{3t}, Al_2O_3, K_2O and TiO_2 concentrations are generally very low (<1%). These data are supported by petrographic observations and whole-rock XRD data analyzed, which indicate that carbonate fluorapatite (CFA) is the main mineral of phosphorite, while the gangue minerals are mainly dolomite, quartz, glauconite, and calcite.

CaO contents range from 27.61 to 54.96 wt.% across the studied phosphorite samples. CaO is a most abundant element in the analyzed phosphorite samples since it occurs in multiple mineral phases, primarily carbonate fluorapatite (CFA) minerals and calcareous cement. The highest values are, therefore, only reported in samples where the matrix is composed mainly of calcite, which might be a phosphatic limestone. However, Troubia phosphorites exhibit the lowest CaO contents among the studied deposits, ranging from 28.55 wt.% to 33.40 wt.%, which likely reflects a lower proportion of calcareous cement. Additionally, the CaO contents are similar to those of many phosphorite deposits of North Africa and Middle-East (e.g., Laouar et al., 2024; Buccione et al., 2021; Kechiched et al., 2020). Moroccan and Egyptian phosphorites display the lowest CaO contents (39.94 wt% and 40.15 wt%, respectively; El Bamiki et al., 2023; El-Shazly et al., 2022), whereas Turkish and Saudi Arabian samples show the highest CaO averages (53.00 wt% and 51.75 wt%, respectively; Gundogar and Sasmaz, 2022; Ahmed et al., 2022).

Table V. 1. Major elements contents of whole-rock phosphorites from Troubia deposit.

Troubia							
Sample	23tbd02	23tbd10	23tbd14	23tbd15	23tbd16	23tbd17	23tbd22
Major oxides (wt%)							
SiO_2	36.37	42.13	37.04	41.89	31.68	26.93	44.13
TiO_2	0.02	0.04	0.03	0.01	0.01	0.01	0.01
Al_2O_3	0.4	0.45	0.13	0.15	0.1	0.09	0.07
Fe_2O_{3t}	0.1	0.13	0.06	0.02	0.05	0.04	0.04
MgO	0.1	0.33	1.51	0.15	0.2	0.18	1.39
Ca0	30.66	28.59	30.97	28.59	30.48	33.4	28.55
K_20	0.06	0.07	0.04	0.01	0.01	0.01	0.02
P_20_5	20.79	18.59	20.05	18.59	22.66	24.8	18.39
SO_3	1.23	0.98	1.26	1.33	1.81	1.8	1.18
LOI	8.21	6.1	7.8	6.9	11.1	9.95	4.5
CaO/P_2O_5	1.47	1.54	1.54	1.54	1.35	1.35	1.55

Table V. 2. Major elements contents of whole-rock phosphorites from Ain Dibba and Ain Kissa deposits.

Ain Dibba										**Ain Kissa**							
Sample	21add03	21add04	21add06	21add08	21bkdd09	21bkdd11	21bdkd14	21bkdd23		21akd06	21akd10	21akd11	21akd14	21akd15	21akd16	21akd18	21akd19
Major oxides (wt%)																	
SiO_2	1.72	37	1.34	0.83	22.86	0.71	1.22	26.85		38.55	14.32	2.21	0.55	28.55	33.81	2.36	32.19
TiO_2	0.02	0.01	0.01	0.01	0.01	n.a.	0.02	0.01		0.07	0.05	0.02	0.01	n.a.	0.03	0.02	0.02
Al_2O_3	n.a.	0.18	0.21	0.14	0.16	0.17	0.16	0.17		1.11	0.97	0.22	0.08	0.23	0.42	0.2	0.26
Fe_2O_{3t}	0.12	0.18	0.16	0.1	0.14	0.1	0.14	0.14		0.4	0.4	0.13	0.04	0.03	0.29	0.13	0.12
MgO	1.2	0.59	n.a.	1.54	0.35	n.a.	0.5	0.41		1.43	1.47	2.99	0.45	1.42	0.43	0.6	0.64
CaO	51.59	33.11	54.72	50.41	39.96	54.96	50.91	37.97		30.01	42.96	51.99	51.46	31.87	33.68	50.66	27.61
MnO	n.a.	0	n.a.	0	0	n.a.	0.01	0		0	0	n.a.	0	n.a.	0	0	n.a.
Na_2O	n.a.	0.82	n.a.	1.17	0.94	n.a.	0.89	0.75		0.69	0.94	n.a.	0.77	n.a.	0.78	0.54	n.a.
K_2O	0.04	0.06	0.02	0.04	0.06	0.03	0.05	0.05		0.15	0.16	0.08	0.03	0.01	0.07	0.05	0.05
P_2O_5	31.89	19.02	16.76	23.07	24.36	23.18	20.7	22.48		14.16	23.52	20	24.14	21.17	20.19	15.02	19.27
SO_3	1.82	n.a.	0.91	n.a.	n.a.	1.38	n.a.	n.a.		n.a.	n.a.	1.44	n.a.	1.46	n.a.	n.a.	1.04
LOI	10.52	7.93	22.2	18.74	7.94	14.45	20.22	7.83		11.42	11.82	18.3.	16.4	9.62.	7.42	26.51	12.22
CaO/P_2O_5	1.62	1.74	3.27	2.19	1.64	2.37	2.46	1.69		2.12	1.83	2.6	2.13	1.51	1.67	3.37	1.43

n.a.: Not analyzed.

P_2O_5, the second most abundant oxide, shows similar content across all phosphorites deposits ranging from 14.16 to 24.8 wt%; only one sample from Ain Dibba deposit that shows the highest value of 31.89 wt%. This is most likely due to that P_2O_5 is the main components of apatite (CFA) in phosphatic particles (pellets, coprolites and bioclasts) as confirmed by the whole-rock XRD data analysis (cf. Fig. IV. 22; Chapter IV). CaO/ P_2O_5 ratios (ranging from 1.43 to 3.37) are similar to those of many phosphorite deposits of North Africa (Buccione et al., 2021) and in the northern deposits where Kechiched et al. (2020) recorded values ranging from 1.4 to 2.7. However, they are, therefore, lower compared to the those of the southern deposits of the Bled El Hadba phosphorites (Laouar et al., 2024). Conversely, the CaO/ P_2O_5 ratios in Troubia deposit appears to be lower (ranging from 1.35 to 1.54) than phosphorites that reported from Ain Dibba, Ain Kissa, and Kef Essenoun deposits, may be related to enriched of phosphatic particles (Kechiched et al., 2020). A plot of CaO against P_2O_5 contents for the phosphorites deposits (Fig. V. 1a) reveals a weak positive and non-significant correlation (r = 0.29, p = 0.28). This indicates that CaO contents are distributed between both CFA minerals in phosphate particles and the calcareous matrix (calcite and dolomite), whereas P_2O_5 exists only in phosphatic particles. Similarity, MgO contents ranging from 0.1 to 2.99 wt% show neither a strong positive nor a significant correlation with CaO contents (r = 0.33, p = 0.41; Fig. V. 1b), because MgO contents are a major constituent of the matrix only (dolomitic matrix). Na_2O content is generally low in all samples ranging from 0.54 to 1.17 wt%, showing a strong positive correlation with P_2O_5 (r = 0.68, p = 0.03) as shown in Fig. V. 1c. This is indicated by the substitution of Na for Ca in the CFA structure (McClellan and Kauvenbergh, 1990). SiO_2 shows high contents reaching up to 37 wt% in Ain Dibba and 38.55 wt% in Ain Kissa deposit, reflecting the observed cherty phosphorite rocks (siliceous matrix). These elevated silica contents are most likely attributed to amorphous siliceous matrix, primarily composed of Opal-CT as confirmed by the whole-rock XRD data analysis (cf. Fig. IV. 22; Chapter IV). In

addition, the highest SiO_2 contents are observed in phosphorite samples containing a high proportion of detrital quartz, reflecting significant terrigenous input from continental weathering during the time of phosphorite deposition. However, the lowest SiO_2 contents (0.71 wt% at Ain Dibba and 0.55 wt% at Ai Kissa) are recorded in calcareous phosphorites. In contrast, SiO_2 contents are enriched across all studied samples of Troubia phosphorites, ranging from 31.68 wt % to 44.13 wt %. It is noteworthy that the phosphorites here are more siliceous than Ain Dibba and Ain Kissa deposits, representing cherty phosphorites with a silica matrix as shown in Chapter IV. A plot of P_2O_5 against SiO_2 contents for the phosphorite deposits (Fig. V1d) show negative correlation in Ain Dibba and Ain Kissa deposits (r = -0.33), and strong negative correlation in Troubia deposit (r = -0.99). It allows for the distinction of two populations (see also Tabs V2 and V3): phosphorites with silica matrix are represented by SiO_2 contents greater than 10 wt%, and phosphorites exhibiting content lower than 3% wt% represent phosphorites with calcareous matrix. P_2O_5 contents are negatively correlated with both populations. The occurrence and deposition of amorphous silica (opal-CT) as a matrix of some phosphorite layers most likely originated from upwelling processes which are believed to be the cause of recycled P and Si between the deep oceanic reservoir and surface water followed by sedimentation (e.g., Abed, 2013), or as supported by incorporation of radiolarians tests, siliceous algae and diatoms or the precipitation of dissolved silica in the depositional environment, giving cherty phosphorites (Ben Hassen et al., 2010; Henchiri, 2007; Maldonado et al., 2011; Prévot, 1988). Notably, the global Large Igneous Provinces (LIPs; Storey et al., 2007; Jones et al., 2016) that provoked climate change at the Paleocene-Eocene Thermal Maximum (PETM) as suggested by Zachos et al. (2001), Ounis et al. (2008), Garnit et al. (2017) and Kechiched et al. (2020), played a critical role in recycling P and Si between the deep ocean and surface waters. This is most likely associated with upwelling of nutrient-rich waters after OM burial in deep zones during the PETM event. The highest MgO contents (up to 2.99 wt%)

are recorded in samples showing the lowest SiO_2 concentrations; and this is related to the dolomitic nature of the phosphorite particle matrix .The SO_3 contents, ranging from 0.91 wt% to 1.82 wt%, are most probably attributed to the presence of traces of gypsum in the matrix of some samples, which is consistent with mineralogical data (cf. Fig. IV. 22).

The other oxides, such as MnO, TiO_2, K_2O, Fe_2O_{3t} and Al_2O_3 display low contents with an average less than 1 wt% each, whereas the highest contents are recorded in the lower layer of the Troubia phosphorite rocks and Ain Kissa phosphorites (Tabls V. 2 and V. 3). The high contents of these elements are mostly related to a high proportion of glauconite minerals in these phosphorite layers, with the formula $(K_{0.79}\ Ca_{0.05}\ (Al_{0.35}\ Fe_{1.06}\ ^{3+}Fe_{0.25}\ ^{2+}\ Mg_{0.41})\ (Si_{3.61}\ Al_{0.39})\ O_{10}(OH)_2$ as given by McRae (1972). This result is supported by the slightly negative correlated between the P_2O_5 and SiO_2, Fe_2O_3 and Al_2O_3 (see Tabs V. 2 and V3. Fig. V. 1d, e, f), whereas Al_2O_3 exhibits a strong positive correlation with Fe_2O_3 ($r = 0.91$, $p < 0.01$), and K_2O ($r = 0.91$, $p < 0.01$; Fig. V. 1g and h). As suggested by Laouar et al. (2024) and Kechiched et al. (2018), the high contents of these elements are recorded in glauconite-rich phosphorites of Djebl El Kouif, Kef Essenoun and Bled El Hadba deposits, indicating the effect of glauconitization process that these phosphorites may have undergone during early diagenesis.

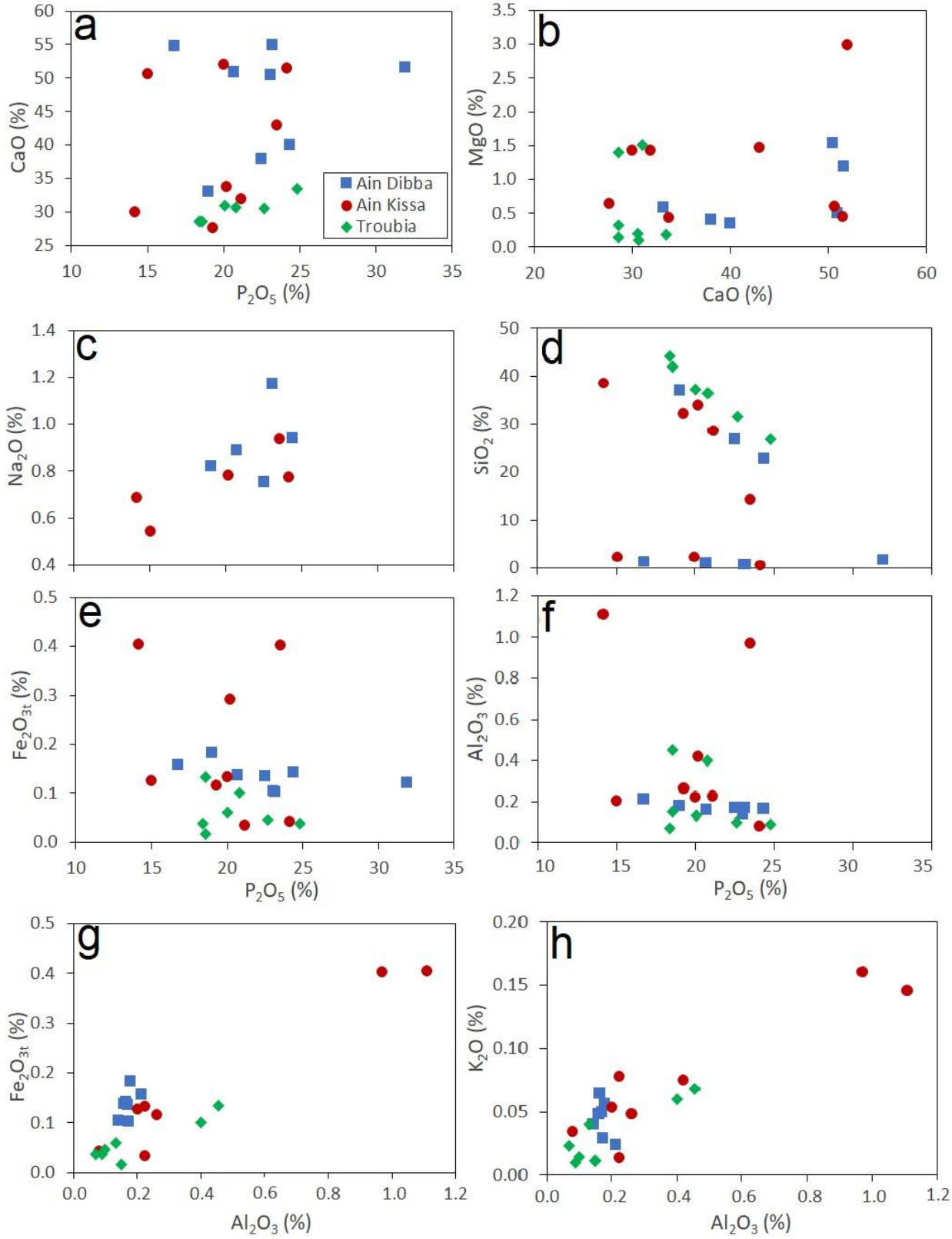

Fig. V. 1. Major element variation diagrams of Ain Dibba, Ain Kissa and Troubia phosphorites. (a): P_2O_5 against CaO; (b): CaO vs. MgO; (c, d, e, f): P_2O_5 vs. Na_2O, SiO_2, Fe_2O_{3t} and Al_2O_3 respectively; (g, h) Al_2O_3 vs. Fe_2O_{3t} and K_2O respectively.

V. 2. 2. Trace elements

Based on the geochemical data of the studied phosphorites (see Tables V. 3 and V. 4), among the analyzed trace elements, Sr shows the highest concentrations, with contents in the range 1206–2438 ppm. This is followed by three groups of elements: The first group consists of Cr and Zn with relatively high concentrations (~200 ppm). The second group comprises Ba, V, Zr, U, Ni, and Cu with concentrations in the range 10–100 ppm each; and the third group, composed of Th, As, Co, Mo, Rb, Nb, Sc and Hf, shows relatively low concentrations. The variation of trace elements is closely linked with the petrography of the studied samples (see Chapter IV).

Table V. 3. Trace elements contents of whole-rock phosphorites from Troubia deposit.

Troubia							
Sample	23tbd02	23tbd10	23tbd14	23tbd15	23tbd16	23tbd17	23tbd22
Trace elements (ppm)							
As	6.2	5.51	6.35	5.42	8.84	6.16	6.23
Zr	31.09	32.48	28.63	31.09	31.04	27.81	30.39
Y	69.07	68.09	79.01	78.08	145.2	131.22	90.19
Sr	1433.15	1263.31	1401.86	1396.42	1366.45	1329.7	1373.72
U	41.44	42.86	44.75	58.44	69.77	80.52	53.86
Zn	49.77	108.94	142.29	199.28	42.71	66.31	124.47
Cr	68.44	83.09	50.74	56.98	88.21	68.87	74.95
V	5	35.22	27.34	42.48	50.83	47.98	42.09
Cr/V	13.69	2.36	1.86	1.34	1.74	1.44	1.78

Table V. 4. Trace elements contents of whole-rock phosphorites from Ain Dibba and Ain Kissa deposits.

Ain Dibba										**Ain Kissa**							
Sample	21add03	21add04	21add06	21add08	21bkdd09	21bkdd11	21bdkd14	21bkdd23		21akd06	21akd10	21akd11	21akd14	21akd15	21akd16	21akd18	21akd19
Trace elements (ppm)																	
Zr	52.42	10.44	27.84	12.23	13.39	37.81	16.67	13.78		24.37	27.3	38.76	17.48	35.34	16.91	9.33	25.9
Y	176.66	141.22	113.44	176.8	168.26	111.59	259.57	176.35		120.27	234.37	150.32	278.81	154.39	195.41	80.27	68.68
Sr	2437.77	1797.25	1406.25	2148.46	1849.84	1729.09	1746.14	1781.29		1366.19	1968.45	1517.87	2049.42	1340.76	1775.29	1439.8	1206.49
U	110.25	63.11	61.96	76.54	106.51	95.04	94.71	99.46		28.13	60.48	73	102.8	71.73	78.94	52.75	60.49
Zn	54.18	63.43	41.21	57.04	61.66	37.11	108.1	82.81		137.05	150.42	86.49	97.35	77.78	102.78	61.51	62.06
Cr	163.94	137.25	116.57	167.53	146.6	101.31	186.27	142.43		178.93	207.41	108.26	213.9	80.31	144.75	114.82	76.33
V	91.07	107.7	61.24	110.46	84.35	62.67	105.78	63.39		87.8	89.83	83.5	118.44	61.4	113.21	104.87	87.24
Rb	n.a.	0.96	n.a.	1.03	0.95	n.a.	0.87	0.97		5.35	4.44	n.a.	0.5	n.a.	2.59	1.49	n.a.
Nb	n.a.	0.36	n.a.	0.36	0.44	n.a.	0.44	0.42		2.59	1.92	n.a.	0.24	n.a.	0.76	0.55	n.a.
Hf	n.a.	0.17	n.a.	0.19	0.22	n.a.	0.29	0.21		0.56	0.58	n.a.	0.28	n.a.	0.3	0.16	n.a.
Ta	n.a.	0.03	n.a.	0.03	0.04	n.a.	0.05	0.04		0.2	0.16	n.a.	0.04	n.a.	0.07	0.04	n.a.
Th	n.a.	1.38	n.a.	1.7	1.66	n.a.	2.16	1.73		1.46	2.83	n.a.	1.76	n.a.	2.13	0.67	n.a.
Sc	n.a.	1.73	n.a.	2.21	2.5	n.a.	5.58	2.39		4.31	6.79	n.a.	5.69	n.a.	2.75	1.27	n.a.
Ba	n.a.	176	n.a.	88.97	144.65	n.a.	48.49	91.09		50.33	61.19	n.a.	57.77	n.a.	76.6	47.88	n.a.
Co	n.a.	0.51	n.a.	0.4	0.4	n.a.	0.17	0.42		0.32	0.3	n.a.	0.18	n.a.	0.46	0.24	n.a.
Ni	n.a.	14.96	n.a.	12.24	15.16	n.a.	19.92	15.92		28.51	29.73	n.a.	17.2	n.a.	23.05	10.9	n.a.
Cu	n.a.	8.27	n.a.	6.21	14.46	n.a.	13.61	40.47		21.76	22.46	n.a.	15.79	n.a.	26.59	11.56	n.a.
Cr/ V	1.8	1.27	1.9	1.52	1.74	1.62	1.76	2.25		2.04	2.31	1.3	1.81	1.31	1.28	1.09	0.87

n.a.: Not analyzed.

Sr contents range from 1263 to 1433 ppm in Troubia and from 1406 ppm to 2438 ppm in Ain Dibba phosphorites, whereas, the Ain Kissa phosphorites shows contents ranging from 1206 to 2049 ppm (see Tables V. 3 and V. 4). The highest Sr contents are recorded in Ain Dibba phosphorites (up to 2438 ppm), and the lowest contents are recorded in Ain Kissa and Troubia deposits (down to 1206 ppm; and 1263 ppm, respectively*).* The Sr contents are enhanced in phosphorite samples that show high P_2O_5 contents (see Tables V. 3 and V. 4). Cr is the second most trace elements recorded in studied phosphorites with contents ranging from 101.3 to 167 ppm in Ain Dibba deposit, and from 108 to 213 ppm in Ain Kissa deposit. However, the lowest Cr contents are observed in two samples from Ain Kissa phosphorites and in Troubia phosphorites (80.3 and 76.3 ppm, and 51 to 88 ppm; respectively*).* Zn contents range from 37.1 to 150.4 ppm in Ain Dibba and Ain Kissa phosphorites; the highest contents are recorded in Troubia phosphorites, reaching up to 199.0 ppm. V contents range from 61.2 to 118.4 ppm, with an average of 89.6 ppm, whereas the highest contents are recorded in the samples from the upper phosphorite layers of both deposits. However, Troubia phosphorites show the lowest V contents ranging from 5 to 51 ppm. U displays relatively high contents ranging from 41 to 110 ppm. The lowest values (28 ppm) are, therefore, only reported in samples from the lower phosphorite layer, which might be a marly phosphatic. Other trace elements analyzed including: Ba, Zr, Ni, and Cu show contents ranging from 10 to 100 ppm each, whereas As, Th, Co, Mo, Rb, Nb, Sc and Hf show the lowest contents (<10 ppm each). It is noteworthy that in the investigated phosphorites, the high Sr, Ba, and U contents are recorded in Ain Dibba phosphorites, while the high Cr, V, Zn, Zr, As, Th, Co, Mo, Rb, Nb, Sc and Hf contents are generally recorded in glauconite-rich samples and clayey matrix of Ain Kissa phosphorites. Unlike Ain Dibba and Ain Kissa phosphorites, samples from the Troubia deposit show low contents of all trace elements (see Table V. 3).

The carbonate-fluorapatite (francolite) has the capacity to absorb several elements that can substitute for Ca (ionic radius 0.99 Å), such as monovalent (Na^{+}, K^{+}), divalent (Sr^{2+}, Pb^{2+}, Ba^{2+}, Mn^{2+}, Cd^{2+}), trivalent (REE^{3+}), tetravalent (Ce^{4+}, Th^{4+}, U^{4+}) elements, as well as hexavalent (U^{6+}) cation. It has been established that some oxo-anions such as VO_4, As_2O_4, SO_2, SO_4 and CO_3 can be substituted into PO_4 structure in apatite group lattices (e.g., Bonnot-Courtois and Fleoteaux, 1989; Emsbo et al., 2015; Ilyin, 1998; Luo et al., 2009; Pan and Fleet, 2002; Provet and Lucas, 1980; Rakovan and Hughes, 2000; Tzifas et al., 2014; Zhu and Jiang, 2017). However, some trace elements such as: V, Cr, Zn and Cd may be adsorbed onto crystal surfaces or may be incorporated into other minerals, such as glauconite and other clay minerals, Fe-Mn oxyhydroxides, and organic matter (e.g., Abed et al., 2016; Belayouni et al., 1982; Hein et al., 2016; Jiang et al., 2007; Liu and Zhou, 2017; Laouar et al., 2024).

Sr, Cr, and V exhibit notable enrichment when compared to the average concentrations found in global phosphorites (Li, 2000). Strontium (Sr) shows the highest concentrations, reaching up to 2438 ppm. This is consistent with previously reported values for marine phosphorites, which typically range from 1200 to 2400 ppm, with an average of approximately 1900 ppm (Tooms et al., 1969). The elevated Sr contents observed in the Ain Dibba and Ain Kissa phosphorites are similar to the findings from other Algerian deposits located in both the northern and southern basins (Kechiched et al., 2018, 2020; Laouar et al., 2024). The ability of Sr^{2+} (ionic radius r = 1.12 Å) to substitute for Ca^{2+} (r = 0.99 Å) within the carbonate-fluorapatite (CFA) crystal lattice explains its abundance in studied phosphorites (Jiang et al., 2020; Jarvis et al., 1994; Lucas et al., 1990; McArthur, 1985; Nathan, 1984; Kechiched et al., 2018; Laouar et al., 2024). This substitution is further supported by the strong positive correlation between Sr and P_2O_5 contents ($r = 0.82$, $p < 0.01$) in the Ain Dibba and Ain Kissa samples (see Appendix 1). However, Troubia deposit shows negative correlations between Sr and P_2O_5 ($r = -0.03$; see Appendix 2). Notably, the highest Sr contents are typically found in phosphatic particles

specifically pellets and coprolites which are composed mainly of CFA, as opposed to glauconite minerals (Kechiched et al., 2018; Laouar et al., 2024). These results indicate that the high Sr contents in Ain Dibba and Ain Kissa phosphorites may be related to the abundance of phosphatic particles. However, the low Sr contents in Troubia deposit is due to less abundance of phosphatic particles and more presence of glauconite particles (see Chapter IV). Ba contents, ranging from 48 to 176 ppm in the Ain Dibba and Ain Kissa phosphorites, are comparable to those observed in northern basin deposits such as Djebel El Kouif, Djebel Dyr, and Tazbent. However, these values are significantly higher than those from the southern basin (e.g., Kef Essenoun), where Ba levels are generally below 50 ppm (Kechiched et al., 2020). Like Sr^{2+}, Ba^{2+} can also substitute for Ca^{2+} in the apatite structure (Khan et al., 2012). Cr displays relatively lower contents (101–214 ppm; mean = 152 ppm) in Ain Dibba and Ain Kissa phosphorites compared to the phosphorites of Djebel Onk and Bled El Hadba in the southern basin, where Cr ranges from 234 to 291 ppm at Kef Essenoun (Kechiched et al., 2020) and from 138 to 319 ppm at Bled El Hadba (Laouar et al., 2024). However, the lowest contents (range from 51 to 88 ppm) are recorded in Troubia phosphorites. Cr enrichment is mainly associated with glauconite minerals, where Cr may substitute for Al in the mineral structure (Laouar et al. (2024). This is supported by a modest positive correlation between Al_2O_3 and Cr contents in the Ain Kissa and Troubia phosphorites (r = 0.49, p = 0.22; r = 0.2; respectively, see Appendix 2), which exhibit more pronounced glauconitization than those of Ain Dibba. Conversely, the Ain Dibba samples, which contain less glauconite, show a negative correlation (r = -0.64, p = 0.12). Also, Zn contents show positive correlation with Al_2O_3 and Fe_2O_{3t} contents in Ain Dibba and Ain Kissa deposits (r =0.86 and 0.84, respectively; p <0.01). In contrast, Zn contents are negatively correlated with both Al_2O_3 and Fe_2O_{3t} in Troubia deposit (r = -0.17 and -0.34; *respectively*), however, it shows slightly positive correlations with SiO_2 and MgO (r = 0.69 and 0.35; respectively; see Appendix 2). This indicates that Zn^{2+}(r =0.68 Å) may substitute for either

Mg^{2+}(r =0.66 Å) or Fe^{3+}(r =0.64 Å) within the glauconite structure, which is generally represented as (K, Na) (Fe^{3+}, Al, Mg)$_2$[(Si, Al, Fe^{3+})$_4$O$_{10}$](OH)$_2$ (e.g., McRae, 1972; Laouar et al., 2024). On the other hand, the ability of Zn^{2+} to substitute for Mg^{2+} within dolomitic matrix in Troubia phosphorites. V^{+5} with their ionic radii, 0.62 Å, also can substitute Fe^{3+} (0.63 Å) or Al^{3+} (0.53 Å), in glauconite with a formula ($K_{0.79}$ $Ca_{0.05}$ ($Al_{0.35}$ $Fe_{1.06}$ $^{3+}$ $Fe_{0.25}$ $^{2+}$ $Mg_{0.41}$) ($Si_{3.61}$ $Al_{0.39}$) $O_{10}(OH)_2$) as given by McRae (1972). This is supported by the high contents (up to 118 ppm) are recorded in glauconite-rich phosphorite samples of Ain Dibba and Ain Kissa phosphorites. This element is reported as a key redox-sensitive element by numerous studies. (e.g., Bian et al., 2022). It is typically incorporated into glauconite during early diagenesis, particularly under suboxic to mildly reducing environmental conditions (e.g., Laouar et al., 2024; Tribovillard et al., 2022). Uranium contents in the studied phosphorites range from 50 to 110 ppm, aligning closely with values reported for the Djebel El Kouif phosphorites in the northern Tebessa Basin (11–126 ppm, average 72 ± 30 ppm; Kechiched et al., 2020) and those found in Late Cretaceous to Paleogene phosphorite deposits globally (40–130 ppm; Baturin and Kochenov, 2001). The positive correlations are observed between uranium and both CaO (r = 0.40, p = 0.13) and P_2O_5 (r = 0.81, p < 0.01) in Ain Dibba and Ain Kissa deposits, and CaO (r =0.556) and P_2O_5 (r =0.748) in Troubia deposit. This suggests that uranium is mainly hosted within the apatite crystal structure. It assumed substitution of tetravalent uranium (U^{4+}) for Ca^{2+} in the apatite crystal structure after being reduced from U^{6+} through U^{5+} from seawater (e.g., Altsch uler et al., 1958; Brookfield et al., 2009; Emsbo et al., 2015; Haddad et al., 2023; Kechiched et al., 2020). Zr, Nb, Rb, Th and Hf are attributed to the siliciclastic group, as indicated by strong positive correlations between (Zr and TiO_2), (Hf and TiO_2), and (Nb and TiO_2), (Rb with TiO_2 and K_2O), due to the similarities in ionic radius (see Appendices 1 and 2). The high content of Zr, Nb, Rb, Hf and Ta are recorded in phosphorite samples from Ain kissa, they are most likely related to glauconite minerals (rich in Fe_2O_3, Al_2O_3, MnO, TiO_2 ,

and K_2O; Kechiched et al., 2018; Laouar et al., 2024). Some trace elements such as Cs, Ni, Co are likely associated with the presence of glauconite, dolomitic matrix and iron oxides (Garnit et al., 2017; Hughes and Rakovan, 2018; Kechiched et al., 2020).

Normalized multi-element geochemical spidergrams are compared at a regional and at a global scale using the average values of global phosphorites (Li, 2000). The spidergrams of the studied phosphorites show that the trace element contents are mostly comparable to those reported from global phosphorites (Fig. V. 2). The PAAS normalization of trace elements (PAAS data are from Taylor and McLennan, (1985)) indicated that the enrichment degree of these elements differs in different layers from the studied phosphorites. Unlike global phosphorites, the strontium content is significantly enriched, particularly in Ain Dibba and Ain Kissa deposits, which can be linked to CFA crystal structure (Kechiched et al., 2020). As a whole, some other trace elements including: U, Zr, Y, Cr, V and Zn, are more depleted than the global phosphorite average. Conversely, samples from the lower and middle phosphorite layers of Ain Kissa exhibit higher V and Cr contents than global phosphorites (Fig. V. 2), suggesting glauconite-rich phosphorite samples (Laouar et al., 2024; Kechiched et al., 2018, 2020; Farhaoui et al., 2022). These elements have very contrasting geochemical behavior and are entirely sensitive to redox.

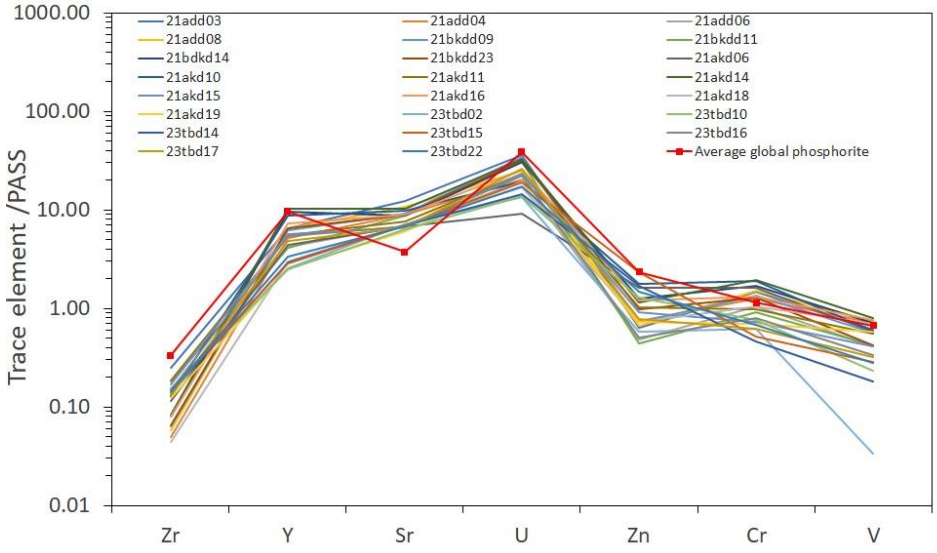

Fig. V. 2. UCC--normalized multi-element spidergram of phosphorite samples from the Troubia, Ain Dibba, and Ain Kissa deposits, according to Taylor and McLennan, (1985), compared to average global phosphorites (Li, 2000).

V. 2. 3. Rare earth elements

The whole-rock REE of Ain Dibba and Ain Kissa phosphorites are shown in Table V. 5.

Table V. 5. Rare earth elements (ppm) from Ain Dibba and Ain Kissa deposits.

Ain Dibba							**Ain Kissa**				
Sample	21add04	21add08	21bkdd09	21bdkd14	21bkdd23		21akd06	21akd10	21akd14	21akd16	21akd18
La	58.36	73.19	71.4	105.68	75.05		54.42	101.07	111.33	87.15	32.49
Ce	23.27	28.69	29.68	39.47	31.38		27.57	52.54	40.25	39.17	12.92
Pr	7.83	9.74	9.66	16.31	10.24		8.1	15.87	16.55	12.24	4.27
Nd	34.49	42.64	42.55	72.11	44.71		34.55	70.23	73.66	53.26	18.78
Sm	6.76	8.26	8.22	14.55	8.64		6.75	14.05	14.71	10.42	3.55
Eu	1.76	2.16	2.16	3.88	2.27		1.8	3.69	3.91	2.77	0.93
Gd	10.06	12.39	12.19	20.94	12.75		9.2	19.06	21.21	15.18	5.3
Tb	1.41	1.75	1.76	2.98	1.8		1.33	2.76	3.01	2.13	0.75
Dy	9.95	12.34	12.39	20.54	12.77		9.33	18.99	21.09	14.76	5.35
Ho	2.47	3.06	3.06	4.95	3.18		2.27	4.57	5.08	3.58	1.36
Er	7.62	9.48	9.5	15.02	9.69		7.04	14.1	15.42	10.92	4.22
Tm	1.04	1.29	1.32	2.09	1.35		1.01	1.99	2.13	1.49	0.58
Yb	6.63	8.23	8.45	13.4	8.57		6.57	13.06	13.64	9.45	3.73
Lu	1.07	1.32	1.37	2.14	1.39		1.07	2.14	2.19	1.52	0.62
Σ REE	**172.71**	**214.53**	**213.71**	**334.03**	**223.79**		**171.01**	**334.11**	**344.17**	**264.04**	**94.85**
LREE	132.46	164.67	163.67	251.99	172.29		133.19	257.44	260.4	205.01	72.94
HREE	40.25	49.86	50.04	82.04	51.5		37.82	76.67	83.77	59.02	21.91
LREE/HREE	3.29	3.3	3.27	3.07	3.35		3.52	3.36	3.11	3.47	3.33

The total rare earth element content (ΣREE) ranges from 173 to 334 ppm in the Ain Dibba phosphorite and from 171 to 344 ppm in the Ain Kissa phosphorites (see Table V. 5).

The highest REE contents are recorded in lower and middle phosphorite layers in both Ain Dibba (∑REE =334 ppm) and Ain Kissa (∑REE =334 and 344 ppm) deposits. LREE (light rare earth elements (La to Eu)) are more abundant than HREE (heavy rare earth elements (Gd to Lu)) (with LREE: 132–260 ppm, average = 193 ppm; and HREEs: 38–84 ppm, average = 59 ppm). The LREE/HREE ratios vary between 3.07 and 3.52 (LREE: La to Eu; HREE: Gd to Lu) indicating LREE enrichment compared to that of the HREE. Similar to many marine phosphorites, especially those belonging to the Tethyan phosphogenic provenance, ΣREEs content in the studied phosphorites corresponds to the intermediate REE content of Tethyan phosphorites, ranging between 100 and 400 ppm (Baioumy and Farouk, 2022), and to those observed in the northern basin at Djebel El Kouif, Djebel Dyr and Djebel Tazbent phosphorites (68–472 ppm; Kechiched et al., 2020). However, the ∑REEs contents are also noticeably lower than those of the Kef Essenoun and Bled El Hadba phosphorites of the southern basin (906 ppm; Kechiched et al., 2020; and 2050 ppm; Laouar et al., 2024; respectively). The francolite ($Ca_5(PO_4)_3F$) can host REE where REE^{3+} tend to replace Ca^{2+} in the crystal lattice due to their close ionic radii and electrical charge (Glenn et al., 1994; Jarvis et al., 1994; Elderfield et al., 1981; Emsbo et al., 2015; Fleet and Pan, 1995). This is referred to as the carbonate fluorapatite (CFA) crystallo-chemical control of REE. On the other hand, ΣREE contents show positive correlation with the P_2O_5 contents ($r = 0.67$, $p = 0.03$; see Appendix 1), suggesting that the francolite is the main holder of the REE in the studied phosphorites. This is supported by high positive correlation between P_2O_5 and REE contents in all of the deposits analyzed across the North Africa phosphorites (Garnit et al., 2017; Kechiched et al., 2020; Ahmed et al., 2022; Edress et al., 2023; El Bamiki et al., 2023), indicating that CFA may represent the dominant process involved in REE enrichment of phosphorites. Notably, the highest REE contents are recorded in the glauconite particles of the phosphatic rocks as suggested by Kechiched et al. (2018) and Laouar et al. (2024). This is again attributed by the high REE contents observed in

the lower and middle layers of Ain Kissa, which are more enriched in glauconite particles than the upper layer. Additionally, the enrichment of REE in glauconite particles are promoted by the high glauconite porosity which are consistent with the SEM-EDS results (see Chapter IV). Rare earth elements, along with phosphate ion (PO_4^{3-}), incorporation into the glauconite mineral structure through substitution and/or adsorption mechanisms onto mineral surface in the depositional environment during early diagenesis (Laouar et al., 2024).

Y is often inserted between Dy and Ho in the REE series according to its ionic radius (e.g., Zhang et al., 1994; Bau and Dulski, 1996). In the studied phosphorites, Yttrium shows relatively high contents ranging from 111 to 279 ppm, with only two samples from the Ain Kissa phosphorite upper layer, which show contents less than 100 ppm (69 and 80 ppm; see Table V. 4). Unlike Ain Dibba and Ain Kissa phosphorites, samples from the Troubia deposit show low contents of Yttrium, ranging from 68 to 90 ppm, with only two samples display high contents (131 and 145 ppm; see Table V. 5). Additionally, a strong positive correlation is observed between the Y contents and ΣREE (r = 0.98; Appendix 1) in the Ain Dibba and Ain Kissa phosphorites samples, suggesting a common source of both REE and Y.

V. 3. Controls on major, trace and REE distribution

Multivariate statistical analyses of whole-rock samples have identified four main components controlling the geochemical properties of phosphorites. Principal Component Analysis (PCA) was carried out on major, trace and REE elements in order to better assess the factors that control the distribution and fractionation of these elements within the primary sub-compositions of phosphorite rocks in the studied samples. PCA is a widely used multivariate statistical method to represent the multivariate nature of the major, trace and REE elements dataset in a reduced dimensional space, facilitating the evaluation of chemical variability across different phosphorite deposits (e.g., Davis, 1986; Wold et al., 1987; Aitchison, 1994). The PCA

results provide insights into the association of major, trace and REE elements with specific rock-forming components, helping to distinguish between geochemical signatures related to mineral phases such as apatite, dolomite, calcite, or siliceous material. This approach can be particularly useful for understanding the diagenetic behavior of these elements, as well as for assessing their economic potential through targeted extraction from enriched phases.

16 variables (including major and trace elements) versus 7 samples from Troubia deposit, and 31 variables (including major, trace and REE elements) versus 10 samples (i.e., observations) from Ain Dibba and Ain Kissa deposits, were assessed using a correlation matrix. The results show that the two main components PC1and PC2 gather a cumulative variance of 67.05% (PC1 = 43.66%, PC2 = 23.39%; Fig. V. 3, for calculations, see supplementary material 1, appendix 1), while other components display less importance in term of variance (e.g., PC3 = 15.40 %, PC4 = 7.33 %) and therefore variable and samples projection will be enabled on the two components having higher variance in Ain Dibba and Ain Kissa phosphorite. In the biplot, there are two major, distinct and opposing trends. The first trend that yield negative PC1 loadings, includes a clustering of major elements such as P_2O_5, CaO, Na_2O, and MnO, along with trace elements, including U, V, Sr, Y, REE, Cr, Sc, and Th, reflecting carbonate fluor-apatite (CFA) and can be interpreted by substitutions/adsorptions mechanisms in the depositional environment, as discussed previously by many authors (e.g., Jarvis et al., 1994; Laouar et al., 2024). The second trend that displays positive PC1 loadings, includes major elements such as Al_2O_3, Fe_2O_3, K_2O, MgO, TiO_2, and SiO_2. This indicates an opposition between CFA and other elements representing the matrix of the phosphorite rocks (dolomitic and siliceous) and glauconite minerals. In this cluster, some trace elements including Ni, Zn, Cu, Zr, Hf and Cs, are relatively enriched. The projection of phosphorite samples on the PC1 versus PC2 distinguishes two sample classes based on these factors: the first are P-rich samples

(P_2O_5 > 20 wt%) falling within the apatite cluster, and the second cluster represents the matrix-rich samples, with sub-compositions such as Si-rich samples indicating cherty composition. Similarly, for the Troubia phosphorites with the first two components, PC1 and PC2, explaining 69.45 % of the total variance (PC1 = 48.27 %, PC2 = 21.18 %; Fig. V. 4, for calculations, see supplementary material 2, appendix 2). PC1 with the highest variance is characterized by positive loading of P_2O_5 and CaO representing CFA as well as As, U, Sr, Cr, V, and Y. This cluster indicates that these elements are mostly included in the apatite component represented by carbonate fluorapatite (CFA), which controls their distribution and can be interpreted to either adsorption or substitution mechanisms during diagenesis (Nathan, 1984; Jarvis et al., 1994; Laouar et al.,2024). The Al_2O_3, TiO_2, Fe_2O_3, K_2O and some other TE (e.g., Zr) have negative loading towards PC1, which may reflect the glauconite minerals, detritus imputes and matrix component. On the other hand, MgO and SiO_2 have a strong negative loading towards PC2 that can reflect dolomitic and siliceous matrix (PCA results are given in appendix 2) and accompanied by some trace elements such as Zn linked to organic matter (Belayouni et al., 1982). Individual samples plotted within the variability space PC1 versus PC2, show an association of three sample groups distinguishes three sample classes based on these factors distinguishes three sample classes based on these factors: samples rich in CaO-P_2O_5 contents (P_2O_5 > 20 wt%), are highly phosphatized and reflect the CFA component, which points to economic phosphorite layers; Si-rich samples indicating cherty phosphorite; and samples highlighting a common presence of dolomitic and siliceous matrix with glauconite minerals within phosphatic rocks.

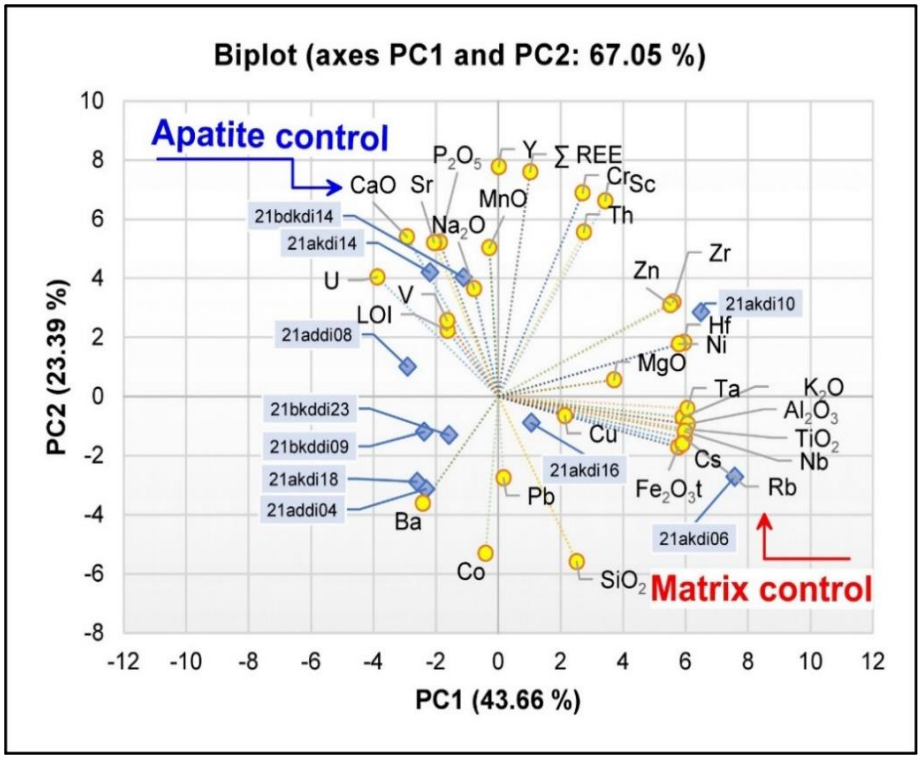

Fig. V. 3. Biplot of the PC1 versus PC2 components from the PCA analysis of Ain Dibba and Ain Kissa phosphorites.

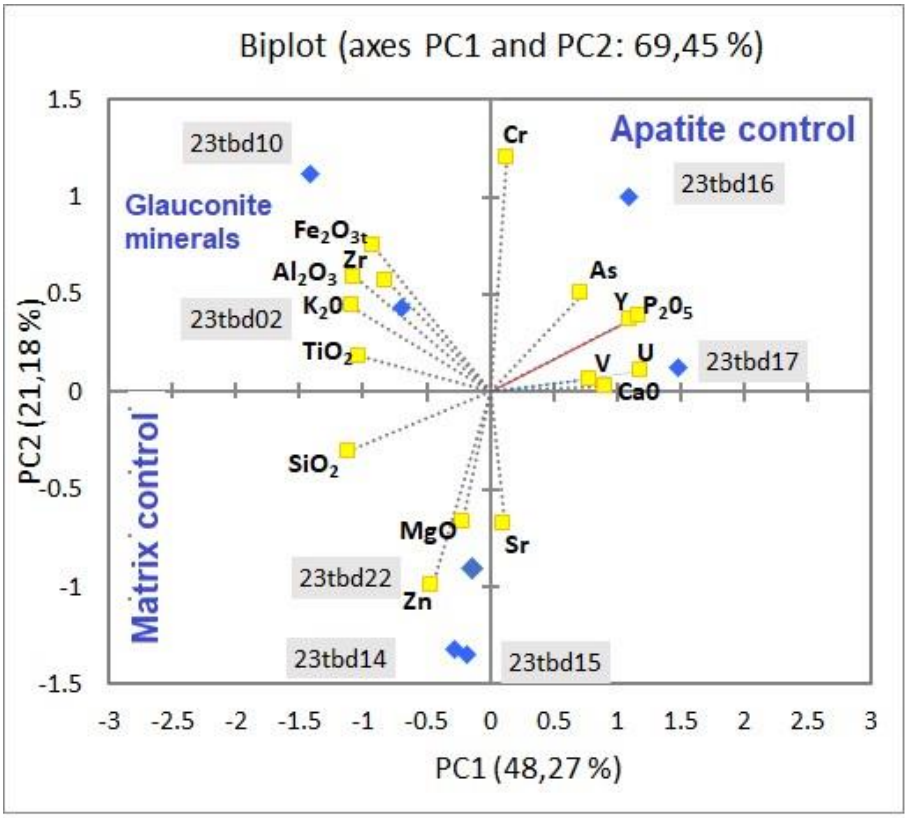

Fig. V. 4. Biplot of the PC1 versus PC2 components from the PCA analysis of Troubia phosphorites.

Conclusion:

Geochemical data of the Troubia, Ain Dibba, and Ain Kissa deposits show less content in terms of P_2O_5 oxide, trace and REE elements. This indicates that they are not as rich as phosphorites from the southern basin (Kef Essenoun and Bled El Hadba), which are a result of a large glauconitization of pre-existing particles, particularly in the southern Tebessa Basin, which leads to an enrichment of REEs (ΣREE up to 2000 ppm). This process is likely a factor in REE enrichment in whole-rock samples (whole-rock REE contents up to 900 ppm), which holds economic potential due to critical element concentrations, are vital for high-tech industry. This, once again, suggests that the major mechanisms controlling the uptake of major, some trace, and REE elements of the all studied phosphatic particles from NNE and NNW basins of Tebessa region include substitutions and adsorption processes onto apatite and glauconite

minerals. These geochemical features indicate that phosphorites from the northern basin were deposited, through upwelling current, in a more open, shallower, oxygenated and agitated environment during the Paleocene-Eocene phosphogenesis in Tebessa region.

Chapter VI
Paleo-depositional environment and REE enrichment

Chapter VI

Paleo-depositional environment and REE enrichment

Trace and REE elements, including Ni, Cr, V, U, Cd, Cu, Ce, Eu and Y, in sedimentary phosphorites have been extensively investigated in recent studies across multi-scale, such as whole-rock, separate particles, matrix, and grain-size fractions (Kechiched et al., 2018, 2020; Dassamiour et al., 2021; Boumaza et al., 2021; Ferhaoui et al., 2022; Laouar et al., 2024; Aouachria et al., 2025). Other studies were focused on the potentially hazardous elements (PHE) contents in phosphorite ores and their wastes across various sizes (Bezzi et al., 2012 ; Boumaza et al., 2021, and 2023; Saouli et al., 2025), allowing for the evaluation of environmental impacts which pose environmental and health risks. Phosphorite deposits show higher concentrations of these elements and are widely used to trace redox conditions during phosphorite deposition and diagenesis in the paleo-depositional environment (e.g., Hatch and Leventhal, 1992; Jones and Manning, 1994; Morford and Emerson, 1999; Baturin and Kochenov, 2001; Morford et al., 2001; Algeo and Maynard, 2004; Tribovillard et al., 2006; Zhou and Jiang, 2009; Pi et al., 2014; Adegoke et al., 2014; Baioumy and Lehmann, 2017; Amireh et al., 2019; Kechiched et al., 2020; Ahmed et al., 2022; Laouar et al., 2024; Ferhaoui et al., 2022).

The rare earth element (REE) results of the studied phosphorites were normalized to Post Archean Australian Shales (PAAS) using the data from (Taylor and McLennan, 1985; McLennan, 1989) (Table VI. 1). The calculation of $Ce/Ce^* = 3Ce_N/(2La_N + Nd_N)$ and Cerium anomaly Cean = log Ce/Ce* are taken from Wright et al. (1987), the calculation $Eu/Eu^* = Eu_N/(Sm_N + Gd_N)^{0.5}$ is taken from Taylor and McLennan (1985), $Pr/Pr^* = 2Pr_N/(Ce_N + Nd_N)$ is

from Bau and Dulski (1996) and $Y/Y^* = 2Y_N/(Dy_N + Ho_N)$ is from Fazio et al. (2007). N refers to PAAS normalized value in all the mentioned calculations.

Table. VI. 1. Post Archean Australian Shale (PAAS) REEs contents (McClellan, 1989).

La	Ce	Pr	Nd	Sm	Eu	Gd	Tb	Dy	Ho	Er	Tm	Yb	Lu
38.2	79.6	8.83	33.9	5.55	1.08	4.66	0.77	4.68	0.99	2.85	0.4	2.82	0.43

VI. 1. PAAS-normalized REE + Y patterns and depositional environment

PAAS-normalized REE and Y patterns are commonly used to assess redox conditions and to understand the processes that occurred during the sedimentary processes as well as post deposition conditions (e.g., Wright et al., 1984; Grandjean and Albarède, 1989; German and Elderfield, 1990; Grandjean-Lécuyer et al., 1993; Reynard et al., 1999; Shields and Stille, 2001; Morad and Felitsyn, 2001; Gnandi and Tobschall, 2003; Fazio et al., 2007; Garnit et al., 2012, 2017; Tostevin et al., 2016; Khan et al., 2016; Kocsis et al., 2016; Auer et al., 2017). Commonly, a seawater-like pattern is characterized by a negative Ce anomaly, HREE enrichment, as well as Y enrichment (Baar et al., 1985; Nozaki et al., 1997; Bau, 1999; Shields and Stille, 2001; Emsbo et al., 2015), whereas a hat-shaped pattern is distinguished by MREE enrichment and HREE depletion (e.g., Reynard et al., 1999; Shields and Stille, 2001; Zhu et al., 2014). Both the REE patterns are characterized by (a) negative Ce anomalies, (b) positive Eu anomalies and (c) positive Y anomalies. The results of the normalized REE and Y are represented in Table VI. 2.

Table VI. 2. Data of the normalized REE and Y of Ain Dibba and Ain Kissa phosphorites.

Ain Dibba							**Ain Kissa**				
Sample	21add04	21add08	21bkdd09	21bdkd14	21bkdd23		21akd06	21akd10	21akd14	21akd16	21akd18
$(La/Sm)_N$	1.25	1.29	1.26	1.06	1.26		1.17	1.05	1.1	1.22	1.33
$(La/Yb)_N$	0.65	0.66	0.62	0.58	0.65		0.61	0.57	0.6	0.68	0.64
$(La/Nd)_N$	1.5	1.52	1.49	1.3	1.49		1.4	1.28	1.34	1.45	1.53
$(Sm/Yb)_N$	0.52	0.51	0.49	0.55	0.51		0.52	0.55	0.55	0.56	0.48
$(Sm/Pr)_N$	1.37	1.35	1.35	1.42	1.34		1.33	1.41	1.41	1.35	1.32
Pr/Pr*	1.35	1.36	1.34	1.41	1.35		1.34	1.32	1.4	1.34	1.35
Ce/Ce*	0.22	0.21	0.22	0.19	0.23		0.27	0.27	0.19	0.24	0.22
Eu/Eu*	0.89	0.98	0.99	1.35	1.01		0.93	1.33	1.35	1.13	0.64
Ce Anom	-0.67	-0.67	-0.65	-0.71	-0.65		-0.57	-0.57	-0.72	-0.62	-0.67
Y/Y*	2.26	2.29	2.17	2.05	2.2		2.08	2	2.14	2.14	2.36
Y/Ho	57.08	57.79	54.97	52.47	55.42		53.02	51.3	54.88	54.62	59.07

The REE patterns of both Ain Dibba and Ain Kissa phosphorites show clearly seawater-like type, with well pronounced Ce negative anomalies and slight HREE enrichment relative to LREE (Fig. VI. 1). This observation is supported by the $(Sm/Pr)_N$ vs $(Sm/Yb)_N$ diagram of Reynard et al. (1999), where the REE patterns show HREE enrichment (Fig. V. I2a), most likely due to strong seawater influence during phosphatization, glauconitization and diagenetic processes. Furthermore, the plot of $(La/Sm)_N$ vs $(La/ Yb)_N$ suggested by Reynard et al. (1999) shows that the studied samples (Fig. VI. 2b) are comparable to those of the modern seawater values (from 0.6 to 1.6) in case of $(La/Sm)_N$ ratios ranging from 1.05 to 1.33, but slightly higher for $(La/Yb)_N$ ratios ranging from 0.57 to 0.68 than those of seawater (from 0.2 to 0.5, see Table VI. 2). This suggests that REE uptake onto apatite/glauconite lattice took place during early diagenesis, although the $(La/Sm)_N$ ratios remain without modification (e.g., Reynard et al., 1999; Fazio et al., 2007; Kechiched et al., 2020; Laouar et al., 2024). In addition, the Y/Ho ratio is a useful parameter that can provide information about the influence of detrital siliciclastic supply and to track the source of REE (e.g., Abedini and Calagari, 2017; Xing et al., 2021; Wu et al., 2022a, b). The studied phosphorite samples display Y/Ho ratios ranging

from 48.2 to 69.2 (see Table VI. 2) and are entirely within the range of seawater values of 60 as reported by Bau and Dulski (1994), thus ruling out any significant influence of terrigenous inputs values of 28 (Bau, 1996; Bau and Dulski, 1996; Nozaki et al., 1997; Webb and Kamber, 2000; Zhao and Jones, 2013; Xing et al., 2021; Wu et al., 2022). Therefore, our data on the REY patterns suggest that the seawater record has been preserved unmodified (Tostevin et al. 2016), indicating that phosphorite REYs were mainly derived from seawater rather than continental detritus. These data exhibit REE patterns that are comparable to those recorded in phosphorite deposits from the northern basin phosphate deposits (Djebel El Kouif, Djebel Dyr and Tazbent; Kechiched et al., 2020), as well as those from the phosphorites upper sub-layer from the Kef Essenoun (southern basin) (Kechiched et al., 2016, 2020; Ferhaoui et al., 2022). These phosphorites also exhibit similarities to numerous phosphorite deposits across North Africa and the Middle East, including the Moroccan phosphorites (Kocsis et al., 2016); the Sra Ouertane and Skarna deposits in the Northern Basin of Tunisia (Garnit et al., 2017); the Al-Kora phosphorites in Jordan (Abed et al., 2016); the Sirhan-Turayf phosphorites in Saudi Arabia (Ahmed et al., 2022); and the Turkish Cretaceous phosphorites (Gundogar and Sasmaz, 2022; Ghasemian et al., 2022).

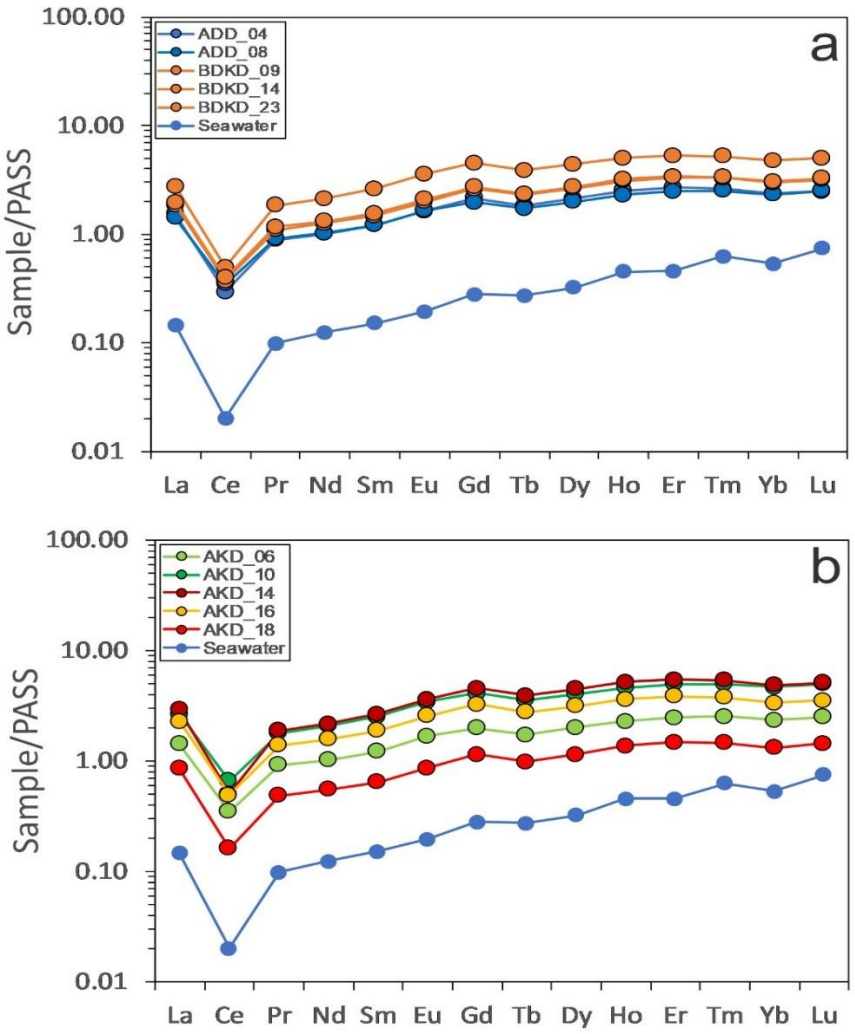

Fig. VI. 1. PAAS (McLennan, 1989)-normalized REE patterns of investigated samples from Ain Dibba (a) and Ain Kissa (b) phosphorites compared to seawater REE patterns (Li, 2000).

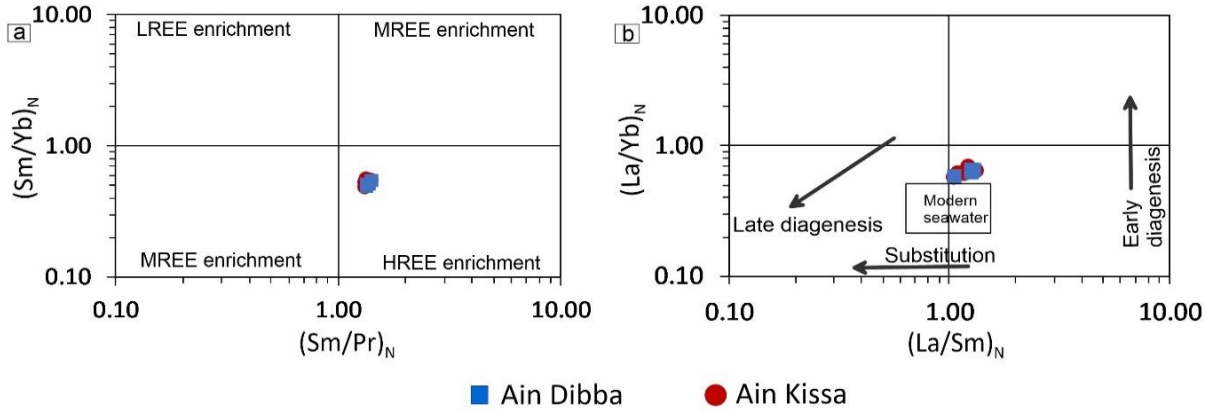

Fig. VI. 2. (a) $(Sm/Pr)_N$ vs. $(Sm/Yb)_N$ diagram (after Garnit et al., 2012; Kechiched et al., 2016) showing HREE-enrichment of the studied phosphorites. (b) $(La/Yb)_N$ vs. $(La/Sm)_N$ diagram (Reynard et al., 1999) showing relatively high $(La/Yb)_N$ ratios compared to those of seawater and a tendency towards early diagenesis.

VI. 2. Investigation on redox conditions

The redox conditions of the depositional environment can be determined by using the different anomalies, such as Ce, Eu and Y, which appear in the PAAS-normalized REE + Y patterns. In addition, many trace elements are highly sensitive to redox conditions such as: U, V, Cr and Fe (e.g., Jones and Manning, 1994; Morford and Emerson, 1999; Tribovillard et al., 2006; Zhou and Jiang, 2009; Baioumy and Lehmann, 2017). The behavior of these elements under different reduction/oxidation conditions is the main key to understand the redox environment during phosphorite deposition.

VI. 2.1. Ce anomaly

In oxidized seawater, cerium is oxidized from the soluble Ce^{3+} to the highly insoluble Ce^{4+}, which is removed from seawater, and consequently creates a negative Ce abundance in seawater (e.g., Moffett, 1990, 1994; Tanaka et al., 2010). The removed Ce^{4+} is most probably adsorbed on Mn-oxides and hydroxides, which may explain the positive Ce anomaly in Mn nodules on the ocean floor (e.g. Elderfield et al., 1981; Wright et al., 1987; Bau and Dulski, 1996; Tachikawa et al., 1999). As a result, the Ce anomaly is taken as a useful indicator for seawater redox conditions (e.g., German and Elderfield, 1990; Shields and Stille, 2001; Ling et al., 2013; Al-Bassam et al., 2021; Baioumy and Farouk, 2022; Gundogar and Sasmaz, 2022).

Ce anomaly values in Ain Dibba and Ain Kissa investigated phosphorites show average values of −0.67 and −0.63 respectively (see Tab. VI. 2). Although all samples show similar Ce anomaly values which indicate oxidizing marine conditions, these values increase slightly in the lower and middle layers of Ain Kissa phosphorite (-0.57), which are richer in glauconite particles and thus REE concentrations, then decrease in the upper layer (-0.72, becomes more strongly negative, with decreasing glauconite and REE concentrations), pointing local semi-reduced environment. This implies that during early diagenesis, the redox conditions in the

sedimentary environment control both the glauconitization process and the intensive uptake of REE, which progressively decrease from the bottom to the top of the phosphorite layers. These data suggest a relative evolution from more reduced conditions during early diagenesis at the bottom towards oxidized environment at the upper layers of the studied phosphorites. This is confirmed by the Pr/Pr* vs. Ce/Ce* diagram proposed by Bau and Dulski (1996), which is used for checking the Ce anomalies. According to Fig. VI. 3a, most of the plotted samples fall in the IIIb field, interpreted as real negative Ce anomaly, indicative of deposition under oxic marine conditions. Accordingly, the obtained negative Ce anomalies can therefore be used as paleo-redox indicator. Although the Ce anomalies are elevated, they are comparable to those found in the other northern basin phosphorites, such as Djebel El Kouif, Djebel Dyr, and Tazbent, which exhibit an average of −0.51 (Kechiched et al., 2020). Conversely, Ain Dibba and Ain Kissa phosphorites recorded more strongly negative Ce anomalies than those observed in the Algerian southern basin (Bled El Hadba: 0.24 to −0.20 (Laouar et al., 2024), and Kef Essenoun: 0.18 to −0.16 (Kechiched et al., 2020)), and the eastern side of the Kesserine Island, i.e., the Tunisian northern, eastern and Gafsa-Metalaoui basins, with values ranging from −0.08 to −0.27 (Garnit et al., 2017). As a result, the depositional environment was more oxidizing in the north-western parts of the Kesserine Island (shallower environment) than in the southern and eastern parts, possibly indicating deeper environments. Additionally, the binary diagram Nd versus Ce anomaly of Wright et al. (1987) (Fig. VI. 3b) shows not only more oxic conditions for the deposition of Ain Dibba and Ain Kissa phosphorites, but also indicate a relatively shift towards fast sedimentation during the phosphorites deposition process compared to the Kef Essenoun and Bled El Hadba southern basin and Tunisian phosphorites (Kechiched et al., 2020; Laouar et al., 2024; Garnit et al., 2017). Indeed, high Nd contents suggest slow sedimentation rate and favor a high rate of REE uptake according to Wright et al. (1987). These findings are consistent with similar data obtained from particles found in the Kef Essenoun and Bled El Hadba deposits

from southern basin, as reported by Kechiched et al. 2018; and Laouar et al.,2024. As noted previously, it is clear that the slight positive shift of $(La/Yb)_N$ values of the Ain Dibba and Ain Kissa phosphorites (0.57–0.68) compared to those of seawater (0.2–0.5; cf. Fig. VI. 2b) (Elderfield and Pagett, 1986; Reynard et al., 1999), provides strong evidence for early diagenetic processes and REE enrichment by two main mechanisms substitution and adsorption onto apatite at the seawater/sediment interface. In contrast, $(La/Sm)_N$ values between 1.05 and 1.33 are similar to those of seawater (0.6-1.6), although there is also a shift towards slightly higher values and, therefore, early diagenesis processes during phosphorites deposition (cf. Fig. VI. 2b). The presence of glauconite minerals in the studied phosphorites is believed to have contributed to REE enrichment through uptake from pore waters under slightly reduced conditions during early diagenesis, where Kechiched et al. (2018) and Laouar et al., (2024) have reported the enrichment of REEs in glauconite grains using "in situ" LA-ICP-MS technique in the southern basin. These data are consistent with SEM observations, which reveal the presence of porosity, microcracks, and fractures in phosphatic particles (i.e., pellets, coprolites, and bioclasts). These features probably facilitated significant REE uptake and contributed to the enrichment of certain chemical elements. However, the phosphorites of the northern basin experienced limited glauconitization, as they were deposited in a shallow, oxic environment. This suggests, once again, sub-oxic to oxic conditions prevail during the north phosphorite deposition, whereas sub-reduced conditions mark the sub-layer of southern phosphorite deposits.

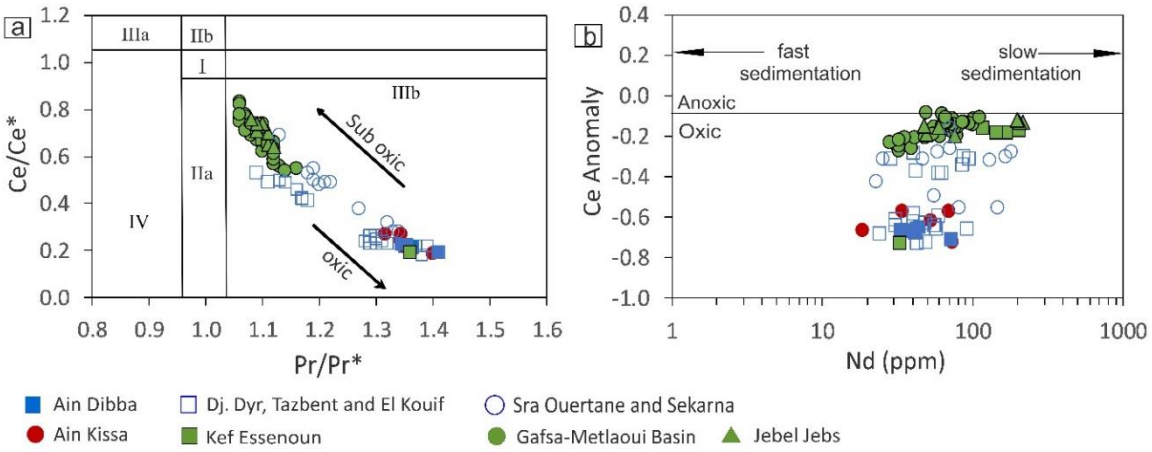

Fig. VI. 3. (a) Pr/Pr* vs. Ce/Ce* diagram (after Bau and Dulski, 1996) showing increasing large oxic conditions for the deposition of Ain Dibba and Ain Kissa phosphorites; all investigated samples fall in the field IIIb which indicaties real negative Ce anomalies: (Field I: no anomaly; Field IIa: positive La anomaly causing apparent negative Ce anomaly; Field IIb: negative La anomaly causing apparent positive Ce anomaly; Field IIIa: real positive Ce anomaly; Field IV: positive La anomaly disguising positive Ce anomaly); (b) Ce anomaly vs. Nd diagram (Wright et al., 1987) showing more oxic conditions for the depositional environment of studied phosphorite along with the Dj. Dyr, Tazbent and El Kouif (Kechiched et al., 2020) from the northern basin compared to those of the phosphorites from the southern basin in Algeria (Kef Essenoun and Bled El Hadba; Kechiched et al., 2020) and from southern and eastern basin in Tunisia (Gafsa-Metlaoui and Jebel Jebs; Garnit et al., 2012).

VI. 2.2. Europium anomaly

Europium typically occurs in the trivalent state, but Eu^{3+} can be reduced to Eu^{2+} under reducing conditions (e.g. Brookins, 1989; Shields and Stille, 2001). Consequently, a positive Eu anomaly is therefore considered an indicator of reducing depositional conditions during early diagenesis (Michard et al., 1983; Stalder and Rozendaal, 2004; Bau et al., 2010). Weak positive Eu anomalies of the studied phosphorites, which ranges from 0.89 to 1.35 for Ain Dibba and from 0.93 to 1.35 for Ain Kissa phosphorites (see Table VI. 2), confirm the prevailing slightly reducing conditions in the basin during phosphorite depostion. Furthermore, the highest Eu anomalies are recorded in phosphorite from the lower and middle sub-layers of Ain Kissa, where are considered to be the *most glauconite*-rich *phosphorite layers*. This indicates that positive Eu anomaly values are strongly related to an increase in glauconitization (increase in SiO_2, Al_2O_3, $Fe_2O_{3(t)}$ and MgO contents) which support diagenetic processes. Similar positive anomalies are also observed in phosphorite deposits of the northern basin (0.6-

1.57 for Dj. El Kouif and Dj. Dyr; Kechiched et al., 2020), but lower compared to those of the phosphorite deposits from the southern basin (1.96–2.14 for Kef Essenoun; Kechiched et al., 2020 and 1.03–3.38 for Bled El Hadba; Laouar et al., 2024). As a result, these weak Eu anomaly values are interpreted as the slight reducing conditions during early diagenesis. In addition, REE vs. Eu/Eu* in Ain Dibba and Ain Kissa phosphorite show a strong positive correlation (r = 0.99, Fig. VI. 4). This indicates that positive Eu anomaly values are strongly related to REE enrichment and is accompanied by an increase in glauconitization. The highest Eu anomalies are accompanied by the highest REE contents, and are recorded in the phosphorites from the southern basin compared to those of the phosphorites from the northern basin (Kechiched et al., 2016, 2020; Laouar et al., 2024). This suggests, once again, that unlike the southern basin, where glauconitization enhanced REE uptake, the weak reducing conditions in the northern basin limited this process. This resulted in a noticeable REE depletion in the northern basin phosphorites.

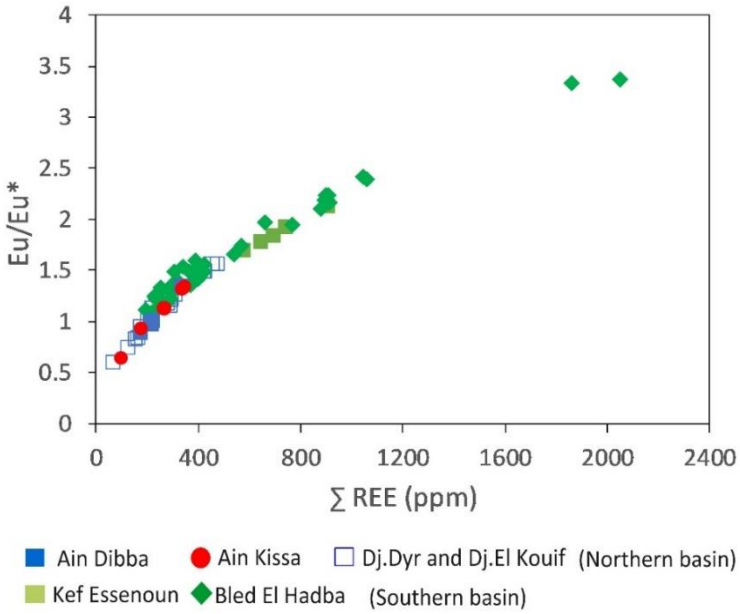

Fig. VI. 4. REE vs. Eu/Eu* variations in Ain Dibba and Ain Kissa phosphorite showing the strong positive correlation compared to those of the phosphorites from the northern basin (Dj. Dyr and Dj. El Kouif; Kechiched et al., 2016,2020) and from southern basin (Kef Essenoun; Kechiched et al., 2016,2020, and Bled El Hadba; Laouar et al.,2024).

VI. 2. 3. Yttrium anomaly

Y in the studied phosphorites is often inserted between Dy and Ho in the REE series according to its ionic radius (e.g., Zhang et al., 1994; Bau and Dulski, 1996). Y/Y* ratios range from 2.00 to 2.36 (average = 2.17) and La/Nd ratios vary from 1.28 to 1.53 (average: 1.43), again indicating that the samples fall within the modern seawater field (Fig. VI. 5a and Table VI. 2; Shields and Stille ,2001). Additionally, the samples reveal a clear positive correlation between Y anomaly and $(La/Nd)_N$ rations, which indicates the close link between Y and La behavior in the seawater and/or sediments-pore water (Fazio et al., 2007). Furthermore, the Ce anomaly also demonstrates negative correlations with both parameters (Ce/Ce* vs. Y/Y* = -0.41; Ce/Ce* vs. La/Nd = -0.15) as depicted in Figure 5b and c, this trend is mostly attributed to early diagenesis. This result is similar to those reported in other North African phosphorites (e.g., Garnit et al., 2017; Kechiched et al., 2020; Ferhaoui et al., 2022; Laouar et al., 2024).

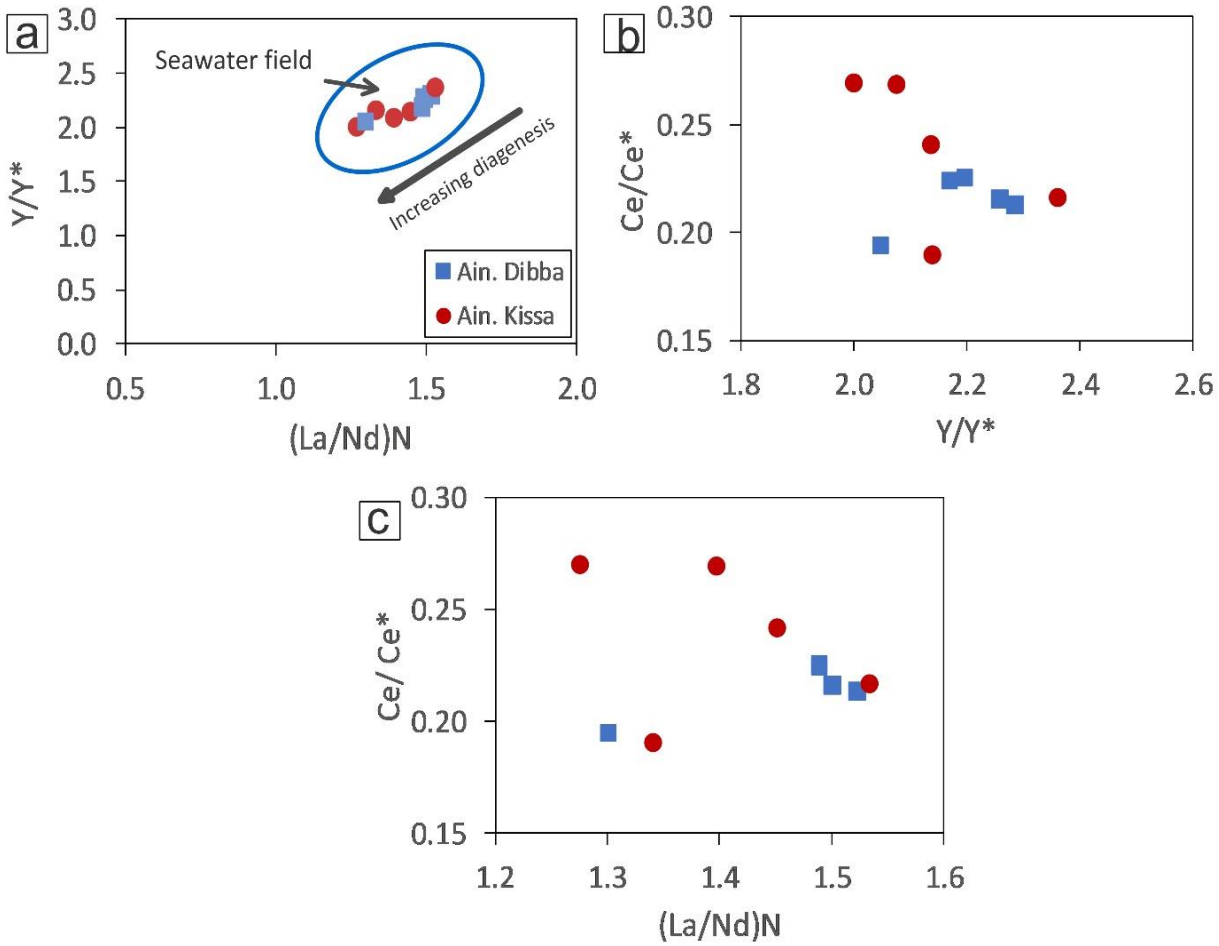

Fig. VI. 5. Binary diagrams of $(La/Nd)_N$ vs. Y/Y* (Fazio et al., 2007), (b) Y/Y* vs. Ce/Ce*, and (c) $(La/Nd)_N$ vs. Ce/Ce*.

VI. 3. Trace elements as redox indicators

Trace elements, including Ni, Cr, V, U, Cd, and Cu, in sedimentary phosphorites have been extensively investigated in recent studies across various scales, such as whole-rock, separate particles, matrix, grain-size fractions, and through processing chain, and their wastes. Phosphorite deposits show higher concentrations of these elements and are widely used to trace redox conditions during phosphorite formation and diagenesis (e.g., Hatch and Leventhal, 1992; Jones and Manning, 1994; Morford and Emerson, 1999; Baturin and Kochenov, 2001; Morford et al., 2001; Algeo and Maynard, 2004; Tribovillard et al., 2006; Zhou and Jiang, 2009; Pi et al., 2014; Adegoke et al., 2014; Baioumy and Lehmann, 2017; Ahmed et al., 2022; Amireh et al., 2019; Kechiched et al., 2020; Laouar et al., 2024;). Additionally, environmental impacts on

soils and sediments near mining plant have been also evaluated (Boumaza et al., 2021, 2023). The enrichment of these elements compared to average mudstones and shales, has been attributed to the activity of organic matters, which are derived essentially from marine plankton and typically associated with marine phosphorites and accumulation at the sediment–water interface, characterize accumulation under mildly denitrifying (reducing) conditions (Gulbrandsen, 1966; Froelich et al., 1988; Khan et al., 2012; Amireh et al., 2019). In terms of redox conditions, their significant enrichment in phosphorites can also be resulted to enhanced uptake from seawater and/or pore-water during redox cycling and diagenesis (Froelich et al., 1988; Scopelliti et al., 2010; Khan et al., 2012). Similar to the majority of Paleocene-Eocene North African phosphorites (Garnit et al., 2017; Kechiched et al., 2020, Laouar et al., 2024), the phosphorites studied from the Ain Dibba and Ain Kissa deposits show high contents of these elements, with the highest are recorded in the lower phosphorite layers (see Tables V. 3 and V. 4, Chapter V). In addition, V and Cr, which are soluble in water under oxic conditions, tend to be enriched in sediments deposited under reducing environments (Piper, 1994). They are, therefore interpreted to have been deposited under mildly reducing conditions during their early diagenesis. Cr enrichments is similar with REE enrichments in the phosphorites samples from the lower layers, with the glauconites being the most enriched particles (e. g., samples 21akd06 and 21akd10 for Ain Kissa and samples 21add03 and 21add04 for Ain Dibba phosphorites; cf. Figs. II. 8 and II. 33, Chapter II; and Tables V.3, 4 and V.5, Chapter V). This would strongly support the idea that glauconitization took place under relatively reducing conditions particularly in the lower phosphorite layers of both deposits which leads to an enrichment of REEs (ΣREE up to 2000 ppm, Laouar et al.,2024; Kechiched et al.,2018). This data is supported by Cr/V ratios, with Piper (1994) pointing out that the Cr/V ratio of seawater is 0.12. This ratio could be much greater in sediments that accumulate under mildly reducing conditions, but approach the seawater value in sediments that accumulate under strongly

denitrifying to sulfate-reducing conditions. All samples from Ain Dibba and Ain Kissa phosphorite show rather high Cr/V ratios between 1.09 and 2.31 (cf. Chapter V, Tables V.3 and V.4) indicating mildly reducing conditions compared to those of seawater. Conversely, the Troubia deposit is more depleted in Cr and V contents than the average shale and phosphorite, and Ain Dibba and Ain Kissa phosphorites. This can be attributed to the less accumulation of plankton associated with marine phosphorite. Although the lower Cr and V contents, Cr/V ratios show high values ranging from 1.34 to 8.56 (cf. Chapter V, Tables V.3 and V.4), where the highest are registered in phosphorite samples rich in glauconite minerals, therefore, indicated that the deposition occurred under reducing conditions.

Conclusion

Geochemical data of Troubia, Ain Dibba, and Ain Kissa phosphorites indicate that the sedimentary environment was characterized by slightly reducing conditions during early diagenesis. This reduced paleo-environment is attributed the intensive uptake of both REE and some trace elements (e.g., Cr, V, Ni, U) mainly from pore- waters, especially in phosphorites from the lower layers of Ain Dibba and Ain Kissa deposits. The negative Ce anomalies, slightly positive Eu anomalies and pronounced positive Y anomalies and some sensitive trace elements, such as V, Cr, and U all show an evolution from sub-oxic to oxic conditions for the deposition and diagenesis of the studied phosphorites. The glauconitization processes is the main factor that control the enrichment of REE through both substitution and adsorption mechanisms. This processes are attributed by the formation the glauconite minerals in the lower and middle phosphorite layers accompanied by concentrated more REE. Conversely, the depositional environment of the phosphorite upper layers was more oxygenated with more negative Ce anomalies, weak positive Eu anomalies, and therefore glauconitization processes were limited and glauconite clearly absent. Similar to many phosphorites that were deposited during the Cretaceous-Eocene period on the southern margin of the Neo Tethys Ocean along the Afro-

Arabian platform, the main origin of these chemical elements was from seawater rather than from terrigenous sources.

Conclusion

Conclusion

Comprehensive geological, petrological, and geochemical investigations of the Troubia, Ain Dibba, and Ain Kissa phosphorites indicate that these deposits host limited economic potential, despite being partially exploited during the French colonial period in the early 20th century. These occurrences are part of the Paleocene–Eocene northern basin of the Kasserine Island and were deposited specifically during the Thanetian stage (59.2–56 Ma), a time marked by large amount marine phosphorites accumulation linked to Tethyan upwelling currents rich on P and Si.

Petrologically, the phosphorite successions consist of thin sub-layers of about 80 cm thick, within the flint-bearing marly limestone, marl and dolostone formations. They are semi-hard to hard facies, with heterogeneous phosphatic particles in their shapes, colors and morphologies (the rock is poorly sorted), and contents which vary from about 50 to 75% of the rock. They are mainly pellets, coprolites, bioclasts, glauconite, gypsum, and detrital quartz. These constituents are cemented by calcareous, siliceous and more rarely a clayey matrix. Mineralogically, the main phosphatic mineral is carbonate-fluor apatite (CFA), while the matrix and /or cement phases are mainly composed of dolomite, calcite and opal-CT, with rare accessory minerals, such as gypsum, detrital quartz and zeolites (clinoptilolite-heulandite). FTIR data reveals the characteristic absorption bands of carbonate-fluorapatite (CFA), indicating calcareous phosphorites due to the high intensity of carbonate gangue (calcite and dolomite). In contrast, the strongest silica intensities (detrital quartz, glauconite and siliceous cement) are recorded in cherty phosphorites. These data are supported by that SEM- EDS analysis which show high porous structure, cracks and fractured surfaces of phosphatic particles, may be related to transport, burial, allowing the enrichment of chemical elements, such as P_2O_5, and REE, through adsorption from both seawater and pore water during early

diagenesis. Notably, the presence of organo-apatitic component within pellets particles and matrix, and the occurrence of silica (opal-CT) as a matrix of some phosphorite layers are attributed to upwelling processes which are believed to be the cause of recycled P and Si between the deep oceanic reservoir and surface water followed by sedimentation. Si may also originate from radiolarians tests, siliceous algae and diatoms and precipitated in the depositional environment as cherty phosphorites. Geochemically, the studied phosphorites show lower P_2O_5 and REE contents, lower Ce and Eu anomalies, and lower redox-sensitive trace element contents than those of the southern (Kef Essenoun and Bled El Hadba) and eastern (Tunisian) basins of the Kasserine Paleo-Island. The highest trace and REE elements are recorded in phosphorites enriched in glauconite minerals. The faster sedimentation is also contributed to poorer contents in glauconite (weak glauconitization processes) and hence, poorer REE contents than the phosphorites of the southern basin. Additionally, the highest Ce/Ce* and lowest Eu/Eu* anomalies in Ain Dibba and Ain Kissa deposits are recorded in the lower layers, enriched in both REE and glauconite contents, whereas the lowest Ce/Ce* and highest Eu/Eu* anomalies, reflecting more oxic conditions, are characteristics of the glauconite-free and REE-poor upper layers. Also, the redox-sensitive (Cr, Ni, V, U) trace element data display transition from relatively sub-oxic to oxic conditions (from the lower to the upper layers). The deposition conditions during early diagenesis were characterized by slightly reducing conditions which are attributed the intensive uptake of both REE and some trace elements (e.g., Cr, V, Ni, U) mainly from pore- waters through substitution and adsorption mechanisms onto apatite and glauconite minerals, especially in phosphorites from the lower layers of Ain Dibba and Ain Kissa deposits. These geochemical features indicate that phosphorites from the northern basin were deposited, through upwelling current, in a more open, shallower, oxygenated and agitated environment during the Paleocene-Eocene phosphogenesis with limited PETM events in Tebessa region.

Notably, like their Tunisian counterparts, the Algerian phosphorites were deposited during the Paleocene–Eocene period and probably record the environmental perturbations associated with the Paleocene–Eocene Thermal Maximum events (PETM; Garnit et al., 2017; Saouli at al., 2025; Kechiched et al., 2020; Ferreira da Silva et al., 2010). It is necessary to estimate REE reserves in phosphates in the Tébessa region using geostatistical tools and artificial intelligence methods. Further work on REE enrichment and extraction is necessary to assess the economic viability of these refining elements. Using stable isotope geochemistry ($\delta^{13}C$ and $\delta^{18}O$) of phosphorite deposits in the Tebessa basin, Algeria, may also be useful to reconstruct climatic conditions and the chemistry of the depositional environment in the Algerian phosphates, focusing on the Paleocene–Eocene period.

References

References

Abed, A.M., 2013. The eastern Mediterranean phosphorite giants: an interplay between tectonics and upwelling. Geo. Arabia. 18, 67–94. https://doi.org/10.2113/ geoarabia180267.

Abed, A.M., Amireh, B.S., 1983. Petrography and Geochemistry of Some Jordanian Oil Shales from North Jordan. J. Pet. Geol. 5, 261-274. http://doi.org/10.1111/j.1747-5457.1983.tb00571.x

Abed, A.M., Jaber, O., Alkuisi, M., Sadaqah, R., 2016. Rare earth elements and uranium geochemistry in the Al-Kora phosphorite province, Late Cretaceous, northwestern Jordan. Arabian J. Geosci. 9, 1–19. https://doi.org/10.1007/s12517-015-2135-6.

Abedini, A., Calagari, A.A., 2017. REEs geochemical characteristics of lower Cambrian phosphatic rocks in the Gorgan-Rasht Zone, northern Iran: implications for diagenetic effects and depositional conditions. J. Afr. Earth Sci. 135, 115–124. https://doi.org/10.1016/j.jafrearsci.2017.08.018.

Abou el-Anwar, A.A., mekky, H.S., Abd el Rahim, S.H. and Aita, S.k. 2017. mineralogical, geochemical characteristics and origin of Late Cretaceous phosphorite in Duwi Formation (Geble Duwi mine), Red Sea region, egypt. Egypt. J. Pet. 26 (1), 157–169, https://doi.org/ 10.1016/j.ejpe.2016.01.004.

Addinsoft, 2021. XLSTAT statistical and data analysis solution. New York, USA. htt ps://www.xlstat.com.

Adegoke, H. I., Adekola, F. A., Fatoki, O. S., Ximba, B. J., 2014. Adsorption of Cr (VI) on synthetic hematite (α-Fe O)$_2$ ^{3} nanoparticles of different morphologies. Korean J. Chem. Eng. 31,142–154.

Ahmad, F., Baioumy, H., Farouk, S., Al-Kahtany, K., El-Sorogy, A., Kirk, J., 2019. Geochemistry and stable isotopes of the upper Campanian–lower Maastrichtian phosphorite-bearing sequence, Central Jordan: implications for their age, origin, and diagenesis. Geol. J. 54, 1–16. https://doi.org/10.1002/gj.3692.

Ahmed, H.A., Aseri, A.A., Ali, K.A., 2022. Geological and geochemical evaluation of phosphorite deposits in northwestern Saudi Arabia as a possible source of trace and rare-earth elements. Ore. Geol. Rev. 144, 104854. https://doi.org/10.1016/j. oregeorev.2022.104854.

Aitchison, J., 1994. Principales of compositional data analysis. J. Multivar. Anal. 24.

Akdogan, G., Ghosh, T., 2014. Identification of REE in some Alaskan coal and ash samples. Mineral Industry Research Laboratory (MIRL) Institute of Northern Engineering, University of Alaska Fairbanks: Fairbanks, AK, USA.

Al-Bassam, K., Rambousek, P., Cech, S., 2021. REE-rich Turonian phosphates in the Bohemian Cretaceous basin, Czech Republic: Assessment as source of critical elements and implications for future exploration. Minerals. 11, 246. https://doi.org/ 10.3390/min11030246.

Albaum, H. G., 1952. The role of phosphorus in the metabolism of plants. In: Wolterink, L. F., (Ed.), The biology of phosphorus: East Lansing. Michigan State Coll. Press, p. 37-75.

Algeo, T. J., Maynard, J. B., 2004. Trace-element behavior and redox facies in core shales of Upper Pennsylvanian Kansas-type cyclo-thems. Chem. Geol. 206, 289-318. https://doi.org/10.1016/j.chemgeo.2003.12.009.

Aouachriaa, R., Kechiched, R., Buccione, R., Mongelli, G., Ameur-Zaimeche, O., Bruguier, O., Kocsis, L., Laouar, R., 2025. Geochemistry and economic evaluation of REE + Y potential in the fine-grained matrix of sedimentary phosphorites from the Tebessa region, eastern Algeria. J. Geochem. Explor. https://doi.org/10.1016/j.gexplo.2025.107889.

Altschuler, Z.S., Berman, S., Cuttita, F., 1967. Rare Earths in Phosphorites Geochemistry and Potential Recovery, 575-B. U.S. Geol. Surv. Prot. Pap. U.S, p. B1. https://doi. org/10.3133/ofr663.

Altschuler, Z.S., Clarke, R.S., Young, E.Y., 1958. Geochemistry of uranium in apatite and phosphorite. U. S. Geol. Surv. Prof. Pap. 314-D, 45–90. https://doi.org/10.3133/ pp314D.

Amireh, B.S., Amaireh, M.N., Abu Taha, S., Abed, A.M., 2019. Petrogenesis, provenance, and rare earth element geochemistry, southeast desert phosphorite, Jordan. J. Afr. Earth Sci. 150, 701–721. https://doi.org/10.1016/j.jafrearsci.2018.09.023.

Antonakos, A., Liarokapis, E., Leventouri, T., 2007. Micro-Raman and FTIR studies of synthetic and natural apatites. Biomater. 28, 3043–3054. https://doi.org/ 10.1016/j.biomaterials.2007.02.028.

Auer, G., Markus, R., Christoph, A.H., Werner, E.P., 2017. The impact of transport processes on rare earth element patterns in marine authigenic and biogenic phosphates. Geochem. Cosmochim. Acta 203, 140–156. https://doi.org/10.1016/j. gca.2017.01.001.

Bai, Y., Zheng, S., Liu, N., Liu, Y., Wang, X., Qiu, L., Gong, A., 2024. The role of rare earths on steel and rare earth steel corrosion mechanism of research progress. Coatings 14, 465. https://doi.org/10.3390/coatings14040465.

Baioumy, H., & Lehmann, B., 2017. Anomalous enrichment of redox sensitive trace elements in the marine black shales from the Duwi Formation, Egypt: Evidence for the late Cretaceous Tethys anoxia. J. Afr. Earth Sci .133, 7–14. https://doi.org/10.1016/j.jafrearsci.2017.05.006.

Baioumy, H., Farouk, S., 2022. The geochemical and economic significance of REE in the Upper Cretaceous-Eocene Tethyan phosphorites. J. Afr. Earth Sci. 194, 104635 https://doi.org/10.1016/j.jafrearsci.2022.104635.

Balaram, V., 2023a. Potential future alternative resources for Rare Earth Elements: Opportunities and challenges. Minerals. 13, 425. https://doi.org/10.3390/ min13030425.

Balaram, V., Santosh, M., Satyanarayanan, M., Srinivas, N., Gupta, H., 2024. Lithium: A review of applications, occurrence, exploration, extraction, recycling, analysis, and environmental impact. Geosci. Front. 15, 101868. https://doi.org/10.1016/j.gsf.2024.101868.

Baturin, G. N., 1982. Phosphorites on the sea floor: Origin, composition and distribution. Elsevier, Amsterdam, 343p.

Baturin, G., Kochenov, A., 2001. Uranium in phosphorites. Lithol. Miner. Resour. 36, 303–321. https://doi.org/10.1023/A:1010406103447.

Bau, M., 1996. Controls on fractionation of isovalent trace elements in magmatic and aqueous systems: evidence from Y/Ho, Zr/Hf and lanthanide tetrad effect. Contrib. Mineral. Petrol. 123, 323–333. https://doi.org/10.1007/s004100050159.

Bau, M., 1999. Scavenging of dissolved yttrium and rare earths by precipitating iron oxyhydroxide: Experimental evidence for Ce oxidation, Y-Ho fractionation, and lanthanide tetrad effect. Geochim. Cosmochim. Acta 63, 67–77. https://doi.org/10.1016/S0016-7037(99)00014-9.

Bau, M., Dulski, P., 1996. Distribution of yttrium and rare-earth elements in the penge and kuruman iron-formations, transvaal supergroup, South Africa. Precambrian Res. 79, 37–55. https://doi.org/10.1016/0301-9268(95)00087-9.

Belayouni, H., Fauconnier, D., Slansky, M., Trichet, J., 1982. In: Doc, B.R.G.M. (Ed.), Etude du contenu organique des dépots phosphatés du bassin de Gafsa, 35, p. 70.

Bellier, J.P., 1985. Foraminifères planctoniques du Crétacé de Tunisie septentrionale. Mém. Soc. Géol. France, nlle série, 146, 67 p. 8 pl.

Ben Abdessalem, N., 1978. Etude palynologique et micro-paleontologique de la serie phosphatee du bassin de Gafsa-Metlaoui (Tunisie). Application a la compre hension des mecanismes de la phosphatogenese. These 3eme cycle. Universite Paris VI, Paris.

Ben Hassen, A., Trichet, J., Disnar, J.R., 2010. Pétrographie et géochimie comparées des pellets phosphatés et de leur gangue dans le gisement phosphaté de Ras-Draaa (Tunisie). Implications sur la génèse des pellets phosphatés. Swiss J. Geosci. 103, 457–473. https://doi.org/10.1007/s00015-010-0029-x.

Bencharef, M. H., Boubaya, D., Aboud, E., Ayfer, S., 2022. Role of an advanced gravity data analysis in improving the geologic understanding of the northern Tebessa region, Northeastern Algeria. J Afr Earth Sci. 196, 104693. https://doi.org/10.1016/j.jafrearsci.2022.104693.

Benitez-Nelson, C.R., 2000. The biogeochemical cycling of phosphorus in marine systems. Earth Sci. Rev. 51, 109-135.

Benni, T., 2013. Phosphate Deposits of Iraq. In UNFC Workshop, Santiago de Chile.

Bernoullia, D. and Gunzenhauser, B., 2001, A dolomitized diatomite in an Oligocene-Miocene deep-sea fan succession, Gonfolite Lombarda Group, Northern Italy. Sediment. Geol. 139, 71–91.

Bezzi, N., Aïfa, T., Hamoudi, S., Merabet, D., 2012. Trace elements of Kef Es Sennoun natural phosphate (Djebel Onk, Algeria) and how they affect the various mineralurgic modes of treatment. Procedia. Eng. 42, 1915–1927. https://doi.org/ 10.1016/j.proeng.2012.07.588.

Bian, L., Chappaz, A., Schovsbo, N.H., Sanei, H., 2022. A new vanadium species in black shales: Updated burial pathways and implications. Geochim. Cosmochim. Acta. 338,1-10. https://doi.org/10.1016/j.gca.2022.09.035.

Blès, J.L., Fleury, J.J. (1971). Carte geologique 1/50 000 Morsott (178) et notice explicative. Publication Service Geologique de l'Algerie.

Blott, S. J., Pye. K., 2001. Gradistat: a grain size distribution and statistics package for the analysis of unconsolidated sediments. Earth. Surf. Process. Lanforms. 26, 1237–1248.

Boggs, S., 2009. Petrology of Sedimentary Rocks. 2nd edition, Cambridge University Press, New York, 600 pp.

Bonnot-Courtois, C., Flicoteaux, R., 1989. Distribution of rare-earth and some trace elements in Tertiary phosphorites from the Senegal Basin and their weathering products. Chem. Geol. 75, 311–328.

Boulemia, S., Hadji, R., Hamimed, M., 2021. Depositional environment of phosphorites in a semiarid climate region, case of El Kouif area (Algerian–Tunisian border). Carb. Evap. 36 (3), 1-15. https://doi.org/10.2478/mipo-2023-0010.

Boumaza, B., Chekushina, T.V., Kechiched, R., Benabdeslam, N., Brahmi, L., Kucher, D.E., Rebouh, N.Y., 2023. Environmental geochemistry of potentially toxic metals in phosphate rocks, products, and their wastes in the algerian phosphate mining area (Tébessa, NE Algeria). Minerals. 13 (7), 853. https://doi. org/10.3390/min13070853.

Boumaza, B., Kechiched, R., Chekushina, T.V., 2021. Trace metal elements in phosphate rock wastes from the Djebel Onk mining area (Tébessa, eastern Algeria): A geochemical study and environmental implications. Appl Geochem. 127, 104910. https://doi.org/10.1016/j.apgeochem.2021.104910.

Boumaza, B., Kechiched, R., Chekushina, T.V., Benabdeslam, N., Senouci, K., Hamitouche, A.E., Merzeg, F.A., Rezgui, W., Rebouh, N.Y., Harizi, K., 2024. Geochemical distribution and environmental assessment of potentially toxic elements in farmland soils, sediments, and

tailings from phosphate industrial area (NE Algeria). J. Hazard. Mater. 465, 133110. https://doi.org/10.1016/j.jhazmat.2023.133110.

Bouzenoune, A., 1993. Minéralisation péridiapiriques de l'Aptien calcaire : les carbonates de fer du gisement hématitique de l'Ouenza (Algérie orientale). Thèse de doctorat, Université Paris VI, 209 p.

Brasier, M.D., Callow, R.H.T., 2007. Changes in the patterns of phosphatic preservation across the Proterozoic-Cambrian transition. *Mem. Assoc. Australas. Palaeontol*. 34, 377-389.

Brookfield, M., Hemmings, D., Van. Straaten, P., 2009. Paleo-environments and origin of the sedimentary phosphorites of the Napo Formation (Late Cretaceous, Oriente Basin, Ecuador). *J. South Am. Earth Sci.* 28, 180-192. https://doi.org/10.1016/j.jsames.2009.02.004.

Brookins, D. G., 1989. Aqueous geochemistry of rare earth elements. In Geochemistry and Mineralogy of Rare Earth Elemnts (ed. B R. Lipin and G. A. McKay), pp. 201-225. Mineral, Sot. Amer.

Buccione, R., Kechiched, R., Mongelli, G., Sinisi, R., 2021. REEs in the north Africa P bearing deposits, paleo-environments, and economic perspectives: a review. Minerals 11, 214. https://doi.org/10.3390/min11020214.

Buccione, R., Kechiched, R., Mongelli, G., Sinisi, R., 2021. REEs in the north Africa P bearing deposits, paleo-environments, and economic perspectives: a review. Minerals. 11, 214. https://doi.org/10.3390/min11020214.

Burnett, W.C., Riggs, S.R., 1990. Phosphate Deposits of the World, vol. 3, Press, Cambridge, Neogene to Modern Phosphorites, Cambridge Univ.

Burollet, P. F., Stainfeld, P., 1956. Notice explicative de la carte geologique de la Tunisie au 50 000e, feuille n °44, E1 Kef, avec une étude sommaire des microfaunes de la région d'El Kef par F Dalbiez. Serv. Min. Ind. Energie. Tunis, 40 pp.

Burollet, P.F., 1956. Contribution à l'étude stratigraphique de la Tunisie centrale. Thèse Sc. Alger. Ann. Min. Géol. Tunis, 18, 350 p.

Chabou-Mostefai, S., 1987. Etude de la série phosphatée tertiaire du Djebel Onk. Thése Doctorat. Université de Droit, d'Economie et des Sciences d'Aix-Marseille, France, Algérie, Stratigraphie, Pétrographie. Minéralogie et Analyse Statistique, p. 376.

Chihi, L., Dlala, M. and Ben Ayed, N., 1984. Manifestations tectoniques synsédimentaires et polyphasées d'âge crétacé moyen dans l'Atlas tunisien central (région de Kasserine). C. R. Acad. Sc. Paris, t. 298, série II, n°4, pp. 141-146.

Cielensky, S., Benchernine, N., Watkowski, T., 1988. Travaux de prospection et d'´ evaluation des phosphates dans la région de Bir El Ater. Internal rapport, EREM, 103 p.

Cook, P. J., McElhinny, M. W., 1979. A reevaluation of the spatial and temporal distribution of sedimentary phosphate deposits in the light of plate tectonics. Econ. Geol. 74 (2), 315-330 https://doi.org/10.2113/gsecongeo.74.2.315.

Cook, P.J., 1984. Spatial and temporal controls on the formation of phosphate deposits– a review. Phosphate Miner., 242–274.

Cook, P.J., Shergold, J.H. Eds., 1986. Phosphate Deposits of the World, Vol. 1. Proterozoic and Cambrian Phosphorites. Cambridge University Press, Cambridge, 418 pp.

Cook, P.J., Shergold, J.H., 1984. Phosphorus, phosphorites and skeletal evolution at the Precambrian-Cambrian boundary. Nature. 308, 231-236.

Cornet, M. M., Bétier, M. G., 1952. Carte géologique de l'Algérie au 1 : 500,000 (2e éd.) [Map]. Algeria. Service de la carte géologique de l'Algérie. Gouvernement Général de l'Algérie, Direction du Commerce, de l'´Energie et de 1952; l'Industrie. https://nla.gov.au/nla.obj-2664093697/view.

Damotte, R., 1993. Late Cretaceous and early Tertiary ostracods from North Africa. Cretac. Res .13, 39-47.

Damotte, R., 1995. The biostratigraphy and paleobiogeography of the Upper Cretaceous-basal Tertiary ostracods from North Africa, Mali and Congo. Cretac. Res. 16, 35–366.

Damotte, R., Fleury, J.J., 1987. Ostracodes maastrichtiens et paléocènes du Djebel Dyr, près de Tébessa (Algérie orientale). Geol. Mediterr. 14, 87-107.

Dassamiour, M., Mezghache, H., Raji, O., Bodinier, J.L., 2021. Depositional environment of the Kef Essennoun phosphorites (northeastern Algeria) as revealed by P_2O_5 modeling and sedimentary data. Arab. J. Geosci. 14 (12), 1–17.

Davis, J.C., 1986. Statistics and Data Analysis in Geology. John Wiley and Sons, New York, p. 646.

De Baar, H. J. W., Bacon, M.P., Brewer, P. G., Bruland, K.W., 1985. Rare earth elements in the Pacific and Atlantic Oceans. Geochim. Cosmochim. Acta. 49, 1943-1959. https://doi.org/10.1016/0016-7037(85)90089-4.

Deer, W. A., Howie, R. A., Zussman, J., 1962. Rock-forming minerals, Non-silicates. John Wiley & Sons, New York, 371 p.

Diab, I., Laouar, R., Bosch, D., Tlili, A., Degaichia, A., Bruguier, O., Zaabat, M., Bouhlel, S., Kechiched, R., 2024. The Ain Dibba and Ain Kissa phosphorites, Tebessa (NE Algeria): REE depletion versus shallow, open depositional environment during the Paleocene-Eocene phosphogenesis in North Africa. J Afr Earth Sci. 220, 105433. https://doi.org/10.1016/j.jafrearsci.2024.105433.

Djabou, R.E., Belafrites, A., 2023. Assessment of radioactivity levels and radiological hazard indices in phosphate and phosphate mine waste samples from Algeria. Radiat Prot Dosim 199 (18), 2218–2223. https://doi.org/10.1093/rpd/ ncad061.

Djoulah, B., Hamimed, M., Belghar, N., Boulemia, S., 2023. Sepiolite as paleo-CO2 barometer of dramatic climate change, and a basic element for paleogeographic reconstitution across Cretaceous–Paleogene, Asserdoune boundary, El Kouif region (Algerian–Tunisian border). Carb. Evap. 38:6. https://doi.org/10.1007/s13146-022-00831-z.

Dong, Y., Gachetti, A., Wu, Q., Palma, M. de, Hu, X., Brachfeld, S., Yang, Z., Wang, J., Wang, Y., Jiang, S., Cui, Y., 2024. Paleoenvironment reconstruction of the eastern Tethys during the pre-onset excursion preceding the PETM. Palaeogeogr, Palaeoclimatol, Palaeoecol. 647, 112234. https://doi.org/10.1016/ j. palaeo.2024.112234.

Dubourdieu, G., 1956. Etude structurale et intérêt pétrolier de l'Ouenza (Confins algéro- tunisien). Bull. Serv. Geol. Algerie 10, 659.

Dubourdieu, G., 1959. Exquise géologique du Dj. Mesloula. Publ. Serv. Carte géol. Algérie, nouvelle série. Bull. (Arch. Am. Art) n 21.

Dupuis, C., Steurbaut, E., Molina, E., Rauscher, R., Tribovillard, N., Arenillas, I., Lefèvre, I., 2001. The Cretaceous-Palaeogene (K/P) boundary in the Aïn Settara section (Kalaat Senan, Central Tunisia): lithological, micropalaeontological and geochemical evidence. Bull Koninklijk Belgisch Instituut Natuurwetenschappen, Aardwetenschappen. 71:169–190.

Durozoy, 1947. Compte rendu de la tournée effectuée dans la région de Chéria ANRH Tébessa 60 p.

Gaud, B., 1977. Etude géologique et hydrogéologique du plateau de Chéria, Wilaya de Tébessa. Rapport inte N°2, A.N.R.H de Tébessa, 68p.

Durozoy, G., 1956. Carte Geologique de l'Algérie au 1/50 000, sheet No 206, Tébessa, with explanatory note, 6 p. Publ. Serv. Carte géol. Algérie, Algiers.

Edress, N.A.A., Abdel-Rahman, E.A., Abdel-Wahab, M.G.F., 2023. Geochemical significance for the composition and depositional environments of the Campanian carbonate-rich phosphorite, Abu-Tartur plateau, Western Desert, Egypt. J. Afr. Earth. Sci. 202, 104938. https:// doi.org/10.1016/j.jafrearsci.2023.104938.

El Bamiki, R., Séranne, M., Chellaï, E.H., Merzeraud, G., Marzoqi, M., Melinte-Dobrinescu, M.C., 2020. The Moroccan High Atlas phosphate-rich sediments: Unraveling the ac cumulation and differentiation processes. Sediment. Geol. 403, 105655.

El Bamiki, R., Séranne, M., Parat, F., Aubineau, J., Chellaï, E.H., Marzoqi, M., Bodinier, J.-L., 2023. Post-phosphogenesis processes and the natural beneficiation of phosphates: Geochemical evidence from the Moroccan High Atlas phosphate-rich sediments. Chem. Geol. 631, 121523.

El Feki, H., Rey, C., Vignoles, M., 1991. Carbonate ions in apatites: infrared investigations in the ν4 CO_3 domain. Calcif Tissue Int 49:269–274.

El Haddi, H., Benbouziane, A., Mouflih, M., 2014. Geochemical siliceous and silicified facies of phosphate series of ouled Abdoun Basin (Morocco). Open J. Geol. 4, 295–302. https://doi.org/10.4236/ojg.2014.47022.

Elderfield, H., Hawkesworth, C.J., Greaves, M.J., Calvert, S.E., 1981. Rare earth elements geochemistry of oceanic ferromanganese nodules. Geochem. Cosmochim. Acta 45, 513–528. https://doi.org/10.1016/0016-7037(81)90184-8.

Elderfield, H., Pagett, R., 1986. Analytical chemistry in marine sciences rare earth elements in ichthyoliths: variations with redox conditions and depositional environment. Sci. Total Environ. 49, 175–197. https://doi.org/10.1016/0048-9697(86) 90239–1.

Elgharbi, S., Horchani-Naifer, K., Ferid, M., 2014. Investigation of the structural and mineralogical changes of Tunisian phosphorite during calcinations. J. Therm. Anal. Calorim. 119(1), 265–71. https://doi.org/10.1007/s10973-014-4132-5.

Elliot, J. C., 1994. Structure and chemistry of the apatites and other calcium orthophosphates. Amsterdam: Elsevier and references therein.

Elliott, R.B., 1973. The chemistry of gabbro/amphibolite transitions in south Norway. Contrib. Miner. Petrol. 38, 71-79.

Emsbo, P., Patrick, I., McLaughlin, P.I., Breit, G.N., Du Bray, E.A., Koenig, A.E., 2015. Rare earth elements in sedimentary phosphate deposits: solution to the global REE crisis? Gondwana. Res. 27, 776–785. https://doi.org/10.1016/j.gr.2014.10.008.

Fazio, A.M., Scasso, R.A., Castro, L.N., Carey, S., 2007. Geochemistry of rare earth elements in early-diagenetic miocene phosphatic concretions of Patagonia, Argentina: phosphogenetic implications. Deep. Sea. Res. II 54, 1414–1432. https:// doi.org/10.1016/j.dsr2.2007.04.013.

Felhi M, Tlili A, Montacer M., 2008. Geochemistry, petrographic and spectroscopic studies of organic matter of clay-associated kero gen of Ypresian series: Gafsa-Metlaoui phosphatic basin, Tunisia. Resour. Geol. 59, 428–436.

Felhi, M., 2010. Les niveaux intercalaires de la série yprésienne du bas sin Gafsa-Métlaoui : Apports de la minéralogie des argiles et de lagéochimie de la matière organique résiduelle à la reconstitu tionpaléoenvironnementale. Ph.D. thesis, Sfax University, p 184.

Ferhaoui, S., Kechiched, R., Bruguier, O., Sinisi, R., Kocsis, L., Mongelli, G., Bosch, D., Ameur-Zaimeche, O., Laouar, R., 2022. Rare earth elements plus yttrium (REY) in phosphorites from the T´ ebessa region (Eastern Algeria): abundance, geochemical distribution through grain size fractions, and economic significance. J. Geochem. Explor. 241, 107058. https://doi.org/10.1016/j.

Ferreira da Silva, E., Mlayah, A., Gomes, C., Noronha, F., Charef, A., Sequeira, C., et al., 2010. Heavy elements in the phosphorite from Kalaat Khasba mine (North- western Tunisia):

Potential implications on the environment and human health. J Hazard. Mater. 182 (1–3), 232–245. https://doi.org/10.1016/j. jhazmat.2010.06.020.

Filippelli, G.M., 2008. The global phosphorus cycle: Past, present, and future. Elements 4, 89–95.

Flandrin, J. (1948). Contribution à l'étude stratigraphique du Nummulitique Algérien. Bull. Serv. Carte géol. Algérie, 2e série, n°19, 340p.

Fleet, M.E., Pan, Y., 1995. Site preference of rare earth elements in fluorapatite. Am. Mineral. 80, 329–335. https://doi.org/10.2138/am-1995-3-414

Flicoteaux, R., Lucas, J., 1984. Weathering of Phosphate Minerals. In: Nriagu, J.O., Moore, P.B. (eds) Phosphate Minerals. Springer, Berlin, Heidelberg. https://doi.org/10.1007/978-3-642 61736-2_9.

Fazio, A.M., Scasso, R.A., Castro, L.N., Carey, S., 2007. Geochemistry of rare earth elements in early-diagenetic miocene phosphatic concretions of Patagonia, Argentina: phosphogenetic implications. Deep. Sea. Res. II 54, 1414–1432. https:// doi.org/10.1016/j.dsr2.2007.04.013.

Folk, R.L., Ward, W.C., 1957. Brazos River bar: a study in the significance of grain size parameters. J. Sediment. Petrol. 27, 3–26.

Föllmi, K.B., 1996. The phosphorus cycle, phosphogenesis and marine phosphate-rich deposits. Earth Sci. Rev. 40 (1–2), 55-124.

Froelich, P.N., Arthur, M. A., Burnett, W.C., Deakin, M., Hensley, V., Jahnke, R., Kaul, L., Kim, K.H., Roe, K., Soutar, A., Vathakanon, C., 1988. Early Diagenesis of organic matter in Peru Continental marin sediments: phosphorite precipitation. Mar. Geol. 80, 309-343. https://doi.org/10.1016/0025-3227(88)90095-3.

Galfati, I., Sassi, A.B., Zaier, A., Bouchardon, J.L., Bilal, E., Joron, J.L., Sassi, S., 2010. Geochemistry and mineralogy of Paleocene-Eocene Oum El Khecheb phos phorites (Gafsa-Metlaoui Basin) Tunisia. Geochem. J. 44, 189e210.

Gallala, W., Saïdi, M., El Hajii, S., Zayani, K., Gaied, M.E. and Montacer, M., 2016. Characterization and valorization of Tozeur-Nefta phosphate ore deposit (Southwestern Tunisia). Procedia Engineering 138, pp. 8–18, DOI: 10.1016/j.proeng.2016.02.047

Garnit, H., Bouhlel, S., Barca, D., Chtara, C., 2012. Application of LA-ICP-MS to sedimentary phosphatic particles from Tunisian phosphorite deposits: insights from trace elements and REE into paleo-depositional environments. Chem. Erde 72, 127–139. https://doi.org/10.1016/j.chemer.2012.02.001.

Garnit, H., Bouhlel, S., Jarvis, I., 2017. Geochemistry and depositional environments of Paleocene–Eocene phosphorites: Metlaoui Group, Tunisia. J. Afr. Earth Sci. 134, 704–736. https://doi.org/10.1016/j.jafrearsci.2017.07.021.

Gaud, B., 1977. Etude hydrogéologique du plateau de Chéria, Rapport interne, DEMRH, 74 p.

German, C.R., Elderfield, H., 1990. Application of the Ce anomaly as a paleoredox indicator: the ground rules. Paleoceanography. 5, 823–833. https://doi.org/ 10.1029/PA005i005p00823.

Ghasemian, S., Öztürk, H., Cansu, Z., 2022. Geochemistry of red and cream phosphorites from the Şemikan phosphorite deposit, SE Turkey: Implication for phosphorite deposi tion conditions in the Upper Cretaceous. J. Afr. Earth Sci. 185, 104398. https:// doi.org/10.1016/j.jafrearsci.2021.104398.

Glenn, R.C., Follmi, K.B., Riggs, S.R., Baturin, G.N., Grimm, K.A., Trappe, J., Abed, A.M., Galli-Olivier, C., Garrison, R.E., Ilyin, A., Jehl, C., Roharlich, V., Sadaqah, R.M., Schidlowski, M., Sheldon, R.E., Siegmund, H., 1994. Phosphorus and phosphorites: sedimentology and environments of formation. Eclogae Geol. Helv. 87, 747–788

Gnandi, H. J., Tobschall, G.H., 2003. Distribution patterns of rare earth elements and uranium in tertiary sedimentary phosphorites of Hahotoe Kpogame, Togo. J. Afr. Earth Sci. 37, 1–10.

Godet, A., Föllmi, K.B., 2021., Sedimentary phosphate deposits. In: Encyclopedia of Geology. Elsevier. 922-930. 10.1016/B978-0-08-102908-4.00045-X.

Golroudbary, S.R., Makarava, I., Kraslawski, A., Repo, E., 2022. Global environmental cost of using rare earth elements in green energy technologies. Sci. Total Environ. 832, 155022. https://doi.org/10.1016/j.scitotenv.2022.155022.

Gonzalez, F.J., Somoza, L., Hein, J.R., Medialdea, T., Leon, R., Urgorri, V., Reyes, J., Martın Rubı, J.A., 2016. Phosphorites, Co-rich Mn nodules, and Fe-Mn crusts from Galicia Bank, NE Atlantic: Reflections of Cenozoic tectonics and paleoceanography. Geochem. Geophys. Geosyst. 17, 346–374, doi:10.1002/2015GC005861.

Goolaerts, S., Kennedy, W.J., Dupuis, C., Steurbaut, E., 2004. Terminal Maastrichtian ammonites from the Cretaceous–Paleo gene global stratotype section and point, El Kef, Tunisia. Cretac. Res. 25, 313–328. https://doi.org/10.1016/j.cretres.2004.01.002.

Grandjean, P., Albarede, F., 1989. Rare earth elements in old biogenic apatites. Geochim. Cosmochim. Acta. 57, 2507 – 2514.

Grandjean-Lecuyer, P., Feist, R., Albarede, F., 1993. Rare earth elements in old biogenic apatites. Geochim. Cosmochim. Acta. 57, 2507 – 2514.

Guiraud, R., Bosworth, W., 1997. Senonian basin inversion and rejuvenation of rifting in Africa and Arabia: Synthesis and implications to plate-scale tectonics. Tectonophysics, v. 282, no. 1-4, p. 39-82.

Gulbrandsen, R.A., 1966. Chemical composition of the phosphorites of the phosphoria formation. Geochem. Cosmochim. Acta. 30, 769–778.

Gundogar, D.Y., Sasmaz, A., 2022. Geochemical approach to determine the possible precipitation parameters of the coniacian–santonian mazida˘ gi phosphates, Mardin, Turkey. Minerals. 12, 1544. https://doi.org/10.3390/ min12121544.

Habashi, F., 1985. The Recovery of the Lanthanides from Phosphate Rock. J. Chem. Tech. Biotechnol. 35A, 5-14. https://doi.org/10.1002/jctb.5040350103.

Haddad, F., Yazdi, M., Behzadi, M., Yakymchuk, C., Khoshnoodi, K., 2023. Mineralogy, geochemistry, and depositional environment of phosphates in the Pabdeh Formation, Khormuj anticline, SW of Iran. Environ. Earth Sci. 82, 418. https://doi. org/10.1007/s12665-023-11090-z.

Haj Ahmed, A., Tlili, A., Zalat, A.A., Jeddoui, Y., 2014. Fossil diatoms from endogangue of the Ypresian phosphatic pellets of the Gafsa-Metlaoui basin: implication on the origin of biogenic silica and depositional environment. Arabian J. Geosci. 8 (2), 1077–1087. 10.1007/s12517-013-1253-2.

Hatch, J.R., Leventhal, J.S., 1992. Relationship between inferred redox potential of the depositional environment and geochemistry of the Upper Pennsylvanian (Missourian) Stark Shale Member of the Dennis Limestone, Wabaunsee County, Kansas, USA. In: Meyers, P.A., Pratt, L.M., Nagy, B. (Eds.), Geochemistry of Metalliferous Black Shales. Chem. Geol., vol. 99, pp. 65 – 82.

Hein, J.R., Conrad, T., Mizell, K., Banakar, V. K., Frey, F. A., Sager, W.W., 2016. Controls on ferromanganese crust composition and reconnaissance resource potential, Ninetyeast Ridge, Indian Ocean. Deep. Sea Res. I 110, 1–19. https://doi.org/10.1016/j.dsr.2015.11.006.

Henchiri, M., 2007. Sedimentation, depositional environment and diagenesis of Eocene biosiliceous deposits in Gafsa basin (southern Tunisia). J. Afr. Earth Sci. 49, 187–200. https://doi.org/10.1016/j.jafrearsci.2007.09.001.

Henchiri, M., Fattah, N., 2013. Extent of diagenetic transformations in severely altered biogenic silica deposits from Tunisia: new insights from mineralogy and geochemistry. Arab J. Geosci (2014). 7, 1179–1186. https://doi.org/ 10.1007/s12517-012-0827-8.

Hessler, A.M., Zhang, J., Covault, J., Ambrose, W., 2017. Continental weathering coupled to Paleogene climate changes in NorthAmerica. Geology. 45, 911–914.

Hiatt, E.E., Budd, D.A., 2001. Sedimentary phosphate formation in warm shallow waters: New insight in the palaeoceanography of the Permian Phosphoria Sea from analysis of phosphate oxygen isotopes. Sediment. Geol. 145, p. 119-133.

Hlaiem, A., 1999. Halokinesis and structural evolution of the major features in eastern and southern Tunisian Atlas. Tectonophysics 306, 79e95.

Hoshino, M., 2020. Potential of apatite for heavy rare earth resource. Chikyukagaku Geochem.5 , 29–59. https:// doi.org/10.14934/chikyukagaku.54.29.

Howard, P., 1979. Phosphate. Econ. Geol. 74, 192-194.

Hughes, J.M, Rakovan, J., 2018. The crystal structure of apatite, Ca5 (PO4)3 (F, OH, Cl). Phosphates. De Gruyter, pp 1–12. https :// doi.org/10.1515/9781501509636-004.

Ilyin, A.V., 1998. Rare-earth geochemistry of old phosphorites and probability of syngenetic precipitation and accumulation of phosphate. Chem. Geol. 144, 243-256. https://doi.org/10.1016/S0009-2541(97)00134-4.

Jarvis, I., Burnett, W.C., Nathan, Y., Almbaydin, F. S.M., Attia, A.K.M., Castro, L.N., Flicoteaux R., Hilmy, M.E., Husain, V., Qutawnah, A.A., Serjani, A., Zanin, Y.N., 1994. Phosphorite geochemistry: state-of-the-art and environmental concerns. J. Swiss Geol. Soc. 87, 643-700.

Jasinski, S.M., 2016. Mineral commodity summaries 2016: U.S. Geological Survey, p. 124–125, http://minerals.usgs.gov/minerals/pubs/commodity/phosphate_rock/mcs-2016-phosp.pdf.

Jiang, S.Y., Zhao, H.X., Chen, Y.Q., 2007. Trace and rare earth element geochemistry of phosphate nodules from the Lower Cambrian black shale sequence in the Mufu mountain of Nanjing, Jiangsu Province, China. Chem. Geol. 244, 584–604. https:// doi.org/10.1016/j.chemgeo.2007.07.010.

Jiang, X.D., Sun, X.M., Chou, Y.M., Hein, J.R., He, G.W., Fu, Y., Li, D.F., Liao, J.L., Ren, J. B., 2020. Geochemistry and origins of carbonate fluorapatite in seamount FeMn crusts from the Pacific Ocean. Mar. Geol. 423, 106135. https://doi.org/10.1016/j.margeo.2020.106135.

Jones, B., Manning, D.A.C., 1994. Comparison of geochemical indices used for the interpretation of palaeoredox conditions in ancient mudstones. Chem. Geol. 111, 111-129. https://doi.org/10.1016/0009-2541(94)90085-X.

Jones, S.M., Hoggett, M., Greene, S.E., Jones, T.D., 2019. Large Igneous Province thermogenic greenhouse gas flux could have initiated Paleocene-Eocene Thermal Maximum climate change. Nat. Commun .10, 5547. https://doi.org/10.1038/s41467-019-12957-1.

Jyothi, R. K., Thenepalli, T., Ahn, J. W., Parhi, P. K., Chung, K. W., Lee, J. Y., 2020. Review of rare earth elements recovery from secondary resources for clean energy technologies: Grand opportunities to create wealth from waste. J. Clean. Prod. 267, 122048. https://doi.org/10.1016/j.jclepro.2020.122048.

Kadri, A., Essid, E.M., Merzeraud, G., 2015. “Kasserine Island” boundaries variations during the Upper Cretaceous-Eocene (central Tunisia). J. Afr. Earth Sci. 111, 244–257. https://doi.org/10.1016/j.jafrearsci.2015.07.027.

Kassatkine, Y., Yahyaoui, A., Chatilov, S., 1980. The works of prospecting andassessment on phosphate executed in 1976–1978 in the mining district of Djebel Onk. SONAREM (Société Nationale de Recherche et d'Exploration Minière) Internal report, Algeria, 2, 140.

Kazakov, A.V., 1937. The phosphate facies: origin of the phosphorite and the geologic factors of formation of the deposits. Proc. Sci. Inst. Fertil. Insectofungic. 145, 1–106.

Kechiched, R., 2011. Typologie géochimique et géostatistique des minerais de phosphates du gisement de Bled El Hadba– Djebel Onk (Algérie). Université Badji Mokhtar, Annaba. 175p.

Kechiched, R., Laouar, R., Bruguier, O., Kocsis, L., Salmi-Laouar, S., Bosch, D., Ameur Zaimeche, O., Foufou, A., Larit, H., 2020. Comprehensive REE+Y and sensitive redox trace elements of Algerian phosphorites (Tébessa, eastern Algeria): a geochemical study and depositional environments tracking. J. Geochem. Explor. 208, 106396. https://doi.org/10.1016/j.gexplo.2019.106396.

Kechiched, R., Laouar, R., Bruguier, O., Salmi-Laouar, S., Ameur-Zaimeche, O., Foufou, A., 2016. Preliminary data of REE in algerian phosphorites: a comparative study and paleo-redox insights. Procedia. Eng. 138, 19–29. https://doi.org/10.1016/ j. proeng. 2016.02.048.

Kechiched, R., Laouar, R., Bruguier, O., Salmi-Laouar, S., Kocsis, L., Bosch, D., Foufou, A., Ameur-Zaimeche, O., Larit, H., 2018. Glauconite-bearing sedimentary phosphorites from the T´ ebessa region (eastern Algeria): evidence of REE enrichment and geochemical constraints on their origin. J. Afr. Earth Sci. 145, 190–200. https:// doi.org/10.1016/j.jafrearsci.2018.05.018.

Kechiched, R., Sinisi, R., Kocsis, L., Bruguier, O., Mongelli, G., Ferhaoui, S., Bosch, D., Ameur-Zaimeche, O., Buccione, R., Laouar, R., 2024. Phosphate deposits in North Africa: an overview of Algerian-Tunisian deposits, geochemistry and paleoenvironments. In: Hamimi, Z., et al. (Eds.), The Geology of North Africa. Regional Geology Reviews. Springer, Cham. https://doi.org/10.1007/978-3-031-

Keller, G., 1988. Biotic turnover in benthic foraminifera across the Cretaceous/Tertiary boundary at El Kef, Tunisia. Palaeogeogr. Palaeoclimatol. Palaeoecol. 66, 153–171.

Keller, G., 1988. Extinction, survivorship and evolution of planktic foraminifera across the Cretaceous-Teritary boundary at El Kef, Tunisia. Mar. Micropaleontol. 13, 239-263.

Keller, G., 1995. Mass extinction and evolution patterns across the Cretaceous-Tertiary boundary. In: International Work-shop on Cretaceous-Tertiary Transitions Proceedings, El Kef section, Tunis 1992, Service Geologique de Tunisie. Annales des Mines et de la Geologie. 35, pp. 23-64.

Keller, G., Mateo, P., Punekar, J., Khozyem, H., Gertsch, B., Spangenberg, J., Font, E., Bitchong, A., Adatte, T., 2018. Environmental changes across the Cretaceous Paleogene Mass

Extinction and Paleocene-Eocene Thermal Maximum: Implications for the Anthropocene. Gondwana Res. 56, 69–89.

Khan, K.F., Dar, S.A., Khan, S.A., 2012. Rare earth element (REE) geochemistry of phosphorites of the Sonrai area of paleoproterozoic Bijawar basin, Uttar Pradesh, India. J. Rare Earths. 30, 507–514. https://doi.org/10.1016/S1002-0721(12)60081.

Khan, S.A., Khan, K.F., Dar, S.A., 2016. REE geochemistry of early Cambrian phosphorites of Masrana and Kimoi blocks, Uttarakhand, India. Arab. J. Geosci. 9, 1–10. https://doi.org/10.1007/s12517-016-2477-8.

Khelifi, F., Caporale, A.G., Hamed, Y., Adamo, P., 2021. Bioaccessibility of potentially toxic metals in soil, sediments and tailings from a north Africa phosphate-mining area: insight into human health risk assessment. J Environ Manag 279, 111634. https://doi.org/10.1016/j.jenvman.2020.111634.

Khelifi, F., Melki, A., Hamed, Y., Adamo, P., Caporale, A.G., 2020. Environmental and human health risk assessment of potentially toxic elements in soil, sediments, and ore-processing wastes from a mining area of southwestern Tunisia. Environ Geochem Health. 42 (12), 4125–4139. https://doi.org/10.1007/s10653-019- 00434-z.

Kocsis, L., Gheerbrant, E., Mouflih, M., Cappetta, H., Ulianov, A., Chiaradia, M., Bardet, N., 2016. Gradual changes in upwelled seawater conditions (redox, pH) from the late Cretaceous through early Paleogene at the northwest coast of Africa: negative Ce anomaly trend recorded in fossil bio-apatite. Chem. Geol. 421, 44–54. https://doi.org/10.1016/j.chemgeo.2015.12.001.

Kocsis, L., Ounis, A., Baumgartner, C., Pirkenseer, C., Harding, I.C., Adatte, T., Chaabani, F., Mohamed, S., 2014. Paleocene – Eocene palaeoenvironmental conditions of the main phosphorite deposits (Chouabine Formation) in the Gafsa Basin, Tunisia. J. Afr. Earth Sci. 100, 586–597. https://doi.org/10.1016/j. jafrearsci.2014.07.024.

Koleva, V., Petkova, V., 2012. IR spectroscopic study of high energy activated Tunisian phosphorite. Vib. Spectrosc .58, 125-132. https://doi.org/10.1016/j.vibspec.2011.09.010

Koritnig, S., 1978. Phosphorus. In: Wedepohl KH (ed) Handbook of geochemistry, vol 11-2. Springer, Berlin, Heidelberg, New York, p B-I-O-19.

Kowalski, W.M., Hamimed, M., 2000. Diapirisme polyphasé ou glacier de sel albien? Dilemme du matériel triasique des confins algéro-tunisiens. Bull. Serv. Géol. Algérie. 11, 29–60.

Kynicky, J., Smith, M.P., Xu, C., 2012. Diversity of rare earth deposits: the key example of China. Elements 8, 361–367.

Laffitte, R., 1939. Thesis, Sciences Paris. Bulletin du Service Geologique de l'Algerie, serie 1. Etude geologique de l'Aures (Vol. 11, p. 484), 1 carte au 1/200000.

Lambert, 1947. Etude hydrogéologique du plateau de Chéria. ANRH de Tébessa, 40p.

Laouar, K., Laouar, R., Bruguier, O., Bosch, D., Kechiched, R., Bouhlel, S., Tlili, A., 2024. Geochemistry of bled El Hadba phosphorites (NE Algeria): glauconitization process versus REE-enrichment. J. Geochem. Explor. 258, 107398. https://doi.org/10.1016/ j. gexplo.2024.107398.

Lasheen, E.S.R., Zakaly, H.M.H., Alotaibi, B.M., Saadawi, D.A., Ene, A., Fathy, D., Awad, H.A., El Attar, R.M., 2022. Radiological risk parameters of the phosphorite deposits, Gebel Qulu El Sabaya: natural radioactivity and geochemical characteristics. Minerals. 12, 1385. https://doi.org/10.3390/min12111385.

Lauriente, D.H., 1996. Phosphate industry overview. [In:] Chemical Economics Handbook; SRI International: Zurich, Switzerland, 94 pp.

Laurino, J.P., Mustacato, J., Huba, Z, J., 2019. Rare Earth Element Recovery from Acidic Extracts of Florida Phosphate Mining Materials Using Chelating Polymer 1-Octadecene, Polymer with 2,5-Furandione, Sodium Salt. Minerals 9, 477. https://doi.org/10.3390/min9080477.

Laville, Fedan. B., 1989. Le système atlasique marocain au Jurassique. Evolution structurale et cadre géodynamique. Sc. Géol. Mém., Strasbourg, 84, 3 – 28.

Laville, E., Piqué, A., Amrhar, M., Charroud, M., 2004. A restatement of the mesozoic atlasic rifting (Morocco). J. Afr. Earth Sci. 38, 145–153. https://doi.org/10.1016/j. jafrearsci.2003.12.003.

Lécuyer, C., Reynard, B., Grandjean, P., 2004. Rare earth element evolution of Phanerozoic seawater recorded in biogenic apatites. Chem. Geol. 204, 63–102. https://doi.org/10.1016/j.chemgeo.2003.11.003.

LeGeros, P.G., Trautz, O.R., LeGeros, J.P., Klein, E., Shirra, W.P., 1967. Apatite crystallites: effects of carbonate on morphology. Science. 155, 1409–1411.

Li, Y.H., 2000. A Compendium of Geochemistry: from Solar Nebula to the Human Brain. Princeton University Press, Princeton, NJ, p. 475.

Ling, H.F., Chen, X., Li, D., 2013. Cerium anomaly variations in Ediacaran-earliest Cambrian carbonates from the Yangtze Gorges area, South China: implications for oxygenation of coeval shallow seawater. Precambrian Res. 225, 110–127. https://doi.org/10.1016/j.precamres.2011.10.011.

Liu Y., 2002. Review on the vibrational spectroscopy of apatites. J Wuhan Inst of Chem Technol. 1:21–7.

Liu, Z.R.R., Zhou, M.F., 2017. Meishucun phosphorite succession (SW China) records redox changes of the early Cambrian Ocean. Geol. Soc. Am. Bull. 129, 1554–1567. https://doi.org/10.1130/B31612.1.

Lucas, J. and Prévot-Lucas, L.,1996. Tethyan Phosphates and Bioproductites. In: Nairn, A.E.M., Ricou, L.E., Vrielynck, B. and Dercourt, J., Eds., The Ocean Basins and Margins, Plenum Press, New York, 367-391. https://doi.org/10.1007/978-1-4899-1558-0_12.

Lucas, J., El, Faleh, E.M., Prévot, L., 1990. Experimental study of the substitution of Ca by Sr and Ba in synthetic apatites. In: Notholt, A.J.G., Jarvis, I. (Eds.), Phosphorite Research and Development, 52. Geol. Soc. (Spec. Pub.), London, 33–47. https:// doi.org/10.1144/GSL.SP.1990.052.01.04.

Lucas, J., Prevot-Lucas, L., 1995. Tethyan phosphates and bioproductites. In: Nairn, A.E., et al. (Eds.), The Ocean Basins and Margins—The Tethys Ocean, 8. Plenum Press, New York, pp. 367–391. https://doi.org/10.1007/978-1-4899-1558-0_12.

Luo, Y., Hughes, J.M., Rakovan, J., Pan, Y., 2009. Site preference of U and Th and phoshorites on the south west African shelf. Marine chemistry, 2189 in Cl, F and Sr apatites. Am. Mineral. 94, 345–351. https://doi.org/10.2138/am.2009.3026

Maldonado, M., Navarro, L., Grasa, A., Gonzalez, A., Vaquerizo, I., 2011. Silicon uptake by sponges: a twist to understanding nutrient cycling on continental margins. Sci. Reports. 11 1, 1–8. https://doi.org/10.1038/srep00030.

Marino, E., Gonzalez, F.J., Somoza, L., Lunar, R., Ortega, L., V´azquez, J.T., Reyes, J., Bellido, E., 2017. Strategic and rare elements in Cretaceous-Cenozoic cobalt rich ferromanganese crusts from seamounts in the Canary Island Seamount Province (Northeastern tropical Atlantic). Ore Geol. Rev. 87, 41–61.

McArthur, J.M., 1985. Francolite geochemistry - compositional controls during formation, diagenesis, metamorphism and weathering. Geochim. Cosmochim. Acta. 49, 23–35. https://doi.org/10.1016/0016-7037(85)90188-7

McLennan, S.M., 1989. Rare earth elements in sedimentary rocks: influence of provenance and sedimentary processes. In: Lipin, B.R., McKay, G.A. (Eds.), Geochemistry and Mineralogy of Rare Earth Elements. *Rev. Mineral*. 21, 169–200.

McRae, S.G., 1972. Glauconite. Earth Sci. Rev. 8, 397-440. https://doi.org /10.1016/ 0012-8252(72)90063-3.

Meissner, C.R. and Ankary, A. 1970. Geology of phosphate deposits in the Sirhan-Turayf Basin, Kingdom of Saudi Arabia. United States Department of the Interior U.S. Geological Survey Special report. https://doi.org/10.3133/20095.

Moffett, J.W., 1990. Microbially mediated cerium oxidation in sea water. Nature 345, 421–423. https://doi.org/10.1038/345421a0.

Moffett, J.W., 1994. A radiotracer study of cerium and manganese uptake onto suspended particles in Chesapeake Bay. Geochim. Cosmochim. Acta 58 (2), 695–703. https://doi.org/10.1016/0016-7037(94)90499-5.

Morad, S., Felitsyn, S., 2001. Identification of primary Ce-anomaly signatures in fossil biogenic apatite: implication for the Cambrian oceanic anoxia and phosphogenesis. Sediment. Geol. 143, 259–264. https://doi.org/10.1016/S0037-0738(01)00093-8.

Morford, J. L., Russell, A. D., Emerson, S., 2001. Trace Metal Evidence for Changes in the Redox Environment Associated with the Transition from Terrigenous Clay to Diatomaceous Sediment, Saanich Inlet, BC. Mar. Geol, 174, 355–369. https://doi.org/10.1016/S0025-3227(00)00160-2.

Morford, J.L., Emerson, S., 1999. The geochemistry of redox sensitive trace metals in sediments. Geochem. Cosmochim. Acta 63, 1735–1750. https://doi.org/10.1016/ S0016-7037(99)00126-X.

Nash, W.P., 1984. Phosphate Minerals in Terrestrial Igneous and Metamorphic Rocks. In: Nriagu, J.O., Moore, P.B. (Eds.), Phosphate Minerals. Springer, Berlin, Heidelberg. https://doi.org/10.1007/978-3-642-61736-2_6.

Nathan, Y., 1984. The mineralogy and geochemistry of phosphorites. In: Nriagu, J.O., Moore, P.B. (Eds.), Phosphate Minerals. Springer, Berlin Heidelberg, pp. 275–291.

Notholt, A. J. G., Jarvis, I., 1989. A decade of phosphorite research and development. J. Geol. Soc. 146(5), 873-876. https://doi.org/10.1144/gsjgs.146.5.0873

Notholt, A., 1985. Phosphorite resources in the Mediterranean (Tethyan) phosphogenic prov ince: a progress report. Sciences Géologiques, bulletins et mémoires 77, 9–17.

Notholt, A.J.G., 1980. Economic phosphatic sediments: mode of occurrence and stratigraphical distribution. J. Geol. Soc. Lond. 137, 793–805. https://doi.org/ 10.1144/gsjgs.137.6.0793.

Notholt, A.J.G., Sheldon, R.P., Davidson, D.F., 1989. Phosphate Deposits of the World, 2. Cambridge University Press, Cambridge, p. 566.

Nozaki, Y., Zhang, J., Amakawa, H., 1997. The fractionation between Y and Ho in the marine environment. Earth Planet. Sci. Lett. 148, 329-340. https://doi.org/10.1016/S0012-821X(97)00034-4.

Ounis, A., Kocsis, L., Chaabani, F., Pfeifer, H.R., 2008. Rare earth elements and stable isotope geochemistry (δ13C and δ18O) of phosphorite deposits in the Gafsa Basin, Tunisia. Palaeogeogr. Palaeoclimatol. Palaeoecol. 268, 1–18. https://doi.org/ 10.1016/j.palaeo.2008.07.005.

Palache, Charles, Berman, Harry, Frondel, Clifford., 1951. Dana's system of mineralogy [7th ed.]. John Wiley & Sons 2, New York, 1124pp.

Pan, Y., and Fleet, M.E., 2002. Compositions of the Apatite-Group Minerals: Substitution Mechanisms and Controlling Factors. *Rev. Mineral. Geochem*. 48, 13-49. https://doi.org /10.2138/rmg.2002.48.2.

Papineau, D., 2010. Global biogeochemical changes at both ends of the Proterozoic: Insights from phosphorites. Astrobiology 10, 201. https://doi.org/ 10.1089/ast.2009.0360.

Passega, R., 1957. Texture as characteristic of clastic deposition. AAPG Bull 41:1952–1984.

Passega, R., 1964. Grain size representation by CM patterns as a geologic tool. J. Sediment Res 34:830–847

Peiravi, M., Dehghani, F., Ackah, L., Baharlouei, A., Godbold, J., Liu, J., Ghosh, T., 2021. A review of rare-earth elements extraction with emphasis on non-conventional sources: Coal and coal byproducts, iron ore tailings, apatite, and phosphate byproducts. Mining, Metallurgy & Exploration, 38, 1-26

Pi, D.H., Jiang, S.Y., Luo, L., Yang, J.H., Hong-Fei Ling, H.F., 2014. Depositional environments for stratiformwitherite deposits in the Lower Cambrian black shale se quence of the Yangtze Platform, southern Qinling region, SWChina: evidence from redox-sensitive trace element geochemistry. Palaeogeogr. Palaeoclimatol. Palaeoecol. 398, 125–131. https://doi.org/10.1016/j.palaeo.2013.09.029.

Pi, D.H., Liu, C.Q., Graham, A., 2013. Trace and rare earth element geochemistry of black shale and kerogen in the Early Cambrian Niutitang Formation in Guizhou province, South China: constraints for redox environments and origin of metal enrichments. Precambrian Res. 225, 218–229. https://doi.org/10.1016/j.precamres.2011.07.004.

Piper, D.Z. and P.K. Link., 2002. An upwelling model for the Phosphoria Sea: A Permian, ocean-margin sea in the northwest United States. American Association of Petroleum Geologists Bulletin, v. 86, p. 1217-1235.

Piper, D.Z., 1994. Seawater as the source of minor elements in black shales, phosphorites and other sedimentary rocks. Chem. Geol. 114, 95–114. https://doi.org/10.1016/ 0009-2541(94) 90044-2.

Prévot, L., 1988. Géochimie et pétrographie de la formation `a phosphate des Ganntour (Maroc): utilisation pour une explication de la genése des phosphorites crétacé- éocénes. Thése de doctorat. Université Louis Pasteur, Strasbourg, p. 325.

Prian, J.P., Cortiel, Ph., 1993. Etude de développement du gisement de phosphate de Djebel Onk (Algérie). Geological expertise report, BRGM-FERPHOS, Tebessa, Algeria, p. 288.

Provet, L., Lucas, J., 1980. Behaviour of some trace elements in phosphatic sedimentary formations. Soc. Econ. Paleontol. Mineral. Publ. 20, 31–39.

Ptáček, P., 2016. Phosphate rocks. In: Ptacek, P. (Ed.), Apatites and Their Synthetic Analogues - Synthesis, Properties and Applications. Intech Open, London. https://doi.org/10.5772/62214. https://www.intechopen.com/chapt ers/49984.

Pufahl, P.K., 2010. Bioelemental sediments. In: James, N.P., Dalrymple, R.W., (Eds.), Facies models, 4th ed. Geological Association of Canada, pp477–503.

Pufahl, P.K., Grimm, K.A., 2003. Coated phosphate grains: proxy for physical, chemical, and ecological changes in seawater. Geology 31, 801–804.

Pufahl, P.K., Groat, L.A., 2016. Sedimentary and Igneous Phosphate Deposits: Formation and Exploration: An Invited Paper. Econ. Geol. 112, 483-516.

Rakovan, J.F., Hughes, J.M., 2000. Strontium in the apatite structure: strontian f luorapatite and belovite-(Ce). Can. Mineral. 38, 839–845. https://doi.org/10.2113/ gscanmin.38.4.839.

Ranchin, G., 1963. Les phosphates de chaux sédimentaire de la région du Djebel Onk (Algérie), S.E.R.M. Paris, p 85.

Rasmussen, B., 1996. Early-diagenetic REE-phosphate minerals (florenctite, gorceixite, crandallite, and xenotime) in marine sandstone: a major sink for oceanic phorous. J. Sci. 296, 601-632.

Regnier, P., Lasaga, A.C., Berner, R.A., Han, O.H., Zilm, K.W., 1994. Mechanism of CO_3^{2-} substitution in carbonate-fluorapatite: evidence from FTIR spectroscopy, 13C NMR, and quantum mechanical calculations. Am. Mineral. 79, 809–818.

Reynard, B., Lécuyer, C., Grandjean, P., 1999. Crystal-chemical controls on rare earth element concentrations in fossil biogenic apatites and implications for paleoenviromental reconstructions. Chem. Geol. 155, 233–241. https://doi.org/ 10.1016/S0009-2541(98)00169-7.

Richard, 1973. Esquisse de synthèse géophysique, géologique de la région de Tébessa. ANRH de Tébessa, 50p.

Riggs, S.R. and Sheldon, R.P., 1990. Paleooceanographic and paleoclimatic controls of the temporal and geographicdistribution of Upper Cenozoic continental margin phosphorites. In W.C. Burnett and S. Riggs (Eds.), Phosphorite Deposits of the World, v. 3, Neogene to Modern Phosphorites. Cambridge University Press, p. 203-222.

Riggs, S.R., 1984. Paleoceanographic model of Neogene phosphorite deposition, U.S. Atlantic Continental Margin. Science, 223:123 131.

Robaszynski, F., 1986. Biostratigraphy and events at the Campanian–Maastrichtian boundary. *Ann. Soc. géol. Belg.*109, 325-331.

Said, R., 1978. Etude stratigraphique et micropaleontologique du passage Crétacé-Tertiaire du synclinal d'Elles (region Siliana-Sers), Tunisie centrale. Thése 3 cycle, Univ. Paris VI, 275 pp.

Salaj, J., 1990. L'Harien (Palboc6ne moyen) et ses limites. 2dme Congrds National des Sciences de la Terre, Tunis, 236.

Salmi-Laouar, S., 2004. Contribution à l'étude géologique et géochimie des isotopes stables (S, O, C) des minéralisations polymétalliques (Zn-Pb-F-Ba-Fe-Hg) de la zone des diapirs du nord de Tébessa (NE, Algérien). Thèse de Doctorat, Université d'Annaba, 181p.

Salsani, A., Amini, A., Shariati, S., Aghanabati, S. A. Aleali, M., 2020. Geochemistry, facies characteristics and palaeoenvironmental conditions of the storm-dominated phosphate-bearing deposits of eastern Tethyan Ocean; A case study from Zagros region, SW Iran. AIMS Geosciences 6(3), pp. 316–354, doi: 10.3934/geosci.2020019.

Sami, L., 2011. Caractérisation géochimique des minéralisations à Pb-Zn, F, Ba, Cu, Fe et Hg des confins Algéro-tunisiens. Thèse. Doct. D'Etat, (FSTGAT) USTHB, Alger. Algérie. 179p.

Santosh, M., Groves, D.I., Yang, C.X., 2024. Habitable planet to sustainable civilization: Global climate change with related clean energy transition reliant on declining critical metal resources. Gondwana Res. 130, 220-233. https://doi.org/10.1016/j.gr.2024.01.013.

Saouli, S., Kechiched, R., Bruguier, O., Mongelli, G., Bosch, D., Ameur-Zaimeche, O., Boumaza, B., Laouar, R., 2025. Multi-scale (whole-rock, grain size, and particles) distribution of potentially hazardous elements (PHEs) in sedimentary phosphorites from Algerian deposits: Geochemical and environmental implications. J. Hazard. Mater. 494, 138414 https://doi.org/10.1016/j.jhazmat.2025.138414.

Sassi, S., 1974. La sedimentation phosphaée au Paléocéne dans le Sud et le Centre- Ouest de la Tunisie. Université Paris Sud Orsay, France, Thése Doctorat, p. 292.

Scopelliti, G., Bellanca, A., Neri, R., Sabatino, N., 2010. Phosphogenesis in the Bonarelli Level from northwestern Sicily, Italy: petrographic evidence of microbial mediation and related REE behavior. Cretac. Res 31, 237-248. https://doi.org/10.1016/j.cretres.2009.11.004.

Shaban, A.M., 2016. A Review on Phosphate Deposits. Book published by American University of Beirut, pp 45.

Sheldon, R.P., 1981. Ancient marine phosphorites. Annual Review of Earth and Planetary Sciences, v. 9, p. 251-284.

Sheldon, R.P., 1989. Phosphorite deposits of the Phosphoria Formation, Western United States. In A.J.G. Notholt, R.P. Sheldon and D.F. Davidson (Eds.), Phosphate Deposits of the World, Volume 2, Phosphate Rock Resources. Cambridge University Press, p. 53-61.

Sheldon, R.P., 1987. Association of phosphatic and siliceous marine sedimentary deposits. In: Hein, J.R. (Ed.), Siliceous Sedimentary Rock-Hosted Ores and Petroleum, Van Norstrand. Reinhold Co, New York, pp. 58–8

Shields, G., Stille, P., 2001. Diagenetic constraints on the use of cerium anomalies as palaeoseawater redox proxies: an isotopic and REE study of Cambrian phosphorites. Chem. Geol. 175, 29–48. https://doi.org/10.1016/S0009-2541(00)00362-4.

Sigal, J., 1977. Essai de zonation du Crétacé méditerranéen à l'aide des Foraminifères planctoniques. Géol. Méditerr. VI, 2, p. 99-108.

Soudry, D., Glenn, C.R., Nathan, Y., Segal, I., VonderHaar, D., 2006. Evolution of the Tethyan phosphogenesis along the northern edges of the Arabian-African shield during the Cretaceous–Eocene as deduced from temporal variations in Ca and Nd isotopes and rates of P accumulation. Earth-Science Reviews, v. 78, p. 27-57. https://doi.org/10.1016/j.earscirev.2006.03.005.

Soudry, D., Nathan, Y., & Ehrlich, S., 2013. Geochemical diagenetic trends during phosphorite formation–economic implications: The case of the Negev Campanian phosphorites, Southern Israel. Sedimentology. 60(3), 800-819.

Stainforth, R.M., Lamb, J.L., Luterbacher, H., Beard, J.H. and Jeffords, R.M., 1975. Cenozoic Planctonic Foraminiferal Zonation and Characteristics of IndexForms. Univ. Kansas Paleont. Contr. 62,425p., 213 Pl.

Storey, M., 2007. Paleocene-Eocene Thermal Maximum and the Opening of the Northeast Atlantic. Science. 316, 587-9. https://doi.o.rg/ 10.1126/science.1135274.

Suciu, N.A., De Vivo, R., Rizzati, N., Capri, E., 2022. Cd content in phosphate fertilizer: Which potential risk for the environment and human health? Curr Opin Environ Sci Health 30, 100392. https://doi.org/10.1016/j.coesh.2022.100392.Scotese, 2008.

Svoboda, k., 1989. The lower Tertiary phosphate deposits of Tunisia. [In:] Notholt, A.J.G., Sheldon R.P. and David-son, D.F., eds. Phosphate Deposits of the World, Volume 2, Phosphate Rock Resources. Cambridge University Press, pp. 284–288

Szilas, C., Bender, K. C, Msolla, M. M., Borggaard, O.K., 2008. The reactivity of Tanzanian Minjingu phosphate rock can be assessed from the chemical. 147:172–7.

Tachikawa, K., Jeandel, C., Roy-Barman, M., 1999. A new approach to the Nd residence time in the ocean: the role of atmospheric inputs. Earth Planet. Sci. Lett. 170, 433-446. https://doi.org/10.1016/S0012-821X(99)00127-2.

Tahri, T., Bouzenzana, A., Bezzi, N., 2019. Characterization and homogenization of Bled El-Hadba phosphate ore, case of Djebel Onk (Algeria). Nauk. Visnyk NHU 2, 28–35. https://doi.org/10.29202/nvngu/2019-2/4.

Tanaka, K., Tani, Y., Takahashi, Y., Tanimizu, M., Suzuki, Y., Kozai, N. and Ohnuki, T., 2010. A specific Ce oxidation process during sorption of rare earth elements on biogenic Mn oxide produced by Acremonium sp. strain KR21-2. Geochim. Cosmochim. Acta. 74, 5463–5477. https://doi.org/10.1016/j.gca.2010.07.010.

Taylor, S.R., McLennan, S.M., 1985. Continental Crust: Its Composition and Evolution. Blackwell, Oxford. 311 p.

Tlili, A., Felhi, M., Fattah, N., Montacer, M., 2011. Mineralogical and geochemical studies of ypresian marly clays and silica rocks of phosphatic series, Gafsa-Metlaoui basin, southwestern Tunisia: implication for depositional environment. Geosci. J. 15 (1), 53–64.

Tlili, A., Felhi, M., Montacer, M., 2010. Origin and depositional environment of palygorskite and sepiolite from the ypresian phosphatic series, South-western Tunisia. Clay Clay Miner. 58, 573–581.

Tooms, J.S., Summerhayes, C.P., Cronan, D.S., 1969. Geochemistry of marine phosphate and manganese deposits. Oceanogr. Mar. Biol. Annu. Rev. 1, 49–100.

Tosquella, J., Martín, M.M., Guerrera, F., Tramontana, M., 2022. The Eocene carbonate platform of the central-western Malaguides (Internal Betic Zone, S Spain) and its meaning for the Cenozoic paleogeography of the westermost Tethys. *Palaeogeogr. Paleoclimatol. Palaeoecol*.589(10),110840.https://doi.org/10.1016/j.palaeo.2022.110840.

Tostevin, R., Shields, G.A., Tarbuck, G.M., He, T., Clarkson, M.O., Wood, R.A., 2016. Effective use of cerium anomalies as a redox proxy in carbonate-dominated marine settings. Chem. Geol. 438, 146–162. https://doi.org/10.1016/j.chemgeo.2016.06. 027.

Tribovillard, N., Algeo, T.J., Lyons, T., Riboulleau, A., 2006. Trace metals as paleoredox and paleoproductivity proxies: an update. Chem. Geol. 232, 12–32. https://doi.org/ 10.1016/j.chemgeo.2006.02.012.

Tzifas, I. Tr., Goldelitsas, A., Magganas, A., Anderoulakaki, E., Eleftheriond, G., Mertzimckis, T.J., Perraki, M., 2014. Uranium-bearing phosphatized limestone of new Greece. J. Geochem. Explor. 143, 62–137. https://doi.org /10.1016/j.gexplo.2014.01.015.

Uda, T., Jacob, K. T., Hirasawa, M., 2000. Technique for enhanced rare earth separation. Science. 289(5488), 2326-2329.

USGS - U.S., 2020. Geological Survey. Mineral Commodity Summaries 2020. U.S. Geol. Surv., p 200. https://doi.org/10.3133/mcs2020.

Vila, J.M., 1980. La chaîne alpine d'Algérie orientale et des confins algéro tunisiens. Thèse de doctorat, Université Paris VI, 665.

Visher, G.S., 1969. Grain size distributions and depositional processes. J. Sediment Res. 39, 1074–1106.

Visse, L., 1951. Le gisement de phosphate de chaux de Djebel Onk. Rapport interne Soc. Dj. Onk, 152 p, 32 pl., 10 pl. h.t.

Visse, L., 1952. Genesis of the southeasterly Algerian-Tunisian phosphatic deposits. In: XIX International Geological Congress, Set 1 (27). Algeria, Algiers, 60 p.

Webb, G.E., Kamber, B.S., 2000. Rare earth elements in Holocene reefal microbialites: A new shallow seawater proxy. Geochim. Cosmochim. Acta. 64, 1557–1565. https://doi.org /10.1016/S0016-7037(99)00400-7.

Wigley, R., Compton, J.S., 2007. Oligocene to Holocene glauconite–phosphorite grains from the Head of the Cape Canyon on the western margin of South Africa. Deep-Sea Res. II 54, 1375–1395.

Winnock, E., 1980. Les dépôts de l'Eocéne inférieur au Nord de L'Afrique. Aperçu Paléogéographique de l'ensemble. Géologie comparée des gisements de phosphates et de pétrole. coll. Interne., Orléans, 6-7 Nov .1979, Doc. B.R.G.M. 24.p 219-243.

Wold, S., Esbensen, K., Geladi, P., 1987. Principal component analysis. Chemom. Intell. Lab. Syst. 2, 37-52. https://doi.org/10.1016/0169-7439(87)80084-9

Wright, J., Schrader, H., Holser, W.T., 1987. Paleoredox variations in ancient oceans recorded by rare earth elements in fossil apatite. Geochim. Cosmochim. Acta. 51, 631–644. https://doi.org/10.1016/0016-7037(87)90075-5.

Wright, J., Seymour, R.S., Shaw, H.F., 1984. REE and Nd isotopes in conodont apatite: variations with geological age and depositional environment. In: Clark, D.L. (Ed.), Conodont Biofacies and Provincialism. Geological Society of America Special Paper. 196. pp. 325–340.

Wu, N., Peng, B., Juhasz, A., Hu, H., Wu, S., Yang, X., Dai, Y., Wang, X., 2024. Mobility and fractionation of rare earth elements during black shale weathering: Implications from acid rock drainage and sequential extraction study. Sci Total Environ 954, 176282. https://doi.org/10.1016/j.scitotenv.2024.176282.

Wu, S., Peng, B., Wu, N., Xie, S., Yang, X., Fang, X., Song, Z., 2024. Mobility and environmental impact of cadmium (Cd) during weathering of carbonaceous black shales in western Hunan, China. J. Hazard Mater. 470, 134267. https://doi.org/ 10.1016/j.jhazmat.2024.134267.

Wu, S., Wang, L., Zhao, L., Zhang, P., El-Shall, H., Moudgil, B., Huang, X., Zhang, L., 2018. Recovery of rare earth elements from phosphate rock by hydrometallurgical processes – a critical review. Chem Eng J. 335, 774–800.

Wu, S.W., Fan, H.F., Xia, Y., Meng, Q.T., Gong, X.X., He, S., Liu, X.Q., Yang, H.Y., Wen, H.J., 2022a. Sources of rare earth elements and yttrium in the early Cambrian phosphorites in Zhijin, southwest China. Ore Geol. Rev. 150, 105146. https://doi. org/10.1016/j.oregeorev.2022.105146.

Wu, S.W., Yang, H.Y., Fan, H.F., Xia, Y., Meng, Q.T., He, S., Gong, X.X., 2022b. Assessment of the effect of organic matter on rare earth elements and yttrium using the zhijin early cambrian phosphorite as an example. Minerals. 12, 876. https://doi. org/10.3390/min12070876.

Xin, H., Jiang, S., Yang, J., Wu, H., Pi, D., 2016. Rare earth element geochemistry of phosphatic rocks in Neoproterozoic Ediacaran Doushantuo Formation in hushan section from the Yangtze Gorges area, South China. J. Earth Sci. 27, 204–210. https://doi.org/10.1007/s12583-015-0653-5.

Xing, J., Jiang, Y., Xian, H., Zhang, Z., Yang, Y., Tan, W., Liang, X., Niu, H., He, H., Zhu, J., 2021. Hydrothermal activity during the formation of REY-rich phosphorites in the early Cambrian Gezhongwu Formation, Zhijin, South China: A micro-and nano-scale mineralogical study. Ore Geol. Rev. 136, 104224. https://doi.org /10.1016/j.oregeorev.2021.104224.

Yerkebulan, R., Perizat, A., Ulzhalgas, N., 2023. Enrichment of low-grade phosphorites by the selective leaching method. Green Proc. Synth. 12(1), 20228150. https://doi.org/10.1515/gps 2022-8150.

Zachos, J. C., H. McCarren, B. Murphy, U. Röhl, and T. Westerhold., 2010. Tempo and scale of late Paleocene and early Eocene carbon isotope cycles: Implications for the origin of hyperthermals, Earth Planet. Sci. Lett., 299, 242–249, https://doi.org/10.1016/j.epsl.2010.09.004.

Zachos, J. C., M. Pagani, L., Sloan, E., Thomas, L., and Billup, k., 2001. Trends, rhythms, and aberrations in global climate 65 Ma to Present, Science. 292, 686 – 693. https://doi.org /10.1126/science.1059412.

Zachos, J.C., Dickens, G.R., Zeebe, R.E., 2008. An early Cenozoic perspective on greenhouse warming and carbon-cycle dynamics. Nature. 451, 279–283.

Zachos, J.C., Schouten, S., et al., 2006. Extreme warming of mid-latitude coastal ocean during the Paleocene–Eocene Thermal Maximum: Inferences from TEX86 and isotope data. Geology. 34, 737–740.

Zaier, A. (1984) Etude stratigraphique et tectonique de la région de Sra Ouertane (Atlas tunisien central). Lithologie, pétrographie et minéralogie de la série phosphatée. Thèse Doct. 3rd Cycle, Faculté des Sciences, University of Tunis, Tunis, 163 p.

Zaïer, A., Beji-Sassi, A., Sassi, S., Moody, R.T.J., 1998. Basin evolution and deposition during the early Paleocene in Tunisia. In: Macgregor, D.S., Moody, R.T.J., Clark Lowes, D.D. (Eds.), Petroleum Geology of North Africa. Geol. Soc. London Spec. Publ. 132, 375-393.

Zargouni, F., 1984. Style et chronologie des deformations des structures de l'Atlas tunisien m′ eridional. Evolution r′ ecente de l'accident Sud-atlasique. C. R. Acad. Sci. Ser. II Univers. 299, 71–76.

Zhang, J., Amakawa, H., Nosaky, Y., 1994. The comparative behavior of Y and lanthanides in seawater on the North Pacific. Geophysic Resources Letter. 21, 2677–2680. https://doi.org/10.1029/94GL02404.

Zhang, S.E., Bourdeau, J.E., Nwaila, G.T., Ghorbani, Y., 2022. Advanced geochemical exploration knowledge using machine learning: predic tion of unknown elemental concentrations and operational prioritiza tion of re-analysis campaigns. *Artif. Intell. Geosci.* 3, 86–100. https://doi.org/10.1016/j.aiig.2022.10.003.

Zhou, C., Jiang, S.Y., 2009. Palaeoceanographic redox environments for the lower Cambrian Hetang Formation in South China: evidence from pyrite framboids, redox sensitive trace elements, and sponge biota occurrence. Palaeogeogr. Palaeoclimatol. Palaeoecol. 271, 279–286. https://doi.org/10.1016/j.palaeo.2008.10.024

Zhu, B., Jiang, S.Y., 2017. A LA-ICP-MS analysis of rare earth elements on phosphatic grains of the Ediacaran Doushantuo phosphorite at Wengan, South China: implication for depositional conditions and diagenetic processes. Geol. Mag. 154, 1381–1397. https://doi.org/10.1017/S001675681700022X.

Zhu, B., Jiang, S.-Y., Yang, J.-H., Pi, D., Ling, H.-F., Chen, Y.-Q., 2014. Rare earth element and SrNd isotope geochemistry of phosphate nodules from the lower Cambrian Niutitang formation, NW Hunan province, south China. Palaeogeogr. Palaeoclimatol. Pal aeoecol. 398, 132–143.

List of the appendices and supplementary material

List of the appendices and supplementary material

Appendix 1. Results of correlation and PCA analysis on clr-data of Ain Dibba and Ain Kissa phosphorite deposits.

Table 1S: Summary statistics:

Variable	Observations	Obs. with missing data	Obs. without missing data	Minimum	Maximum	Mean	Std. deviation
TiO_2	10	0	10	0.0100	0.0666	0.0247	0.0195
SiO_2	10	0	10	0.5477	38.5498	17.8342	15.8958
CaO	10	0	10	30.0108	51.4646	42.1136	8.3517
K_2O	10	0	10	0.0342	0.1606	0.0727	0.0441
Fe_2O_{3t}	10	0	10	0.0422	0.4037	0.1968	0.1256
Al_2O_3	10	0	10	0.0810	1.1093	0.3602	0.3703
P_2O_5	10	0	10	14.1566	24.3625	20.6648	3.6538
MgO	10	0	10	0.3518	1.5386	0.7761	0.4900
Na_2O	10	0	10	0.5426	1.1716	0.8292	0.1697
MnO	10	0	10	0.0007	0.0072	0.0020	0.0019
LOI	10	0	10	7.4198	26.5051	13.6230	6.5681
Zr	10	0	10	9.3311	27.2951	16.1890	5.7943
Y	10	0	10	80.2708	278.8143	183.1340	61.7968
Sr	10	0	10	1366.1910	2148.4608	1792.2155	243.9696
U	10	0	10	28.1278	106.5135	76.3434	25.3788
Zn	10	0	10	57.0366	150.4165	92.2130	33.0312
Cr	10	0	10	114.8247	213.8977	163.9905	32.2795
V	10	0	10	63.3856	118.4363	98.5820	16.8586
Rb	10	0	10	0.4962	5.3518	1.9145	1.6820
Nb	10	0	10	0.2409	2.5923	0.8078	0.7916
Cs	10	0	10	0.0398	0.3380	0.1258	0.1033
Ba	10	0	10	47.8803	175.9963	84.2962	43.6891
Hf	10	0	10	0.1583	0.5759	0.2953	0.1531
Ta	10	0	10	0.0310	0.1967	0.0689	0.0586
Pb	10	0	10	0.6040	2.6026	1.2331	0.5891
Th	10	0	10	0.6720	2.8326	1.7487	0.5656
Sc	10	0	10	1.2672	6.7879	3.5200	1.9197
Co	10	0	10	0.1676	0.5054	0.3373	0.1167
Ni	10	0	10	10.8993	29.7307	18.7576	6.4754
Cu	10	0	10	6.2111	40.4651	18.1173	10.1329
∑ REE	10	0	10	94.8511	344.1684	236.6956	82.3114

Table 2S: Correlation matrix (Pearson (n)):

Variables	TiO_2	SiO_2	CaO	K_2O	Fe_2O_{3t}	Al_2O_3	P_2O_5	MgO	Na_2O	MnO	LOI	Zr	Y	Sr	U	Zn	Cr
TiO_2	**1**																
SiO_2	0.3991	**1**															
CaO	-0.4694	**-0.9961**	**1**														
K_2O	**0.9613**	0.4128	-0.4766	**1**													
Fe_2O_{3t}	**0.9275**	0.5751	-0.6338	**0.9490**	**1**												
Al_2O_3	**0.9957**	0.4241	-0.4937	**0.9758**	**0.9487**	**1**											
P_2O_5	-0.4276	-0.3121	0.3240	-0.2589	-0.3535	-0.3732											
MgO	0.6593	-0.0466	-0.0283	0.6187	0.5426	0.6625	-0.1447	**1**									
Na_2O	-0.1754	-0.2358	0.2138	-0.0731	-0.1005	-0.1321	0.6783	0.3959	**1**								
MnO	-0.1123	-0.5030	0.4956	-0.1581	-0.1704	-0.1379	0.0052	-0.0871	0.0978	**1**							
LOI	-0.1772	**-0.8220**	**0.8133**	-0.2858	-0.3884	-0.2341	-0.2805	0.1332	-0.1441	0.4816	**1**						
Zr	**0.8347**	0.1678	-0.2366	**0.8495**	**0.7698**	**0.8535**	0.0342	0.5289	0.0530	0.1104	-0.2388	**1**					
Y	-0.1745	-0.3902	0.3819	-0.0985	-0.1578	-0.1346	0.7144	-0.1181	0.4153	0.4815	-0.0698	0.3888	**1**				
Sr	-0.4373	-0.3929	0.3962	-0.3058	-0.3671	-0.3778	**0.8982**	0.0860	**0.7872**	-0.0358	-0.1297	-0.0305	0.6610	**1**			
U	-0.7415	-0.3295	0.3752	-0.6450	-0.6761	-0.7202	**0.8016**	-0.6373	0.3374	0.2092	-0.1463	-0.3242	0.6065	0.6005	**1**		
Zn	**0.8088**	0.1743	-0.2355	**0.8041**	0.7644	**0.8229**	-0.0978	0.4114	-0.1147	0.2490	-0.1710	**0.9630**	0.3867	-0.1647	-0.3540	**1**	
Cr	0.3287	-0.3198	0.2710	0.3385	0.1890	0.3479	0.4113	0.3891	0.3472	0.3550	0.0286	0.7386	**0.7847**	0.4389	0.1034	0.6766	**1**
V	-0.2778	-0.3876	0.3907	-0.3285	-0.2548	-0.2713	-0.0563	-0.0200	0.0958	0.1585	0.4277	-0.1863	0.2352	0.2486	-0.0404	-0.1454	0.1683
Rb	**0.9914**	0.4358	-0.5057	**0.9560**	**0.9526**	**0.9924**	-0.4322	0.6507	-0.1718	-0.1684	-0.2084	**0.8121**	-0.1968	-0.4238	-0.7528	**0.7889**	0.2749
Nb	**0.9973**	0.4060	-0.4761	**0.9499**	**0.9086**	**0.9896**	-0.4350	0.6635	-0.1709	-0.1084	-0.1805	**0.8272**	-0.1847	-0.4479	-0.7389	**0.7954**	0.3368
Cs	**0.9815**	0.4498	-0.5190	**0.9361**	**0.9494**	**0.9814**	-0.4582	0.6255	-0.2003	-0.1829	-0.2070	**0.7924**	-0.2130	-0.4447	-0.7565	**0.7757**	0.2444
Ba	-0.3883	0.4663	-0.4151	-0.2455	-0.1838	-0.3464	0.2551	-0.2673	0.2984	-0.4653	-0.5789	-0.4711	-0.2259	0.2472	0.2253	-0.5581	-0.4196
Hf	**0.9265**	0.2504	-0.3217	**0.9235**	**0.8549**	**0.9364**	-0.1444	0.5908	-0.0278	0.0644	-0.2104	**0.9783**	0.2040	-0.1921	-0.4932	**0.9470**	0.6268
Ta	**0.9940**	0.3699	-0.4419	**0.9510**	**0.9073**	**0.9899**	-0.3797	0.6577	-0.1402	-0.0561	-0.1814	**0.8768**	-0.0869	-0.3942	-0.6943	**0.8480**	0.4180
Pb	0.0427	0.4462	-0.4351	0.1868	0.1313	0.0621	0.3487	-0.0784	0.2948	-0.4132	-0.6358	-0.0093	-0.1914	0.0798	0.2492	-0.1702	-0.2250
Th	0.2828	-0.0130	-0.0241	0.4205	0.4126	0.3449	0.5939	0.2336	0.5196	0.2773	-0.3676	0.6830	0.7595	0.5207	0.2536	0.6485	0.6683
Sc	0.4353	-0.2612	0.2152	0.4741	0.3369	0.4529	0.2985	0.2750	0.1546	0.4747	0.0318	**0.8239**	0.7598	0.2342	0.0524	**0.8234**	**0.9302**

Co	-0.0565	0.7245	-0.7046	0.0211	0.2007	-0.0091	0.0464	-0.0002	0.2285	-0.6500	-0.7184	-0.2682	-0.4066	0.0961	-0.0696	-0.3363	-0.5347
Ni	**0.8587**	0.3839	-0.4453	**0.8737**	**0.8787**	**0.8827**	-0.1085	0.4315	-0.0406	0.0928	-0.3675	**0.9528**	0.2841	-0.1756	-0.4008	**0.9601**	0.5721
Cu	0.2619	0.4201	-0.4254	0.2639	0.3148	0.2759	0.0847	-0.1836	-0.3152	-0.1244	-0.5055	0.3484	0.1056	-0.1689	0.1391	0.4073	-0.0039
Somme REE	-0.0142	-0.3080	0.2895	0.0724	0.0169	0.0296	**0.6700**	-0.0340	0.3962	0.4640	-0.1297	0.5296	**0.9834**	0.6000	0.5065	0.5277	**0.8171**

continues

Variables	V	Rb	Nb	Cs	Ba	Hf	Ta	Pb	Th	Sc	Co	Ni	Cu	Somme REE
TiO_2														
SiO_2														
CaO														
K_2O														
Fe_2O_{3t}														
Al2O3														
P_2O_5														
MgO														
Na_2O														
MnO														
LOI														
Zr														
Y														
Sr														
U														
Zn														
Cr														
V	**1**													
Rb	-0.2347	**1**												
Nb	-0.2962	**0.9818**	**1**											
Cs	-0.2040	**0.9972**	**0.9703**	**1**										
Ba	-0.1153	-0.3728	-0.3735	-0.3867	**1**									
Hf	-0.2090	**0.9046**	**0.9216**	**0.8864**	-0.4534	**1**								
Ta	-0.2609	**0.9776**	**0.9949**	**0.9656**	-0.4116	**0.9545**	**1**							
Pb	-0.6813	0.0274	0.0624	0.0009	0.6204	0.0047	0.0269	**1**						

Th	-0.0762	0.2926	0.2546	0.2700	-0.1516	0.5603	0.3321	0.1004	**1**					
Sc	0.0609	0.3818	0.4305	0.3513	-0.5104	0.7285	0.5126	-0.2180	0.7326	**1**				
Co	-0.2366	0.0168	-0.0621	0.0294	0.7514	-0.2229	-0.1090	0.5229	-0.0454	-0.6113	**1**			
Ni	-0.1742	**0.8571**	**0.8453**	**0.8486**	-0.3719	**0.9576**	**0.8876**	0.0001	0.6585	0.7076	-0.1011	**1**		
Cu	-0.6757	0.2762	0.2494	0.2847	-0.2145	0.2955	0.2599	0.2128	0.3133	0.1293	0.1638	0.3964	**1**	
Somme REE	0.1708	-0.0323	-0.0297	-0.0499	-0.2734	0.3565	0.0689	-0.1575	**0.8496**	**0.8299**	-0.3869	0.4404	0.1792	**1**

Values in bold are different from 0 with a significance level alpha=0.01

Table 3S: Eigenvalue and Variances of extracted components from Principal Component Analysis:

	F1	F2	F3	F4	F5	F6	F7	F8	F9
Eigenvalue	13.5346	7.2507	4.7748	2.2724	1.2864	0.7569	0.6297	0.3212	0.1733
Variability (%)	43.6599	23.3894	15.4025	7.3303	4.1497	2.4415	2.0314	1.0362	0.5591
Cumulative %	43.6599	67.0493	82.4518	89.7821	93.9318	96.3733	98.4046	99.4409	100.0000

Table 4S: Correlations between variables and factors:

	F1	F2	F3	F4	F5	F6	F7	F8	F9
TiO_2	0.9791	-0.1308	0.1060	-0.0742	-0.0762	0.0039	-0.0329	-0.0033	-0.0234
SiO_2	0.4083	-0.6660	-0.4927	0.1681	0.3060	0.0938	0.0155	0.1219	-0.0346
CaO	-0.4775	0.6443	0.4771	-0.1368	-0.2890	-0.0829	-0.0296	-0.1255	0.0600
K_2O	0.9612	-0.0839	-0.0654	-0.1105	-0.0995	0.0451	-0.0736	-0.1453	0.1185
Fe_2O_{3t}	0.9388	-0.2040	-0.1091	-0.0711	0.1007	0.0486	0.1210	-0.1749	0.0495
Al_2O_3	0.9870	-0.1106	0.0387	-0.0952	-0.0421	-0.0123	-0.0214	-0.0223	0.0116
P_2O_5	-0.3065	0.6223	-0.6630	-0.1097	-0.1798	-0.1390	-0.0857	-0.0897	0.0124
MgO	0.6034	0.0681	0.1551	-0.6835	-0.2330	-0.1188	0.1760	0.2000	0.0269
Na_2O	-0.1266	0.4357	-0.4777	-0.6600	-0.1521	0.1528	0.2495	0.0410	-0.1412
MnO	-0.0469	0.6004	0.3725	0.2610	-0.0297	0.5402	0.3645	0.0698	0.0028
LOI	-0.2659	0.2669	0.8841	-0.1412	-0.2110	-0.0041	0.0506	-0.0886	0.0378
Zr	0.9127	0.3813	-0.1014	0.0392	-0.0177	-0.0329	-0.0871	0.0136	-0.0236
Y	0.0016	0.9278	-0.2857	0.1472	0.1840	0.0001	-0.0134	0.0411	-0.0113
Sr	-0.3366	0.6221	-0.5017	-0.4233	0.0181	-0.2506	0.0173	0.0238	0.0688
U	-0.6326	0.4818	-0.4752	0.3105	-0.1131	0.0147	-0.0552	-0.0658	-0.1583
Zn	0.8984	0.3702	0.0172	0.2089	0.0902	0.0067	0.0176	0.0070	0.0575
Cr	0.4395	0.8223	-0.0503	-0.1059	0.0460	-0.0159	-0.2184	0.2568	-0.0285
V	-0.2674	0.3064	0.4109	-0.3739	0.6923	-0.0663	-0.0729	-0.1458	-0.1250
Rb	0.9724	-0.1677	0.0825	-0.0938	-0.0150	-0.0569	0.0189	-0.0691	-0.0453
Nb	0.9720	-0.1406	0.1063	-0.0770	-0.0951	0.0313	-0.0578	0.0521	-0.0455
Cs	0.9615	-0.1901	0.0983	-0.0765	0.0228	-0.0844	0.0338	-0.0874	-0.0865
Ba	-0.3952	-0.4307	-0.6420	-0.2727	0.1576	0.2776	-0.1752	0.0447	0.1930
Hf	0.9709	0.2188	-0.0130	-0.0052	-0.0277	0.0277	-0.0858	0.0053	-0.0200
Ta	0.9863	-0.0485	0.0918	-0.0604	-0.0633	0.0285	-0.0542	0.0497	-0.0512
Pb	0.0271	-0.3287	-0.7247	-0.0443	-0.4663	0.2643	-0.2205	-0.1296	-0.1063
Th	0.4456	0.6644	-0.5048	-0.0128	0.0643	0.0311	0.2431	-0.1861	0.0788
Sc	0.5573	0.7906	0.0023	0.1143	0.0323	0.1019	-0.1709	0.0496	0.0905
Co	-0.0669	-0.6322	-0.6535	-0.2523	0.1853	-0.0918	0.2488	0.0000	0.0221
Ni	0.9422	0.2121	-0.1450	0.1151	0.1602	0.0596	0.0268	-0.0500	-0.0247
Cu	0.3471	-0.0777	-0.3880	0.6950	-0.1935	-0.3688	0.2469	0.0737	0.0125
Somme REE	0.1657	0.9073	-0.3081	0.1536	0.1736	0.0063	0.0138	-0.0224	0.0068

Table 5S: Factor scores:

Observation	F1	F2	F3	F4	F5	F6	F7	F8	F9
21addi04	-2.3205	-3.1283	-1.3007	-1.0845	1.7603	0.7705	-0.2294	0.3948	0.6737
21addi08	-2.9140	1.0111	0.2149	-3.4096	-0.7028	-0.5523	0.9096	0.3699	-0.3168
21bkddi09	-2.3756	-1.1880	-2.9288	-0.1767	-1.2136	0.9443	-1.1069	-0.5971	-0.4559
21bdkdi14	-1.1127	4.0327	1.6997	1.2298	0.1722	1.7790	0.8606	0.0307	-0.0442
21bkddi23	-1.5802	-1.3031	-2.2990	2.4779	-1.4351	-0.7512	0.7585	0.6058	0.2530
21akdi06	7.5706	-2.7144	1.5652	0.0375	-0.0707	0.3498	-0.3244	0.7518	-0.4452
21akdi10	6.4854	2.8550	-1.1658	-0.9676	-0.6769	-0.3003	-0.0701	-0.6107	0.6487
21akdi14	-2.1982	4.2075	0.6576	0.6722	0.8773	-1.0048	-1.4219	0.4817	-0.0898
21akdi16	1.0496	-0.8891	-1.2783	0.8378	1.9947	-0.7967	0.8360	-0.7722	-0.4675
21akdi18	-2.6043	-2.8833	4.8355	0.3832	-0.7055	-0.4383	-0.2120	-0.6548	0.2441

Appendix 2. Results of correlation and PCA analysis on clr-data of Troubia phosphorite deposit.

Table 1S: Summary statistics:

Variable	Observations	Obs. with missing data	Obs. without missing data	Minimum	Maximum	Mean	Std. deviation
TiO_2	6	0	6	0.008	0.040	0.017	0.012
SiO_2	6	0	6	26.931	44.128	37.187	6.796
Ca0	6	0	6	28.552	33.399	30.046	1.912
K_20	6	0	6	0.010	0.068	0.031	0.026
Fe_2O_{3t}	6	0	6	0.016	0.134	0.062	0.045
Al_2O_3	6	0	6	0.070	0.455	0.211	0.171
P_20_5	6	0	6	18.395	24.798	20.638	2.639
MgO	6	0	6	0.100	1.395	0.392	0.497
As	6	0	6	5.420	8.840	6.393	1.252
Zr	6	0	6	27.810	32.480	30.650	1.551
Y	6	0	6	68.090	145.200	96.975	33.210
Sr	6	0	6	1263.310	1433.150	1360.458	58.605
U	6	0	6	41.440	80.520	57.815	15.273
Zn	6	0	6	42.710	199.280	98.580	59.099
Cr	6	0	6	56.980	88.210	73.423	11.228
V	6	0	6	5.000	50.830	37.267	16.700

Table 2S: Correlation matrix (Pearson (n)):

Variables	TiO_2	SiO_2	Ca0	K_20	Fe_2O_{3t}	Al_2O_3	P_20_5	MgO	As	Zr	Y	Sr	U	Zn	Cr	V
TiO_2	**1**															
SiO_2	0.320	**1**														
Ca0	-0.313	**-0.950**	**1**													
K_20	**0.875**	0.361	-0.295	**1**												
Fe_2O_{3t}	**0.919**	0.179	-0.155	**0.962**	**1**											
Al_2O_3	**0.899**	0.281	-0.241	**0.956**	**0.927**	**1**										
P_20_5	-0.360	**-0.995**	**0.961**	-0.391	-0.211	-0.335	**1**									
MgO	-0.225	0.532	-0.427	-0.098	-0.186	-0.354	-0.449	**1**								
As	-0.382	-0.494	0.261	-0.334	-0.194	-0.386	0.491	-0.076	**1**							
Zr	**0.636**	**0.682**	**-0.810**	0.629	0.566	0.634	-0.734	-0.021	-0.048	**1**						
Y	-0.569	-0.773	0.625	-0.690	-0.495	-0.695	**0.795**	-0.107	**0.772**	-0.583	**1**					
Sr	-0.607	0.002	0.024	-0.233	-0.417	-0.216	-0.012	-0.036	0.154	-0.096	-0.078	**1**				
U	-0.648	-0.739	**0.672**	**-0.848**	-0.690	**-0.790**	**0.765**	-0.145	0.422	-0.786	0.890	-0.088	**1**			
Zn	-0.031	**0.661**	**-0.642**	-0.208	-0.353	-0.168	-0.693	0.355	-0.625	0.229	-0.491	0.004	-0.176	**1**		
Cr	0.320	-0.130	-0.040	0.255	0.434	0.205	0.140	0.161	0.646	0.305	0.385	-0.500	-0.007	-0.588	**1**	
V	-0.379	-0.194	0.064	-0.737	-0.588	-0.731	0.225	0.199	0.315	-0.325	0.667	-0.438	0.744	0.223	0.229	**1**

Values in bold are different from 0 with a significance level alpha=0.01

Table 3S: Eigenvalue and Variances of extracted components from Principal Component Analysis:

	F1	F2	F3	F4	F5
Eigenvalue	7.490	3.812	2.283	1.527	0.888
Variability (%)	46.812	23.822	14.266	9.547	5.552
Cumulative %	46.812	70.635	84.901	94.448	100.000

Table 4S: Correlations between variables and factors:

	F1	F2	F3	F4	F5
TiO_2	-0.780	-0.487	0.154	-0.355	-0.068
SiO_2	-0.773	0.583	0.230	0.083	0.054
Ca0	0.710	-0.524	-0.399	-0.168	0.185
K_20	-0.850	-0.501	-0.060	0.034	0.148
Fe_2O_3t	-0.722	-0.677	0.070	-0.066	0.109
Al_2O_3	-0.826	-0.515	-0.197	-0.081	-0.086
P_20_5	0.803	-0.553	-0.203	-0.084	0.031
MgO	-0.093	0.514	0.463	0.202	0.687
As	0.550	-0.349	0.430	0.579	-0.236
Zr	-0.809	-0.030	0.332	0.250	-0.416
Y	0.917	-0.234	0.308	0.060	-0.082
Sr	0.139	0.323	-0.586	0.725	-0.093
U	0.960	0.017	0.078	-0.259	-0.071
Zn	-0.311	0.849	-0.017	-0.357	-0.236
Cr	0.000	-0.570	0.791	0.212	0.065
V	0.607	0.296	0.616	-0.375	-0.155

Table 5S: Factor scores:

Observation	F1	F2	F3	F4	F5	F6	F7	F8	F9
21addi04	-2.3205	-3.1283	-1.3007	-1.0845	1.7603	0.7705	-0.2294	0.3948	0.6737
21addi08	-2.9140	1.0111	0.2149	-3.4096	-0.7028	-0.5523	0.9096	0.3699	-0.3168
21bkddi09	-2.3756	-1.1880	-2.9288	-0.1767	-1.2136	0.9443	-1.1069	-0.5971	-0.4559
21bdkdi14	-1.1127	4.0327	1.6997	1.2298	0.1722	1.7790	0.8606	0.0307	-0.0442
21bkddi23	-1.5802	-1.3031	-2.2990	2.4779	-1.4351	-0.7512	0.7585	0.6058	0.2530
21akdi06	7.5706	-2.7144	1.5652	0.0375	-0.0707	0.3498	-0.3244	0.7518	-0.4452
21akdi10	6.4854	2.8550	-1.1658	-0.9676	-0.6769	-0.3003	-0.0701	-0.6107	0.6487
21akdi14	-2.1982	4.2075	0.6576	0.6722	0.8773	-1.0048	-1.4219	0.4817	-0.0898
21akdi16	1.0496	-0.8891	-1.2783	0.8378	1.9947	-0.7967	0.8360	-0.7722	-0.4675
21akdi18	-2.6043	-2.8833	4.8355	0.3832	-0.7055	-0.4383	-0.2120	-0.6548	0.2441